Development and Characterization of High-Entropy Alloys for High Temperature Applications

Submitted in

fulfillment of the requirements for the degree of

Doctorof Philosophy

by

Vikas Kukshal

ID: 2014RME9049

Under the Supervision of

Dr. Amar Patnaik
and
Prof. I. K. Bhat

DEPARTMENT OF MECHANICAL ENGINEERING

MALAVIYA NATIONAL INSTITUTE OF TECHNOLOGY JAIPUR

November 2018

DECLARATION

I, **Vikas Kukshal**, declare that this thesis titled, "**DEVELOPMENT AND CHARACTERIZATION OF HIGH-ENTROPY ALLOYS FOR HIGH TEMPERATURE APPLICATIONS**" and the work presented in it, are my own. I confirm that:

- This work was done wholly or mainly while in candidature for a research degree at this university.
- Where any part of this thesis has previously been submitted for a degree or any other qualification at this university or any other institution, this has been clearly stated.
- Where I have consulted the published work of others, this is always clearly attributed.
- Where I have quoted from the work of others, the source is always given. With the exception of such quotations, this thesis is entirely my own work.
- I have acknowledged all main sources of help.
- Where the thesis is based on work done by myself, jointly with others, I have made clear exactly what was done by others and what I have contributed myself.

Date:

Vikas Kukshal
(2014RME9049)

CERTIFICATE

This is to certify that the thesis entitled "**DEVELOPMENT AND CHARACTERIZATION OF HIGH-ENTROPY ALLOYS FOR HIGH TEMPERATURE APPLICATIONS"** being submitted by **Vikas Kukshal (2014RME9049)** is a bonafide research work carried out under my supervision and guidance in fulfillment of the requirement for the award of the degree of **Doctor of Philosophy** in the **Department of Mechanical Engineering**, Malaviya National Institute of Technology, Jaipur, India. The matter embodied in this thesis is original and has not been submitted to any other University or Institute for the award of any other degree.

Place: Jaipur
Date:

Dr. Amar Patnaik
Associate professor
Dept. of Mechanical Engineering
MNIT Jaipur

Prof. I. K. Bhat
(Former Director MNIT Jaipur)
Vice-Chancellor
MIT-World Peace University
Pune

ACKNOWLEDGEMENT

The journey of Ph.D. would not have been possible without the blessing of almighty God and guidance and support of several people. There are many people without whom the Ph.D. would not have been possible at all. So it's very important to acknowledge all my mentors, family and friends for standing by me throughout the duration of Ph.D. work. There are no words to show my gratitude to Dr. Amar Patnaik, Associate Professor in the Department of Mechanical Engineering, MNIT Jaipur and Prof. I. K. Bhat, Vice-Chancellor, MIT World Peace University, Pune for their valuable guidance and consistent encouragement throughout the research work.

A person that plays a very important role, not only in my Ph.D. work but also in nurturing my carrier is Dr. Amar Patnaik. It has been a very long association with him and he is a driving force that allows me to do something beyond my reach. He is the key person in my professional development and a constant source of inspiration. The Ph.D. would not have been possible without his continuous support and guidance in spite of being so busy in the academic and administrative work.

I would like to thank Prof. Udaykumar R Yaragatti, Director MNIT Jaipur for providing facilities for carrying research work at MNIT Jaipur. I would also like to thank Prof. Shyam Lal Soni, Director NIT Uttarakhand for providing me continuous support and encouragement to complete my Ph.D. I would also like to extend my appreciation to Departmental Research Evaluation Committee members Prof. G. S. Dangayach, Dr. M. L. Meena and Dr. Mukesh Kumar for their valuable suggestions during the evaluation of Ph.D. work.

I owe my sincere gratitude to Advanced Research Lab. for Tribology, MNIT Jaipur for extending all the possible facility for fabrication and testing. The Ph.D. work is one such task which cannot be completed without the fellow research scholars. I owe all my gratitude to all of them for contributing in one way or other during the course of my Ph.D. work. My sincere thanks to the technical staff of MNIT Jaipur for providing all necessary support.

The Ph.D. could not have been possible without the support of my fellow faculty members at NIT Uttarakhand. I thank all of them for letting me do my work freely at MNIT Jaipur. I also thank all my mentors during the course of my Ph.D. work from whom I seek guidance when struck in some problem.

I genuinely thank my parents for continuously encouraging me for successful completion of my Ph.D. work. Last, but not the least, I would like to be grateful my wife Poonam, who always encouraged me even in the most difficult time. Without her support and motivation, this work would not have been completed.

Date:

MNIT Jaipur **Vikas Kukshal**

ABSTRACT

Existing metals and alloys are susceptible to working conditions at high temperatures causing rapid oxidation resulting in the reduction of mechanical strength. While Ni-based superalloys and variety of steels are extensively used for high temperature applications in the different industries, still they suffer from the limitations of temperature, pressure and environmental conditions. Conventional alloys are based on one of the commercially available elements which have limited applications to a specific area, even though consisting of various elements to either enhance the property of alloy or facilitate in the fabrication process. Since various industry demands low-density alloys for high temperature application, there is a strong rationale for developing novel alloys fulfilling this requirement. Since a decade, a novel set of materials known as high-entropy alloys (HEAs) or multi-component equimolar or near-equimolar alloys has emerged as a potential source for providing a number of solutions in various fields. Compared to the predictable metallic alloys based on the combination of specific elements, HEAs generally contain five or more principal elements with the concentrations range of 5 and 35 at.%. HEA exhibits exceptional properties such as improved hardness, high tensile strength, high compressive strength, excellent wear and corrosion resistance, explaining their potential applications in different facets.

The alloy design for a particular application is based on the appropriate selection of elements for the development of high-entropy alloys wherein each element plays an imperative role in altering its property. Many HEAs system have been reported extensively in the recent years focusing on the effect of various elements such as Al, Cr, Cu, Mo, Ti and Vn on HEAs. The dominant factor controlling the properties of the HEAs is the configuration of its crystal structure after casting and homogenization process. HEAs may contain single solid solution rather numerous HEAs available in the literature also contains multiple phases comprising of secondary solid solution phases and/or intermetallic phases such as β, Laves and σ.

The developed microstructure in a cast alloy is always not beneficial but many times detrimental resulting in the deterioration of the properties. In case of conventional superalloys, topologically closed packed (TCP) phases can be a source of degradation of mechanical properties. On the contrary, the sluggish diffusion effect can cause thermal stability of microstructures in HEAs and hence exhibits enhanced improvement in the properties. Furthermore, $AlCoCrFeMo_{0.5}Ni_x$ shows increased hardness as compared to commercial Ni-based superalloys at 1273 K. With the advantages of the high entropy

superalloys over conventional alloy, the effect of the addition of other elements on HEAs can be further investigated.

Although numerous equiatomic HEAs have been investigated in the past, there are very few studies reporting the near-equiatomic multi-principal alloy system. In addition, there is no detailed investigation on the effect of Mn, Co and Ti on the phase formation and its impact on the properties of the non-equiatomic HEAs. Mn, Co and Ti is selected as the alloying elements as it falls in the category of transition elements which is in close proximity to that of the majority of elements in the base alloy and thus likely to result in the formation of the solid solution, desirable for the high temperature applications.

The work reported in the thesis work includes casting of alloys and investigating the influence of Manganese (Mn), Cobalt (Co) and Titanium (Ti) on microstructure, phase evolution, physical, mechanical, corrosion, thermal and wear behaviour of $AlCr_{1.5}CuFeNi_2$ high entropy alloy. The alloys are designed based on the various thermodynamic parameters available in the literature. The alloys were investigated using X-ray diffraction (XRD), Optical Microscope, Scanning Electron Microscopes (SEM), Transmission Electron Microscope (TEM) Vickers micro-hardness tester, Universal Testing Machine (UTM) and Pin on disc tribometer.

Finally, multiple criteria decision-making (MCDM) hybrid entropy - TOPSIS (Technique for Order of Preference by Similarity to Ideal Solution) approach is used to rank the alloys based on the various physical, mechanical, corrosion, thermal and wear behaviour. The ranking obtained from implementation of hybrid TOPSIS Entropy method is: Mn_1> (Rank 1) >$Mn_{0.75}$ (Rank 2) >$Mn_{0.50}$ (Rank 3) >$Mn_{0.25}$ (Rank 4)>Ti_1 (Rank 5)>$Ti_{0.75}$ (Rank 6)>$Ti_{0.50}$ (Rank 7)>Mn_0 (Rank 8)>$Ti_{0.25}$ (Rank 9)> $Co_{0.25}$ (Rank 10)>$Co_{0.50}$ (Rank 11)> $Co_{0.50}$ (Rank 12)> Co_1(Rank 13). The outcome of the thesis work would definitely help in understanding the behaviour of high-entropy superalloys and their use in high temperature application. This will prove to be advantageous to the research community to further work on developing high temperature resistant high-entropy alloys.

****

TABLE OF CONTENTS

Content				Page No.
DECLARATION				**i**
CERTIFICATE				**ii**
ACKNOWLEDGEMENT				**iii**
ABSTRACT				**v**
TABLE OF CONTENTS				**vii**
LIST OF FIGURE				**xii**
LIST OF TABLES				**xvi**
Chapter 1	**INTRODUCTION**			**1-7**
	1.1	Back ground and motivation		1
	1.2	High-Entropy alloys		3
		1.2.1	Core effects of HEAs	3
			1.2.1.1 High-entropy of HEAs	3
			1.2.1.2 Sluggish diffusion of HEAs	4
			1.2.1.3 The lattice distortion effect	4
			1.2.1.4 The ‘cocktail’ effect	4
		1.2.2	Classification of HEAs	4
			1.2.2.1 Refractory HEAs	4
			1.2.2.2 Light HEAs	5
			1.2.2.3 Bulk Metallic Glass HEAs (BMGHEAs)	5
			1.2.2.4 High-Entropy Superalloys (HESAs)	5
	1.3	Thesis framework		6
Chapter 2	**LITERATURE REVIEW**			**8-41**
	2.1	Conventional alloys and Superalloys: Issues and challenges		8
	2.2	Thermodynamic behaviour of high-entropy alloys		9
	2.3	Microstructure and phase evolution of high-entropy alloys		10
		2.3.1	Influence of Al as alloying element	11
		2.3.2	Influence of Cr as alloying element	12
		2.3.3	Influence of Cu as alloying element	13

2.3.4 Influence of Mo as alloying element 14

2.3.5 Influence of Ti as alloying element 14

2.4 Physical, mechanical and thermal behaviour of high-entropy alloys 15

2.4.1 Thermal behaviour of HEAs 32

2.5 Corrosion and Tribological characteristics of high-entropy alloys 34

2.5.1 Corrosion behaviour of HEAs 34

2.5.2 Wear analysis of HEAs 37

2.6 Research gap 39

2.7 Proposed objectives of the research work 40

Chapter 3 MATERIALS AND METHODS 42-63

3.1 Materials and fabrication technique 42

3.1.1 Properties of elements used for the development of HEAs 42

3.1.2 Properties of alloying element in HEAs 46

3.2 Alloy preparation 47

3.2.1 Alloy melting and casting 47

3.3 Thermodynamics parameters of HEAs 49

3.4 Phases Evolution of alloys 51

3.5 Microstructural examination 52

3.6 Physical and Mechanical characterization 52

3.6.1 Density 52

3.6.2 Hardness 53

3.6.3 Mechanical Characterization 53

3.7 Corrosion behaviour of HEAs 55

3.8 Thermal conductivity 56

3.9 Pin on disc 56

3.10 Experimental Design 57

3.11 Multi criterion decision-making (MCDM) 59

Chapter 4 THERMODYNAMIC AND MICROSTRUCTURAL ANALYSIS OF HIGH –ENTROPY ALLOYS 64-83

4.1 Thermodynamic and microstructural analysis of $AlCr_{1.5}CuFeNi_2Mn_x$ (x = 0, 0.25, 0.5, 0.75 and 1.0) high entropy alloys 64

4.1.1 Thermodynamic behaviour of 64

$AlCr_{1.5}CuFeNi_2Mn_x$ alloys
4.1.2 Phase evolution and microstructure of $AlCr_{1.5}CuFeNi_2Mn_x$ alloys 66
4.2 Thermodynamic and microstructural analysis of $AlCr_{1.5}CuFeNi_2Co_x$ (x = 0, 0.25, 0.5, 0.75 and 1.0) high entropy alloys 70
4.2.1 Thermodynamic behaviour of $AlCr_{1.5}CuFeNi_2Co_x$ alloys 70
4.2.2 Phase evolution and microstructure of $AlCr_{1.5}CuFeNi_2Co_x$ alloys 72
4.3 Thermodynamic and microstructural analysis of $AlCr_{1.5}CuFeNi_2Ti_x$ (x = 0, 0.25, 0.5, 0.75 and 1.0) high entropy alloys 77
4.3.1 Thermodynamic behaviour of $AlCr_{1.5}CuFeNi_2Ti_x$ alloys 77
4.3.2 Phase evolution and microstructure of $AlCr_{1.5}CuFeNi_2Ti_x$ alloys 79
Chapter 5 PHYSICAL, MECHANICAL AND THERMAL BEHAVIOUR OF HIGH ENTROPY ALLOYS 84-98
5.1 Physical, mechanical and thermal behaviour of $AlCr_{1.5}CuFeNi_2Mn_x$ high-entropy alloys 84
5.1.1 Density of $AlCr_{1.5}CuFeNi_2Mn_x$ high-entropy alloys 84
5.1.2 Microhardness and tensile strength of $AlCr_{1.5}CuFeNi_2Mn_x$ high-entropy alloys 85
5.1.3 Specific strength and Young's modulus of $AlCr_{1.5}CuFeNi_2Mn_x$ high-entropy alloys 86
5.1.4 Compressive strength and flexural modulus of $AlCr_{1.5}CuFeNi_2Mn_x$ high-entropy alloys 87
5.1.5 Thermal conductivity of $AlCr_{1.5}CuFeNi_2Mn_x$ high-entropy alloys 88
5.2 Physical, mechanical and thermal behaviour of $AlCr_{1.5}CuFeNi_2Co_x$ high-entropy alloys 89
5.2.1 Density of $AlCr_{1.5}CuFeNi_2Co_x$ high-entropy alloys 89
5.2.2 Microhardness and tensile strength of $AlCr_{1.5}CuFeNi_2Co_x$ high-entropy alloys 90
5.2.3 Specific strength and Young's modulus of $AlCr_{1.5}CuFeNi_2Co_x$ high-entropy alloys 91
5.2.4 Compressive strength and flexural modulus of $AlCr_{1.5}CuFeNi_2Co_x$ high-entropy alloys 92
5.2.5 Thermal conductivity of $AlCr_{1.5}CuFeNi_2Co_x$ high-entropy alloys 93

5.3 Physical, mechanical and thermal behaviour of $AlCr_{1.5}CuFeNi_2Ti_x$ high-entropy alloys 93
5.3.1 Density of $AlCr_{1.5}CuFeNi_2Ti_x$ high-entropy alloys 94
5.3.2 Microhardness and tensile strength of $AlCr_{1.5}CuFeNi_2Ti_x$ high-entropy alloys 94
5.3.3 Specific strength and Young's modulus of $AlCr_{1.5}CuFeNi_2Ti_x$ high-entropy alloys 95
5.3.4 Compressive strength and flexural modulus of $AlCr_{1.5}CuFeNi_2Ti_x$ high-entropy alloys 96
5.3.5 Thermal conductivity of $AlCr_{1.5}CuFeNi_2Ti_x$ high-entropy alloys 97

Chapter 6 Wear and Corrosion analysis of high-entropy alloys 99-139

6.1 Sliding wear behaviour of $AlCr_{1.5}CuFeNi_2Mn_x$ high- entropy alloys 99
6.1.1 Influence of applied load on specific wear rate of $AlCr_{1.5}CuFeNi_2Mn_x$ alloys 99
6.1.2 Influence of sliding velocity on specific wear rate of $AlCr_{1.5}CuFeNi_2Mn_x$ alloys 100
6.1.3 Influence of temperature on specific wear rate of $AlCr_{1.5}CuFeNi_2Mn_x$ alloys 101
6.1.4 Taguchi design of experiment and Analysis of variance (ANOVA) for $AlCr_{1.5}CuFeNi_2Mn_x$ alloys 102
6.1.5 Microstructural examination of worn surface of $AlCr_{1.5}CuFeNi_2Mn_x$ alloys 107
6.2 Corrosion behaviour of $AlCr_{1.5}CuFeNi_2Mn_x$ high-entropy alloys 109
6.3 Sliding wear behaviour of $AlCr_{1.5}CuFeNi_2Co_x$ high-entropy alloys 110
6.3.1 Influence of applied load on specific wear rate of $AlCr_{1.5}CuFeNi_2Co_x$ alloys 110
6.3.2 Influence of sliding velocity on specific wear rate of $AlCr_{1.5}CuFeNi_2Co_x$ alloys 111
6.3.3 Influence of temperature on specific wear rate of $AlCr_{1.5}CuFeNi_2Co_x$ alloys 112
6.3.4 Taguchi design of experiment and Analysis of variance (ANOVA) for $AlCr_{1.5}CuFeNi_2Co_x$ alloys 113
6.3.5 Microstructural examination of worn surface of $AlCr_{1.5}CuFeNi_2Co_x$ alloys 117
6.4 Corrosion behaviour of $AlCr_{1.5}CuFeNi_2Co_x$ high-entropy alloys 120
6.5 Sliding wear behaviour of $AlCr_{1.5}CuFeNi_2Ti_x$ high- 121

entropy alloys
6.5.1 Influence of applied load on specific wear rate of $AlCr_{1.5}CuFeNi_2Ti_x$ alloys 121
6.5.2 Influence of sliding velocity on specific wear rate of $AlCr_{1.5}CuFeNi_2Ti_x$ alloys 122
6.5.3 Influence of temperature on specific wear rate of $AlCr_{1.5}CuFeNi_2Ti_x$ alloys 123
6.5.4 Taguchi design of experiment and Analysis of variance (ANOVA) for $AlCr_{1.5}CuFeNi_2Ti_x$ alloys 124
6.5.5 Microstructural examination of worn surface of $AlCr_{1.5}CuFeNi_2Ti_x$ alloys 129
6.6 Corrosion behaviour of $AlCr_{1.5}CuFeNi_2Ti_x$ high-entropy alloys 130
6.7 Multi Criteria Decision Making for ranking of alternatives 132
Chapter 7 SUMMARY AND FUTURE SCOPE 140-144
7.1 Summary of research findings 140
7.2 Conclusions 142
7.3 Scope for future work 144
REFERENCES
APPENDICES
Appendix-I LIST OF PUBLICATIONS
Appendix-II BRIEF BIO DATA OF THE AUTHOR

*****

LIST OF FIGURES

Figure No.	Figure caption	Page No.
Figure 1.1	Component life and temperature of various high temperature processes	2
Figure 3.1	Schematic of High-temperature vacuum induction furnace	47
Figure 3.2	The cast samples of (a) $AlCr_{1.5}CuFeNi_2Mn_x$ (b) $AlCr_{1.5}CuFeNi_2Co_x$ (c) $AlCr_{1.5}CuFeNi_2Ti_x$	48
Figure 3.3	Pictorial view of X-ray diffractometer	51
Figure 3.4	Pictorial view of Scanning electron microscope	52
Figure 3.5	Pictorial view of Transmission electron microscope	52
Figure 3.6	Schematic of density measurement setup	53
Figure 3.7	Pictorial view of Hardness testing machine	53
Figure 3.8	Sample for tensile test	54
Figure 3.9	Universal Testing Machine	54
Figure 3.10	Schematic of Corrosion Testing Machine	55
Figure 3.11	Schematic of Thermal conductivity analyzer	56
Figure 3.12	Schematic of pin-on-disc Tribometer	56
Figure 4.1	ΔH_{mix} and ΔS_{mix} of $AlCr_{1.5}CuFeNi_2Mn_x$ as a function of δ	66
Figure 4.2	EDAX analysis of $AlCr_{1.5}CuFeNi_2Mn$ alloy and relative intensity of each element confirming uniform distribution in the alloy	67
Figure 4.3	XRD pattern for $AlCr_{1.5}CuFeNi_2Mn_x$ alloys	67
Figure 4.4	Optical micrograph of $AlCr_{1.5}CuFeNi_2Mn_x$ alloys (a) $AlCr_{1.5}CuFeNi_2Mn_0$ (b) $AlCr_{1.5}CuFeNi_2Mn_{0.25}$ (c) $AlCr_{1.5}CuFeNi_2Mn_{0.5}$ (d) $AlCr_{1.5}CuFeNi_2Mn_{0.75}$ (e) $AlCr_{1.5}CuFeNi_2Mn$	68
Figure 4.5	SEM images of $AlCr_{1.5}CuFeNi_2Mn_x$ alloys	69
Figure 4.6	(a) TEM micrograph of $AlCr_{1.5}CuFeNi_2Mn$ alloy (b) SAED pattern for region 1	70
Figure 4.7	ΔH_{mix} and ΔS_{mix} of $AlCr_{1.5}CuFeNi_2Co_x$ as a function of δ	72
Figure 4.8	EDS analysis of $AlCr_{1.5}CuFeNi_2Co$ alloy and relative intensity of each element in the alloy (Al- Red; Cr- Green; Cu- Cyan; Fe-Yellow; Ni-Blue; Co- Magenta)	73

Figure 4.9	XRD pattern of $AlCr_{1.5}CuFeNi_2Co_x$ (x = 0, 0.25, 0.5, 0.75 and 1.0) alloys	74
Figure 4.10	Optical micrograph of $AlCr_{1.5}CuFeNi_2Co_x$ alloys (a) Co_0 (b) $Co_{0.25}$ (c) $Co_{0.50}$ (d) $Co_{0.75}$ (e) Co	75
Figure 4.11	SEM images of $AlCr_{1.5}CuFeNi_2Co_x$alloys: (a) x = 0, (b) x = 0.25, (c) x =0.50, (d) x = 0.75 and (e) x = 1	76
Figure 4.12	(a) TEM micrograph of $AlCr_{1.5}CuFeNi_2Co$ alloy (b) SAED pattern for region 1	77
Figure 4.13	The graph showing ΔH_{mix} and $\Delta S_{mix}$of $AlCr_{1.5}CuFeNi_2Ti_x$ alloys as a function of δ	79
Figure 4.14	EDS analysis of $AlCr_{1.5}CuFeNi_2Ti_{0.5}$ alloy and relative intensity of each element confirming uniform distribution in the alloy	80
Figure 4.15	XRD pattern of $AlCr_{1.5}CuFeNi_2Ti_x$ (x = 0, 0.25, 0.5, 0.75 and 1.0) alloys	80
Figure 4.16	Optical micrograph of $AlCr_{1.5}CuFeNi_2Ti_x$ alloys (a) Ti_0 (b) $Ti_{0.25}$ (c) $Ti_{0.50}$ (d) $Ti_{0.75}$ (e) Ti_1	81
Figure 4.17	SEM images of $AlCr_{1.5}CuFeNi_2Ti_x$alloys: (a) x = 0, (b) x = 0.25, (c) x =0.50, (d) x = 0.75 and (e) x = 1	82
Figure 4.18	(a) TEM micrograph of $AlCr_{1.5}CuFeNi_2Ti$ alloy (b) SAED pattern for region 1 (c) SAED pattern for region 2	83
Figure 5.1	Microhardness and tensile strength of $AlCr_{1.5}CuFeNi_2Mn_x$ high-entropy alloys	86
Figure 5.2	Specific strength and Young's modulus of $AlCr_{1.5}CuFeNi_2Mn_x$ high-entropy alloys	87
Figure 5.3	Compressive strength and flexural modulus of $AlCr_{1.5}CuNi_2FeMn_x$ high-entropy alloys	88
Figure 5.4 (a)	Variation of thermal conductivity as a function of x in $AlCr_{1.5}CuFeNi_2Mn_x$.	89
Figure 5.4 (b)	Variation of thermal conductivity as a function of temperature.	89
Figure 5.5	Microhardness and tensile strength of $AlCr_{1.5}CuFeNi_2Co_x$ high-entropy alloys	91

Figure 5.6	Specific strength and Young's modulus of $AlCr_{1.5}CuFeNi_2Co_x$ high-entropy alloys	91
Figure 5.7	Compressive strength and flexural modulus of $AlCr_{1.5}CuNi_2FeCo_x$ high-entropy alloys	92
Figure 5.8 (a)	Variation of thermal conductivity as a function of x in $AlCr_{1.5}CuFeNi_2Co_x$	93
Figure 5.8 (b)	Variation of thermal conductivity of $AlCr_{1.5}CuFeNi_2Co_x$ alloy as a function of temperature	93
Figure 5.9	Microhardness and tensile strength of $AlCr_{1.5}CuFeNi_2Ti_x$ high-entropy alloys	95
Figure 5.10	Specific strength and Young's modulus of $AlCr_{1.5}CuFeNi_2Ti_x$ high-entropy alloys	96
Figure 5.11	Compressive strength and flexural modulus of $AlCr_{1.5}CuNi_2FeTi_x$ high-entropy alloys	97
Figure 5.12 (a)	Variation of thermal conductivity as a function of molar in $AlCr_{1.5}CuFeNi_2Ti_{x.}$	97
Figure 5.12 (b)	Variation of thermal conductivity of $AlCr_{1.5}CuFeNi_2Ti_x$ alloy as a function of temperature	97
Figure 6.1	Effect of applied load on specific wear rate of $AlCr_{1.5}CuFeNi_2Mn_x$ alloys	100
Figure 6.2	Effect of sliding velocity on specific wear rate of $AlCr_{1.5}CuFeNi_2Mn_x$ alloys	101
Figure 6.3	Effect of temperature on specific wear rate of $AlCr_{1.5}CuFeNi_2Mn_x$ alloys	102
Figure 6.4	Influence of control parameters on means for $AlCr_{1.5}CuFeNi_2Mn_x$ alloys	104
Figure 6.5	Influence of control parameters on average S/N ratio for $AlCr_{1.5}CuFeNi_2Mn_x$ alloys	105
Figure 6.6	SEM images of $AlCr_{1.5}CuFeNi_2Mn_x$ alloys (a)$AlCr_{1.5}CuFeNi_2Mn_0$ (b)$AlCr_{1.5}CuFeNi_2Mn_{0.25}$ (c)$AlCr_{1.5}CuFeNi_2Mn_{0.5}$ (d)$AlCr_{1.5}CuFeNi_2Mn_{0.75}$ (e)$AlCr_{1.5}CuFeNi_2Mn$	108
Figure 6.7	Potentiodynamic-polarization curves of $AlCr_{1.5}CuFeNi_2Mn_x$ HEAs in 3.5 wt. % NaCl at ambient temperature	109

Figure 6.8	Effect of applied load on specific wear rate of $AlCr_{1.5}CuFeNi_2Co_x$ alloys	111
Figure 6.9	Effect of sliding velocity on specific wear rate of $AlCr_{1.5}CuFeNi_2Co_x$ alloys	112
Figure 6.10	Effect of temperature on specific wear rate of $AlCr_{1.5}CuFeNi_2Co_x$ alloys	112
Figure 6.11	Influence of control parameters on means for $AlCr_{1.5}CuFeNi_2Co_x$ alloys	115
Figure 6.12	Influence of control parameters on average S/N ratio for $AlCr_{1.5}CuFeNi_2Co_x$ alloys	115
Figure 6.13	SEM images of $AlCr_{1.5}CuFeNi_2Co_x$ alloys (a)$AlCr_{1.5}CuFeNi_2Co_0$ (b)$AlCr_{1.5}CuFeNi_2Co_{0.25}$ (c)$AlCr_{1.5}CuFeNi_2Co_{0.5}$ (d)$AlCr_{1.5}CuFeNi_2Co_{0.75}$ (e)$AlCr_{1.5}CuFeNi_2Co_1$	119
Figure 6.14	Potentiodynamic-polarization curves of $AlCr_{1.5}CuFeNi_2Co_x$ HEAs in 3.5 wt. % NaCl at ambient temperature	120
Figure 6.15	Effect of applied load on specific wear rate of $AlCr_{1.5}CuFeNi_2Ti_x$ alloys	122
Figure 6.16	Effect of sliding velocity on specific wear rate of $AlCr_{1.5}CuFeNi_2Ti_x$ alloys	122
Figure 6.17	Effect of temperature on specific wear rate of $AlCr_{1.5}CuFeNi_2Ti_x$ alloys	123
Figure 6.18	Influence of control parameters on means for $AlCr_{1.5}CuFeNi_2Mn_x$ alloys	127
Figure 6.19	Influence of control parameters on average S/N ratio for $AlCr_{1.5}CuFeNi_2Mn_x$ alloys	127
Figure 6.20	SEM images of $AlCr_{1.5}CuFeNi_2Ti_x$ alloys (a)$AlCr_{1.5}CuFeNi_2Ti_0$ (b)$AlCr_{1.5}CuFeNi_2Ti_{0.25}$ (c)$AlCr_{1.5}CuFeNi_2Ti_{0.5}$ (d)$AlCr_{1.5}CuFeNi_2Ti_{0.75}$ (e)$AlCr_{1.5}CuFeNi_2Ti_1$	130
Figure 6.21	Potentiodynamic-polarization curves of $AlCr_{1.5}CuFeNi_2Ti_x$ HEAs in 3.5 wt. % NaCl at ambient temperature	131
Figure 6.22	Graph ranking of alternatives	139

LIST OF TABLES

Table No.	Table caption	Page No.
Table 3.1	Characteristics of elements used for the development of HEAs	42
Table 3.2	Physical and mechanical properties of Aluminium	43
Table 3.3	Physical and mechanical properties of Chromium	43
Table 3.4	Physical and mechanical properties of Copper	44
Table 3.5	Physical and mechanical properties of Iron	44
Table 3.6	Physical and mechanical properties of Nickel	45
Table 3.7	Physical and mechanical properties of the alloying elements	46
Table 3.8	Characteristics of alloying elements	47
Table 3.9	Designation of various HEAs	48
Table 3.10	The chemical mixing enthalpy (ΔH_{ij}^{mix}, kJ/mol) of binary atomic pairs calculated by Miedama's approach	51
Table 3.11	The factor and its various levels	58
Table 3.12	Design of experiment for L_{25} orthogonal array	58
Table 3.13	Description of the different performance defining attributes	62
Table 4.1	δ, VEC, ΔX, ΔH, ΔS and Ω for $AlCr_{1.5}CuFeNi_2Mn_x$ alloys	65
Table 4.2	Thermodynamic Parameters δ, VEC, ΔX, ΔH, ΔS and Ω for $AlCr_{1.5}CuFeNi_2Co_x$ alloys	71
Table 4.3	The various thermodynamic parameters δ, VEC, ΔX, ΔH, ΔS, and Ω for $AlCr_{1.5}CuFeNi_2Ti_x$ alloys	78
Table 5.1	Density of $AlCr_{1.5}CuNi_2FeMn_x$ high-entropy alloys	85
Table 5.2	Density of fabricated$AlCr_{1.5}CuNi_2FeCo_x$ high-entropy alloy	90
Table 5.3	Density of $AlCr_{1.5}CuNi_2FeTi_x$ high-entropy alloys	94
Table 6.1	Design of experiment using L_{25} orthogonal array for $AlCr_{1.5}CuFeNi_2Mn_x$ alloys	103
Table 6.2	Results of ANOVA for $AlCr_{1.5}CuFeNi_2Mn_x$ alloys	104
Table 6.3	Mean response table for S/N ratio ($AlCr_{1.5}CuFeNi_2Mn_x$ alloys)	105
Table 6.4	The optimal setting significant input parameters	106
Table 6.5	Comparison of predicted and confirmation experiment	107
Table 6.6	Electrochemical parameters of Mn_0, $Mn_{0.25}$, $Mn_{0.5}$, $Mn_{0.75}$ and Mn_1 alloys from potentiodynamic - polarization curve	110

Table 6.7	Design of experiment using L_{25} orthogonal array for $AlCr_{1.5}CuFeNi_2Co_x$ alloys	113
Table 6.8	Results of ANOVA for $AlCr_{1.5}CuFeNi_2Co_x$ alloys	114
Table 6.9	Mean response table for S/N ratio ($AlCr_{1.5}CuFeNi_2Co_x$ alloys)	116
Table 6.10	The optimal setting significant input parameters	116
Table 6.11	Comparison of predicted and confirmation experiment	117
Table 6.12	Electrochemical parameters of Co_0, $Co_{0.25}$, $Co_{0.5}$, $Co_{0.75}$ and Co_1 alloys from potentiodynamic- polarization curve	120
Table 6.13	Design of experiment using L_{25} orthogonal array for $AlCr_{1.5}CuFeNi_2Ti_x$ alloys	124
Table 6.14	Results of ANOVA for $AlCr_{1.5}CuFeNi_2Ti_x$ alloys	125
Table 6.15	Mean response table for S/N ratio ($AlCr_{1.5}CuFeNi_2Ti_x$ alloys)	126
Table 6.16	The optimal setting significant input parameters	127
Table 6.17	Comparison of predicted and confirmation experiment	128
Table 6.18	Electrochemical parameters of $AlCr_{1.5}CuFeNi_2Ti_x$ derived from the potentiodynamic polarization curves by linear fitting	132
Table 6.19	Performance Defining Attribute (PDA)	133
Table 6.20	Experimental data of PDAs	134
Table 6.21	Normalized decision matrix	135
Table 6.22	Evaluation of criteria weights by entropy method	136
Table 6.23	Weighted normalized decision matrix	137
Table 6.24	Closeness coefficient and ranking of alloys	138

Chapter 1
INTRODUCTION

1.1 Background and motivation

There is an urgent need of self-reliance of an individual as well as of any organizations for the economic growth of any country, especially like India. This is due to the fact that there is a tremendous decrease in the past reliable sources for the livelihood such as agriculture and more dependency on the industrialization. The reason is the drastic climatic changes leading to meager contribution of the water-dependent sectors. With the upcoming need of more and more industries globally, the demand of new materials in different sectors such as energy, agriculture, automotive, chemical industry, heavy electrical equipment and other high temperature application area has increased manifold [1]. Figure 1.1 shows the various high temperature processes and the life of the component [2]. The most important consideration for the selection of material for a specific application is its behaviour in the working environment for a span of time. The materials used in different applications are subjected to the harsh environment such as high temperature, high pressure, corrosion, wear and so on. The proper selection of material helps in increasing the efficiency of the machine component and thereby increasing its service life. The development of new materials will render the country capable of competing globally.

Over the past several years, researchers are continuously working for the development of new materials that can sustain extreme conditions for a longer period. Existing metals and alloys in some manner are vulnerable to environmental degradation at high temperatures, which causes rapid oxidation and hence loss of strength. Such materials undergo undesirable phase transformations, rapid microstructure alterations, enhanced creep, and thus much-reduced life. Nickel, Cobalt, Chromium, Titanium and stainless steels are some of the common alloys that find wide applications as structural materials for high temperature applications in different industries. In spite of their superior capabilities, these alloys too suffer from the limitations of temperature, pressure and environment over a period. Therefore, it has become very crucial to develop novel materials with significantly improved mechanical, thermal, corrosion, fracture and wear properties to be operated at higher temperature [3].

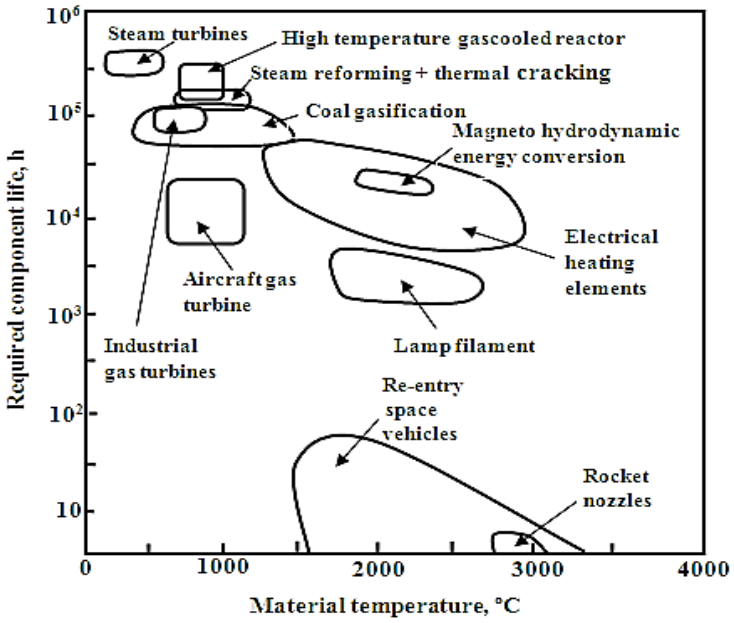

Figure 1.1.Component life and temperature of various high temperature processes [2]

Over the past decades, an intensive period of alloy development was witnessed improving the application of the superalloys to a large extent. The alloys with nickel, iron-nickel and cobalt-base employed at high temperature (540 °C) application are called superalloys [4]. The superalloys are mostly used in high temperature applications such as nuclear reactors, aircraft jet engines, gas turbines and furnace.The commonly used superalloys IN-718 is an iron-nickel-base alloy, a development to the family of stainless steel. The superalloys are either cast or wrought based on the specific requirement. The crystal structure of nickel, cobalt and Iron base superalloys are usually face-centered cubic (FCC) structure at high temperature. The alloying elements transform the cobalt and iron base superalloys to FCC structures whereas Nickel always remains in the FCC phase at all temperature. The Ni-base superalloys are used as high strength and corrosion resistant material at high temperature [5]. Moreover, Ni-base superalloys find wide application in the high temperature field where the components are subjected to static, fatigue and creep loading and offer excellent resistance to mechanical and chemical degradation [6].

Superalloys are also vulnerable to an extreme working environment, which sometimes leads to the failure of the crucial components at high temperature and corrosive environment. Conventionally, a minor percentage of various elements is combined with cobalt-based superalloys to enhance its working capability. While, Ni, Co, Fe based superalloys are used extensively in various fields, still they suffer from the influence of high temperature, pressure and chemicals, if exposed for a longer period. A new set of alloys called High-entropy alloys

(HEAs) gave a new dimension to the existing superalloy sand can sustain mechanical stresses and chemical attack during its service life when exposed to severe conditions.

1.2 High-Entropy alloys

For more than a decade, HEAs or multi-component equimolar or near-equimolar alloys has emerged as a potential source of materials for providing a number of solutions in various fields. Compared to the conventional metallic alloys based on the combination of specific elements in small quantity, HEAs generally contain five or more primary elements with each element lying in the range from 5 to 35 at.% [7]. Yeh et al. defined these alloys as HEAs and Cantor et al. as multi-component alloys [7, 8]. The HEAs are also defined in terms of the magnitude of configurational entropy (ΔS). $\Delta S<0.69R$ implies low entropy alloy, $0.69R<\Delta S<1.69R$ implies medium entropy alloys and $\Delta S>1.61R$ implies high entropy alloys, ΔS is the configurational entropy of ideas solid solution and R is the gas constant [9]. HEAs exhibits exceptional properties such as improved hardness [10, 11], high tensile strength [12, 13], high compressive strength [14, 15], excellent wear [16, 17] and corrosion resistance [18, 19], explaining their potential applications in different areas. HEAs exhibits exceptional properties due to its core effects as discussed in the next section.

1.2.1 Core effects of HEAs

The outstanding features of HEAs are due to its unique features caused by configurational entropy, sluggish diffusion of atoms, distortion in crystal lattice and formation of cocktail between elements [9]. These effects of the HEAs are explained below.

1.2.1.1. High-entropy of HEAs

HEAs are distinguished from conventional alloys due to their high-entropy nature. Yeh et al. [7] proposed that the multi-component in HEAs increase the entropy and stabilize the formation of crystal structures. The influence of the increase in entropy supplements the formation of solid solutions [20]. Gibbs rule determines the phases (P) existing in an alloy, which is given by equation as

$$P = C - F + 1 \quad (1)$$

Where C denotes the number of components and F indicates the degrees of freedom. According to the Gibbs rule, an alloy consisting of five components may have maximum six equilibrium phases at a constant reaction. However, HEAs shows an unexpected behaviour and form solid-solution as compared to the intermetallic phases [7, 8, 21]. The solid-solution consists of major and minor elements called solvent and solute. As far as HEAs are

considered, it is not possible to distinguish between the solvent and solute due to their high configurational entropy. However, this is not always true for all the equimolar multi-component alloys system.

1.2.1.2. Sluggish diffusion of HEAs

One of the special characteristics of HEAs is its ease of formation of nuclei due to nano-sized precipitate and the slow growth [7, 22]. Yeh [9] studied the diffusion in the HEAs, stainless steel and pure metals and observed that HEAs have lowest diffusion rate. Another explanation of the slow diffusion is given in terms of interruption in substitutional diffusion and increase in activation energy.

1.2.1.3. The lattice distortion effect

The HEAs consists of elements of different atom sizes resulting in the severe lattice distortion and formation of a complex structure with concentrated phases. Moreover, the lattice is affected by the atoms placed in the site and the other atom in the surrounding. Therefore, the lattice distortion is very high as compared to the conventional alloys. The uncertainty in the location of an atom also increases the configuration entropy and diminishes the X-ray diffraction peak [23, 24].

1.2.1.4. The 'cocktail' effect

Ranganathan [21] introduces the fancy phrase 'cocktail' for HEAs. The cocktail implies a mixture that has better properties as compared to the conventional alloys. There exists a lot of uncertainty in the behaviour of the elements forming the cocktail. Furthermore, the meaning is explained in terms of the improved physical and mechanical properties as discussed in the available literature [25-28].

1.2.2 Classification of HEAs

The appropriate selection of elements while designing an alloy plays a key role in determining the specific application. The selection of the elements for the development of the alloy is based on the desired properties. The HEAs are classified as refractory alloys, light alloys, bulk metallic glass and superalloys. The different types of HEAs are described below.

1.2.2.1 Refractory HEAs

The refractory HEAs consist of the refractory elements that can sustain high temperature and meant specifically for the high temperature structural applications as proposed by Senkov et al. [29]. The refractory HEAs consist of body-centered cubic (BCC) crystal structure as its

primary phase. However, the BCC phase of the HEAs is much harder than the BCC phase of the metals. These alloys have high hardness and are capable of resisting thermal softening upto 1600 °C temperature. The sluggish behaviour of HEAs is the main reason for the improved properties [30, 31].

1.2.2.2 Light HEAs

In order to conserve the energy, the demand for the lightweight alloys is increasing rapidly. The lightweight alloys have moderate strength and the certain temperature limitations. However, the HEAs have high strength and are capable of resisting high temperatures. There is a group of elements having a low density such as Al, Mg, Ti, Si, V and Li that are used as a light HEAs combined with other elements. Some of the example of the light HEAs with low density are $Al_{20}Be_{20}Fe_{10}Si_{15}Ti_{35}$ [31], AlNbTiV alloy [32] and $Al_{20}Li_{20}Mg_{10}Sc_{20}Ti_{30}$ [33].

1.2.2.3 Bulk Metallic Glass HEAs (BMGHEAs)

The metallic glasses are considered to be of high strength and corrosion resistant. The HEAs and the BMG have multiple components but the configurational entropy of HEAs is very high and do not have a solvent. The high configuration of the HEAs can be advantageous to the glass forming ability of BMGs [34-36]. However, the majority of HEAs are crystalline in nature and does not support the theory of glass formation. In contrast, HEAs can form the metallic glasses in accordance with the rules of the glass formation if the alloys exhibit high negative enthalpy of mixing and large atomic size difference between the elements [37,38].

1.2.2.4 High-Entropy Superalloys (HESAs)

The most prevalent superalloy used in the various applications is the Ni-based superalloys. The reduction in the amount of the Ni in the alloys can reduce the cost to a large extent. The capability of HEAs to from solid solution and the slow diffusion property may aid to reduce the thermal gradient of the gamma prime phase. HESAs were first introduced in the year 2015 [39]. In comparison to the Ni superalloys, the $Al_{0.1}Co_{1.5}CrFeNi_{1.5}Ti_{0.4}$ alloy shows lower density, better oxidation resistance and high hot hardness [40]. The strength of the HESAs is very high at high temperature (20 ºC to 1200 ºC) as compared to the Ni superalloys [41].

The purpose of this study is to investigate the influence of Manganese (Mn) Cobalt (Co) and Titanium (Ti) on the physical, mechanical, thermodynamic, microstructural, thermal, corrosion and wear behaviour of $AlCr_{1.5}CuFeNi_2$ high entropy alloy. Further, the steady state dry sliding behaviour of the developed HEAs was experimentally determined. Moreover, Taguchi design of experiment was used to study the effect of various factors on

the properties of the HEAs. Finally, the optimization technique is applied to the developed alloys to determine the ranking for the alloys.

1.3 Thesis framework

The framework of the present research work is as follows:

Chapter 2: Literature review
Thischapterincludesthe research work conducted during the evolution of high-entropy alloys from its preliminary stage to the present scenario. The various issues highlighted in the previous literature are addressed and emphasized related to the present study. The research gaps are identified from the extensive literature survey, and hence the objectives are formulated. The succinct description related to the microstructures, crystal structures, physical, mechanical, corrosion, thermal and wear is provided in this chapter.

Chapter 3: Materials and methods
This chapter deals with the description of the various elements used in the development of the HEAs and the various experimental technique used to determine the properties of the alloys. The equipment used for the fabrication process and the machine utilized in the physical, mechanical and wear characterization of HEAs is explained. The Taguchi design of experiment was used to study the effect of various factors on the behaviour of the HEAs is also presented in this thesis work.

Chapter 4: Thermodynamic and Microstructural Analysis of High - Entropy Alloys
This chapter comprises of thermodynamic and Microstructural examination of Mn, Co and Ti added $AlCr_{1.5}CuFeNi_2$ HEAs. The various thermodynamic parameters are determined for all the three compositions. The microstructural investigations of the samples are studied in detail.

Chapter 5: Physical, mechanical and thermal behaviour of high entropy alloys
This chapter is dedicated to mechanical, thermal and corrosion behaviour of the developed alloys. The mechanical properties such as compressive strength, Young's modulus are described for each composition. The thermal conductivity of the alloys is also determined at ambient temperature as well as at high temperatures. The corrosion behaviour of the alloys is studied in the NaCl salt solution.

Chapter 6: Wear and Corrosion analysis of high-entropy alloys

The chapter deals with the one factor at a time study for the alloys for all the three compositions at ambient temperature. The wear test is also performed using a Taguchi design of experiment with variation in molar ratio, load, speed, distance and temperature. Subsequently, the optimization technique is used to rank the developed alloys based on the physical, mechanical, wear and corrosion properties of the alloys.

Chapter 7: Conclusions and future scope

This chapter provides a conclusion based on the results of the research work and also identify the future scope of the present study.

The next chapter deals with the literature review on the various topics covered in the present research work. From the past studies, the research gaps are identified and the objectives of the current research work are reported.

****

Chapter 2
LITERATURE REVIEW

The review of literature is envisioned to provide the past information available in the field of the current research work. The review is intended to recapitulate the past studies on the basis of various aspects of the related to present work. This chapter summarizes the subject matters concerned to the high-entropy alloys (HEAs). The topic briefly reviews all the relevant literature and discusses the need for further research in order to improve the various properties for the high temperature applications. The following topics are discussed keeping in view the present research work.

2.1 Conventional alloys and Superalloys: Issues and challenges
2.2 Thermodynamic behaviour of high-entropy alloys
2.3 Microstructure and phase evolution of high-entropy alloys
2.4 Physical, mechanical and thermal behaviour of high-entropy alloys
2.5 Corrosion and Tribological characteristics of high-entropy alloys

2.1 Conventional alloys and Superalloys: Issues and challenges

Materials play a crucial role in increasing the efficiency of the machinery used for power generation and conveyance purposes. Researchers are continually working in the field of materials for developing novel alloys, which can be used for high temperature applications. The main area of concern for the prevailing metals and alloys is the extreme environmental condition that leads to the failure of the component. The aluminium alloys possess remarkable property due to which it has been used for most of the areas in the past few decades. The property of aluminium alloy includes low density, comparatively high specific strength, improved corrosion at normal environment and better electric and thermal conductivity. On the contrary, the aluminium alloy can be used only within the specified range of values for all the properties and hence new processing route along with the new design strategy are required for the better property as compared to the existing ones.

Perhaps the problems with the existing alloys are its specific application which limits its use to all the high-temperature applications [42]. Another critical factor is the economic and physical viability of the alloys. The weight and the size of the desired component should be considered while developing new alloys.

As compared to the conventional alloy of Al, Fe, Cu and Mg, superalloy has emerged as the promising material overcoming the challenges existing at high-temperature application. Presently, the superalloys are the backbone of many industries including energy generation, oil and gas extraction, metallurgical and aerospace industry. Superalloys provide the benefit of low weight material along with the increase in the efficiency of the machine. Despite all these advantages, there is a considerable challenge in the field of material to overcome the shortages of the existing superalloys. A jet engine consists of parts made from superalloy but the manufacturing process is quite lengthy along with the risk of defects at each stage.

It's challenging to decide the requirement and to finalize the elements to be used for the development of the alloys. Exhaustive affirmation of limiting property such as ductility, hardness, fatigue, creep, fracture, corrosion resistance, etc. is very much needed as compared to the indirect method. The indirect method of measurement of a property is not recommended for the novel alloy. The experimental method of deterring the property should be designed if it does not exist. The use of superalloy in extreme service condition such as high temperature and pressure further enhances the changes of the failure for these alloys. There is a need for developing alloys with low cost and improved properties as compared to conventional superalloys for aeronautical, oil and gas and marine sectors.

2.2 Thermodynamic behaviour of high-entropy alloys

The unique behavior of HEAs is due to the unusual behaviour as compared to the existing alloys. It has also been analyzed that there are various factors other than high entropy for the existence of simple microstructures in HEAs. There are various other factors that establish the formation of microstructure in the HEAs, which are used to validate the experimental results. The factors includes atomic size difference, enthalpy of mixing, entropy of mixing, electronegativity, valence electron concentration. These parameters play a very significant role in the formation of solid solution in HEAs and provide the guidelines for designing the novel HEAs.

There is a range of values of parameters that confirms the formation of solid solution in HEAs as stated by Sheng and Liu [43]. The value of entropy of mixing (ΔS) should lie in between 11 to 19.5 J/(K.mol), the enthalpy of mixing (ΔH_{mix}) should lie in the range from -22 to 7 kJ/mol and atomic size difference (δ) from 0 to 8.5. However for bulk metallic glasses, the range of values are as follows: $7 \leq \Delta S \leq 16$ J/(K.mol), $-49 \leq \Delta H_{mix} \leq -5.5$ kJ/mol and $\delta \geq 9$.Inanother study, Guo et al. [44] investigated the phase stability of the alloys with respect to the valence electron concentration (VEC). The VEC is used to predict the phases available

in the alloy. A higher value of VEC (≥8) results in the formation of the FCC phase whereas the BCC phase exists at lower VEC (<6.87).

Pi and Pan [45] introduced a new thermodynamic parameter $\Delta S_r \Delta H_{h(sol.)}$ for determining the microstructure of HEAs. If the alloys have a smaller value of $\Delta S_r \Delta H_{h(sol.)}$, there are high chances of the formation of either FCC or BCC phases. However, complex phases such as amorphous phases exist in the alloy for the more significant value of $\Delta S_r \Delta H_{h(sol.)}$. HEAs also exhibit the complicated structures forming topologically close-packed (TCP) phases. It is observed that the TCP phases can enhance the wear resistance properties of the HEAs. Dong et al. [46] interrelated the electro-negativity difference (ΔX) with the formation of the TCP phases. It was found that at ΔX> 0.133, the stable TCP phases exist in HEAs. However, it is true for most of the alloys consisting of Co, Cr, Cu, Fe, Mo, Ni, Ti, V, Nb, and Si but not for the alloys consisting of large amount of Al.

Tian et al. [47] studied the design of single-phase HEAs and concluded that the VEC value lies between 4.33-7.55 for BCC phase and 7.80 ~ 9.50 for FCC phase. It was further stated that the hardness of the alloys is directly dependent on the atomic size difference. The average value of VEC around 6.5-7 and δ≈ 6% yield the higher strength in the HEAs. Melnick and Soolshenko [48] proposed a method to calculate the Gibbs free energy of multicomponent refractory alloys and found that the alloys consisting of W, Ta, Mo, Nb, V, Ti, Hf and Cr elements have minimum energy. Sonkusare et al. [49] investigated the phase stability of CoCuFeMnNi HEA and found that the phenomenon of sluggish diffusion in HEA is not observed in the developed alloy and indicated that the diffusion phenomenon is not common and depends on the alloy to alloy.

2.3 Microstructure and phase evolution of high-entropy alloys

The general guidelines for the alloy design are governed by the Hume-Rothery rule [50]. It consists of the following conditions in relation with the solute and the solvent: (1) Comparable atomic radius (<15%) (2) Similar crystal structure (3) Same valence state and (4) Similar electronegativity. In general, elements from the periodic table belonging to the same family results in a solid solution. A large variety of microstructure exists in different types of the alloys. The commonly occurring structures in HEAs are only FCC or BCC in nature. Various investigators have studied the effect of the various elements on the microstructure and phase evolution. The common among all the elements from the periodic table includes Al, Cr, Ti, Vn. The observed microstructures and the phases found in the HEAs are discussed in this section.

2.3.1 Influence of Al as an alloying element

The effects of the elements on equiatomic CoCrFeMnNi Cantor alloy is studied in various research papers. A lot of research is based on Cantor alloys by altering the elements present in the alloy. Wang et al. [51] investigated that the AlCrFeCoNi HEA exhibits the BCC crystal structure as observed from the diffraction pattern. The microstructure shows the dendritic area consisting of Al, Ni and an interdendritic area consisting of Cr, Fe. However, the Co is found to be uniformly distributed in the alloy. In a similar study, Li et al. [52] investigated the effect of Mn, Ti and V addition on AlCrFeCoNiCu alloy. It was observed that the alloying of Mn in AlCrFeCoNiCu depicts additional long rod of Cr rich phase whereas the addition of Ti modifies the dendrite structure AlCrFeCoNiCu HEAs to eutectic structure. In comparison, the addition of V changes the dendritic microstructure from modulated plates to ellipse shaped particles. Li et al. [27] investigated FeNiCrCuCo and FeNiCrCuMo HEAs and found that the alloys consist of a single FCC phase and on replacing Al by Cu or Co, the alloy shows either BCC or BCC+FCC phase. It is also found that as the Cu promotes the formation of the FCC phase as it comprises of FCC structure. On the other hand, Al does not support the formation of FCC structure in spite of having a FCC structure.

Zhang et al. [53] studied the CoCrFeNiTi alloy and observed that the alloy depicts FCC phase and on the addition of Al (0, 0.5, 1.0, 1.5 and 2.0 in molar ratio), the FCC structure changes to BCC structure. The surface morphology of the alloys shows dendritic structure mainly due to Co, Ni, Ti and Al and interdentrites due to Fe and Cr. The microstructure of CoCrFeNiTiAl alloy consists of subgrains and nanosized precipitates. Chou et al. [54] reported that the $Al_xCoCrFeNi$ ($0 \leq x \leq 2$) alloys transform from FCC structure to BCC structure on the addition of the aluminium alloy. In another study, Li et al. [55] studied $Al_xCoCrFeNi$ alloys (x = 1, 1.5, 2, 2.5 and 3 in molar ratio) and found that the alloys exhibits ordered BCC (B2) structure. It is concluded that in the absence of Cu, the presence of Al advocates the formation of BCC structure. As the Al content increases, the crystal lattice distortion and the alloy strengthening increases.

Wang et al. [56] also studied the effect of Al contents (0-2.0 in molar ratio) on CoCrFeNi high-entropy alloy (HEA). The as-cast $Al_xCoCrFeNi$ alloys show FCC, BCC or FCC+ BCC crystal structure. The addition of Al content promotes the formation of BCC phase thus increasing hardness. The BCC phases have a two-phase structure on nano-scale composed by spinodal decomposition. Liu et al. [57] studied $Al_{0.8}CoCrCuFeNi$ HEA and observed a new phase as confirmed from the neutron diffraction. The mechanical testing of the alloy also revealed the presence of BCC structure and exhibited higher yield strength. Lin

et al. [58] studied the microstructure of the $Al_{0.5}CoCrFeNi$ alloy and found that the alloy consists of FCC phase and Al-Ni rich phases as a droplet. Zhang and Fu [59] concluded that the influence of Al on CoCrFeNiTi alloy supports the formation of BCC phase in cast condition as well after annealing. Zhuang et al. [60] added Si, Cr, Ti, Zr and Nd in FeCoNiCuAl alloy and observed that the similar microstructure (Dendritic) and phases (BCC+FCC) were found for Si, Cr and Ti alloys. However, the influence of Zr or Nd confirms the presence of intermetallic phases.

Guo et al. [61] investigated the effect of Al addition on the nonequimolar $CrCuFeNi_2$alloy. The alloys presented a different behaviour as compared to the other multi-component alloys. The microstructure revealed the rod-like features of submicron size in the eutectic alloy as compared to the sunflower structure in hyper-eutectic alloys. The annealing behaviour of FeCoNiCuAl alloy was investigated by Zhuang et al. [62]. At a temperature above 973 K, the FCC phase consisting of needle-shaped Cu was found to precipitate from BCC dendrite.

Chen et al. [63] investigated the $FeNiCrCo_{0.3}Al_{0.7}$ alloy and revealed that during mechanical alloying, the alloy forms solid solution with the presence of BCC structure. However, during the spark plasma sintering, the transformation of the BCC phase to FCC phase is observed. A subsequent investigation by Fan et al. [64] on $(FeCrNiCo)Al_xCu_y$ reveals that the alloy consists of FCC phase and spinodal decomposition tissues. The addition of Al (x= 0 to1.8) on Al_x–Co–Cr–Fe–Ni alloy was investigated by Wang et al. [65]. The phase varied at the different content of Al and mainly consisted of FCC, FCC+BCC and σ phase. In another study, the influence of Al (x= 0-20 at.%) addition on $(FeCoNiCrMn)_{100-x}Al_x$was investigated by He et al. [66]. The transformation of the phases took place in the following manner: FCC to FCC+BCC and then finally to single BCC structure.

Vida et al. [67] investigated the influence of sp (Al, Ga, Ge, Sn) elements on the NiCoFeCr alloy. It was concluded that the phase transformed from the FCC structure to BCC structure on addition the elements. The addition of Al ($0<x<5$) on CrMnFeCoNi alloy was investigated by Sun et al. [68]. The phase change takes place from FCC structure to FCC+BCC structure with the increase in the Al content in the alloy.

2.3.2 Influence of Cr as an alloying element

The effect of Al, V, Cr and Sn on the thermodynamic stability of X-NbTaTiZr alloy was investigated upto 1500˚C by Poletti at al. [69]. BCC structure was observed in AlNbTaTiZr and VNbTaTiZr alloys while an intermetallic phase along with BCC solution was present in

CrNbTaTiZr and SnNbTaTiZr alloys. It was found that the phases remain unchanged upon heat treatment using Cr and Sn HEAs while phase transformation was identified using Al and V alloys. They also observed that the reason for phase transformation was due to inter-diffusion between the zones of dendrites and the interdendrities.

Hsu et al. [70] investigated the hot hardness and microstructure behaviour of $AlCoCr_xFeMo_{0.5}Ni$ HEAs. It was found that B_2 and σ phases were present in the cast microstructure of $AlCoCr_xFeMo_{0.5}Ni$. With the increase in the Cr content, the amount of σ phase increased as a result of the change of conversion of dendritic B_2 phase to σ phase. Superior hardness values compared to Ni-based superalloys and a good softening resistance was identified in by their investigation in the $AlCoCr_xFeMo_{0.5}Ni$ alloys. Fu et al. [71] studied the influence of Cr on the microstructure and properties of $CoFeNiAl_{0.5}Ti_{0.5}$ alloy fabricated by spark plasma sintering (SPS) and mechanical alloying (MA) process The results show the formation of a single FCC structure in $CoFeNiAl_{0.5}Ti_{0.5}$ HEA while adding Cr, additional BCC phase was identified along with FCC structure. It was also stated that two phases FCC1 and FCC2 were present in bulk HEA with the same lattice parameter. The SAED pattern for both FCC1 phase of $CrCoFeNiAl_{0.5}Ti_{0.5}$ and FCC phase of $CoFeNiAl_{0.5}Ti_{0.5}$ HEA are found to be similar.

2.3.3 Influence of Cu as an alloying element

Wu et al. [72] investigated the influence of Cu on the microstructure of $CoCrCu_xFeMoNi$ (x=0.1-1.0 in molar ratio) HEAs. Solid solution FCC and BCC structures were recognized in $CoCrCu_xFeMoNi$ high-entropy alloys. Peritectic and eutectic reaction took place successively in Cu_0 and $Cu_{0.1}$alloys having rich phases of Fe, Co and Ni. The investigation revealed that $Cu_{0.3}$ undergoes semi-peritectic reaction due to the abundant Mo dendritic structure and the melt. However, the remaining liquids are subjected to the eutectic reaction. It was also concluded that the two reaction increases with the increase in the Cu content in the alloy.

Lin and Tsai [73] studied the microstructural behaviour of $Cu_{0.5}CoCrFeNi$ HEAs. The results revealed that the hardness of $Cu_{0.5}CoCrFeNi$ alloy remain unaffected after several heat treatments and it was also observed that the FCC phase structures were unaffected by aging the $Cu_{0.5}CoCrFeNi$ alloy specimens to 1350 °C. The alloys exhibit the FCC matrix rich in Cu and Cr phase. While aging at 1100-1350 °C, the Cr-rich phase precipitates to FCC matrix. High temperature aging resulted in the separation of Cu atoms in matrix phases. Lin and Tsai [74] examined the microstructure of annealed $FeCoNiCrCu_{0.5}$ alloy at 350 °C - 1250 °C with a range of 300 °C. It was found that the specimens contain a matrix of three-phase viz. (1) Cu

deficient (2) Cr-rich (3) Cu-rich. FCC phase was observed in as-cast as well as annealed $FeCoNiCrCu_{0.5}$ alloy. From the TEM analysis, it was observed that as-cast alloy depicts the Cu-rich phase precipitates of spherical and elliptical shape with less than 20 nm in size. However, with the increase in the annealing temperature, precipitate upto the size of 100-300 nm was determined. Hsu et al. [75] studied the corrosion behaviour of $FeCoNiCrCu_x$ (x=0.5 & 1) alloys in NaCl solution. It was found that the zones of dendrites and interdentrites were observed in the as-cast $FeCoNiCrCu_{0.5}$ and FeCoNiCrCu alloys. Corrosion due to galvanic action was a major part among these alloys. Cu segregation was observed in interdendrites due to weak bonding force with remaining elements. They concluded that for the damage due to the addition of Cu increases with increasing the copper content.

2.3.4 Influence of Mo as an alloying element

Shun et al. [13] investigated the influence of Mo (x=0, 0.3, 0.5, and 0.85, in molar ratio) on microstructure and mechanical properties of CoCrFeNi. The alloys demonstrate a homogeneous structure with grain size ranging from 300 - 500 μm. The FCC structure was affected by the atomic size and due to lack of positive or negative enthalpy atom pairs. The phases present in the alloy were FCC, FCC+σ, and FCC+σ+μ for Mo = 0, 0.3, 0.5 and 0.85 respectively. It was also reported that $Mo_{0.85}$ alloy material is a high strength alloy having mechanical properties such as fracture strain of 21% and compressive strength of 1441 MPa. A similar investigation as above was conducted by Dong et al. [76] by varying Mo content for $AlCrFeNiMo_x$ (x = 0, 0.2, 0.5, 0.8, 1.0) HEAs. Two BCC phases were present in the microstructure of AlCrFeNi, $AlCrFeNiMo_{0.2}$, and $AlCrFeNiMo_{0.5}$ alloys. It was found that with the increase in the Mo content there was phase change from two BCC phases to one BCC and from eutectic to hypoeutectic than to hypereutectic. Among all the HEAs $AlCrFeNiMo_{0.2}$ exhibited highest fracture strength and plastic strain leading to better mechanical material for industrial applications.

Shun et al. [77] studied the influence of addition Mo on $Al_{0.3}CoCrFeNi$ HEA aging at 700 °C. An increase in 65-89% hardness was observed on aging for 144 hrs. The age hardening is attributed to the presence of Ni, Al-rich phase and σ phase due to (Cr, Mo)(Co, Fe, Ni) in the $Al_{0.3}CoCrFeNiMo_{0.1}$ alloy.

2.3.5 Influence of Ti as an alloying element

Wang et al. [25] investigated the effect of Ti (0, 0.5, 0.8 and 1.0) alloys on microstructure behaviour of CoCrCuFeNi alloys. With the increase in the Ti content, the alloy changes its

microstructure from ‘FCC’ to ‘FCC + Lave phases’ along with an amorphous phase. It was also found that the strength of alloys increases from 230 MPa to 1272 MPa and among all the alloys, the highest strength was exhibited by $CoCrCuFeNiTi_{0.5}$. These alloys also exhibit properties of paramagnetism and super paramagnetism due to the presence of Ti in the amorphous phase.

Li et al. [52] investigated the influence of Ti on AlCrFeCoNiCu high entropy alloy. From the study, a change in the microstructure from the dendrite to eutectic cell was observed. It could also increase in the FCC phase relatively. Interestingly they concluded that there was a decrease in the strength of AlCrFeCoNiCu high entropy alloy showing it ultimate strain and compressive strength at lowest. Wang et al. [78] studied the properties of $Fe_{36}Ni_{18}Mn_{33}Al_{13}Ti_x$ (x = 0, 2, 4, 6 at.%) alloy and found that Ti has a contrary effect on the ductility property. From the fracture behaviour, the brittle fracture at ambient temperature and ductile fracture at higher temperature (973 K) was observed. As the Ti content increases, the yield strength was found to increase due to decrease in the lamellar spacing obeying Hall-Petch-type relationship. Fu et al. [79] studied the $Al_{0.6}CoNiFeTi_x$ HEA and found that the alloy consists of BCC + FCC phases in the supersaturated solid solution during the mechanical alloying process. On addition of Ti content to the alloy, only FCC phase was observed in $Ti_{0.4}$ alloy. The alloys exhibit FCC rich phase and a small amount of BCC phase after the SPS process. Shun et al. [77] investigated the effect of addition Ti on $Al_{0.3}CoCrFeNi$ high entropy alloy aging them at 700 °C. An overall increase in hardness of 80% was observed on $Al_{0.3}CoCrFeNi$ alloy after aging. The $Al_{0.3}CoCrFeNiTi_{0.1}$ underwent an age hardening and found (Ni, Co, Ti)-rich B_2 phase.

2.4 Physical, mechanical and thermal behaviour of high-entropy alloys

Being amorphous, the HEAs ($Cu_{0.5}NiAlCoCrFeSi$) prepared by the arc melting method) showed three times higher hardness than with that of 304 SS. The prepared HEAs showed tremendous resistance to corrosion in all acidic environments. The resulted microstructure of HEAs showed to be non-crystalline-amorphous phase consists of (1) small amount of HEAs contained to be BCC with the dendritic phase of lattice constant of 2.91 Å and (2) the rest of the alloy was composed of interdendritic phase, amorphous in nature consisting of nanoprecipitates. Consequently, HEAs was less resistant to pitting corrosion as suggested by Chen et al. [63]. The aging temperature between 350-800 ºC resulted in a combination of FCC+ BCC solid structure leading to the optimal hardness of 285 HV. The segregation effect on Al-Ni and Al (Ni, Co, Cr, Fe) transforms the FCC structure to BCC solid solution owing

to the negative enthalpy than the other combination of the principal elements in the HEAs. The aged HEAs showed significant corrosion resistant than those as cast and 304L stainless steel. The difference obtained is as a result of the transformed microstructure induced during aging as suggested by Lin et al. [74]. Studying the properties of HEAs for corrosion resistance applications is becoming more popular via the surface modification process as coatings to combat the corrosion. The studies have shown HEAs can be a better replacement for the MAX phase ternary coatings concerning its ability for being anti-oxidant/ tribological property and also corrosion resistant.

Hsueh et al. [80] studied the equimolar deposition of $Al_{21.6}Cr_{17.8}Si_{21.6}Ti_{17.2}Zr_{21.8}$ on Al 6061 alloy substrate with magnetron sputtering. The nitrogen atoms in the composition were sufficient enough to cause the higher order of disorder as a result 22.4% of nitrogen. The increase in nitrogen content results in increased hardness from 11.5 to 17 GPa at 15% leading to coarse and amorphous clusters leading to decrease the hardness after 15%. The deposited coating showed a better corrosion resistance than the target material when tested in H_2SO_4 aqueous solution. Thermal spray technique was sued in the deposition of $Ni_xCo_{0.6}Fe_{0.2}Cr_ySi_zAlTi_{0.2}$ HEAs on an alloy substrate as studied by the Wang et al. [81]. The deposited coatings showed an increase in hardness of 1045 HV after heat treatment at 800 °C for 10 hrs. Increase in temperature from 800 to 1100 °C during heat treatment resulted in increased hardness 964 HV. XRD analysis of the deposited coatings showed that heat treatment resulted in two times higher intensity with the BCC or Cr_3Si unidentified structure.

The transformation from FCC to BCC and mixed phase of FCC+BCC is evident when Al replaced with Cu in the formation of FeNi-CrCuCo HEAs. The investigation was conducted to study the effect of the addition of Al on the HEAs by Li et al. [27] and it was found that decreased peak diffraction is showing the induced aberrance of the crystal structure. The microstructure showed it to be a typical coarse dendritic phase owing to the addition of Al. The addition of Al leads to the increment in hardness to 566 HV as a result of (1) Transformed BCC structure (2) increased mixing enthalpy, showing the combinative force of Al addition in HEAs. The investigation of addition of carbon, vanadium and silicon in Fe-C-V structure by Fras et al. [82] depicts that change in microstructure after solidification resulted in (1) ferrite matrix (2) ferrite + granular pearlite (3) granular pearlite (4) granular pearlite + lamellar pearlite (5) matrix of lamellar pearlite. This also depicts that addition of alloying elements like vanadium brings down the elongation from 7.2 to 0.2% due to the existence of lamellar pearlite and cementite phase. It is also determined from the outcome that irrespective of the alloy composition the ferrite structure promotes the ductility.

The decrement in ductility is also evident when the ferrite shifts to lamellar pearlite. However, a similar trend was followed by the addition of Si in Fe-C-V system. On a general note, the addition of silicon reduces the ductility (7.2 to 2.1%).

An alloy consisting of one principal element as a matrix (such as Fe, Cu, Ti, Mg, Al, etc.) to make it viable to be used in the highly corrosive environment. Li et al. [55] studied one such matrix alloy by varying the Al content in $Al_xCoCrFeNi$ alloy. The Al-rich alloy system showed a 1.46 times increase in hardness by varying Al from 20 to 42.8 wt.%. The higher hardness depicts that higher binding ability of Al element with another element by making the string combative force with typical dendritic structure. The inhomogeneous distribution of Al revealed to have FCC or L12 structure in alloy but the presence of Ni in the alloy makes it to have high enthalpy energies as determined by HR-TEM measurements.

The elements added in the formation of HEA alloy is not solely dependent on high mixing entropy of each element to form solid solution in the equiatomic alloy is suggested by Pi et al. [83]. The author also depicted that formation of the amorphous phase in the alloy leads to the confusion as it is inhabited to make solid solution. The other requirements being atomic size as well the mixing enthalpy of the elements to constitute HEAs in forming solid solution. The above argument lies in the cluster formation which makes the element to have negative mixing enthalpy not favouring the formation of solid solution. Thus elements constitute to form solid solution will result in higher compressive fracture strength of 1219 MPa. Senkov et al. [84] prepared $Ta_{20}Nb_{20}Hf_{20}Zr_{20}Ti_{20}$ refractory alloy by hot isostatic pressing for 3 hrs at T = 1473 K and P = 207 MPa and fabricated by the vacuum arc melting method. The fabricated new refractory alloy paved way to fabricate several other compositions with FCC or BCC structure with desirable strength and ductility. The Vickers hardness of the refectory alloy varied between 4.5 to 5.3 GPa with yield strength ranging between 405 to 477 MPa when melted at 1873 K. Surprisingly; developed alloys have more density and lower ductility when measured at room temperature. The increase in hardness may attribute the elastic interactions happened due to solid solution formation. Despite the compression straining (8%), alloy retained a yield strength of 1270 MPa and ductility ($\varepsilon >$ 50%). Thus, the prepared alloy shows a superior mechanical property. Praveen et al. [85] observed the formation of solid solution of multi-component AlCoCrCuFe and NiCoCrCuFe HEAs. The fabrication method adopted was Spark plasma sintering, which resulted in BCC with σ phase and FCC with same σ phase, the hardness of 770 HV and 400 HV for AlCoCrCuFe, and NiCoCrCuFe respectively. The theoretical density of the alloy by

removing one element in a group increases the density from 6.75 to 8.53 g/cm^3, but opposite trend was showcased for the experimental values from 99 to 92%.

Liu et al. [86] depicted the conventional method of developing HEAs is by selecting one or two elements as principal elements to achieve the desirable solid solution phase with properties. Thus the principal role of elements in an alloy system is to have high solubility. TEM micrographs of the prepared alloys of $FeCoCuNiSn_{0.2}$ and $FeCoCuNiSn_{0.5}$ have small precipitates of intermetallic compounds of $Cu_{81}Sn_{22}$, which results in increased hard and brittle phase but decreases the tensile strength but there was no evidence of intermetallic compounds of $Cu_{81}Sn_{22}$ was observed. The tensile strength of the $FeCoCuNiSn_x$ increases with increase in Sn content up to 0.07. However, Sn content beyond 0.07% induces the opposite trend with increased strain. Jinhong et al. [15] prepared $AlCrFeCuNi_x$ HEAs by vacuum arc and casting method in an argon atmosphere to study the microstructure and mechanical properties. The microstructural analysis of the as-cast $AlCrFeCuNi_x$ showed that BCC, FCC and also one compound phase was present in the prepared HEAs. Changing the nickel content from 1 to 1.4 naturally decrease the hardness CrFe rich alloy. Micrographic features show that CrFe rich alloy possesses more compressive strength than those with FCC phase. The increased nickel content from 0.1 to 0.77% results in decreased strength as a result of increased shear concentration.

Wang et al. [56] studied the effect of Al-rich $Al_xCoCrFeNi$ HEAs. The samples were prepared by varying the aluminium by 0 to 20 wt.% by arc remelting method. The result shows that varying the aluminium from 0 to 0.4wt.% resulted in single crystal FCC structure, BCC with 111 reflection when aluminium is just raised to 0.5 wt.%. It is evident that FCC peaks were disappeared with 0.9 wt.% of aluminium is added. The microstructure reveals that the prepared HEAs possess columnar cellular structure, columnar dendrite structure and equiaxed nondendritic structure for $Al_{(0\text{-}0.3)}$, $Al_{(0.4\text{-}0.6)}$, $Al_{(0.9\text{-}1.5)}$ respectively. Interconnected structure of finest spinoidally decomposed $Al_{0.9}$ shows high hardness among Al_0-$Al_{2.0}$ series owing to the modulated plate structure.

Shun et al. [87] the addition of Mo as a principal element in $CoCrFeNiMo_x$ show the distortion of lattice structure when more Mo is added from 0.3 to 0.85 and thereby causing increasing hardness from 135 to 420 HV. The increase in hardness may attribute to the increase in σ phase in the lattice. The addition of Mo also improves the yield stress and compressive strength significantly from 136 MPa to 871 MPa and 929 MPa to 1441 MPa respectively. It was also evident that the reduction in fracture strain from 75 to 21% owing to the increased stress concentration causing dislocations at the interface by the prolonged

cracking during compression. The two main factors attribute to the strengthening of the alloy is (1) the formation of σ and μ phases in the solid solution and (2) strengthening of FCC matrix. These σ and μ phases belong to the family of TCP (Topological Closely Packed) structures.

The $FeNiCrCo_{0.3}Al_{0.7}$ was synthesized using MA and SPS. Formations of BCC structure with lattice parameter 3.01 Å and partial BCC along with FCC with lattice parameter 3.72 Å was evident during the solid solution melting. The formation of HEAs prepared by the spark plasma sintering resulted in 2033±41 MPa, 2635±55 MPa, and 8.12±0.51% for yield strength, strength due to compression and compression ratio respectively. The fracture form of the alloy prepared by spark plasma sintering is typically characterized by the rough facets, intercrystalline fracture and tears edges. The tear edges and rough facets are the results of the plasticity and the deformation respectively owing to the solid solution strengthening as studied by Chen et al. [63]. Fu et al. [88] studied the Co-Ti rich $Co_{0.5}FeNiCrTi_{0.5}$ HEAs prepared by MA and SPS. The result showed an increase in yield strength by 2.65 GPa and compressive strength by 2.69 GPa. The compressive strength and compression ratio are enhanced by 33.2 and 11% respectively when compared to CoFeNiCrTi alloy. The prolonged milling time to 49 hrs increased the lattice strain in BCC and FCC structure is 0.39 to 0.91% and 0.69 to 1.04% respectively. The increase in milling also decreases the diffraction intensity after milling the powders to 6 hrs. Thus, high milling time is the reason behind the high lattice strain and the formation of the nanocrystalline structure.

The $Al_{0.6}CoNiFeTi_{0.4}$ alloy was prepared by adopting the conventional technique of MA and SPS by Chen et al. [89]. The structure obtained in solid solution during mechanical alloying is purely FCC, however, a mixed phase of FCC and BCC for SPS. Al-Ti rich alloy resulted in a high density of 98.2% exhibiting superior mechanical properties. The alloys hardness was found to be 712±12 HV whereas the yield strength and compressive strength values were 2732 MPa, 3172 MPa, respectively. The obtained high hardness is associated with the high order of BCC phase existing in the alloy. The mechanical properties of the Mo-rich and its subsequent microstructure are studied by Dong et al. [76] of $AlCrFeNiMo_x$ alloy prepared by vacuum arc melting. The variation of Mo from 0 to 0.5 resulted in two BCC phases. Out of two one being a type of AlNi intermetallic compound and other being the FeCr solid solution. When Mo content varied beyond 0.5, there exists a σ phase by replacing the FeCr solid solution. The addition of 0.2% Mo achieves the fracture strength and plastic strain of 3222 MPa and 0.287 with increased hardness from 472.4 to 911.5. The BCC

dendrites strengthening and the hardening of σ phase are two main reasons behind the strengthening of alloys possessing excellent mechanical properties to be used in industrial applications. Synthesis of nanocrystalline AlCrCuFeNiZn HEAs prepared by hot compaction for 15 min at 600 ºC and 650MPa is studied by Pradeep et al. [90]. The samples showed a mixed phase of with Ni-Al, Cr-Fe and Fe-Cr rich 60 vol.% BCC and Cu-Zn rich 40 vol.% FCC. The nanocrystalline size of 20-30 nm formed as a result of spinodal decomposition resulted in very high hardness of 870 HV though the material is not homogenous, but the phase decomposition is prevalent. This exhibits the high mixing enthalpy of an alloy formed during slid solution phases.

Synthesis of Al-Cu rich (FeCrNiCo)Al_xCu_y with TiC reinforcement is studied by the Fan et al. [64]. The mechanical properties such as hardness, yield strength and fracture strength particularly for $Al_{0.75}$-Cu0.25 with 10% TiC reinforcing in the (FeCrNiCo) alloy is 621 HV, 1637 MPa and 2972 MPa respectively. These findings attribute to three reasons. (1) The FCC dendrites formed during solid solution, (2) decomposition of spinodal tissues and (3) Al-Ni rich elements with 1:1 molar ratio forming intermetallic compounds with other elements. The uniform distribution of the TiC particles yields in a higher value of yield strength and hardness as much as 73% and 65%. The proper interface between the TiC ceramic and the HEAs exhibit a clean surface owing to the sedimentation of particles in the remelting process. Thus forming cluster free ceramic particles with HEAs is evident. The addition of Mn and V in the CoCrFeNi HEAs system is studied for its mechanical properties for annealed and as-solidified condition by Salishchev et al. [91]. FCC single phase dendrite structure was established for CoCrFeNi and CoCrFeNiMn alloys. Tetragonal crystal with σ-phase intermetallic compounds for FeCrCo-NiV and FeCrCoNiMnV alloys. Heat treatment for about 5 hrs does not affect the crystal structure rather grains were rearranged to the equiaxed structure with size of about 200nm by transforming dendritic phase to granular one. The effect of heat treatment on CoCrFeNiV alloy forms two phases namely Cr-V rich σ-phase matrix and Ni-rich with smaller proportion of V and Cr. Alloying HEAs with V and Mn resulted in increase of hardness by more than two times; 587 HV, 636 HV and 1002 HV, 1025 HV for as solidified and σ-phase for CoCrFeNiV and CoCrFeNiMnV respectively.

The conventional vacuum arc melting method was adopted in forming in Al-rich Al_x–Co–Cr–Fe–Ni in HEAs system for the variation in microstructural changes and the mechanical properties as reported by Wang et al. [25]. The hot hardness transition temperature for the HEAs system occurred is between 810 K- 930 K. Among Al-rich alloy system, Al_0 and $Al_{0.3}$ showed maximum softening coefficient, hot hardness transition

temperature was high for $Al_{0.5}$ and $Al_{0.9\text{-}1}$ exhibited hardness. The refractory materials like Mi-Ta and Al-Hf rich AlMoNbTaTiZr and AlHfNbTaTiZr HEAs were developed to study the changes in the phase composition on microstructure and physical properties by Senkov et al. [30]. The study reveals that AlMoNbTaTiZr High Entropy Alloy was enriched with Mo, Ta and Nb possessing two BCC dendrites with close lattice parameters of equiaxed grains and the former with Al and Zr. The densities of the two alloys were measured to be 7.40 and 9.05 gm/cm^3 with hardness including 5.8 and 4.9 GPa respectively. The yield strength of the prepared HEAs was observed to be 2000 MPa and1841 MPa at 290 K but as the temperature was increased to 1273 K the yield strength reduced to 745 MPa and 298 MPa for AlMoNbTaTiZr and AlHfNbTaTiZr respectively. The effect of annealing temperatures between 800- 1150 °C to study the microstructural orientation after the recrystallization effect on the prepared CoCrFeMnNi HEAs for a different time was reviewed by Otto et al. [92]. Arc melting followed by drop casting technique was adopted to prepare different thickness of samples for the measurement. The studies revealed that hardness was first increased when annealed to the temperature below recrystallization temperature and then dropped suddenly for higher annealing temperatures owing to the effect of changes happen due to recrystallization. The samples were also studied for the annealing twins by EBSD technique. The result showed that grain growth exponent was increased to 3 with the activation energy of 325 KJ/mol. The studies concluded that annealing twins per grains is independent of annealing temperature and the time.

Fang et al. [93] discussed the conventional method of spark plasma sintering and mechanical alloying helps in ease of preparing HEAs by introducing a non-metallic carbon in the composition. Commonly encountered dendrites of a mixed phase of FCC+BCC were evident for mechanical alloyed for Ni-Al rich HEAs. Whereas, a major phase of FCC with BCC dendrites were evolved during spark plasma sintering for Fe-Ni rich. The difference in phase existence was attributed to the nanoscale deformation in grains in spark plasma sintering technique. Deformation twins were evident for only FCC dendrites irrespective of the method of manufacturing method involved. The compressive strength and hardness for CoC-Al rich HEAs prepared are 2131 MPA and 617 HV. The effect of Ti addition in the Al-rich $Al_{0.6}$CoNiFe alloy was developed by the sintering method to analyze the changes in the microstructure and mechanical properties are demonstrated by Fu et al. [79]. The addition of Ti results in the formation of FCC dendrite in the super solid solution by eliminating BCC structure and exhibiting compressive strength and hardness values lower than the hot oppressing sintered technique showing significant plasticity involved in reducing hardness as

well as compressive strength. Both the alloy showed a significantly same FCC lattice parameter irrespective of the alloy is prepares by hot pressing or hot pressed sintering. The addition of titanium and aluminium in the Co-Ni rich HEAs prepared by arc melting in argon atmosphere is studied for its microstructural changes in high temperature by Chang and Yeh [39]. The addition of titanium (Ti_y) and aluminium (Al_x) is limited to 0.5 (x+y =0.5). The increase in aluminium content and a decrease in titanium content evolve FCC dendrites with γ matrix. The alloy shows a better hardness even at elevated temperature due to the existence of the γ matrix and the extra protection by the chromium oxide layer on the surface of the alloy.

Jiang et al. [94] variation of Mo from 0-1% and Ni from 1-2% results in eutectic microstructures in the solid solution with the improved mechanical properties for the CoFeNiVMo alloy. Eutectic microstructures are obtained by limiting the Mo content to 0.6 and Ni to 1.4. The results also indicate that limited addition of Mo and Ni would result in increased hardness from 238.1 to 624.6 HV and yield strength of 686.9 MPa, ductility more than 80%. The increased hardness attributes to the high concentration of Mo which yields to the solid solution strengthening. Results also depicted that changes in microstructure from eutectic to hypereutectic plays a vital role in increasing hardness. Thus, for the same concentration of Mo and Ni content, the Mo-rich alloy resulted in the higher hardness possessing hypereutectic microstructure. The formation of solid solution eutectic HEAs are not dependent on the valence electron concentration, electron negativity, entropy of mixing and dendrites formation after heat treatment.

Sistla et al. [95] studied the effect of varying the ratio of Al/Ni in the AlFeCoCrNi alloy system prepared using an additive manufacturing technique resulted in a phase transformation from BCC to FCC dendrites. Changing the concentration of aluminium in the alloy showed an increase in hardness by the spinodal decomposition causing the disorientation of the grain structure. This disorientation of the lattice parameter from 0.288 to 0.357 nm resulted in the decreased hardness from 670 to 149 HV as measured by using differential thermal analysis. The synthesis of Al/Ni ratio in the alloy can lead the improved mechanical properties with high softening resistance. Two equiatomic AlCoCrCuMnFe and AlCoCrCuMnTi HEAs produced by vacuum arc melting were compared for the compressive strength along with the hardness by the Wang et al. [96]. Comparing the Fe rich alloy, the Ti-rich alloy showed the high yield strength, hardness, compressive strength of 1568 MPa, 554.8 HV, 1947 MPa respectively, which shows 41.1, 24, and 27.4% higher than Fe rich alloy. The

author also proposed two components Kn and φ. Kn increasing with increase in n and φ decreases with an increase in n.

A set of carbon-rich CoCrFeNiMn alloy containing 0, 2, 3.4 and 4.8% is prepared by Stepanov et al. [97] using vacuum arc melting. The alloys were annealed to a temperature 600 to 1200 °C at an interval of 200 °C. Solid solution of CoCrFeNiMn resulted in FCC structure with $C_{0.1}$ containing an insignificant nanoscale fraction of carbides, $C_{0.175}$ and $C_{0.25}$ coarse carbides with 5 and 9.5% volume fraction. The microhardness of the alloy was increased to 275 HV for $C_{0.25}$. The increase in hardness values attributes the precipitation of carbides during annealing at a temperature more than 800 °C by the strong hardening. Further, increase in annealing temperature decreases the carbon solubility thereby reducing the hardness value by 5%. Slight variation of carbon content from 0.175 to 0.25% has a sensitive impact which decreases hardness from 275 to 165 HV. Maulik et al. [98] theory based on density-functional calculations revealed that the effects of heterogeneity in the microstructure could strongly affect the strength and ductility. Hardenability and deformability can be multiplied by 2 times by the atomic level heterogeneity and the stacking fault energy in contrast to the Gaussian distribution measured in the bond length between crystal structure. This atomic-level heterogeneity promotes the dislocation nucleation during solid solution strengthening thereby enhancing the hardness and ductility. The increase in hardness results from the uniform bond lengths and atom size between solvent and solute. Proper dispersion of Mg molecules the solid solution has a significant effect on hardness, which increases hardness from 533 to 853 HV.

The effect of Al, Ti and Hf is studied by Zhang et al. [99] for its mechanical properties and corrosion resistance in the CuZrY alloy. The prepared alloy shows that compressive strength of the Z_2 (Al+Hf-rich) HEAs obtained is 1751 MPa, which is higher than Z_1 (Ti+Hf-rich) and Z_3 (Al+Ti-rich) HEAs with the compressive elastic modulus of more than 50 GPa for Z_2 alloy. The increased compressive strength and elastic modulus is a result of stiffness obtained during the solid solution strengthening. The other reason may be due to the HCP dendrites with δ value is 6.56% for Z_2 which is higher than Z_1 and Z_3. Hsu et. Al [100] suggested that the presence of another principal element in the alloy system can significantly affect the alloying behaviour of the primary element. The examination on the influence of gold silver and iron in the alloy system depicts that addition of some of these alloying element can be chemically incompatible with the other alloys indicating multi-element mixing cannot be expected. Since the hardness of the gold is slightly higher than the silver and thus multielement mixing of gold with cooper can be anticipated and form a hypo

eutectic dendrites confirming that gold can be used as a mixing agent. Multielement mixing of element should not only promote positive enthalpies but also the entropy contribution to counterbalance the positive enthalpies. Maximum positive enthalpy for the adequate mixing of the six alloy elements should be below 10KJ/mol to achieve effective hardness. The hardness of the Al+Cu rich, golden layer+ Cu rich, silver layer +Cu rich is 419, 104, 451 HV respectively for the mixing enthalpy is 4 KJ/mol.

Wang and Zhang were [101] studied the effect of the addition of Co in Ti-rich CrFeNiAl alloy. The compressive strength of the Co_1 alloy at room temperature was found to be 3.14 GPa with 23.3% ductility. However, the addition of Co more than 1.5%, decreases compressive strength slightly. Better ductility is achieved as a result of dimple-shaped structure observed from the fracture morphology. It is learned that solid solution strengthening attributed to the improved strength as a result of the strengthening of Ti and Al in the multielement mixing process.

Varalakshmi et al. [102] studied the formation of single solid solution from binary, ternary, quaternary, quinary and hexanary alloys. The formation of single solid solution is evident after milling for minimum 10 hrs for the binary to quaternary alloys. It is required to milling for 150-20 hrs for quandary and hexanary alloys. The longer the milling time the proper is the solid solution mixing of the alloys as a large number of components in the alloy system could lead to the slower diffusivity. The highest hardness is obtained for the hexanary alloy with a value of 2 GPa than the others, which suggests that solid solution mixing have high strength. Trigger stress on the effect of Al and Nb in Ti-Al-Nb alloy is studied by Paradkar et al. [103]. The test evokes the interest to examine stress-induced martensitic transformation (SIMT). The addition of 8-12 at.% Nb and 15-18 at.% Al decreases the trigger stress of the alloy. The rank of the trigger stress for the Nb-rich alloy is as follows, 489 MPa> 373 MPa>310 MPa for Ti–15Al–8Nb, Ti–18Al–8Nb, Ti–15Al–12Nb for 1600 μm, 448 MPa, 349 MPa, 255 Mpa for 1250 μm and 459 MPa, 365 MPa and 273 MPa for 510 μm respectively. All the composition of three different alloys exhibited SIMT but the stress transformation from β to α depends on alloy composition and grain size too. Since β is a martensitic stabilizer and the minimum trigger stress required for β transformation was lower for Ti–15Al–12Nb which denotes that increase in Nb also increases trigger stress whereas an increase in Al also decreases trigger stress. Varalakshmi et al. [104] synthesized the equiatomic HEAs by mechanical alloying using nanocrystalline CuNiCoZnAlTi. The resulted solid solution is composed of BCC dendrites with crystal size less than 10 nm. Thermal analysis showed that the prepared alloys are thermally stable even at a higher temperature of

800 °C by retaining its nanocrystalline structure with the mixed phase of BCC+FCC dendrites. One such method of producing HEAs is mechanical alloying and results of compressive strength and hardness are 7.55 and 2.36 GPa as a result of solid solution strengthening with nanocrystalline structure. Maximum enthalpy for the adequate mixing of the elements occurred is 11.5 J/mol K.

The effect of Cr and Mo on the softening resistance and the hot hardness is studied by the Hsu et al. [70] in the formation of $AlCoCr_xFeMo_{0.5}Ni$ alloy system. It is revealed that increasing Cr content from 0 to 2 in the alloy system increases the hardness from 601 to 867 HV owing to the transformation of σ phase in the volume fraction. This result in the matrix phase transforms from B2 to σ phase. All the prepared Cr-MO rich alloy possess high hardness than the Ni-rich alloy promoting to have a potential to be used in high-temperature applications. The SEM images showed that Cr from 0.5-1.0 has no eutectic phase. However, exhibit a simple dendrite structure. In the multielement mixing of 5 to 6 alloys, Ni, Fe and Co occupy the same place whereas Co and Mo occupy same sized space in the opposite site in the crystal structure. The heat treatment of the alloys above 600 °C exhibits a high plastic strain thereby yield stress dropped by 30-40% showing that the prepared alloy is sensitive to the temperature more than 600 °C.

Ye et al. [105] the laser cladding technique is one such significant and a potential method for producing HEAs of multi element with ease in controlling dilution ratio during formation of single solid solution. A novel Al-rich FeCoNiCuCr alloy is manufactured in the form of a thin layer. The results showed that high aluminium cladding exhibit higher hardness as well as the abrasion resistance and corrosion resistance. In order to achieve simple nanocrystalline structures with a cooling rate between 10^3-10^6 K/s, laser cladding approach is justified. Microstructure obtained using laser cladding is the combination of simple FCC+BCC dendrites with Thomson structure, which causes the grains to orient to spherical shape during heat treatment.

Micro-compression tests were carried out to study the micromechanical behaviour of Al-rich CoCrCuFeNi alloy by Liu et al. [57]. The XRD pattern shows that the alloy has a main phase of FCC structure but the reduced peaks in the reflection of atoms are the result of the distorted atomic planes. Thus reduced peaks allowed the author to measure for existence of BCC phase and interestingly, one FCC and one BCC was evident by the conventional XRD test and it was termed as FCC1 and FCC2. When x varied from 0.5 to 0.8 in Al_x, the increase in hardness was witnessed due to the lattice distortion and change in phase from FCC to BCC. When x is increased to 1, the phase becomes BCC completely thereby

increasing hardness to the maximum value. The highest yield strength of 958 MPa was achieved when Al is added to 1% and it is 20% higher than when Al was between 0.5-0.8. The synthesis of Si, Mn and Mo in the FeCoNiCrCu alloy by laser cladding and arc melting is done by Zhang et al. [106]. The hardness of the coating prepared by the laser cladding technique was 375 HV, which was 50% higher than that was prepared by arc melting method with poor quality coating. The HEAs was composed of simple FCC with very high microhardness, corrosion resistance and softening resistance. The addition of Si, Mn and Mo resulted in uniformly distributed equiaxed and columnar structures with improved coating quality and microhardness to 450 HV, but it was noticed that element segregation was increased with transformation of microstructure to dendrites. The coating showed a better corrosion resistance in 5% H_2SO_4.

Praveen et al. [85] studied the alloying behaviour quinary AlCoCrCuFe and NiCoCrCuFe multi component HEAs alloy. XRD analysis shows the presence of FCC+BCC structure during mechanical alloying, whereas FCC+ σ phase involving FCC+BCC during SPS. The hardness obtained for AlCoCrCuFe and NiCoCrCuFe was 700 and 400 HV respectively. The author suggest to achieve nanocrystaline structure is possible with enthalpy of mixing is neat and less than 20 KJ/mol. The alloy produced using mechanical alloying is metastable. However, stable microstructures were obtained even after 900 °C is only in SPS. When Al is replaced by Ni in the AlCoCrCuFe system, a microstructure transform from BCC to FCC can be evident. Tsao et al. [107] investigated the Al-Ni-Fe rich CrMn alloy, synthesised by arc melting and casting method to study the age hardening property from quinary alloy. The study involved a heat treating of ingot for 8 hrs at temperature of 650-750 °C and quenching in water. These results consist of Ni rich FCC interdendtritic phase, Cr rich BCC phase with small fraction of cross-like β-FCC phase. Aging to a temperature of 650 °C eliminates β-FCC phase from the alloy and then second phase of β_1-FCC phase has occurred at temperature of 750 °C. In addition to this, the existed β_1-FCC phase becomes larger globular grain inside the matrix. The hardness of the as-cast, 650 °C aged, 750 °C aged is 298.8, 636.2, 898.5 HV respectively, implying that age hardening improves the grain structure during solid solution thereby improving the hardness value.

Kuznetsov et al. [108] measured the tensile properties of as-cast and wrought condition hexanary AlCrCuNiFeCo alloy. Multistep forging was adopted to reduce the particle size to an average of 1.5 μm from coarse dendritic to fine equiaxed structures. The yield strength, ultimate tensile strength and tensile ductility was 1040, 1170 and 1% for the forged alloy against the 790, 790, 0.2% of as-cast condition. The tests showed that brittle to

ductile transition was occurred between 700-800 °C for as-cast and for wrought alloy; it was 600-700 °C. Super plastic behaviour was evident in the temperature range 800-1000 °C as the tensile elongation was 400 and 800% at temperature 1000 °C. HEAs usually possess low ductility. Therefore annealing treatment is necessary to be carried out as suggested by the author.

Zhang and Fu [59] were studied in detail the effect of heat treatment on the microstructure of Al-rich hexanary $CoCrFeNiTiAl_x$ alloy system. The alloy was prepared using vacuum arc melting and heat treated to a temperature of 1000 °C for 2hrs. Upon the addition of Al has witnessed a phase transformation from simple BCC to α-Fe, Cr BCC in the solid solution. FCC structure was observed for the alloy without Al content. Thus, annealing promotes the intermetallic segregation of elements to form solid solution mixing. The mixing entropy was observed to be 13.38 J/Kmol and with the reduced grain size after annealing was 4-10 nm. Eutectic dendrite structure was disappeared after the addition of aluminium exceeds 1%, thereby segregation of dendrite and interdendrite is detected for as-cast and as-received respectively. Zhu et al. [109] fabricated the quinary AlCoCrFeNi alloy with the help of cermet Ti (C, N) binder by sintering and mechanical alloying. XRD pattern shows that the alloy was composed of binder and single solid solution FCC structured alloy. The result showed that cermet binder helps in co-enhancement of hardness, microstructure and toughness. The developed novel material had Vickers hardness and fracture toughness of 1787 MPa and 11.4 MPa $m^{1/2}$ respectively. The obtained values are superior to those fabricated with high quality cermet binder as a result of W-rich binder phase and the equiatomic ratio of binder and the elements in the alloy. As the concentration of binder increases, the probability of occupying the lattice sites by the binder increases and thereby significantly increase in the distortion energy can be expected and hence the solid solution strengthening increases.

Yuhu et al. [110] investigated the effect of Fe-Mo rich $AlNiCrFe_xMo_{0.2}CoCu$ alloy fabricated by using powder metallurgy technique. The hardness of the alloy varied from 3170 to 2290 HV when varying Fe and Mo from 0.5 to 2.0. The XRD analysis showed that phase existed in the alloy composed of BCC+ FCC+ σ for x=0.5 to 2.0. Simultaneously, the fracture strength of the prepared alloy was 1100 MPa, compressive fracture strength and yield strength was as high as 1258 MPa and 1132 MPa respectively, with the improved plasticity of 30.2%. The increased fracture strength attributes to the intermetallic multi element stability of the solid solution phases.

Fu et al. [88] synthesised the inequi-atomic Co-Ti rich quinary nanocrystalline CoFeNiCrTi alloy by spark plasma sintering and mechanical alloying. XRD analysis depicts the alloy was composed of FCC+BCC when fabricated with mechanical alloying, while FCC +σ phase structure was witnessed during spark plasma sintering. The yield strength, compression ratio, Vickers hardness and compressive strength after SPS was reported to be 2.65 GPa, 10%, 846 HV and 2.69 GPa exhibiting superior mechanical properties. Alloy prepared by SPS, the compressive strength was enhanced by 33.2% and compression ratio by 11%. The observation reveals that alloy fabricated after SPS follows elastic deformation when the load reach to a yield point depicting that plastic deformation would not be characterized from the stress-strain curve.

Fu et al. [111] studied deformation twinning and alloying behaviour of the inequi-atomic Al-Ti rich hexanary alloy (CoFeNiCrAlTi). The phases found in the alloy consist of FCC and a metastable BCC during mechanical alloying, while two FCC and a new BCC phase dendrites were witnessed during SPS. The yield strength, compression ratio, hardness and compressive strength was measured to be 2.08 GPa, 11.5%, 573 HV and 2.52 GPa respectively. The compressive strength of the Al-Ti rich hexanary alloy is slightly higher than CoFeNiCrAlTi alloy fabricated by copper mold casting. Fracture test on the Al-Ti rich alloy concluded that intergranular and plastic fracture was dominant behaviour.

Lilensten et al. [112] fabricated a new refractory quinary alloy fabricated by arc melting technique consisted of $Ti_{35}Zr_{27.5}Hf_{27.5}Nb_5Ta_5$.the fabricated alloy showed a density as high as 8780 kg/m^3 and hardness value close to 2400 MPa. XRD analysis showed a martensitic structure (α-type) was dominant. HR-TEM analysis revealed that hexagonal twinning of the grains was obtained after the heat treatment as a result of stress relaxation. Hardness of the equimolar composition of the alloy exhibited hardness more than 3826 MPa after heat treatment.

Ng et al. [113] designed the Co free quinary AlCrCuFeNi alloy to study the effect of Co on tensile property and phase stability in the microstructure. A unique methodology was adopted by combining heat treatment and thermodynamic calculations to develop the alloy. The hardness value was found to be 218 HV. However, when the alloy was annealed at 700 °C for 24 hrs, the result showed an increment to 410 HV but decrease in hardness was witnessed from 382 HV to 305 HV when the alloy was annealed at temperature 900 °C and 1100 °C. Significant variation was also encountered in tensile properties after heat treatment. The yield strength and the ultimate strength of the as-cast and 700 °C annealed alloys were 630, 1085 and 922, 1326 MPa respectively, with an elongation of 4.2%. The alloy showed a

brittle nature with many cracks on the fracture surface. The increase in hardness attributes to the changes in the microstructure after heat treatment from BCC to FCC+ α phase dendrites.

Damping behaviour of the quinary Al-rich $Al_xCoCrFeNi$ was studied by Ma et al. [114]. Effect of variation of aluminium from 0 to 1% in the alloy is studied using dynamic mechanical analyser (DMA) from ambient temperature to 773 K. The frequency range varied from 1 to 16 Hz. The results showed that Al-rich alloy had a small elastic storage modulus and therefore, a large resistance to structural changes. However, Al free and Al lean alloys possess higher damping capabilities owing to the much higher loss tangent witnessed during the experimentation. Therefore, it can be concluded that increase in temperature reduces elastic storage modulus by increasing loss tangent and effect of frequency cannot be ignored. The prepared alloy exhibited significant damping capability superior to Fe-Al alloys. Interesting feature of the research involves in the microstructural changes. As the Al concentration increases transforms the bamboo like structure to dendrites to equiaxed structure. Al rich alloy showing higher storage modulus in which FCC dendrites tend to decreases linearly whereas, BCC dominant phases changes or becomes constant as the temperature increases.

Wu et al. [115] fabricated equi-atomic quaternary HfNbTiZr alloy to investigate the tensile and structural stability. The compressive fracture strength and plastic strain measured is about 969 MPa and 14.9% respectively. The alloys tend to retain its BCC structure after furnace cooling from 1573 K. True stress increases to about 850 MPa with its strain counterpart of about % and the gradual increase in load increases strain but stress becomes almost constant. Secondary phases was not evident even after performing the heat treatment indicates that solid solution strengthening was successful and the yield strength and ultimate strength reported to be higher than in the literature.

Nanocyrstalline pentanary AlNiFeCrZn alloy was synthesised by mechanical alloying by Babu et al. [116] to study the thermal behaviour of the prepared alloys. The pentanary alloy was mainly composed of BCC dendrites with crystal size of 10 nm in size. Alloys exhibited no phase transformation even at a temperature of 8500 °C and tend to retain its grain structure and found to be thermally stable. The hardness and young's modulus values after nano indentation test was 7.427 and 153.03 GPa, respectively.

A Hexanary component of Al-rich alloy was fabricated by He et al. [66] to study the tensile properties after the structural changes. The formation of single solid solution resulted in microstructural changes from single FCC (relatively low strength) to duplex FCC+ BCC (increased brittleness with reduced ductility). As the concentration of Al changed, the

changes in the tensile properties were also changed. The prepared alloy showed the ratio of hardness to tensile strength is 3.13 ± 3.53. The yield strength, tensile strength and elongation of the alloy with Al< 8% and 8 %< Al< 16% content is 220 and 310 MPa, 500, 1174 MPa and 6.017, 25.4% respectively. The hardness was sharply increased to 538 HV in $Al_{8\%}$ but it was remained same when the Al concentration increased to 16%.

Studies on the solid solution strengthening on spark plasma sintered hexanary Al-rich AlxCoCrCuFeNi alloy by Sriharitha et al. [117] suggest that the prepared alloy exhibited superior thermal stability when tested at temperature 400-600 °C in Ar atmosphere. It was noticed that heat treatment on the prepared alloys had no significant effect on the hardness values and it was 160 HV. Increase in Al content seems to increase the solid solution strengthening as concluded by Hall-Petch analysis. When compared with the Inconel 718, the prepared alloys seem to overwhelm properties and can be used to replace the conventional superalloys. Juan et al. [118] fabricated two refractory quinary and hexanary HfMoTaTiZr and HfMoNbTaTiZr alloy by vacuum arc melting to study the mechanical properties. The refractory alloy exhibit superior strength at high temperature but, they tend to behave brittle nature at ambient condition. The plasticity of the quinary alloy was over 50% at ambient condition and insufficient strength at the high temperature. The author designed to change the composition from quinary to hexanary by retaining its toughness at room temperature. The synthesised two alloys had a BCC structure with the yiled strength of the hexanary alloy was 1828 MPa at elastic strain 12% compared to the parent alloy. The hardness of 542 and 505 GPa was measured for the hexanary and the quinary alloy. Interestingly, the hardness of the measured values is three times higher than the rule of mixture values.

Zaddach et al. [119] synthesised a euqi-atomic and two nonequi-atomic NiFeCrCoMn by arc melting technique. All the alloys were heat treated to temperature 575- 1100 °C. Euqi-atomic alloy measured after annealing temperatures had highest toughness and ductility. The reason may attribute to the absence of oxide particles that form with Mn in the alloys. As the temperature increased the toughness was reduced sharply. The results for the best combination of elements in strength and ductility were possible by adding up NiFeCrCo with yield strength and elongation was nearly 220 MPa and 70% after heat treating at 1100 °C.

A quaternary Al rich and the quinaryequi-atomic alloy structure was heat treated at 773, 973 and 1173 K for 30 min to study the influence of iron on the mechanical properties by Fazakas et al. [120]. The prepared alloys were relatively hard and ductile compared to conventional HEAs. The alloy showed significant strength and after being heat treated at 973 K as a result of homogeneous deformation. It can be concluded that annealed alloys showed a

significantly higher hardness than the as-cast alloys and the values are 1074 and 980 MPa respectively. Juan et al. [121] studied the solid solution strengthening of Mo-rich hexanary ductile refractory alloy by vacuum melting in argon atmosphere. The increase in Mo from 0 to 1 increases the yield strength from 1015 to 1512 MPa. Simple BCC structure was evident in all as-solidified alloys. The Mo concentration can significantly affect solid solution strengthening linearly, which acts as an additive and also decrease lattice parameter, however, opposite trend was witnessed for densities. Mo-rich alloys exhibit better ductility and 50% more plasticity than the Mo-lean alloy at ambient temperature.

Vaccum arc melting technique was adopted in the fabrication of quinary based alloy to study the annealing effect after carbon addition by Stepanov et al. [97] revealed that the microstructure of the solid solution is composed of single FCC as-solidified alloy. A small fraction of M_7C_3 nanoscale carbides for C=0.1, coarse carbides of M_7C_3 with the volume fraction of 5% and 9.5% respectively. Microhardness values increases from 160 to 275 HV as the carbon increase from 0.1 to 0.25. Surprisingly, no significant change in hardness was witnessed by increasing annealing temperature. It should also be remembered that addition of elements in the alloy system reduces the carbon solubility. It was also evident that dendrite segregation of the elements annealing at 1200 °C with volume of the particle were 3± 1% for the emerged secondary phase.

A systematic approach to study the precipitation behaviour of the quartenary FeCoNiCr alloy by the He et al. [122] with small amount of Ti and Al reveals that, a sharp decrease in strength was witnessed when temperature exceeds 800 °C but it was as high as 900-1000 MPa and ductility above 40% when temperature was well below 800 °C. A small addition of Ti and Al resulted in precipitation hardening mechanism by overcoming other mechanism such as grain boundary hardening, solid solution strengthening, and dislocation hardening and so on. It is to be remembered that what plays a major role in solid solution mixing in the final stage irrespective of the orientation of the grain structure due to shearing or orowan bowing mechanism can be nullified. So in order for the alloy to have a best possible combination of strength and ductility, the alloy should be aged between 700- 800 °C.

Arc melting technique was adopted in fabricating Al rich multi component HEAs by varying Al from 0 to 1 in steps of 0.25 resulted in BCC+ C15 (FCC) phase for $Al_{0\text{-}0.25}$ and BCC+ two C14 (HCP) phase for $Al_{0.5\text{-}1}$ as studied by the Yurchenko et al. [123]. The significant characteristic of adiditon of Al as resulted by thermodynamic modelling is existence of two BCC+C15 phases and decreasing the density of the alloy. The prepared quinary Al-rich alloy exhibited brittle nature at ambient and 600 °C. A sharp increase in yield

strength was noticed at 800 °C from 440 to 1250 MPa for Al-rich and Al-lean alloys as well. The results obtained from the specific tests were compared with the HEAs resulted in the literature and Ni based super alloys as well. Varvenne et al. [124] fabricated HEAs by selecting a new class of random elements FCC phase structure having toughness and higher strength and it is compared with the theoretical model. Author correlated the strengthening process is a consolidation of effective matrix by the embedding solute around the alloy. Therefore, dislocation interactions at the grain level leads to random local concentration by achieving strengthening. This research also demonstrates the parameters such as temperature, composition and materials that strength of the HEAs is dependent on.

The studies based on Fe-Cr-rich HEAs are investigated for compressive tensile properties fabricated by copper-mold casting by Rao et al. [125] reveals that microstructure of FCC phase composition was established for as-cast HEAs, whereas FCC dendrites was segregated to form BCC phase for X=1.2-1.4. The results on the yield strength, elongation and ultimate strength were 439 MPa, 23.4% and 884 MPa respectively. Resulted FCC phase was composed of fine poly hedra of elements of Cr, Fe and Mn in the dendrites. They also reported that phase selection and solid solution strengthening was based crystal size of length 0.5-1 µm.

2.4.1 Thermal behaviour of HEAs

The detailed structural evolution of hexanary HEAs involving the variation of aluminium in forming amorphous alloys exhibited an equiatomic crystalline icosahedral phase as studied by Kim et al. [126]. The Al_{-10} rich among the other three alloy exhibited a Zr_2Cu-type icosahedral phase at 970 K. The formation of Zr_2Cu- type phase retards the decomposition after the melting move beyond 970 K thereby enhancing the thermal stability. Contrarily, the other two alloys formed with Ti_2Ni-type and $MgZn_2$-type decreases thermal stability by accelerating the decomposition. It is also mentioned that formation of atomic complexity dwells in the equiatmoic substitution and alloy composition.

Studies on Al-rich quinary HEAs by Chou et al. [54] on thermo-physical and electrical properties by arc melting method depicted that change in aluminium from 0 to 2% resulted in a change in phase transformation from single FCC to single BCC with duplex FCC/BCC dendrites. XRD studied revealed weak lattice distortion was involved by the variation of aluminium. Due to weak distortion capability of the lattice electrical and thermal conductivity was much small than those pure metals. The transport property of the electron and photon were similar and comparable to those of semi-metals. Investigation by Dolique et

al. [127] on interesting properties of magnetism, mechanical and tribological involving each element in the range of 5 to 35% reveals that nanocrstalized structures with the random solid solution are stable even at higher temperatures. Thin film deposition of hexanary HEAs by magnetron sputtering on mosaic targets was successful. Thermal stability of the developed thin films were stable at a temperature of 510 °C of heat treatment (Annealing) but resulted in a distorted thin films beyond 510 °C. Heat treatment of on thin films has shown the phase transition took place at 310 °C involving a disappearance of BCC dendrites to form AlCr binary phase. Tariq et al. [128] studied AlCoCrCuFeNi HEA and concluded that the endothermic line taking place after the peaks due to the exothermic peaks are due to the phase change and disintegration of the crystal structure at higher temperature.

Lu et al. [129] studied the heat transfer and thermal expansion capability of the quinary HEAs resulted in an increased thermal diffusivity. The increment was 20% and 50% at 423 and 573 K. The increase in thermal diffusivity is achieved by the lattice dilation for a different temperature range. The increase in thermal diffusivity is as a result of slight shift in reflection peaks to lower angle forming BCC dendrites at temperature range 450 to 600 K. The effect of addition of aluminium in mol fraction to hexanary HEAs fabricated by spark plasma sintering resulteda dense alloys as investigated by sriharitha et al. [117]. The studies on thermal stability in Ar atmosphere for 2- 10 hrs in a 400-600 °C temperature range resulted in fine crystal structure and excellent thermal stability. 160 HV of specific hardness was achieved for sintered Al-$_{0.5}$ with no change in hardness. Hall-Petch analysis was carried out to study the effect of the addition of Al and it showed that addition of aluminium increases the solid solution strengthening. Laplanche et al. [130] studied the CoCrFeMnNi HEAs and correlated the elastic modulud with the different properties. It was concluded that there is no linear dependency of α on temperature.

Investigation of the multi component HEAs by Caro et al. [131] revealed that, HEAs not only are thermally stable but also possess potential to resist radiation. It is resulted due to the equilibrium thermodynamic state extreme disorder of the dendrites with the stabilized entropy. It is said that disorder in the dendrites keeps the damage energy longer in such a way to reduce the photon and electron conductivity. The result of the analysis by Caro et al. also suggested guidance in the selection of HEAs possessing photon and electron conductivity. A classical theory on molecular dynamics based on Lennard-Jones approach was adopted in the investigation of the effect of disorder in thermal conductivity. The addition of more impure atoms in the solid solution once the thermal conductivity has reached the critical point doesn’t reduce the thermal conductivity more. Therefore, in order to reduce thermal

conductivity below the critical point (ultra low), hence a combined effect of local strain field and mass defect scattering should occur in the solid solution surpassing the minimum limits suggested in the theoretical aspects studied by Giri et al [132].

2.5 Corrosion and Tribological characteristics of high-entropy alloys

2.5.1 Corrosion behaviour of HEAs

Corrosion behaviour of quinary HEAs in 3.5% NaCl solution as depicted by Hsu et al. [75] that the increase in Copper in HEAs increased the tendency of these alloy to the localised corrosion as revealed by immersion (for 30 days) and polarization tests. It may be attributed to the formation of interdendrites, and these interdendrites deplete against active cell segregation in the alloy and galvanic action attack.

The comparison of HEAs for electrochemical kinetics with stainless steel in aqueous environment has depicted a higher degree of magnitude of disorder. The investigation revealed that HEAs has better corrosion resistance than the 304 steel in both acidic and NaCl medium but pitting action was more predominant in HEAs as studied by Chen et al. [133]. 94.06, 310.43 KJ/mole and 219.97 and 343.18 KJ/mole were the energy for HEAs and steel in NaCl and in acidic solution respectively, showing that corrosion resistance of HEAs were significantly high than its counterpart. Chen et al. [134] investigated the corrosion behaviour of Cu-rich HEAs. The investigation was carried out in a 288 °C high purity water resulted in a bulk glassy like structures. A weight loss was as low as 4.5 $\mu g/mm^2$ in sodium sulphate solution for $Cu_{-0.5}$ immersed for 12 weeks.

The investigation on the addition of aluminium in a multi component HEAs revealed that corrosion resistance upon the addition of aluminium in both H_2So_4 (acid) and NaCl (base) solution. Lee et al. [135, 136] revealed the reasons attributes to the corrosion and it was pitting corrosion. Al free HEAs exhibited tremendous resistance to general corrosion than the HEAs with Al in acidic solution. Chou et al. [137] studied the effect of molybdenum in three aqueous environments such as basic, acidic and marine to study the electrochemical properties in ambient temperature (25 °C). The corrosion resistance of the HEAs with Mo free was significantly high than that of the HEAs with Mo contribution in the alloy. It was resulted due to Mo rich alloy was susceptible to the pitting action in NaCl solution. An investigation carried out by Chou et al. [138] to study the behaviour of HEAs for pitting potential and pitting temperature in chloride solution. The critical pitting temperature obtained for 0.1, 0.5 and 1 mol/L NaCl solution was 70, 60 and 60 °C respectively. The positive effect was witnessed for both pitting potential as well the pitting temperature as the

ratio exceeds 0.5. Passivity and transpassive corrosion was evident overcoming pitting corrosion as showed by the potentiodynamic polarization curve.

Examination of the heat treatment on microstructure and corrosive behaviour quinary HEAs studied by Lin et al. [74]. XRD studies revealed that alloy was composed of FCC phase when heat treated the alloy at 1250 °C and subsequently microstructure studies showed that Cu-rich phase had spinodal decomposition when treated between a range of 350 °C to 1250 °C. The corrosion resistance of the alloy was degraded by the presence of Cu rich matrix in the alloy. Hsueh et al. [80] investigated the effect of Nitride-rich quinary HEAs films on aluminium alloy and mild steel substrates deposited by magnetron sputtering technique. The difference in atomic size resulted in low crystalline structure. Despite the deposition of 22.4% of nitrogen the resulted film formed in amorphous state. The film deposited with 30% nitrogen showed better corrosion resistance among all the deposited films. It is also revealed that corrosion resistance of the film depends on the interface bonding, film structure and nitrogen content. The increase in substrate bias from 0 to -100 V changes hardness from 16.9 to 19.6 GPa and young's modulus from 231.5 to 227.5 GPa.

Qiu et al. [139] prepared the quinary HEAs by laser cladding technique to study the microstructure and corrosion resistance. Solid solution strengthening resulted in combined FCC and BCC phase owing to the rapid solidification and phases less than 6. This combined FCC and BCC structure minimise the chances of forming brittle compounds. Better corrosion resistance was witnessed for 1 mol/L in NaCl than 0.5 mol/L H_2SO_4.

The migration and segregation of species in the quadnary HEAs alloy system created a negative vacancy for Cr, whereas positive for the others in the alloy. Low activation energy during the migration of a each element may have caused the negative vacancy for Cr in the alloy system. However, Co, Fe and Ni migrated with activation energy of 1.07, 1.32 and 1.36 respectively compared to a value of 0.68 for Cr. the other reason may be that Cr is not thermodynamically stable in the quandary alloy system and thereby segregating out to form a Cr metal by creating a negative vacancy as revealed by middleburgh et al. [140]. Zhang et al. [141] investigated the synthesised the laser surface allying technique to improve the corrosion and cavitation resistance of the premixed high purity elemental powders. The analysis showed that proper synthesis of the technique including the elemental powders results in a good metallurgical bonding with the substrate. Solid solution of the alloy resulted in a single phase BCC structure as a result of tremendous mixing entropy than the combined effect of atom size difference and valence electron concentration. The microhardness of the HEAs alloy system was 3 times harder than the steel and improvement in corrosion as well as, the

cavitation resistance was 7.6 times than steel was witnessed. In another study, Shang et al. [142] studied the effect of CoCrFeNi (W1-xMox) HEA coating on Q235 steel substrate and concluded that the Mo addition also improves the corrosion resistance.

Equimolar quinary Ni-rich alloy system with promising mechanical properties at cryogenic temperatures was achieved by Ye et al. [19]. The XRD analysis revealed that coating was formed with identical Fe-Co-Ni rich and Mn-Ni-rich dendrites. The nobler corrosion resistance of the coating in both 3.5% NaCl and 0.5 M H_2So_4 acid solution was witnessed than the steel. EDS analysis on the corroded sample showed that corrosion started with the Cr dendrite. The Cr-Ti-rich equimolar HEAs was synthesised to study the effect of Cr and Ti by nonconsumable arc melting. Multi phase microstructure with BCC, FCC and intermetallics were identified after the solid solution strengthening. The septenary alloy system exhibited a short range pair of Ti-Co, Cr-Fe, Al-Ni and Co-Cr in liquid structure as revealed by Ab initio molecular dynamics (AIMD). The addition of Cr and Ti facilitates the formation of BCC and FCC dendrites respectively in the alloy system as investigated by Xiao et al. [143].

Wang et al. [144] synthesised the HEAs with direct laser fabrication technique for high temperature applications. The aged samples at temperature in a range between 600 to 1200 °C were examined for microstructure, corrosion and mechanical properties. Formation of FCC phase for the synthesized HEAs is a result of fast rate of cooling during deposition whereas, for the as deposited alloy B2 solid structure was evident. Microstructure of the HEAs ageing between 800-1200 °C resulted in needle-like, plate-like and wall shaped precipitates across the boundaries. Microstructures obtained in the Al-Ni rich were susceptible to the galvanic corrosion which corrode preferentially than the Fe-Cr rich alloy.

High entropy alloy coatings have evoked the interest of researchers worldwide owing to its tremendous mechanical and corrosive properties [145]. Deposition of Ti-rich HEAs synthesized on steel substrate is studied to micro-hardness, mechanical and microstructure properties. Phase identification revealed that formation of FCC+BCC for x=0.5 to 1, FCC+BCC+Ti_2Ni for x=1.5, and FCC+BCC+Ti2Ni+ ordered BCC dendrites for x=2. However, the microhardness of the coatings was in the range of 615 to 730 HV. Interestingly, addition of Ti increased hardness to 3.6 times than the steel. The prepared alloy exhibited excellent cavitation resistance in distilled water but weak in NaCl solution.

The chemical segregation upon the homogenization by the addition in Al content resulted in a multi phase structure are inevitable as investigated by Shi et al. [146]. As we know that heat treatment to a temperature of 1250 °C for 1000 hrs to homogenise the

microstructure with chemical segregation leads to the improved corrosion resistance. The author also depicts to further increase in corrosion resistance by adopting suitable annealing methodology. The addition of Al to 0.5% in the alloy system with the suitable heat treatment results in a 97% of A1 and 3% of B2 phases with excellent hardness.

A short communication by Luo et al. [147] on the corrosion behaviour depicted that depleted Cr and enriched Fe and Mn were evident during the solid solution strengthening. Owing to the reason mentioned above and the formation of the metal hydroxide the prepared alloy showed a weak corrosion resistance. The average grain size was 8 and 30 μm for the synthesized alloy and the steel respectively. It is also revealed corrosion resistance of the steel is not greatly affected by the grain size in micrometer range. Microstructure studies depicted that pit were evident on the surface when tested in H_2So_4 solution. Shi et al. [148] investigated the corrosion behaviour of quinary HEAs via the electrochemical-AFM technique. Micro and sub-micro surface studies were carried out to depict the changes in the surface affected by the corrosion 3.5% NaCl solution. Microstructure of the Al-rich (x=0.7) alloy is formed FCC with small traces of BCC dendrites. The studies revealed that the height difference of 40.33±2.87 was evident between FCC and BCC dendrites. Formation of pits at the intersection between FCC and BCC and inside BCC phase as well can be seen.

2.5.2 Wear analysis of HEAs

Wu et al. [149] investigated the effect of the aluminium content in the $Al_xCoCrCuFeNi$ HEAs. From their observation it was found that there was change in the wear mechanism from delamination to oxidative wear and decrease in the wear coefficient. However, they observed increase in the hardness values and volume fraction of BCC phase. A simple FCC structure was observed at low Al content (x=0.5) and big debris were resulted due to presence of deep grooves and periodic delamination on the worn surface. Both FCC and BCC structures were observed at medium Al content (x=1.0) and deep grooves were present on the worn surface in FCC region and in BCC region it was smooth. Though the oxidative wear present in the smooth region the dominating mechanism is only delamination wear. Fully BCC phase microstructure was observed at higher content of aluminium (x=2.0) resulted in smooth worn surface with fine debris of high oxygen content. Thus, from their investigation they concluded that the wear resistance increases with increasing the aluminium content. This resulted in high hardness and resistance in plastic deformation and delamination.

Hsu et al. [17] designed AlCoCrFeMoNi high entropy alloy by replacing Cu with Mo in the AlCoCrCuFeNi alloy in order to increase the mechanical and thermal stability. The

wear behavior of $AlCoCrFe_xMo_{0.5}Ni$ alloy was further investigated by varying the Fe content. As the Fe content increases from 0.6 to 2.0 the change in microstructure was observed from dendritic to polygrain. With increase in Fe content the BCC structure was increased. The hardness and wear resistance were reported as declined with the increase in Fe content. It was also reported that majorly abrasion type of wear mechanism tool place by observing the worn surface and worn debris. Due to presence of more oxides at higher level of Fe content ($Fe_{2.0}$) these resulted in low wear resistance. Wang et al. [16] introduced a new concept – "high entropy microstructure". An alloy is said to have high entropy microstructure if it consists of five or more than five elements with each element having concentration in the range of 5–35%. The high entropy microstructure consists of very fine grain size without evidence of any large grain sized intermetallic phases which increases the toughness of material during impact wear and high stress wear test. The high entropy microstructure concept was introduced by changing the properties of white cast iron. This was done by addition of elements having a strong tendency of carbide formation to the parent material. By doing so, it was reported that the carbide growth was retarded due to mutual competition of carbide forming elements to form their own distinct carbide. Elements like Ti, Mo, W, and V which have strong tendency towards carbide formation were added simultaneously to Fe–20Cr–5C alloy. With increasing the number of foreign elements, the primary $M_7C_3$was eliminated from the original white cast iron. This phenomenon was due to the segregation of several carbides having fine grain size such as eutectic M_7C_3, M_6C and MC. The newly developed alloys have shown a great improvement in the wear resistance.

Huang et al. [150] developed an equimolar ratio TiVCrAlSi alloy using laser coating on Ti–6Al–4V alloy. The SEM analysis of the microstructure revealed that the developed coating was bonded metallurgically to the substrate. From different analysis, they showed that the newly developed coating TiVCrAlSi was comprised of having $(Ti, V)_5Si_3$ precipitates distributed in the BCC matrix. The formation of intermetallic compound $(Ti, V)_5Si_3$ was energetically favourable because its formation was accompanied by large enthalpy variation which equipoise the effect of entropy. They also reported that the wear resistance of TiVCrAlSi clad on Ti–6Al–4V alloy showed a significant improvement during the adhesive wear test. The wear resistance of TiVCrAlSi clad was enhanced due to the presence of silicide phase in the ductile BCC matrix.

There are only few studied based on the investigation of non-equimolar HEAs. Liu et al. [151] studied the sliding wear behaviour of $AlCrCuFeNi_2/Si_3N_4$ pair in three different test conditions viz. dry, simulated rainwater, and deionized water. The wear rate was found lower

in the liquid condition as compared to the dry condition. The mechanism of wear in dry condition includes the detachment of large size debris. Furthermore, the wear mechanism observed in the deionized water includes abrasive wear, adhesion and plastic deformation. In case of the simulated rainwater, the corrosion and the microabrasion were the prime mechanism of wear.

Yu et al. [152] investigated the influence of H_2O_2 solution on sliding wear behaviour of AlCoCrCuFeNi and AlCoCrFeNi$Ti_{0.5}$.The adhesion and the delamination were the main cause of the wear phenomenon against $Cr_{18}Ni_9Ti$ steel and ZrO_2 ceramic counterpart. This resulted in the high COF and large material removal. In comparison, the SiC ceramic exhibits low COF and less wear. Yadav et al. [153] investigated the sliding wear behaviour of $AlCrFeMnV_{100-x}X$ alloy, where X=Pb and Bi (x= 0, 5, 10 atom percent). The result shows an insignificant change in COF value on Pb addition whereas Bi addition led to the decrement in COF value. The wear rate was found to lower by 21% and 25% with the addition of Pb and Bi. The surface morphology of the worn surface indicates the oxidative wear along with the abrasive wear. Yu et al. [154] studied the wear behaviour of AlCoCrFeNi and AlCoCrFeNi$Ti_{0.5}$ under lubricating conditions. In case of the gear oil, both the alloys show the abrasive groves on the surface. The $Ti_{0.5}$ alloys being harder results in smaller groves as compared to the other alloys. The influence of Boron on the wear behaviour of $Al_{0.5}$CoCrCuFeNi alloy was studied by Xiaotao et al. [155]. The boron addition increases the hardness of the alloy. As the Boron content becomes ≥ 0.6, there wear resitance behaviour of the alloy increases. This is due to the presence of ductile FCC phase and hard boride particles.

Ye et al. [156] studied the sliding wear behaviour of TiZrHfNb alloy. The investigation focuses on the two region, i.e. one elastic and other plastic. It was observed that in elastic region, the COF value declines with the increase in the load. However, the COF value was found to be almost constant in the plastic region.

2.6 Research gap

From the literature review based on the various criteria considered in the present research work on high-entropy alloys, following knowledge gap are concluded.

1. Though much work is reported on properties of equimolar high-entropy alloys (HEAs) but only few researchers have worked on a specific molar ratio based high entropy alloy.

2. The effect of the addition of various alloying element on the thermodynamic and Microstructural behaviour of equimolar HEAs has been studied extensively in the last one decade, but the effcet of the addition of elements on specific molar ratio based HEAs is still not explored comprehensively.
3. The effect of the addition of Mn, Co and Ti on the physical, mechanical and thermal behaviour of non-equimolar alloy is yet to be explored.
4. The past studies are available on the corrosion and wear behaviour of specific equi-molar HEAs. However, there are only few studies based on the corrosion and sliding wear behaviour of the non-equimolar HEAs.
5. The use of statistical techniques to rank different alloys based on any Multi-Criteria Decision Making (MCDM) method is rarely reported in the literature.

2.7. Proposed objectives of the research work

Based on the research gap from the available literature, the objectives of the present research work are outlines as follows:

1. Development of $AlCuCr_{1.5}FeNi_2Mn_x$, $AlCuCr_{1.5}FeNi_2Co_x$ and $AlCuCr_{1.5}FeNi_2Ti_x$ (where x = 0, 0.25, 0.5, 0.75 and 1.0 in molar ratio) multi-component high-entropy alloy by high temperature vacuum induction casting.
2. To study the thermodynamic behaviour of the cast high-entropy alloys and investigate the influence of Manganese, Cobalt and Titanium on microstructure and phase evolution of $AlCuCr_{1.5}FeNi_2$ high entropy alloy.
3. To investigate the effect of Mn, Co and Ti on physical, mechanical and thermal behaviour of $AlCuCr_{1.5}FeNi_2$ alloys.
4. To study the corrosion behaviour of the alloys in NaCl solution and sliding wear characteristics of the alloys using one-factor at a time and Taguchi design of Experiment.
5. To rank the cast alloys based on the various physical, mechanical, corrosion, thermal and wear behaviour using hybrid Entropy-TOPSIS (Technique for Order of Preference by Similarity to Ideal Solution) approach.

Chapter Summary

This chapter consists of

- ❖ Review of research works on various aspects of HEAs.
- ❖ The knowledge gap from past studies on HEAs.

- The objectives of the present research work.

The next chapter describes the materials and methods used to fulfil the objectives of the research work. The chapter provides information about the properties of the various elements used for casting alloys, thermodynamicbehaviour of the alloys, description of various equipment used for the testing purpose. It also describes the procedure for implementing the design of experiment and ranking of alloys based on the various properties.

*****

Chapter 3
MATERIALS AND METHODS

The outline of the current chapter illuminate the use of the various elements used for the development of high-entropy alloys (HEAs). The attributes of the constituent elements are tabulated to provide a brief overview of their physical and mechanical capabilities. Moreover, the processing technique is discussed in complete detail. The chapter also includes the details of the specific standard used for various physical and mechanical testing. The overview of the machines and the testing parameters used for the testing purpose is also described. The details of the Taguchi design of experiment (DOE) used in the present work is described and the significance of the control factors is further categorized using analysis of variance (ANOVA) in the wear test. Lastly, the muti-criteria decision making (MCDM) technique used to determine the ranking of the results obtained from various techniques is illustrated.

3.1 Materials and fabrication technique

3.1.1 Properties of elements used for the development of HEAs

Selection of elements while designing an alloy is the most essential design criteria. Most of the elements from the periodic table have been used for the development of HEAs. Each element has its distinct property and plays a vital role in the development of alloys. The most common elements used so far in the development of the alloys are Al, Cr, Cu, Fe and Ni.

Table 3.1 Characteristics of elements used for the development of HEAs [34, 157].

Element	Atomic number	Atom radius (pm)	Pauling Electo-negativity	Valence electron concentration (VEC)	Structure at RT_a	Density (g/cm^3)	Melting temperature (K)
Al	13	143.17	1.61	3	FCC	2.70	933
Cr	24	124.91	1.66	6	BCC	7.19	2180
Cu	29	127.8	1.90	11	FCC	8.94	1358
Fe	26	124.12	1.83	8	BCC	7.88	1811
Ni	28	124.59	1.91	10	FCC	8.91	1728

HEAs are one of the recent developed concepts in the area of material science. HEAs possess diverse ranges of attractive mechanical and physical properties like improved wear resistance and high hardness, exceptional capabiities at hig temperatures, ductility at lower temperature and

superplastic behavior. The properties of elements used for the development of the alloys are prsented in Table 3.1

a) Aluminium

Aluminium (Al) is the user friendly and the most widely consumed non-ferrous metal in the world. Aluminium being the second most used and 3rd group of elements in the periodic table having atomic number 13 and atomic weight 26.9815 based on ^{12}C and 26.9874 based on ^{16}O (Lewis J.E. 1961). It does not have any natural isotopes. The purity of the aluminium describes its physical properties to some extent. Melting and boiling point of Al are 660.2 °C and 2480 °C respectively. Al is well recognised for its resistance to corrosion with its low density of 2.7 g/cm^3 and justifies its use in some applications having thermal and electrical conductivity. Table 3.2 shows the physical and mechanical properties of Aluminium.

Table 3.2 Physical and mechanical properties of Aluminium [158]

S.No.	Physical Properties	Value
1	Melting Point	660.2
2	Boiling Point	2480
3	Structure	FCC
4	Density at 20 ^{0}C	2.7 g/cm^3
5	Thermal expansion coefficient (°C^{-1} x 10^{-6})	23.86
6	Thermal conductivity, e.g. units at 100 ^{0}C	0.57 W/mK
7	Modulus of elasticity	69 GPa
8	Tensile Strength	110 MPa

b) Chromium

Chromium (Cr) is odorless, tasteless, highly corrosive resistant and malleable metal introduced by NL Vanqueli in 1780. Chromium is a glossy, brittle, highly polished and hard metal available in silver-gray color. A layer of oxide is developed when Cr is used in oxygen environment and also acts as a protective layer. The physical attributes of Cr are presented in Table 3.3.

Table 3.3 Physical and mechanical properties of Chromium [159]

S. No.	Physical properties	Value
1	Melting temperature	1907 °C
2	Boiling temperature	2672 °C
3	Structure	BCC

4	Density at 20 ^{0}C g/cm^3	7.19
5	Thermal expansion coefficient (^{0} C^{-1} x 10^6)	4.9
6	Thermal conductivity, e.g. units at 100 ^{0}C	93.9 W/mK
7	Modulus of elasticity	279 GPa

c) Copper

Copper (Cu) is soft, malleable, and ductile metal in nature. Cu is generally used as heat and electricity conductor, in strain gauge and thermocouple for temperature measurement as it possesses very high thermal and electrical conductivity in nature. Cu is the metal that can be directly used (native metal) and need not to extract from the ore (McHenry C., 1992). The Cu exhibits the unique properties desirable for the development of alloys for the high temperature application. Table 3.4 shows the physical and mechanical properties of Cu.

Table 3.4 Physical and mechanical properties of Copper [160]

S. No.	Physical properties	Value
1	Melting temperature	1084 °C
2	Boiling temperature	2562 °C
3	Structure	BCC
4	Density at 20 ^{0}C (g/cm^3)	8.96
5	Thermal expansion coefficient (/^{0} C x 10^{-6})	16.6
6	Thermal conductivity, e.g. units at 100 ^{0}C	401 W/mK
7	Modulus of elasticity	117 GPa
8	Tensile Strength	210 MPa

d) Iron

Iron is denoted by symbol ‘Fe’ originated from the Latin word “Ferrum” and it is relatively soft metal, malleable, dull in color with moderate conductor of heat and electricity as well with BCC structure in nature. It is relatively low in cost and most commonly used metal. The Physical and mechanical properties of Fe are tabulated in Table 3.5.

Table 3.5 Physical and mechanical properties of Iron [161]

S. No.	Physical properties	Value
1	Melting Point	1535.1 °C
2	Boiling Point	2750 °C

3	Structure	BCC
4	Density at 20 ^{0}C (g/cm^3)	7.87
5	Thermal expansion coefficient (°C^{-1} x 10^{-6})	11.8
6	Specific heat capacity	0.44 J/gK
7	Heat of vaporization	349.60 kJ/ mol
8	Thermal conductivity, e.g., units at 100 °C	80.4 W/mK
9	Modulus of elasticity	210 GPa

e) Nickel

Nickel (Ni) is a silvery white metal capable of taking a high polish. In its commercially pure form (99.5 %) it has wide and important industrial applications. It can be forged, welded, machined, and rolled into sheets. Nickel is ductile, durable, and highly resistant to corrosion in many media. Nickel retains its strength and ductility at high temperatures. Fabricated nickel has mechanical properties resembling those of mild steel; it is, however, unlike steel, resistant to corrosion, and this fact, together with the fact that it is non-toxic, leads to its use in the manufacture of plant for food handling and pharmaceutical processing.

Table 3.6 Physical and mechanical properties of Nickel [162]

S. No.	**Physical properties**	**Purity, %**
1	Melting Point	1453
2	Boiling Point	2732
3	Structure	FCC
4	Density at 20 ^{0}C	8.908 g/cm^3
5	Thermal expansion coefficient (°C^{-1} x 10^{-6})	13.3
6	Thermal conductivity, e.g. units at 100 ^{0}C	0.198 W/mK
7	Modulus of elasticity	170 GPa

The most important use of nickel is in austenitic chromium-nickel steels which are renowned for their resistance to corrosion. Ni can easily drawn into wire and resist the corrosion at high temperature. It is widely used in gas turbine application and rocket engine. The physical and mechanical properties of Ni are shown in Table 3.6

3.1.2 Properties of alloying element in HEAs

a) Manganese

Manganese (Mn) is the most abundantly available twelfth element in the earth's crust. Of the heavy metals, only iron is more abundant. Manganese deficiency in higher plants causes mottled chlorosis (lack of chlorophyll) in which the leaves become pale or yellow while the veins remain green. In man, it has been suggested that "apresoline disease" may well be a manganese deficiency (G. C. Cotzias., 1962).

There are four types of impurities usually found in manganese ores (A. H. Sully., 1955):

a) Metallic impurities of iron (which is the most common), lead, zinc and silver, and in some ores nickel, tungsten and copper;
b) Gangue impurities which are slag forming such as silica, alumina, lime, magnesia or baryta;
c) Volatile impurities such as water, carbon dioxide andorganic matter;
d) Non-metallic impurities such as sulphur and phosphorus.

b) Cobalt

Cobalt (Co) was found by Georg Brandt, a Swedish chemist, in 1739. Cobalt is used for electroplating of different objects to make a surface which can resist the oxidation. There exists various Co based alloys used for various applications such as jet engines, gas turbines and different stainless steels. High-speed cutting tools are fabricated using Satellite alloys, which are the combination of cobalt, chromium and tungsten.

c) Titanium

Titanium (Ti), a versatile metal which is lighter and heavier than steel and aluminium respectively, and it is as strong as steel and aluminium. Titanium finds its applications in underwater parts of the boats and ships, propeller shafts and etc owing to its superior resistance against corrosion and also finds its place in high temperature applications such as rockets, missiles and aero structure.

Table 3.7 Physical and mechanical properties of the alloying elements [162-164]

S.No.	Physical properties	Mn	Co	Ti
1	Melting Point (°C)	1244	1493	1660
2	Boiling Point (°C)	2095	2927	3286
3	Crystal Structure	Cubic	HCP	HCP
4	Density at 20 ^{0}C (g/cm^{3})	7.21	8.90	4.5
5	Coefficient of thermal expansion (° C^{-1} x 10^{-6})	21.7	13.0	8.6

6	Thermal conductivity e.g. units at 100 °C (W/mK)	7.81	0.165	21.9
7	Modulus of elasticity (GPa)	158	206	117

Recent studies have shown the use of titanium in biomedical application such as artificial hips, pins used in setting bones and other biological implants also uses titanium. High cost of the titanium makes its use to be limited. Table 3.7 and Table 3.8 present the physical properties and characteristics of Mn, Co and Ti.

Table 3.8 Characteristics of alloying elements [157]

Element	Atomic number	Atom radius (pm)	Pauling Electronegativity	Valence Electron concentration
Mn	25	135	1.55	7
Co	27	125.10	1.88	9
Ti	22	146	1.54	4

3.2 Alloy preparation

3.2.1 Alloy melting and casting

The $AlCr_{1.5}CuFeNi_2Mn_x$ HEAs samples were cast using high-temperature vacuum induction furnace (Make: Jet Technocrats, India), as shown in Figure. 3.1 under inert gas environment. The elements Al, Cr, Cu, Fe, Ni and Mn with high purity (above 99.9%) in granular form were used for the casting of the alloys.

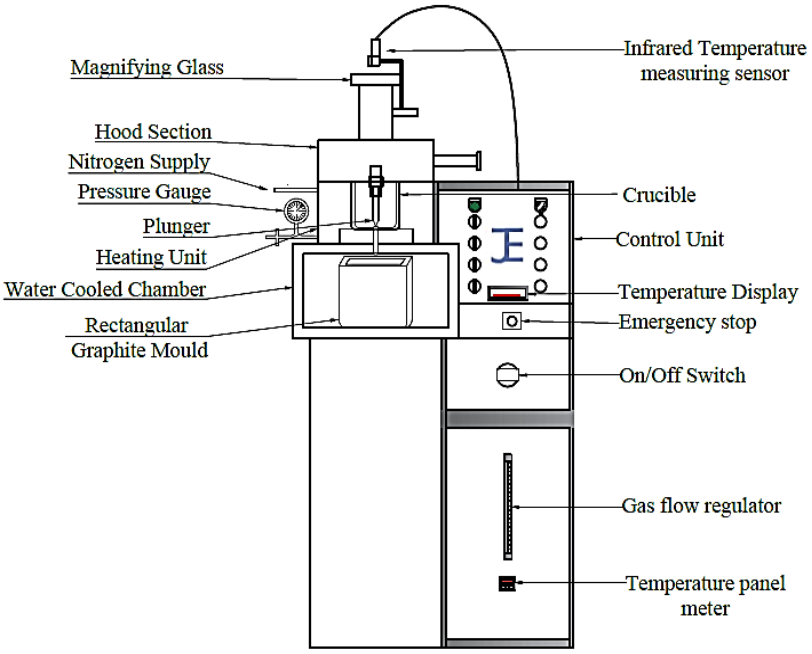

Figure 3.1. Schematic of High-temperature vacuum induction furnace

The $AlCr_{1.5}CuFeNi_2Mn_x$ alloys are abbreviated as Mn_0, $Mn_{0.25}$, $Mn_{0.5}$, $Mn_{0.75}$ and Mn_1 where x = 0, 0.25, 0.5, 0.75 and 1.0, respectively. The designations of the alloys are shown in Table 3.9. The elements of all the alloys weighing approximately 800 gm was melted at approximately 2000 ºC in the ceramic crucible surrounded by water-cooled chamber under argon atmosphere. Each alloy was melted five times with electromagnetic stirring to improve the chemical uniformity.

Table 3.9 Designation of various HEAs

S. No.	Designation	Composition
1	Mn_0	$AlCr_{1.5}CuFeNi_2Mn_0$
2	$Mn_{0.25}$	$AlCr_{1.5}CuFeNi_2Mn_{0.25}$
3	$Mn_{0.50}$	$AlCr_{1.5}CuFeNi_2Mn_{0.5}$
4	$Mn_{0.75}$	$AlCr_{1.5}CuFeNi_2Mn_{0.75}$
5	Mn_1	$AlCr_{1.5}CuFeNi_2Co_1$
6	$Co_{0.25}$	$AlCr_{1.5}CuFeNi_2Co_{0.25}$
7	$Co_{0.50}$	$AlCr_{1.5}CuFeNi_2Co_{0.5}$
8	$Co_{0.75}$	$AlCr_{1.5}CuFeNi_2Co_{0.75}$
9	Co_1	$AlCr_{1.5}CuFeNi_2Co_1$
10	$Ti._{25}$	$AlCr_{1.5}CuFeNi_2Ti_{0.25}$
11	$Ti_{0.50}$	$AlCr_{1.5}CuFeNi_2Ti_{0.5}$
12	$Ti_{0.75}$	$AlCr_{1.5}CuFeNi_2Ti_{0.75}$
13	Ti_1	$AlCr_{1.5}CuFeNi_2Ti_1$

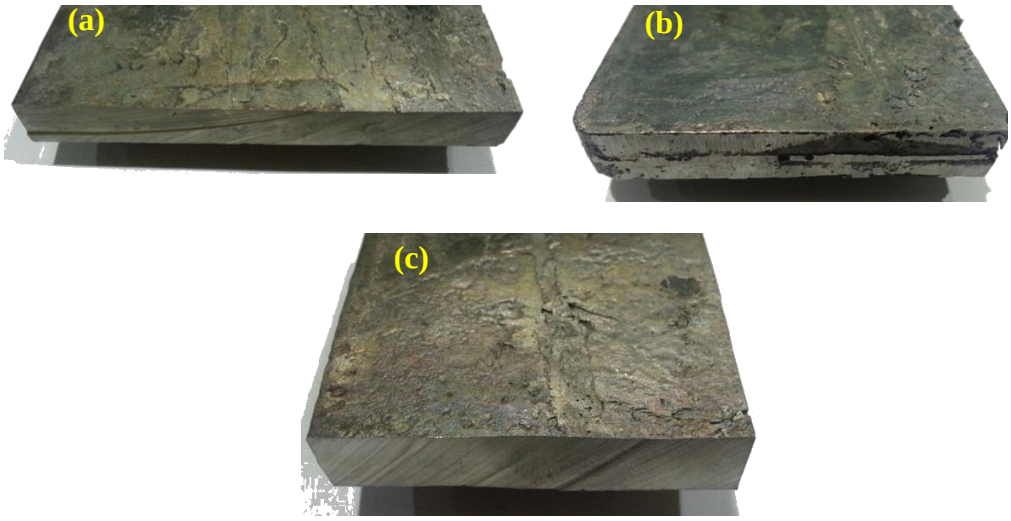

Figure 3.2. The cast samples of (a) $AlCr_{1.5}CuFeNi_2Mn_x$ (b) $AlCr_{1.5}CuFeNi_2Co_x$ (c) $AlCr_{1.5}CuFeNi_2Ti_x$

The dimension of produced samples was 140 mm× 90 mm×10 mm. The HEAs samples were heat-treated in the furnace at a temperature of 1150 °C for 48 hrs and then furnace cooled. The alloy exhibited an insignificant decrease in the weight due to the slight evaporation of aluminium. The chemical composition of each alloy as measured by EDAX analysis is close to its nominal composition.

3.3 Thermodynamics parameters of HEAs

The thermodynamic relationship between different elements plays a critical role in determining the microstructure and the mechanical properties of the alloys. Gibbs free energy is the foremost criteria for establishing the formation of the solid solution, which is given as

$$\Delta G_{mix} = \Delta H_{mix} - T\Delta_{Smix} \tag{3.1}$$

The Eq. 3.1 gives the relation between absolute temperature (T), Enthalpy of mixing (ΔH_{mix}) and Entropy of mixing (ΔS_{mix}). For n numbers of components, the enthalpy of mixing can be calculated from the Eq. 3.2 [66].

$$\Delta H_{mix} = \sum_{i=1, i\neq j}^{n} \Omega_{ij} c_i c_j \tag{3.2}$$

Where $\Omega_{ij} = 4\Delta H_{mix}^{AB}$, is the regular solution interaction for i^{th} and j^{th} component, C_i and C_j is the atomic % of i^{th} and j^{th} component and ΔH_{mix}^{AB} is the enthalpy of mixing of two elements A and B in an alloy.

According to the Boltzmann's theory for n number of components with gas constant R and concentration C_i, the configuration entropy for the formation of a solid solution is given by Eq. 3.3.

$$\Delta S_{mix} = -R\sum_{i=1}^{n} C_i \ln C_i \tag{3.3}$$

There are many models consisting of various thermodynamic parameters for the prediction of proper composition of HEAs. Initially, Hume-Rothery for was the only method for the development of the binary alloys. With the advancement in the material and formation of ternary, quaternary and quinary alloys, a new parameters Ω, including the two parameters ΔH_{mix} and $\Delta S_{mix}$for the prediction of the behavior of the alloys was established as given by Eq. 3.4. A new term T_m was included in the Eq. 3.4, which is the average melting temperature of all then elements present in the alloy and is given by the Eq. 3.5.

$$\Omega = \frac{T_m \Delta S_{mix}}{|\Delta H_{mix}|} \tag{3.4}$$

$$T_m = \sum_{i=1}^{n} (T_m)_i \quad (3.5)$$

There are other factors that depict the behavior of the various elements in a multi component alloy such as the atomic size difference (δ), Pauling electronegativity (X) and total valence electron in an alloy per quantity of atoms (VEC) as given by Eq. 3.6, 3.7 and 3.8.

$$\delta = \sqrt{\sum_{i=1}^{n} C_i \left(1 - r_i / \bar{r}\right)^2} \quad (3.6)$$

$$\Delta X = \sqrt{\sum_{i=1}^{n} C_i \left(X_i - \bar{X}\right)^2} \quad (3.7)$$

$$VEC = \sum C_i (VEC)_i \quad (3.8)$$

The other terms used in the equations are defined as:

$\bar{r}$= Average atomic radius of all elements in an alloy calculated as $\bar{r} = \sum_{i=1}^{n} c_i r_i$

$\bar{x}$= Arithmetical mean of electro-Negativity of all the elements in an alloy is calculated by Eq. 3.9

$$\bar{X} = \sum_{i=1}^{n} c_i x_i \quad (3.9)$$

The properties of all the elements used in the present study for the calculation of the thermodynamic parameters are listed in Table 3.1 and 3.2.

Various researchers has reported the thermodynamic theories for the development of solid solution in HEAs. Zhang et al. [165] proposed additional parameters to depict the characteristics of the various constituent in HEAs, i.e. the atomic size difference (δ), the ΔH_{mix} and ΔS_{mix} as defined by Eq.3.10-3.12.

$$\delta = \sqrt{\sum_{i=1}^{n} C_i \left(1 - r_i / \bar{r}\right)^2} \quad (3.10)$$

Where n implies the elements present in the multi-component alloy, C_i and r_i is the atomic % and atomic radius of i^{th}component and $\bar{r} = \sum_{i=1}^{n} c_i r_i$ indicate the average of the atomic radius of all elements existing in the alloy.

$$\Delta H_{mix} = \sum_{i=1, i \neq j}^{n} \Omega_{ij} c_i c_j \quad (3.11)$$

where, $\Omega_{ij} = 4\Delta H_{mix}^{AB}$, ΔH_{mix}^{AB} is the enthalpy of mixing of two liquid AB in an alloy. The chemical mixing enthalpy of the elements used in the present work is shown in Table 3.10.

$$\Delta S_{mix} = -R\sum_{i=1}^{n} C_i \ln C_i \qquad (3.12)$$

Where R = gas constant.

Table 3.10 The chemical mixing enthalpy (ΔH_{ij}^{mix}, kJ/mol) of binary atomic pairs calculated by Miedama's approach [166].

Element	Al	Cr	Cu	Fe	Ni	Mn
Al	_	_	_	_	_	_
Cr	-10	_	_	_	_	_
Cu	-1	12	_	_	_	_
Fe	-11	-1	13	_	_	_
Ni	-22	-7	4	-2	_	_
Mn	-19	2	4	0	-8	_
Co	-19	-4	6	-1	0	_
Ti	-30	-7	-9	-17	-35	_

3.4 Phases Evolution of alloys

The polished sample of size 10 mm × 10 mm × 1mm was used to determine the crystal structure of the alloys using an X-ray diffractometer of X'Pert PRO, PANalytical utilizing CuKα radiation operating at 45 kV/40 mA and a scanning step 0.03° from 2θ = 10° to 100°.The HEAs samples were heat-treated in the furnace at a temperature of 1150 °C for 48 hrs and then furnace cooled. The samples were sectioned, ground and polished with 1 µm diamond suspension and etched with Glyceregia before the examination. Microstructures of the developed alloys were examined using scanning electron microscope (SEM). The surface morphology of the alloys was studied using Nova Nano FE-SEM 450-FEI consisting of backscatter electron (BSE) as well as energy dispersive spectroscopy (EDS) detectors for phase recognition and composition investigation of alloys.

Figure 3.3. Pictorial view of X-ray diffractometer

3.5 Microstructural examination

The samples were sectioned, ground and polished with 1 μm diamond suspension and etched with Glyceregia before the examination. The samples were observed under optical microscope at lower magnification and the images were recorded. Microstructures of the developed alloys were examined using scanning electron microscope (SEM). The surface morphology of the alloys was studied using Nova Nano FE-SEM 450-FEI, USA consisting of backscatter electron (BSE) as well as energy dispersive spectroscopy (EDS) detectors for phase recognition and composition investigation of alloys.

Transmission electron microscope (TEM) is used to study the crystal structure of the alloy, having dendritic and interdendritic phases. The specimen were first prepared to required thickness using diamond cutting, ground and polished to achieve the thickness to 100 μm. The process of pre-thinning was done in MetaServ® 250 (Make: Buehler) High Speed Twin grinder-polishers followed by the Precision Ion Polishing System II (PIPS II, GATAN) to bombard the delicate specimen in order to make enough thin to study in TEM. The prepared specimen was then studied in Tecnai G^2 20 (FEI) S-Twin with accelerating voltage between 20 and 200 kv. The pictorial view of SEM and TEM is shown in Figure 3.4 and Figure 3.5.

Figure 3.4. Pictorial view of Scanning electron microscope

Figure 3.5. Pictorial view of Transmission electron microscope

3.6 Physical and Mechanical characterization

The physical and mechanical properties of any materials are intuited by executing tests in established laboratory consistently through different experiments that clone the results as near as possible to actual conditions. The physical and mechanical characterization of HEAs given below:

3.6.1 Density

The density of the alloys depends on the concentration of each element and was determined by the micromechanical approach of the rule of mixture, using the individual density of elements. The theoretical density, ρ_{cal}, of the alloys was calculated by Eq. 3.13.

$$\rho_{alloy} = \frac{\sum C_i A_i}{\sum C_i A_i / \rho_i} \qquad (3.13)$$

where A_i represents atomic weight, C_i represents concentration and ρ_i represents the density of element i. The actual density of the HEAs was determined experimentally using by Archimedes' Principle,i.e. comparing weight of the sample in air and water. The experimental density (ρ_{expt}) was determined using analytical balance ME204 of Mettler Toledo. The schematic view of the density measurement is shown in Fig. 3.6.

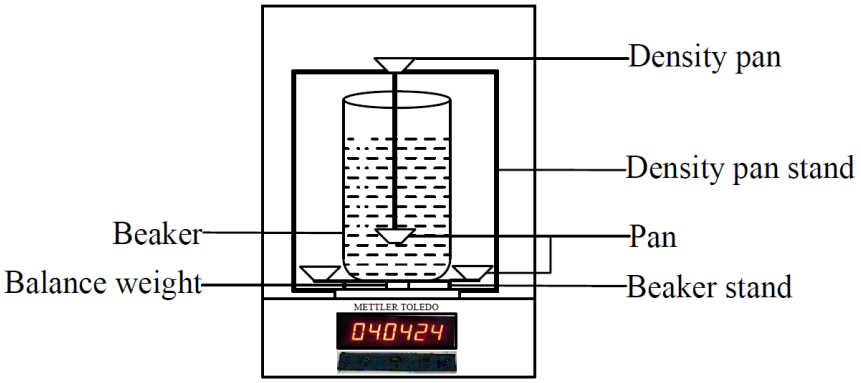

Figure 3.6. Schematic of density measurement setup

3.6.2 Hardness

A load of 200 g was applied to the polished samples for the dwell time of 15s in order to determine the Vicker's microhardness using UHL VMHT microhardness tester. Each sample was indented at ten points on both the sides to obtain the average data. The schematic view of hardness testing machine is shown in Fig. 3.7.

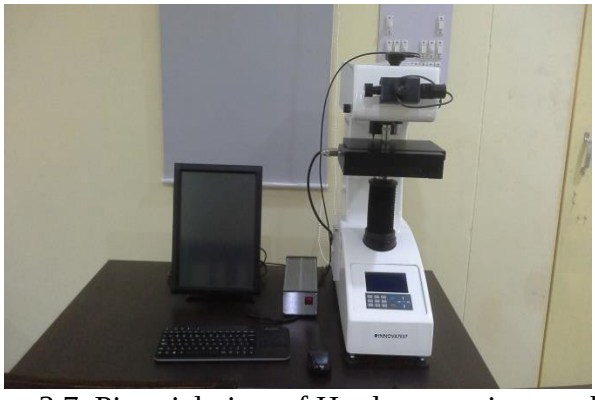

Figure 3.7. Pictorial view of Hardness testing machine

3.6.3 Mechanical Characterization

The mechanical properties were determined experimentally at ambient temperature using Instron 8862 testing machine as shown in Figure 3.9. The various mechanical tests such as

tensile, flexural and compressive were performed on the same machine at room temperature. The samples for all the test were prepared using electric discharge machining as per the different ASTM standards. The specimens were polished carefully from all the sides with different grades of SiC paper before each test. The average value of three reading was considered for each test. The tensile test specimens were prepared as per ASTM E8 and the experiment was performed at rate of 0.05 mm/min. The sample for the tensile test is shown in Figure 3.8.

Figure 3.8. Sample for tensile test

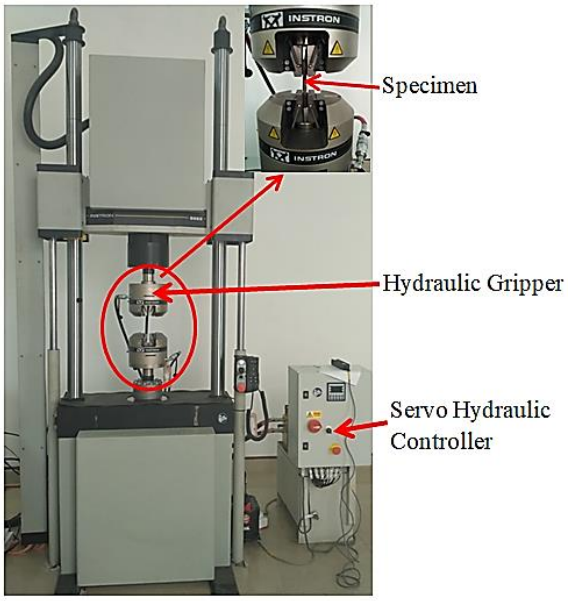

Figure 3.9. Universal Testing Machine

The samples for the compression test were prepared using ASTM E9-09. The compressive strength was measured at an initial strain rate of 10^{-3} s^{-1}. The test was performed at room temperature on cylindrical samples of size ϕ 4 mm×4 mm in size.

The specimen for the flexural test was of 150 mm × 30 mm × 10 mm dimension as per the ASTM E855-08. The test was carried at a span length of 100 mm at 2 mm/s cross-sectional speed. The flexural modulus of the samples is calculated by Eq. 3.14.

$$\text{Flexural modulus} = \frac{L^3F}{4wh^3d} \qquad (3.14)$$

where, L is the span length, F is the applied load, w is the width, h is the height and d is the deflection of the specimen

3.7 Corrosion behaviour of HEAs

The electrochemical corrosion test was performed at room temperature on sample of size 10 mm ×10 mm by potentiodynamic-polarization measurement using 3.5 wt.% NaCl solution. The specimens were finished using various grit of SiC paper and then polished with 1 µm diamond suspension. The technique (GAMRY Reference 600TM) utilized for corrosion test with measurements recorded at a scan rate of 0.5 mVs^{-1}in the range of -1.5 V to 0.5 V. The experiment is performed with three electrodes i.e. Specimen, saturated Calomel and platinum electrode. The electrochemical impedance spectra was attained at the open circuit potential in the frequency range of 10^5-10^{-2} Hz with amplitude of 5 mV. All the samples were dipped in NaCl solution (pH ≈ 6) for one and half hour before the test, allowing the system to reach equilibrium with the electrolyte exposing the sample of size 1 cm^2 to the electrolyte. The Eq. 3.15 was used to detrmine the corrosion rate of the samples.

$$K_{corr} = \frac{i_{corr}\ K.\ EW}{\rho} \qquad (3.15)$$

Where: i_{corr} = Corrosion current density (A/cm^2), ρ = mass density ($g\ cm^{-3}$), EW= Equivalent weight of the electrode (g), k = 3272 mm/(A-cm-year), K_{corr}= Corrosion rate in millimetres per year (mmpy). The schematic view of the Corrosion Testing Machine is shown in Fig. 3.10.

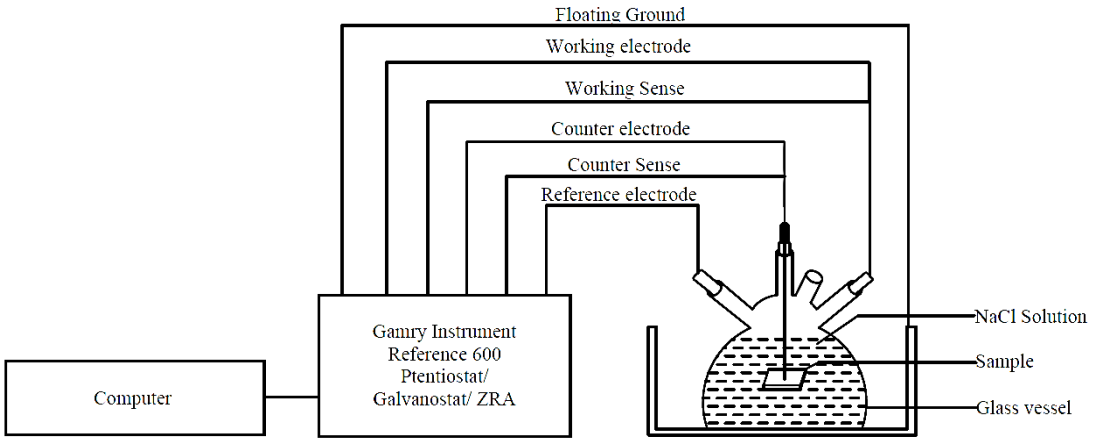

Figure 3.10. Schematic of Corrosion Testing Machine

3.8 Thermal conductivity

Thermal conductivity of the HEAs sample were conducted on a principle of Transient Plane Source (TPS) using Hot Disk Thermal Constant Analyzer (Model: TPS 500, Make: Gothenburg, SWEDEN). A rapid measurement of thermal conductivity within a span of 2.5s is offered by the instrument. The samples of size of 25 × 25 ×2 mm were used for the measurement. A spiral-shaped hot disk, being coated with Kapton serves as heat source having a radius r, and temperature response sensor was placed between two samples and data acquisition using HOT disk software. The thermal conductivity is measured as a function of time by flow of electrical power through the HEAs. The schematic of Thermal conductivity analyzer is shown in Figure 3.11.

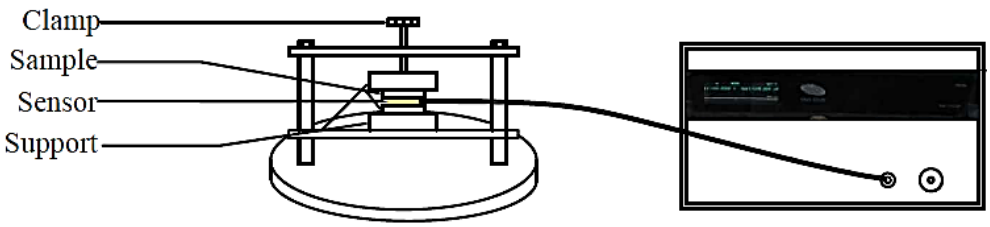

Figure 3.11. Schematic of Thermal conductivity analyzer

3.9 Pin on disc

The dry sliding wear test was performed on the samples as per ASTM G-99 on pin-on-disk tribometer (Model: TR 20, Make: Ducom, Bangalore, India) as shown in Figure 3.12. The samples were transformed in the form of pin and disc was made to rotate against the sample. The tribometer has one counter body, a disc that made of EN-31 hardened steel (with hardness 60-70 HRC). The machine is equipped with the lever mechanism for the application of the load.

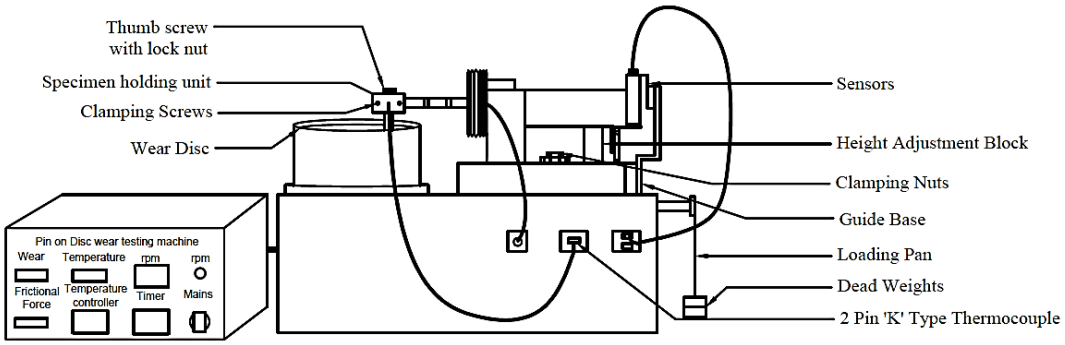

Fig. 3.12 Schematic of pin-on-disc Tribometer

A wear track of diameter 50 mm was fixed for all the tests and based on this, the sliding velocity is calculated to be 0.5, 1, 1.5, 2 and 2.5 m/sec in the experimental work. The loss of material from the samples is sensed from the deviation in the length using the LVDT. The specific wear rate is determined from the loss in mass of the samples. The coefficient of friction and frictional force applied are monitored continuously and recorded the readings separately using user friendly WINDCOM 2007 software for individual test run. After every experiment, the weight loss of the alloy is assessed by ±0.001 g accurate precision balance and the specific wear rate (mm^3/N-m) is calculated by Eq. 3.16.

$$W_s = \frac{\Delta m}{\rho V s t F_n} \tag{3.16}$$

Where, Δm= mass loss of the sample after the test (gm.), ρ = density of the alloy (g/cm^3), Vs = sliding velocity (m/s), t = test duration (s), and F_n = normal load (N).

3.10 Experiment Design

Taguchi is a statistical analysis tool based on orthogonal array, results in a reduced number of experiments with best possible selection of control factors. Genichi Taguchi was first introduced Taguchi method in 1940. The method was developed for designing the experiments to study the effect of different parameters on performance characteristics. This method helps in optimizing the performance characteristics used in the engineering fields frequently. The Taguchi's experimental design provides the optimal set of experiments thus reducing the time required for performing the experimental work. Therefore, this process combines experimental and analytical concepts to calculate the most effective control factor on the resulting response for a significant enhancement in the overall performance. In Taguchi's optimization technique, the important stage involves is the selection of control factors and usually, it is selected by the experimenter's experience. The selected five control factors, i.e. Normal Load (N), Molar ratio, temperature (°C), sliding speed (m/s) and sliding distance (m) along with their levels are presented in Table 3.10.

The present study involves L_{25} orthogonal array experiment design as shown in Table 3.11 is implemented to study the influence of control parameter on specific wear rate. Signal-to-Noise ratio (S/N) is the measure of performance in the Taguchi technique, which depicts the logarithmic function of desired optimized output. S/N is in the ratio of the mean and standard deviation and expressed in decibels (dB). S/N ratio is categorized in three general characteristics, they are; Lower value is desirable, larger value is desirable and nominal value

is desirable[167]. For specific wear rate, consider lower value is desirable characteristic and is determined in the form of logarithmic scale of the loss function as depicted by Eq. 3.12.

$$\frac{S}{N} = -10 \log \frac{1}{n}\left(\sum_{i=1}^{n} y_i^2\right) \quad (3.17)$$

Here, n denotes the number of observations, and y_i = observed data. The results were processed using the MINITAB software specialized in the experimental design applications. Analysis of variance (ANOVA) is then applied to evaluate the significance of factor setting in order to obtain the output characteristic of the HEAs.

Table 3.11 The factor and its various levels

Factor	**Level**				
	1	2	3	4	5
A:Normal Load (N)	10	20	30	40	50
B: Mn (molar ratio)	0	0.25	0.5	0.75	1
C: Temperature (ºC)	30	50	70	90	110
D:Sliding speed (m/s)	0.5	1	1.5	2	2.5
E: Sliding distance (m)	500	1000	1500	2000	2500

Table 3.12 Design of experiment for L_{25} orthogonal array

Experiment No.	**Load (N)**	**Molar ratio (mole)**	**Temperature (°C)**	**Sliding speed (m/s)**	**Sliding distance (m)**
1.	1	1	1	1	1
2.	1	2	2	2	2
3.	1	3	3	3	3
4.	1	4	4	4	4
5.	1	5	5	5	5
6.	2	1	2	3	4
7.	2	2	3	4	5
8.	2	3	4	5	1
9.	2	4	5	1	2
10.	2	5	1	2	3
11.	3	1	3	5	2
12.	3	2	4	1	3

Experiment No.	Load (N)	Molar ratio (mole)	Temperature (°C)	Sliding speed (m/s)	Sliding distance (m)
13.	3	3	5	2	4
14.	3	4	1	3	5
15.	3	5	2	4	1
16.	4	1	4	2	5
17.	4	2	5	3	1
18.	4	3	1	4	2
19.	4	4	2	5	3
20.	4	5	3	1	4
21.	5	1	5	4	3
22.	5	2	1	5	4
23.	5	3	2	1	5
24.	5	4	3	2	1
25.	5	5	4	3	2

3.11. Multi criterion decision-making (MCDM)

The MCDM technique is applied to the intricate problems to judge the various alternatives based on certain criteria. The different steps involved the technique is described below:

1. Selection of Performance Decision Attributes(PDA)

The decision making is multi attributed task. While selecting best composite material many number of mechanical, physical and wear properties are involved. It is a crucial phase in TOPSIS to decide PDA from these many numbers of properties at specific conditions. The identified PDA for present investigation are shown in Table 3.13.

2. Decision matrix

Decision matrix is formed after finalize the alternatives and attributes. Consider m alternatives to be evaluating n performance decision attributes (PDA). The decision matrix is expressed in m× n order as,

$$D = \begin{pmatrix} x_{11} & x_{12} & \dots & x_{1N} \\ x_{21} & x_{22} & \dots & x_{2N} \\ \vdots & \vdots & \vdots & \vdots \\ x_{M1} & x_{M2} & \dots & x_{MN} \end{pmatrix} \quad (3.18)$$

Where, x_{ij} are the value of j^{th} PDA for i^{th} alternative.

3. Weights for each PDA using entropy method

There are numerous MCDM methods available to prioritize the attributes such a way by assigning the rank based on their weightage like; (1) ELECTRE, (2) Composite Programming, (3) Promethee, (4) Eigenvector method, (5) The weighted least square method, (6)The weighted evaluation technique, (7) AHP method, (8) The Entropy method and may more. In the present investigation, the entropy method is implemented to derive the weights of the PDA. The weight for individual criterion is determined without direct involvement of decision maker. Entropy generally used as a criterion for measurement of represented disorder. It is based on the principle that a wide data distribution shows more disorder than a packed distribution. The weights for individual PDC is calculated by below mentioned procedure.

a. The projection value (P_{ij}) is obtained by normalizing the decision matrix ($D_{M\times N}$).

$$P_{ij} = \frac{x_{ij}}{\sum_{i=1}^{M} x_{ij}} \tag{3.19}$$

b. The entropy of j^{th} criterion is calculated using eq. 3.16

$$E_j = -\gamma \sum_{j=1}^{N} P_{ij} \ln(P_{ij}) \tag{3.20}$$

where, γ is constant and is calculated as $\gamma = \frac{1}{\ln(M)}$

c. The dispersion (ε) indicates the degree of diversity of each criterion considered in present study. For higher value of ε, the criterion in the problem is important. The ε is determined as:

$$\varepsilon = 1 - E_j \tag{3.21}$$

4. Finally, weights of all the PDC is calculated as;

$$W_j = \frac{DP_j}{\sum_{j=1}^{N} DP_j} \tag{3.22}$$

5. The TOPSIS method

The ranking of all composition under present investigation is determined using TOPSIS by following steps;

a. The decision matrix ($D_{M\times N}$) is normalised as $R = [r_{ij}]$

$$r_{ij} = \frac{a_{ij}}{\left[\sum_{i=1}^{M}(x_{ij})^2\right]^{1/2}} \quad (3.23)$$

b. Weighted normalized matrix (V_{ij}) is calculated by multiplying each column of matrix by its associated weight (W_j) as:

$$V_{ij} = W_j \times r_{ij} \quad (3.24)$$

c. The positive ideal solution (PIS) (i^+) and the negative ideal solution (NIS) (i^-) are determined using equation 3.25:

$$i^+ = (V_1^+, V_2^+ \ldots . V_N^+)$$
$$\text{and} \quad (3.25)$$
$$i^- = (V_1^-, V_1^- \ldots . V_N^-)$$

where,

$$V_i^+ = \begin{Bmatrix} (\max_i V_{ij}), & \text{if j is benifit criterion} \\ (\min_i V_{ij}), & \text{if j is cost criterion} \end{Bmatrix} \text{ and}$$

$$V_i^+ = \begin{Bmatrix} (\min_i V_{ij}), & \text{if j is benifit criterion} \\ (\max_i V_i^+), & \text{if j is cost criterion} \end{Bmatrix} \text{ for } j = 1, 2 \ldots . N$$

d. The Euclidian distances between each of the alternatives and the PIS and NIS is calculate using equation 3.26:

$$\Delta_i^+ = \sqrt{\sum_{j=1}^{N}\left(V_i^+ - V_{ij}\right)^2} \quad (3.26)$$

and

$$\Delta_i^- = \sqrt{\sum_{j=1}^{N}\left(V_{ij} - V_i^-\right)^2}$$

For i = 1,2,…..,m

e. At the last, the closeness index (λ)of the attributes is evaluated and organized from highest to lowest value according to λ and the attribute with the highest value of λ is most preferable :

$$\lambda = \frac{\Delta_i^-}{\Delta_i^+ + \Delta_i^-}, \text{for } i = 1, 2 \ldots . m \quad 3.23$$

Table 3.13 Description of the different performance defining attributes

Performance defining Attribute(PDA)	**Description of PDA**	**Performance inference of PDA**
P-1	The density of the alloy is calculated using the equation: $\rho_{cal} = \frac{\sum C_i A_i}{\sum C_i A_i / \rho_i}$, where, where A_i represents atomic weight, $C_i$represents concentration and ρ_i represents the density of element i.	Lower value is desirable
P-2	Hardness is resistance to indentation under the applied load on Vicker's scale.	Higher the better
P-3	Compressive strength is a measure of resistance to withstand compressive load measured on universal testing machine (UTM)	Higher value is desirable
P-4	Flexural strength is the resistance offered by the material to bending.	Higher value is desirable
P-5	Young's modulus is the measure of stiffness of the alloys.	Higher value is desirable
P-6	Thermal conductivity is the property of material to conduct heat	Higher value is desirable
P-7	Corrosion rate determines the speed of deterioration of any materials in a given environment	Lower value is desirable
P-8	Specific wear rate: load = 10 N, Sliding Velocity = 0.5 m/s and Temperature= 30 ºC	Lower value is desirable
P-9	Specific wear rate: Load = 20 N, Sliding Velocity = 0.5 m/s and Temperature = 30 ºC	Lower value is desirable
P-10	Specific wear rate: Load = 30 N, Sliding Velocity = 0.5 m/s and Temperature = 30 ºC	Lower value is desirable
P-11	Specific wear rate: Load = 40 N, Sliding Velocity = 0.5 m/s and Temperature = 30 ºC	Lower value is desirable
P-12	Specific wear rate, Load = 50 N, Sliding Velocity = 0.5 m/s and Temperature = 30 ºC	Lower value is desirable

Chapter summary

This chapter includes:

- The descriptions of materials used in this study.
- The details of composition and alloy preparation.
- The physical, mechanical and thermal characterization of HEAs.
- The description of dry sliding wear and Taguchi experimental design approach.
- Evaluation of optimal combination of physical, mechanical and specific wear rate by TOPSIS method.

The next chapter presents thermodynamic and microstructural analysis of high -entropy alloys.

*****

Chapter 4

THERMODYNAMIC AND MICROSTRUCTURAL ANALYSIS OF HIGH-ENTROPY ALLOYS

The fundamental thermodynamics properties of the individual elements play a vital role in predicting the phases existing in the high-entropy alloys (HEAs). The exclusive properties of HEAs are due to the formation of solid solution and hence the parameter that dictates its formation is important to understand. There are various thermodynamic criteria that help in defining an alloy as HEAs and explaining its nature. The parameters includes atomic size difference (δ), Valence electron concentration (VEC), Pauling electronegativity (ΔX), Enthalpy of mixing (ΔH), configuration entropy (ΔS) and melt interaction parameter between ΔH and ΔS (Ω).The thermodynamic results obtained from the theories given by different researchers are discussed in details. The extensive study of the microstructures obtained from Optical Microscope, X-ray diffraction pattern (XRD), Scanning Electron Microscope (SEM) and Transmission Electron Microscopy (TEM) is explained in detail. This chapter thus describes the thermodynamic and Microstructural behaviour $AlCr_{1.5}CuFeNi_2Mn_x$, $AlCr_{1.5}CuFeNi_2Co_x$and$AlCr_{1.5}CuFeNi_2Ti_x$alloys.

4.1 Thermodynamic and microstructural analysis of $AlCr_{1.5}CuFeNi_2Mn_x$ (x = 0, 0.25, 0.5, 0.75 and 1.0) high entropy alloys

The thermodynamic parameters play an important role in designing an alloy and predicting the phases present in the alloy. Thermodynamics relates the chemical nature of the alloys with the formation of its microstructures. This section describes the thermodynamic parameters and the microstructural analysis of $AlCr_{1.5}CuFeNi_2Mn_x$ of HEAs.

4.1.1 Thermodynamic behaviour of $AlCr_{1.5}CuFeNi_2Mn_x$ alloys

The properties of all the elements for calculating the thermodynamic parameters of $AlCr_{1.5}CuFeNi_2Mn_x$ alloys are presented in Table 3.1 and Table 3.8 respectively. The calculated value of various thermodynamic parameters δ, VEC, ΔX, ΔH, ΔS, and Ω for $AlCr_{1.5}CuFeNi_2Mn_x$ alloys are given in Table 4.1. The optimum value of configurational entropy is not only the criterion that leads to the solid solution formation. Beside entropy, the difference in the atomic sizes of the elements and their enthalpy during the reaction plays a very imperative role. The ΔS value for Mn_0, $Mn_{0.25}$, $Mn_{0.5}$, $Mn_{0.75}$ and Mn_1 are found to be 13.01, 13.85, 14.22, 14.43 and 14.54 $Jk^{-1}mol^{-1}$, respectively. There is a continuous increase in the ΔS value with addition of Mn content in the multi-component alloys. The increase in the

ΔS value increases the possibility of solid solution formation. The expected range of ΔH_{mix} for the formation of solid solution is -20 kJ/mole to 5 kJ/mole [165]. The ΔH_{mix} for the cast alloy varies from -5.54 to -6.15 $kJmol^{-1}$ for x=0 to x=1. There is a continuous decline in the ΔH_{mix} value as the amount of Mn increases. As the value of ΔH_{mix} tends to positive, more are the chances of formation of simple crystal structure in the alloy.

Table 4.1 δ, VEC, ΔX, ΔH, ΔS and Ω for $AlCr_{1.5}CuFeNi_2Mn_x$ alloys

Alloy	**δ (%)**	**VEC**	**ΔX**	**ΔH ($kJmol^{-1}$)**	**ΔS ($Jk^{-1}mol^{-1}$)**	**Ω**	**T_m(k)**
Mn_0	5.37	7.85	0.12	-5.54	13.01	3.91	1665.60
$Mn_{0.25}$	5.35	7.81	0.13	-5.75	13.85	3.99	1656.35
$Mn_{0.5}$	5.33	7.79	0.14	-5.92	14.22	3.97	1654.18
$Mn_{0.75}$	5.30	7.76	0.14	-6.05	14.43	3.94	1652.17
Mn_1	5.26	7.73	0.14	-6.15	14.54	3.90	1650.29

The value of δ continuously decreases with the addition of Mn content because it acts as a catalyst and enhances the proper mixing of the elements. The calculated value of δ is found to vary from 5.37 % for x =0 to 5.26% for x=1. There is a slight decrement in δ value for Mn_0 to Mn_1but are within the proposed limit i.e. $\delta \leq 6.6\%$. Since the value of δ is not too large, this indicates that the difference in the atomic size of the elements is small and results in the formation of the solid solution. The small atomic size difference of the alloys prevents the lattice distortion thus minimizing the strain energy essential for stability of structure. On the other hand, the value of Ω increase for x =0.25 and further decreases with increase in Mn content. This indicates that the value of Ω increases with the increase in the number of the elements in the alloy. The developed alloys fulfill the criterion for the stable solution as $\Omega \geq 1.1$ for HEAs as stated by Zhang et al. [168].

The calculated value of ΔX for the alloys varies from 7.85 to 7.73. The electro negativity difference (ΔX) is only concerned with the composition of the alloys. However, the value can be used to indicate the formation of TCP phase. The VEC value of the cast alloys varies from 7.85 for Mn_0 to 7.73 for Mn_1. The VEC value helps in the forecasting of the stability of the FCC and the BCC phases. The stability of the FCC phase is considered at VEC ≥8 whereas the BCC phase is stable at VEC≤6.87.The melting temperature (T_m) of the alloy decrease slightly by 15.31 K on addition of Mn.

Figure 4.1 shows the variation of ΔH_{mix} and ΔS_{mix} for different compositions varying from x=0 to x=1 as a function of atomic size difference (δ). Each symbol of the figure 4.1 indicates the molar ratio as presented in Table 4.1. The ΔH_{mix} is directly related to the δ whereas the ΔS_{mix} varies inversely with δ. As the entropy of mixing increase, the probability of formation of random or ordered solid solution becomes higher. This implies that higher ΔS_{mix} and lower δ leads to the development of simple crystal structure. Although in this case, δ keeps on increasing and hence lowering the entropy of the alloys. The ΔH_{mix} value continuously increases with the increase in the δ. These values are in the limiting range as the addition of higher amount of Mn may lead to the high lattice distortion and hence may result in the formation of many intermetallic compounds.

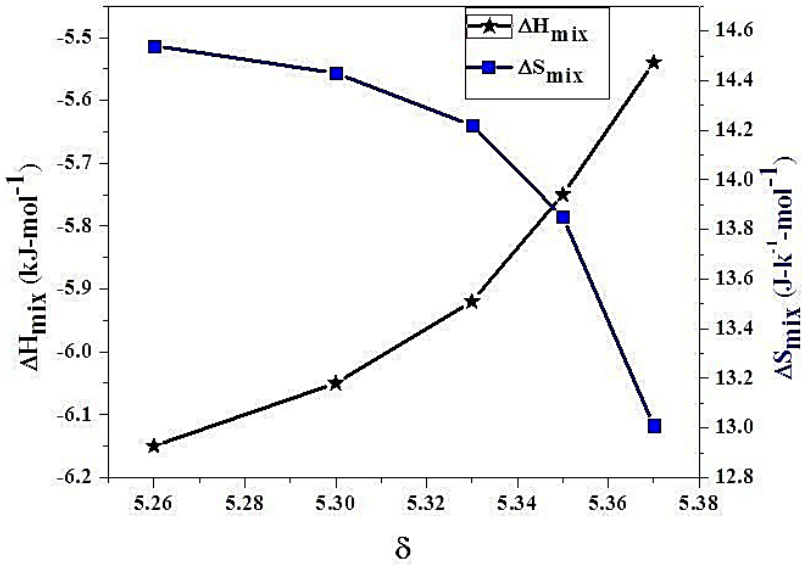

Figure 4.1. ΔH_{mix} and ΔS_{mix} of $AlCr_{1.5}CuFeNi_2Mn_x$ as a function of δ

4.1.2 Phase evolution and microstructure of $AlCr_{1.5}CuFeNi_2Mn_x$ alloys

The EDAX or EDS analysis of the $AlCr_{1.5}CuFeNi_2Mn$ alloy clearly indicates the distribution and the presence of each element in the alloy as shown in Figure 4.2. The phase formation in the alloy is one of the important parameters to determine the properties of the alloys. Figure 4.3 shows the XRD pattern of as cast $AlCr_{1.5}CuFeNi_2Mn_x$ alloys. It is observed that the alloys are mainly composed of body-centered cubic (BCC) and face-centered cubic (FCC) structures. The $AlCr_{1.5}CuFeNi_2$ base alloy show more FCC structure as compared to $AlCr_{1.5}CuFeNi_2Mn_x$ which corresponds to the Cu matrix (FCC) solid solution consisting of other elements Al, Cr, Fe and Ni. At x =0, the sharp peaks of FCC structure can be seen depicting the higher amount of Al, Cu and Ni while very small peaks of BCC structure are seen due to the presence of elements namely Fe and Cr. Peak shift from FCC to BCC structure is found from x=0 to x=1 in addition to the diminishing of FCC peaks. The

$AlCr_{1.5}CuFeNi_2Mn$ shows prominent BCC phase due to the presence of Fe and Mn replacing the Cu to the certain extent.

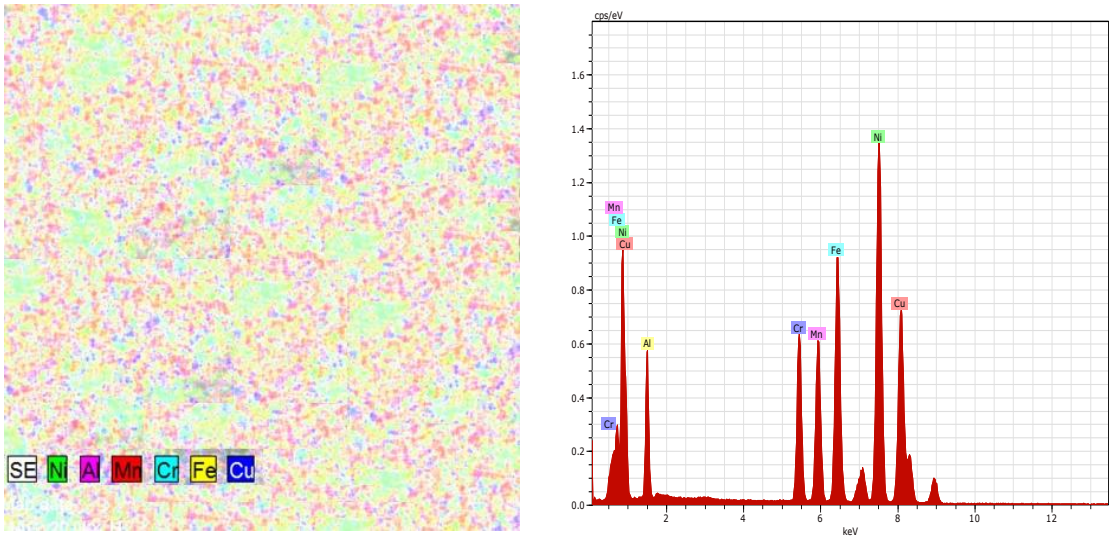

Figure4.2. EDAX analysis of $AlCr_{1.5}CuFeNi_2Mn$ alloy and relative intensity of each element confirming uniform distribution in the alloy

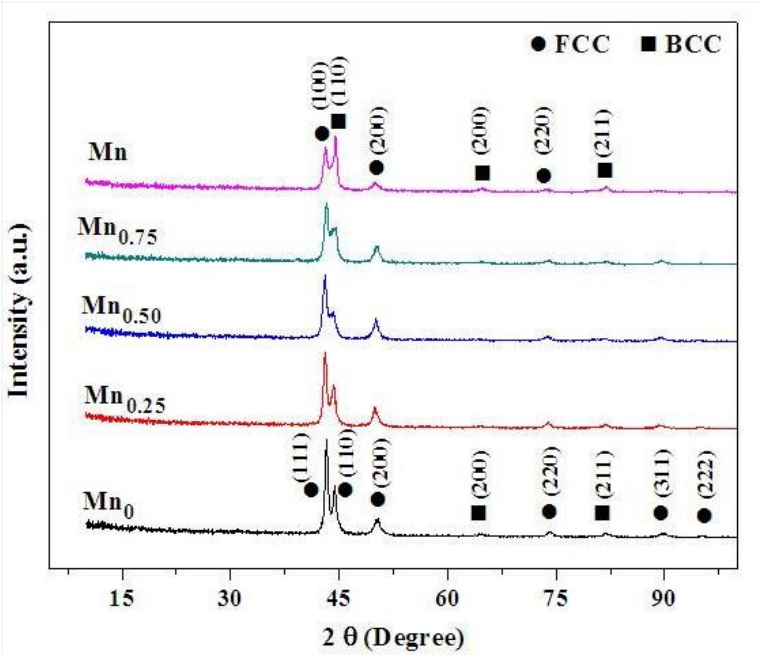

Figure 4.3. XRD pattern for$AlCr_{1.5}CuFeNi_2Mn_x$ alloys

The solid solution formation of alloys is explained with reference to the difference in the atomic size of the elements and the enthalpy of mixing. Lattice parameters of alloys for x=0, 0.25, 0.5, 0.75 and 1 as calculated from the Braggs formula [169] are 3.611, 3.625, 3.626, 3.639 and 3.646 Å, respectively. However, the lattice expansion of the alloys is not large on addition of the Mn. This is due the atomic radius of various elements which are in

the order of Al>Mn>Cu>Cr,Ni>Fe as shown in Table 4.1. The large atomic radius of Mn results in the increase inlattice structure of the alloy.

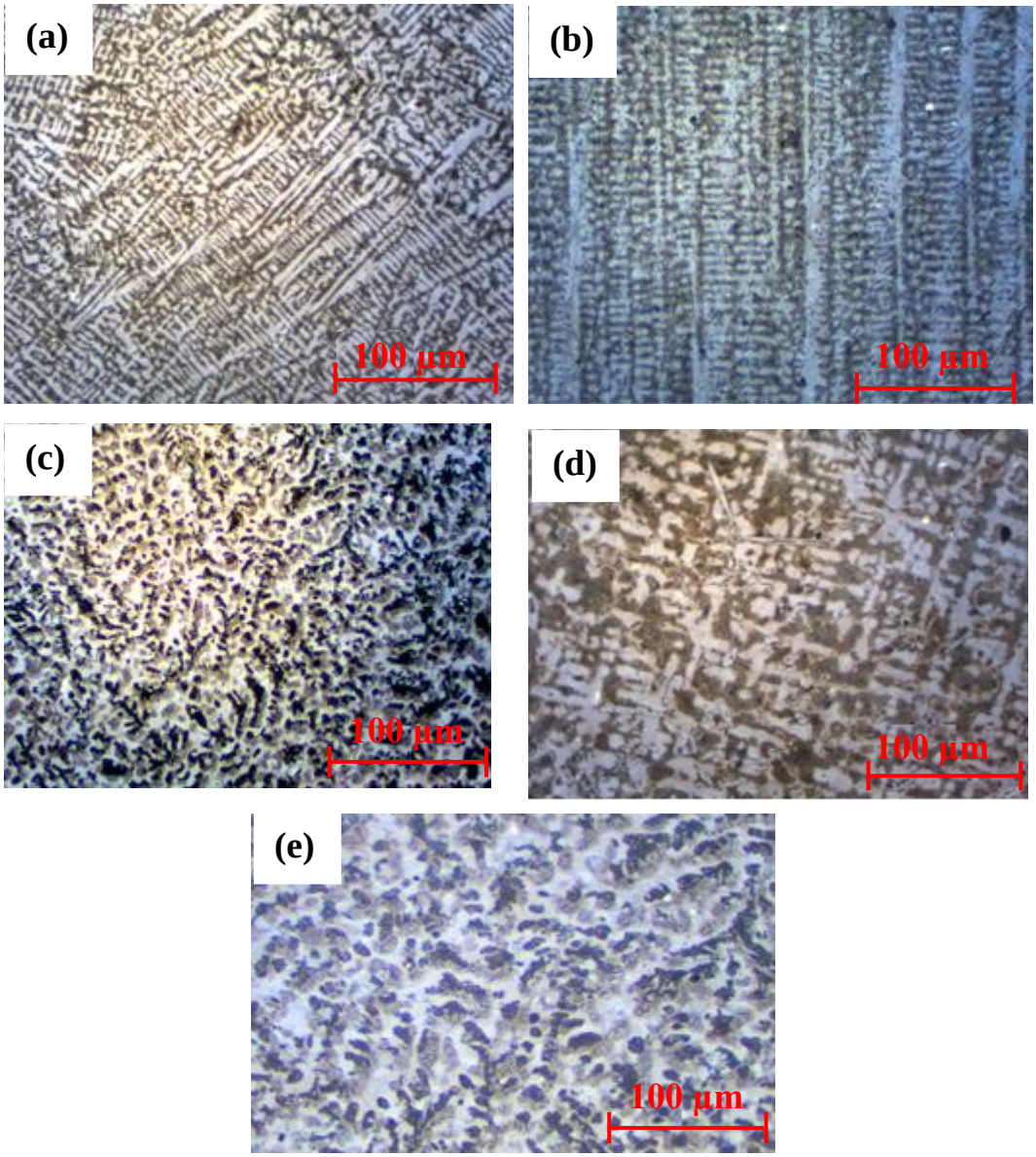

Figure 4.4. Optical micrograph of $AlCr_{1.5}CuFeNi_2Mn_x$ alloys (a) $AlCr_{1.5}CuFeNi_2Mn_0$ (b) $AlCr_{1.5}CuFeNi_2Mn_{0.25}$ (c) $AlCr_{1.5}CuFeNi_2Mn_{0.5}$ (d) $AlCr_{1.5}CuFeNi_2Mn_{0.75}$ (e) $AlCr_{1.5}CuFeNi_2Mn$

The optical micrograph of Mn_0, $Mn_{0.25}$, $Mn_{0.5}$, $Mn_{0.75}$ and Mn_1 samples are shown in Figure 4.4. The etched sample shows the distinguished regions due to the presence of elements. There are three distinct phases present in the alloys as observed from Figure 4.4 (a). A dark phase, a light phase and an intermediate phase are observed in the images. The dark region is due to the accumulation of Cu as compared to the other elements. The light region is due to the presence of FCC phase of Al and Ni.

The SEM images of $AlCr_{1.5}CuFeNi_2Mn_x$alloys are shown in Figure 4.5. The microstructures of all composition depict similar features representing mainly two regions i.e.

one dark and another ligh. The examination of SEM images of the alloys in the homogenised condition indicates dark dendrite core (DC) regions as compared to bright interdendritic (ID) regions. The dark region (DC) represents the presence of BCC phase as compared to the bright region (ID) which is due to the formation of FCC phase. Due to the presence of Cr and Fe, the alloys displays BCC phase whereas the Cu and Ni solid solution along with the other elements present in the matrix results in the FCC phase.

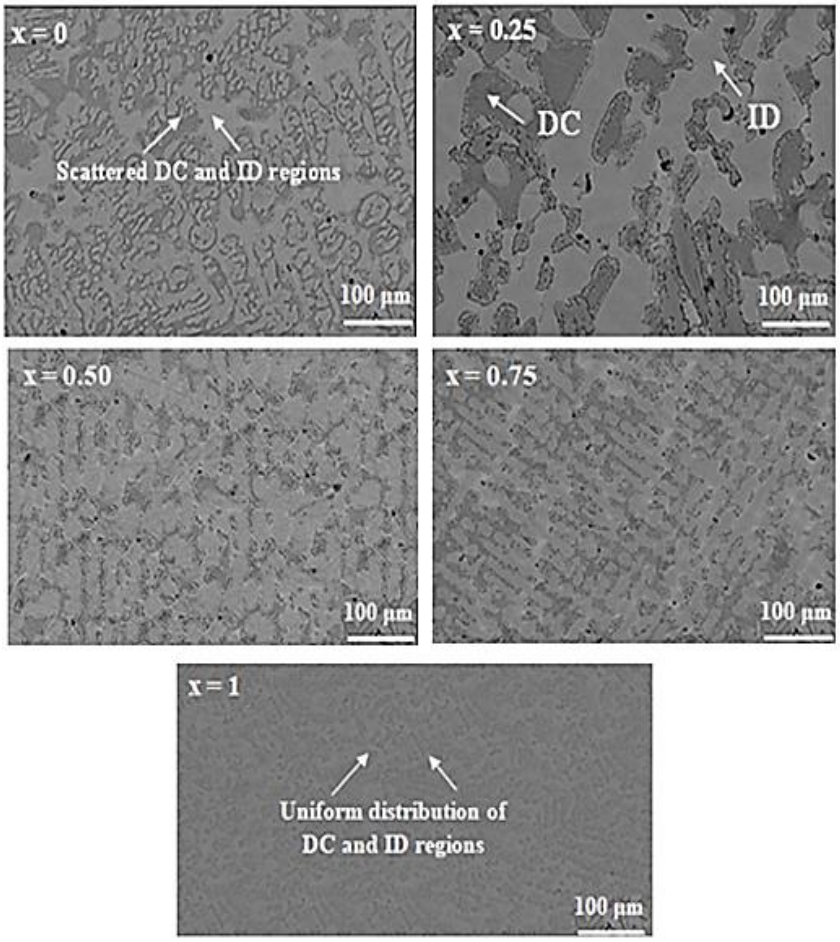

Figure 4.5. SEM images of $AlCr_{1.5}CuFeNi_2Mn_x$ alloys

As the amount of Mn increases, the BCC phase becomes more prominent as compared to the FCC phase. The microstructures at the higher content of Mn also show the presence of dense dendritic region as compared to the interdendritic region. It is also observed that the dark region is more uniform and predominant at x=1. The TEM micrograph of the AlCr1.5CuFeNi2Mn alloy and the SAED pattern for region 1 is shown in Figure 4.6 (a). The bright field image of the alloy shows three distinct phases. The different regions are marked as 1, 2 and 3. The SAED pattern for the region 1 is shown in Figure 4.6 (b). The SAED pattern depicts the weak reflection of the FCC structure.

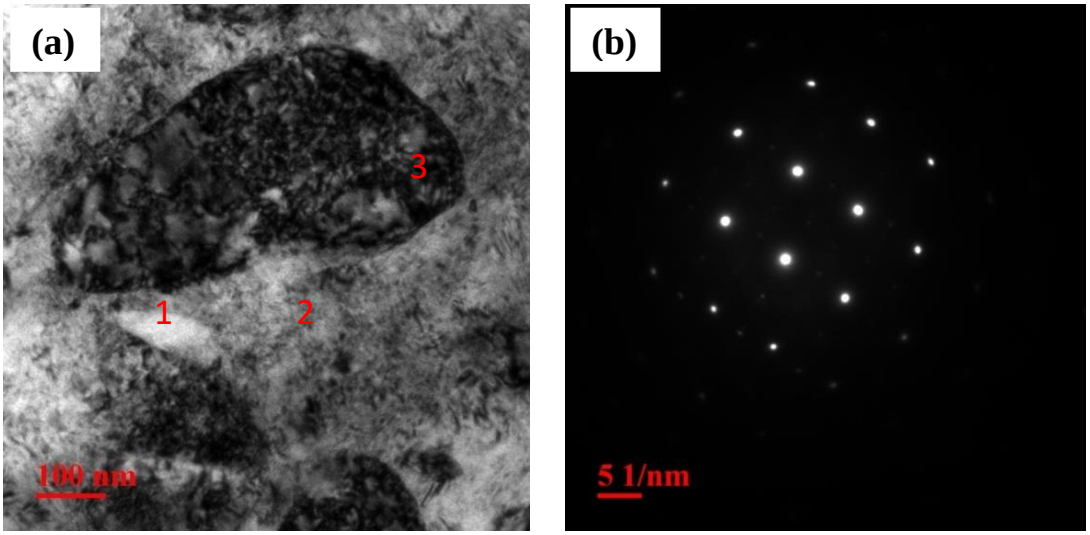

Figure 4.6.(a) TEM micrograph of $AlCr_{1.5}CuFeNi_2Mn$ alloy (b) SAED pattern for region 1

4.2 Thermodynamic and microstructural analysis of $AlCr_{1.5}CuFeNi_2Co_x$ (x = 0, 0.25, 0.5, 0.75 and 1.0) high-entropy alloys

The thermodynamic parameter of the $AlCr_{1.5}CuFeNi_2Co_x$ alloys are determines and the kinetic study provides a wide range of information about the developed alloy. The various thermodynamic parameters can help in prediction the metallurgy of the alloy to the large extent. This section describes the thermodynamic parameters and the Microstructural analysis of $AlCr_{1.5}CuFeNi_2Co_x$ of HEAs.

4.2.1 Thermodynamic behaviour of $AlCr_{1.5}CuFeNi_2Co_x$ alloys

The properties of all the elements for calculating the thermodynamic parameters are presented in Table 3.1 and Table 3.8, respectively. The calculated value of various thermodynamic parameters i.e. δ, VEC, ΔX, ΔH, ΔS, and Ω for $AlCr_{1.5}CuFeNi_2Co_x$ alloys are given in Table 4.2. The δ value for Co_0, $Co_{0.25}$, $Co_{0.5}$, $Co_{0.75}$ and Co_1 are found to be 5.37, 5.19, 5.04, 4.92 and 4.82 respectively. The atomic size difference of the alloys decreases from 5.37% to 4.82% on addition of cobalt. The decrease in the δ with the addition of the cobalt content indicates the formation of solid solution at a higher percentage of cobalt. The melt interaction parameter (Ω) increases from 3.91 to 4.36 on increasing the value of cobalt from 0 to 1 attributing to the formation of a solid solution. HEAs consists of simple phases when the $\delta \leq 6.6\%$ and $\Omega \geq 1.1$. Both the parameters for the cast HEAs are within the proposed range of values resulting in the formation of simple structures [170]. On the

contrary, the intermetallic and the amorphous phases result at a high value of δ and a small value of Ω [171].

The chemical enthalpy of mixing for the binary alloy system is presented in table 4. The value of enthalpy of mixing slightly increases on the addition of the cobalt and then further starts decreasing at x=1. The value of ΔH_{mix} varies from -5.54 $kJmol^{-1}$ at x=0 to 5.59 $kJmol^{-1}$at x=0.5 and then starts increasing to -5.58 $kJmol^{-1}$ at x=1. The negative value of ΔH_{mix} increases the bonding strength between the elements due to their proper chemical reaction. Also, a decrease in the absolute value of ΔH_{mix} at x=1 also predicts the formation of highly stable phase. The similar observation is also reported by Miedema et al. [172]. The value of VEC for Co_0, $Co_{0.25}$, $Co_{0.5}$, $Co_{0.75}$ and Co_1 are found to be 7.85, 7.89, 7.93, 7.97 and8 respectively. It is observed that the alloy tends to form, FCC structure as compared to BCC structure on addition of Co content.

Table 4.2 Thermodynamic Parameters δ, VEC, ΔX, ΔH, ΔS and Ω for $AlCr_{1.5}CuFeNi_2Co_x$ alloys.

Alloy	**δ (%)**	**VEC**	**ΔX**	**ΔH ($kJmol^{-1}$)**	**ΔS ($Jk^{-1}mol^{-1}$)**	**Ω**	**T_m(k)**
Co_0	5.37	7.85	0.12	-5.54	13.01	3.91	1665.45
$Co_{0.25}$	5.19	7.89	0.12	-5.57	13.85	4.13	1662.58
$Co_{0.5}$	5.04	7.93	0.12	-5.59	14.22	4.24	1666.34
$Co_{0.75}$	4.92	7.97	0.13	-5.59	14.43	4.31	1669.85
Co_1	4.82	8.00	0.13	-5.58	14.54	4.36	1673.12

The ΔS value for Co_0, $Co_{0.25}$, $Co_{0.5}$, $Co_{0.75}$ and Co_1 are found to be 13.01, 13.85, 14.22, 14.42 and 14.54 $Jk^{-1}mol^{-1}$, respectively. The increase in the value of ΔS_{mix} with the addition of the cobalt content confirms to the highly randomised distribution of the elements thus assures the formation of the simple stable phase. The melting temperature (T_m) of the alloy remains almost constant on addition of Co.

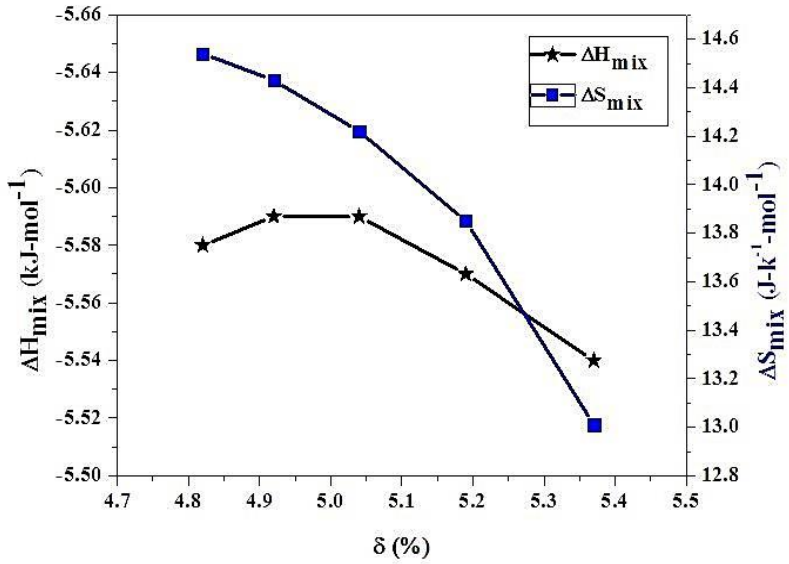

Figure 4.7. ΔH_{mix} and ΔS_{mix} of $AlCr_{1.5}CuFeNi_2Co_x$ as a function of δ.

Figure 4.7 shows the variation of ΔH_{mix} and ΔS_{mix} against atomic size difference (δ) for different compositions varying from x=0 to x=1. Each symbol of the figure 4.7 indicates the molar ratio as presented in Table 4.2. It is observed that the absolute value of ΔH_{mix} and ΔS_{mix} decreases as the δ value increases representing the similar trend with respect to δ. The decrease in the ΔH_{mix} facilitates the formation of the stable solid solution and simple structures. The value of ΔS_{mix} increases the randomness of the elements and hence increases the probability of proper mixing in the liquid state. The atomic size of the alloys shows a decrease in 0.55% from x=0 to x=1, prohibiting the formation of the intermetallics in the alloy.

4.2.2 Phase evolution and microstructure of $AlCr_{1.5}CuFeNi_2Co_x$ alloys

The EDS analysis of the alloy indicates the uniform distribution and the presence of each element in the alloy as shown in Figure 4.8. The phase formation in the alloy is one of the important parameters which determine the properties of the alloys. Figure 4.9 shows the XRD pattern of as-cast $AlCr_{1.5}CuFeNi_2Co_x$ (x=0, 0.25, 0.5, 0.75, 1) alloys. It is found that the base alloy is mainly composed of body-centered cubic (BCC) and face-centered cubic (FCC) structures. The $AlCr_{1.5}CuFeNi_2$ base alloy show combined BCC and FCC phase as compared to $AlCr_{1.5}CuFeNi_2Co_x$ due to the segregation of the Cu matrix (FCC) in the solid solution consisting of other elements Al, Cr, Fe and Ni. At x=0, the sharp peaks of FCC structure can be seen depicting the higher amount of Al, Cu and Ni. However, small peaks of BCC structure are observed due to the presence of elements namely Fe and Cr. As the Co content

increases in the HEAs, the rightward shift of peak from (110) to (200) is observed. Co being a FCCstabiliser, yields significant FCC phase as compared to the BCC phase with the increase in Co content [173].

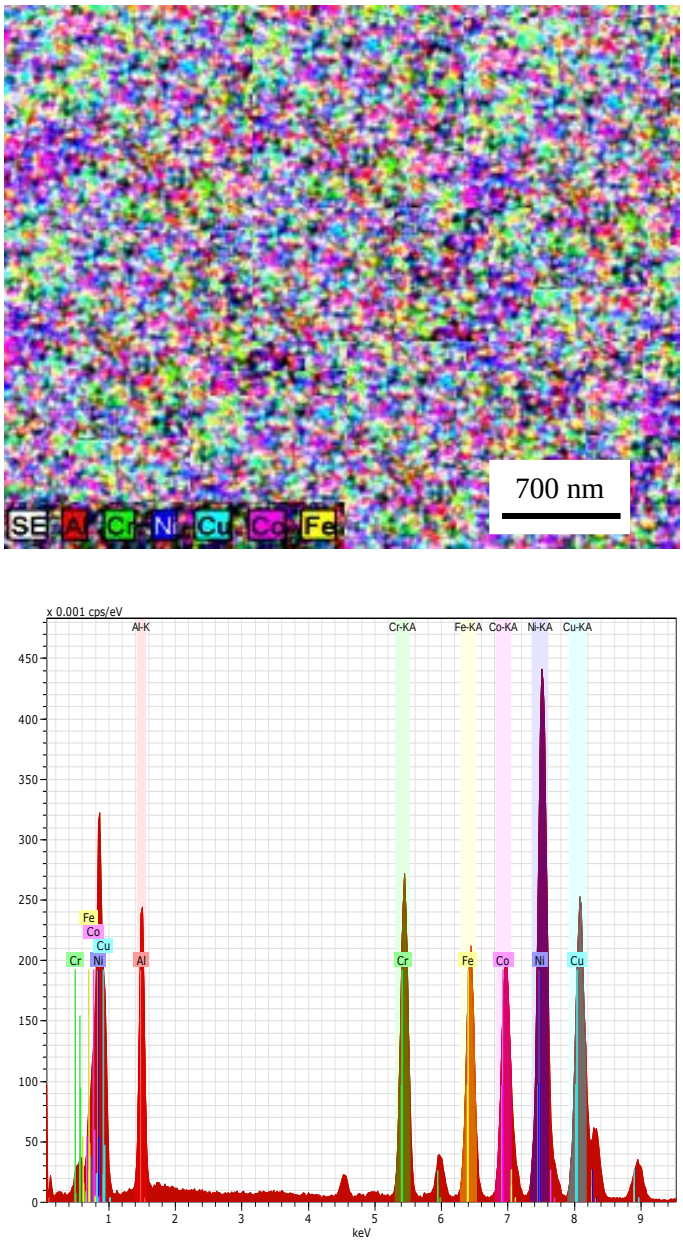

Figure 4.8. EDS analysis of $AlCr_{1.5}CuFeNi_2Co$ alloy and relative intensity of each element in the alloy (Al- Red; Cr- Green; Cu- Cyan; Fe-Yellow; Ni-Blue; Co- Magenta).

The density of the diffraction peak for the all the compositions is found to decrease from Co_0 to Co_1. The disappearance of the diffraction peak is attributed to the formation of the solid solution, crystal refinement and lattice distortion [174].

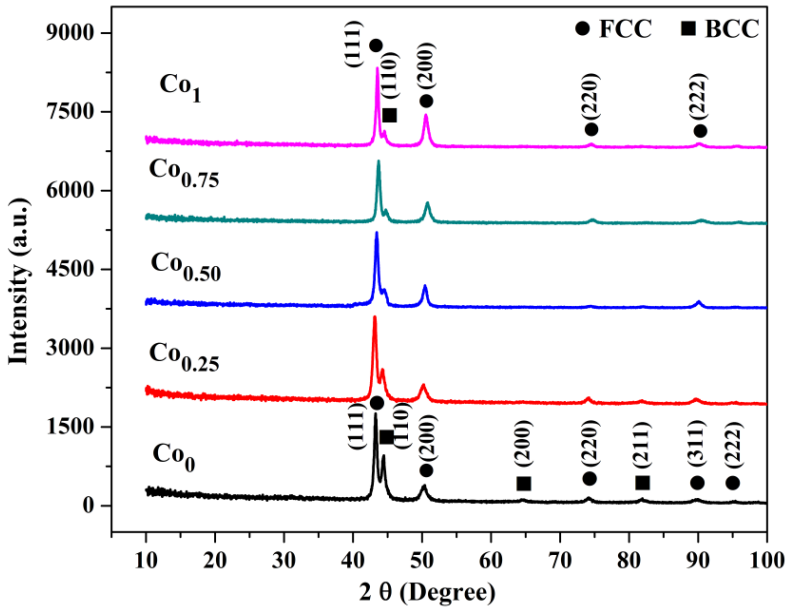

Figure 4.9.XRD pattern of $AlCr_{1.5}CuFeNi_2Co_x$ (x = 0, 0.25, 0.5, 0.75 and 1.0) alloys

The $AlCr_{1.5}CuFeNi_2Co$ shows prominent FCC phase due to the presence of Co, diminishing the quantities of other elements. Based on the XRD pattern, the lattice parameter for the FCC and BCC phase of the samples are calculated to be 3.62 Å and 2.88 Å. The atomic radius of the Co is almost similar to most of the elements of the alloys and hence the lattice parameters for all the compositions are almost constant. The formation of the FCC phase is also in accordance with the calculated VEC values of the alloys.

The optical micrograph of $AlCr_{1.5}CuFeNi_2Co_x$ alloys is shown in Figure 4.10. Optical image of the $AlCr_{1.5}CuFeNi_2$ (Figure 4.10 (a)) shows dark, light and intermediate distinct regions. Each of the regions represents three distinct phases. These regions are very much exposed for Co_0 but decreases with the increase in the Co content. The three phases are mode dense in the Co_1 as compared to other alloys. The microstructures of the cast HEAs are shown in Figure 4.11. The SEM image of the base alloy (Figure 4.11 (a)) depicts the presence of interdendritic and the dendritic region indicated by bright and the dark–field. The dark region (DR) represents the presence of BCC phase as compared to the bright region (ID) which is due to the formation of FCC phase. Figure 4.11 (b) shows the presence of Cu in the alloys as it is segregated in many regions. As the percentage of Co increases in the alloy (Figure 4.11 (b)–(d)), the dark and the bright-field are uniformly distributed in the matrix phase as compared to the base alloy. Figure 4.11 (e) shows the predominant FCC phase in the alloy due to the presence of a highest amount of Co content in the alloy resulting in the conversion of BCC to FCC phase.

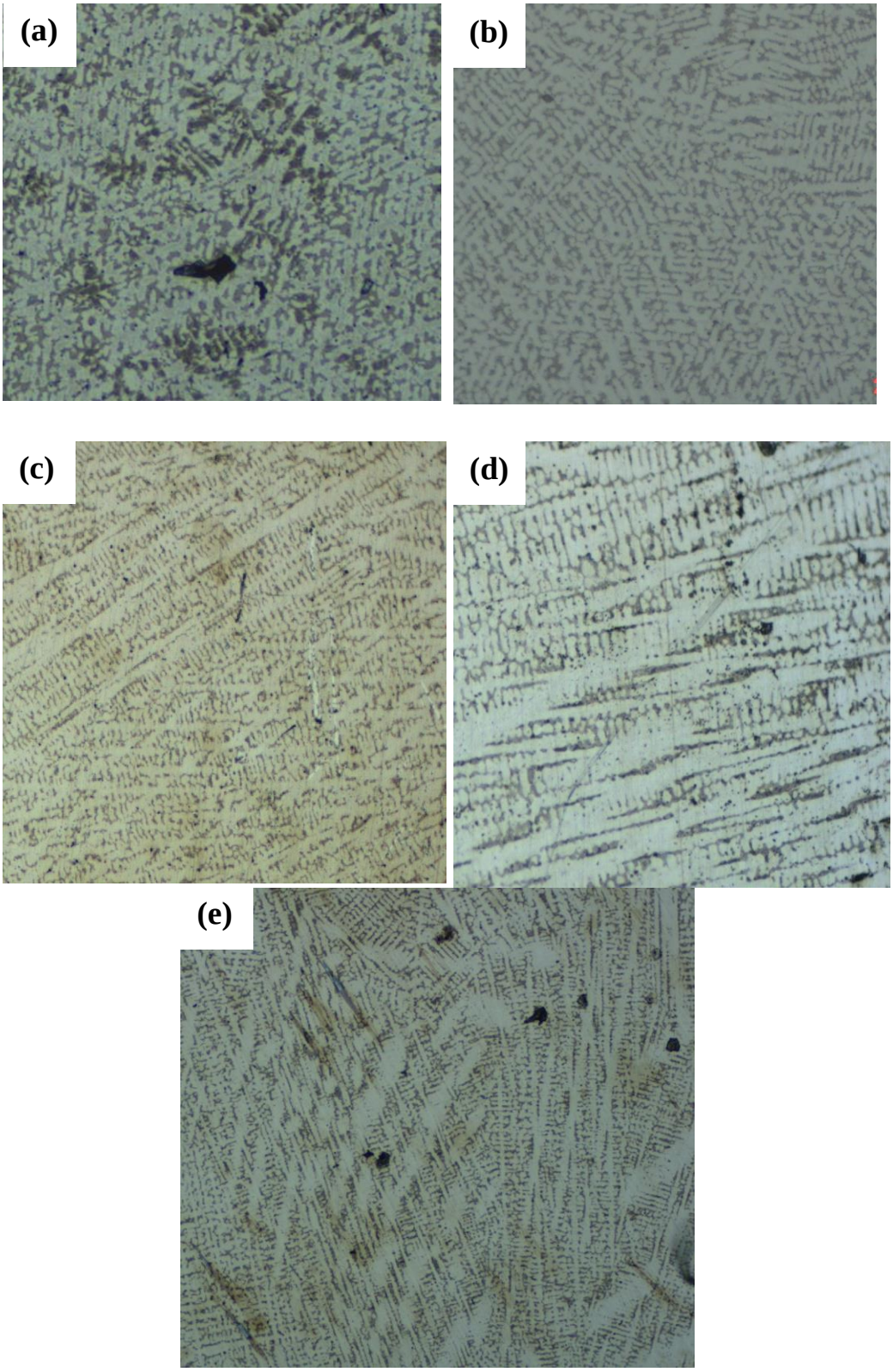

Figure 4.10. Optical micrograph of $AlCr_{1.5}CuFeNi_2Co_x$ alloys (a) Co_0 (b) $Co_{0.25}$ (c) $Co_{0.50}$ (d) $Co_{0.75}$ (e) Co

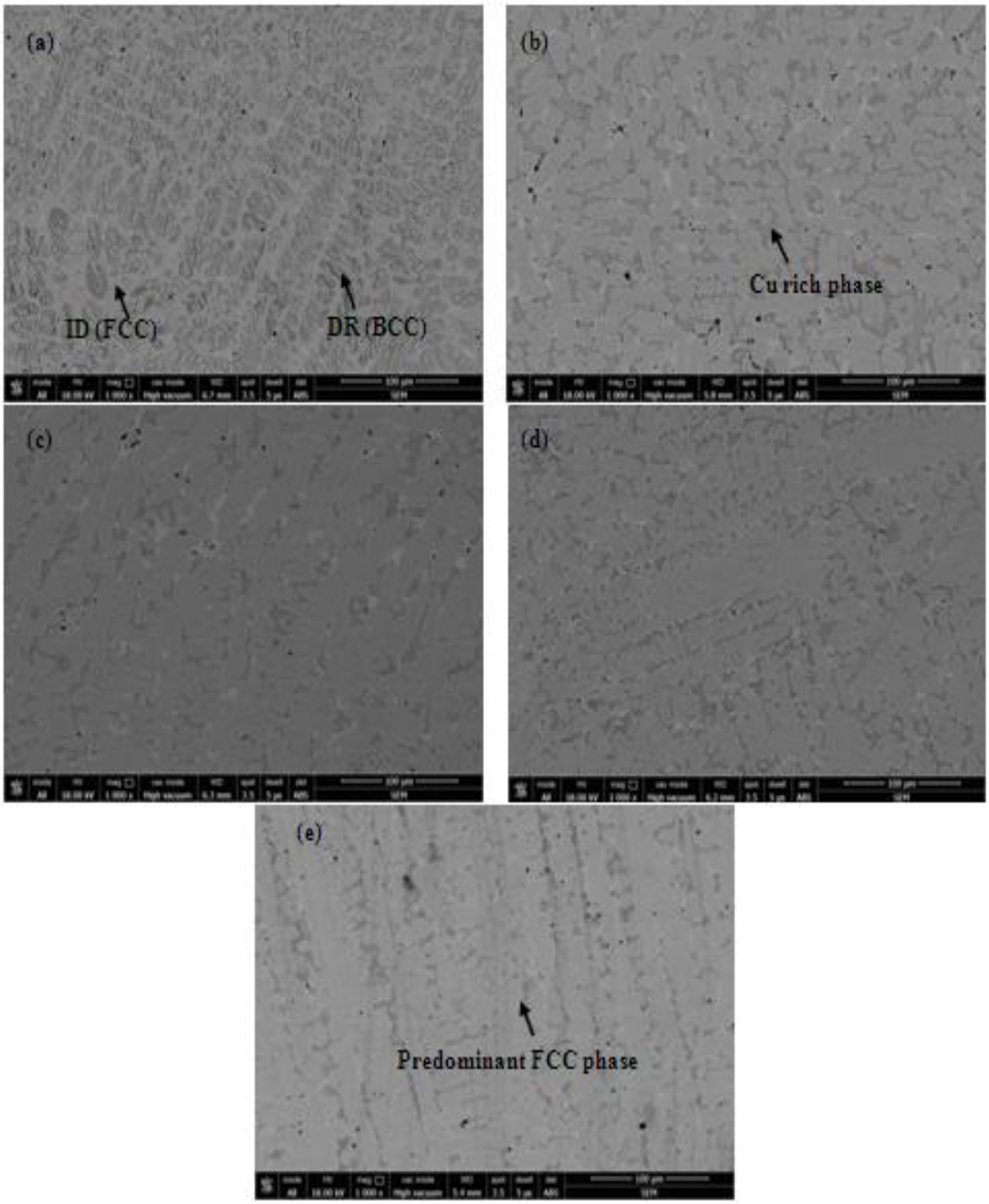

Figure 4.11 SEM images of $AlCr_{1.5}CuFeNi_2Co_x$ alloys: (a) x = 0, (b) x = 0.25, (c) x =0.50, (d) x = 0.75 and (e) x = 1

The TEM micrograph of the $AlCr_{1.5}CuFeNi_2Co$ alloy and its SAED pattern for region 1 is shown in Figure 4.12. The bright field image of the alloy shows three distinct phases. The different regions are marked as 1, 2 and 3. The SAED pattern for the region 1 is shown in Figure 4.12 (b). The SAED pattern depicts the weak reflection of the FCC structure.

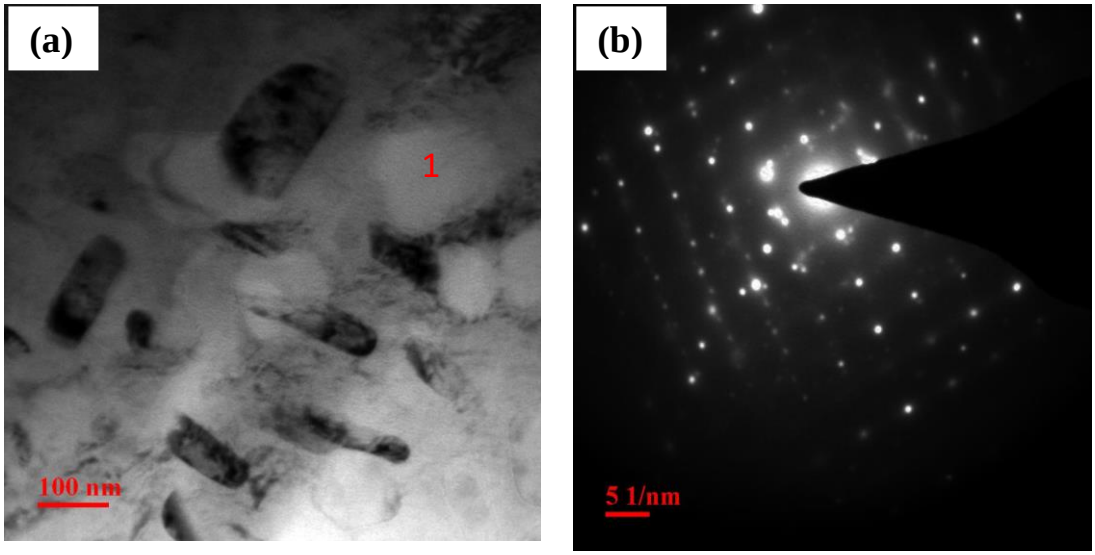

Figure 4.12 (a) TEM micrograph of $AlCr_{1.5}CuFeNi_2Co$ alloy (b) SAED pattern for region1

4.3 Thermodynamic and microstructural analysis of $AlCr_{1.5}CuFeNi_2Ti_x$ (x = 0, 0.25, 0.5, 0.75 and 1.0) high entropy alloys

This section describes the influence of Ti addition to the $AlCr_{1.5}CuFeNi_2$ alloy. The thermodynamic behaviour of the alloy is discussed in detail along with the evolved microstructure studied through different technique.

4.3.1 Thermodynamic behaviour of $AlCr_{1.5}CuFeNi_2Ti_x$ alloys

The properties and the chemical enthalpy of mixing of all the elements Al, Cr, Cu, Fe Ni and Ti used for the development of alloys are listed in Table 3.2. Table 4.3 summarizes the various thermodynamic parameters δ, VEC, ΔX, ΔH, ΔS, and Ω for $AlCr_{1.5}CuFeNi_2Ti_x$ alloys. The entropy of mixing (ΔS) of Ti_0, $Ti_{0.25}$, $Ti_{0.50}$, $Ti_{0.75}$ and Ti_1 is calculated as 13.01, 13.85, 14.22, 14.43 and 14.54 $Jk^{-1}mol^{-1}$ respectively as stated by Guo and Liu [34], if the value of ΔS lie between 11 to 19.5 J/(K.mol), the alloys forms the solid solution. It is observed that the ΔS value continuously increases with the addition Ti content. This is attributed to the continuous increase in the randomness of the atoms of various elements as the Ti at.% increases. Consequently, the mixing of the elements takes place properly in the molten state.

The calculated value of ΔH_{mix} is -5.54, -8.13, -10.35, -12.24 and -13.87 kJ/mole for Ti_0, $Ti_{0.25}$, $Ti_{0.50}$, $Ti_{0.75}$ and Ti_1 alloy respectively. The ΔH_{mix} value of the alloys is estimated on the basis of the enthalpy of mixing of the binary solution. The value of ΔH_{mix} should be in the range of -15 to 5 kJ/mol for the formation of random solid solution. There is a continuous

increase in the negative value of ΔH_{mix} with the increase in the Ti content. The value of ΔH_{mix} from -10 kJ/mol to the positive values indicates the formation of solid solution whereas the ΔH_{mix} value less than -10 kJ/mol may sometimes results in the formation of intermetallic. Thus it can be predicted from the estimated value that the alloys consists of solid solution as well as the intermetallics.

The value of δ for the $AlCr_{1.5}CuFeNi_2Ti_x$ alloys continuously increase from 5.37% to 7.19%for x=0 to x=1. The δ should be less than 6.6%, for the formation of the solid solution. It is observed from the Table 4, that the δ value is under the prescribed limit up to $Ti_{0.50}$ but beyond that the δ value lies in the range for the formation of the intermetallic compounds. On the other hand, Ω for the $AlCr_{1.5}CuFeNi_2Ti_x$ alloys decreases from 3.91 for x=0 to 1.78 for x= 1. Though the value of Ω for the alloys is well in the range (>1.1) for the formation of solid solution, still the tremendous decrease in the Ω from x=0 to x=1 gives a sign of the formation of intermetallic compounds with the further increase in the Ti content. The estimated value of ΔX is 0.12, 0.13, 0.14, 0.14 and 0.14for Ti_0, $Ti_{0.25}$, $Ti_{0.50}$, $Ti_{0.75}$ and Ti_1 respectively. There is a slight increase in the value of ΔX from Ti_0 to $Ti_{0.50}$ whereas the value of ΔX remains almost same for $Ti_{0.50}$, $Ti_{0.75}$ and Ti_1 alloys.

Table 4.3 The various thermodynamic parameters δ, VEC, ΔX, ΔH, ΔS, and Ω for $AlCr_{1.5}CuFeNi_2Ti_x$ alloys

Alloy	**δ (%)**	**VEC**	**ΔX**	**ΔH ($kJmol^{-1}$)**	**ΔS ($Jk^{-1}mol^{-1}$)**	**Ω**	**T_m(k)**
Ti_0	5.37	7.85	0.12	-5.54	13.01	3.91	1665.45
$Ti_{0.25}$	5.99	7.70	0.13	-8.13	13.85	2.84	1668.99
$Ti_{0.5}$	6.47	7.57	0.14	-10.35	14.22	2.31	1678.7
$Ti_{0.75}$	6.86	7.45	0.14	-12.24	14.43	1.99	1687.74
Ti_1	7.19	7.33	0.14	-13.87	14.54	1.78	1696.19

The VEC of the $AlCr_{1.5}CuFeNi_2Ti_x$ alloys decreases from 7.85 to 7.33 for Ti_0 toTi_1. There is a continuous decrease in the VEC value for the HEAs with increase in the Ti content. The VEC value of the alloys aids in forecast the phases present in the multi-component system. The obtained values lie in the FCC+BCC phase as suggested by the Guo et al. [44]. The observation is also supported by the X-ray diffraction pattern of the alloys.

Figure 4.13 shows the relationship between ΔH_{mix} and $\Delta S_{mix}$of $AlCr_{1.5}CuFeNi_2Ti_x$as a function of δ. Each symbol of the figure 4.13 indicates the molar ratio as presented in Table 4.3. The results indicate that the alloy contains both solid solution and intermetallic compounds. The limiting value of ΔH_{mix} (-10 kJ/mol to 5kJ/mol), ΔS_{mix} (>13.38J/Kmol) and δ (< 4%) provides the confirmation for an alloy to behave as solid solution. As observed from Figure, the ΔH_{mix} values are deviating from the solid solution to the intermetallic compounds for all the Ti based alloys. Only $AlCr_{1.5}CuFeNi_2$ alloy exhibits the ΔH_{mix} value within the prescribed range. The absolute value of ΔH_{mix} continuously increases with the increase in the δ value. The relationship between the ΔH_{mix} and δ does not support the formation of solid solutions. The value of ΔS_{mix} for the alloys $Ti_{0.25}$, $Ti_{0.50}$, $Ti_{0.75}$ and $Ti_1$is in accordance with the prescribed value but the other parameters disturbs the alloys to exhibit the simple phases.

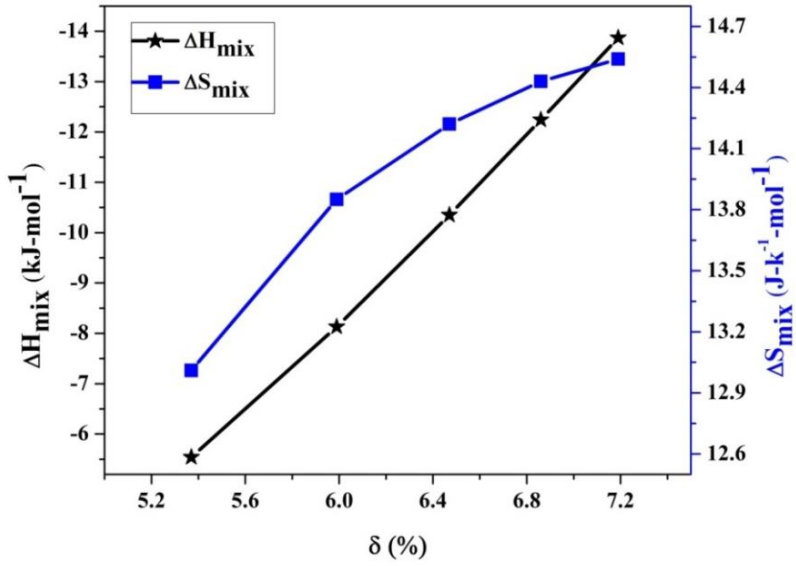

Figure 4.13.The graph showing ΔH_{mix} and ΔS_{mix} of $AlCr_{1.5}CuFeNi_2Ti_x$ alloys as a function of δ

4.3.2 Phase evolution and microstructure of $AlCr_{1.5}CuFeNi_2Ti_x$ alloys

The phases present in the alloy and the analysis of the microstructure play an important role in predicting the physical and mechanical properties of the alloys. The EDS analysis of the $AlCr_{1.5}CuFeNi_2Ti_{0.5}$ alloy is shown in Figure 4.14. It is observed that the elements Al, Cr, Fe, Ni and Ti present in the alloy are uniformly distributed whereas the Cu is accumulated in some regions.

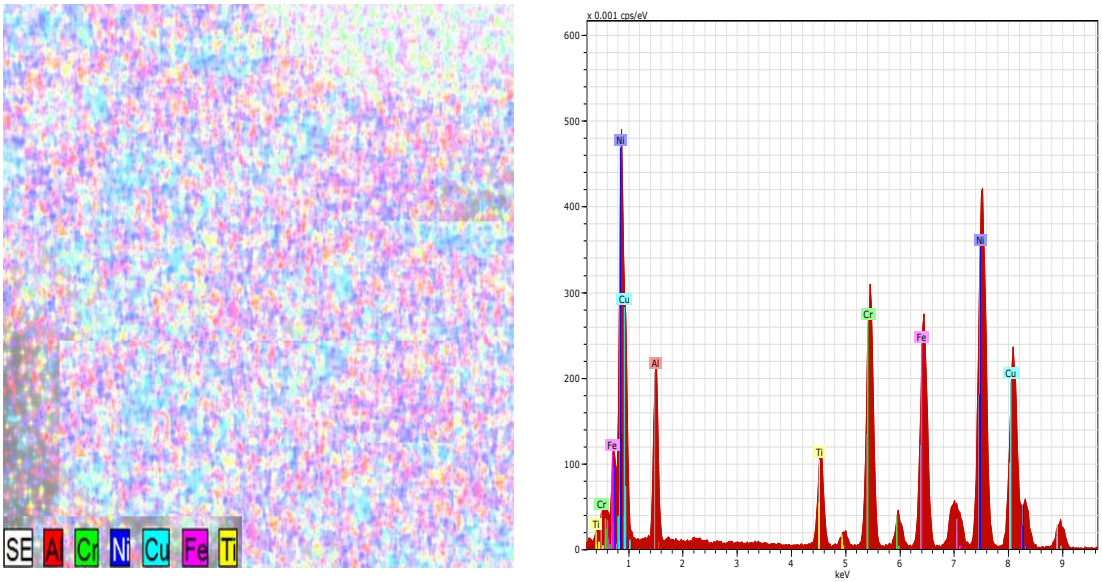

Figure 4.14. EDS analysis of $AlCr_{1.5}CuFeNi_2Ti_{0.5}$ alloy and relative intensity of each element confirming uniform distribution in the alloy

Figure 4.15 shows the XRD pattern of $AlCr_{1.5}CuFeNi_2Ti_x$(x=0, 0.25, 0.5, 0.75 and 1) alloys. The alloys shows the mixed phase FCC+BCC along with the laves phase. Few unknown phases are also present in the alloys which cannot be detected in through the XRD graph. It is clearly observed that on addition of Ti in the $AlCr_{1.5}CuFeNi_2$ alloy, there is an inclusion of intermetallic phases and some unknown phases in addition of FCC+BCC phase.

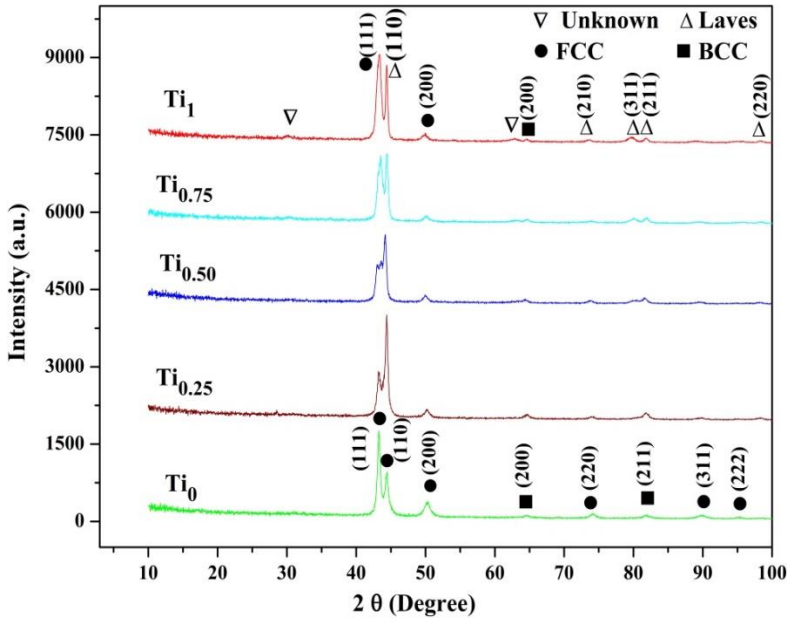

Figure 4.15 XRD pattern of $AlCr_{1.5}CuFeNi_2Ti_x$ (x=0, 0.25, 0.5, 0.75 and 1.0) alloys.

The $AlCr_{1.5}CuFeNi_2$alloy comprises of simple FCC and BCC crystal structures. It is further observed that there is a peak shift in the right direction. There is a large lattice expansion of the alloy due to the addition of the Ti in the HEAs. The large atomic radius of the Ti attributes to the increase in the lattice structure of the alloy. The optical micrograph of $AlCr_{1.5}CuFeNi_2Ti_x$ alloys are shown in Figure 4.16 ((a)-(e)). The optical image depicts the different zones at lower magnifications. The optical images are majorly divided in the three distinct regions i.e. dark, bright and intermediate one. Three different phases are clearly distinct and also supported by the XRD analysis of the alloys.

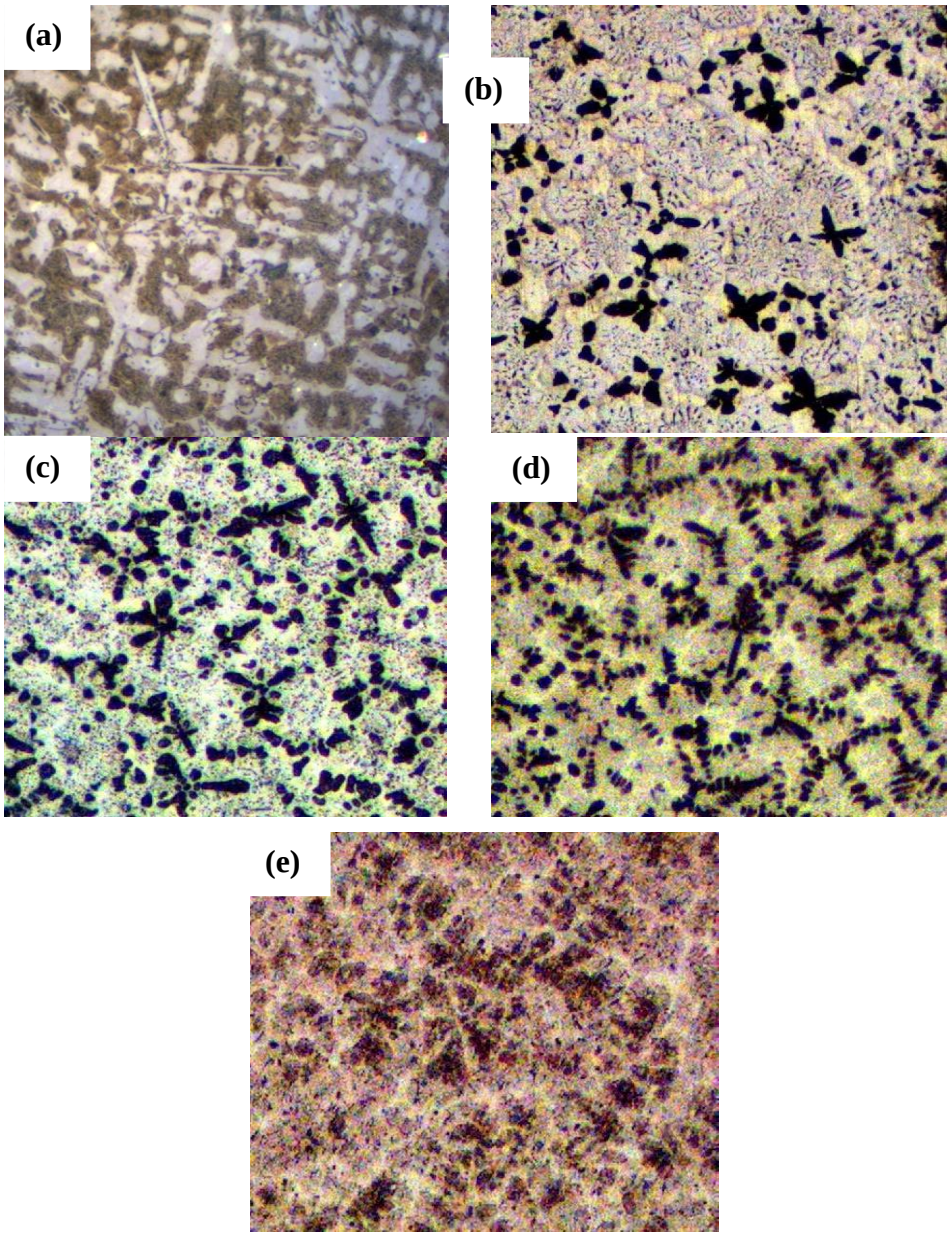

Figure 4.16. Optical micrograph of $AlCr_{1.5}CuFeNi_2Ti_x$ alloys (a) Ti_0 (b) $Ti_{0.25}$ (c) $Ti_{0.50}$ (d) $Ti_{0.75}$ (e) Ti_1

The SEM micrograph of $AlCr_{1.5}CuFeNi_2Ti_x$alloys is shown in Figure 4.17. The $AlCr_{1.5}CuFeNi_2Ti_x$ alloys depict the dendritic and interdendritic microstructure. The arms like

dendritic microstructure are mainly the FCC structures. The Cu having more electro negativity is present in the interdendritic region. As observed from the EDS, apart from the FCC and BCC phases present in the dendritic and interdendritic region, there are other phases present in the alloys. Predominantly, the intermediate region shows the presence of Laves phases. Some of the regions present in the microstructure are still unknown.

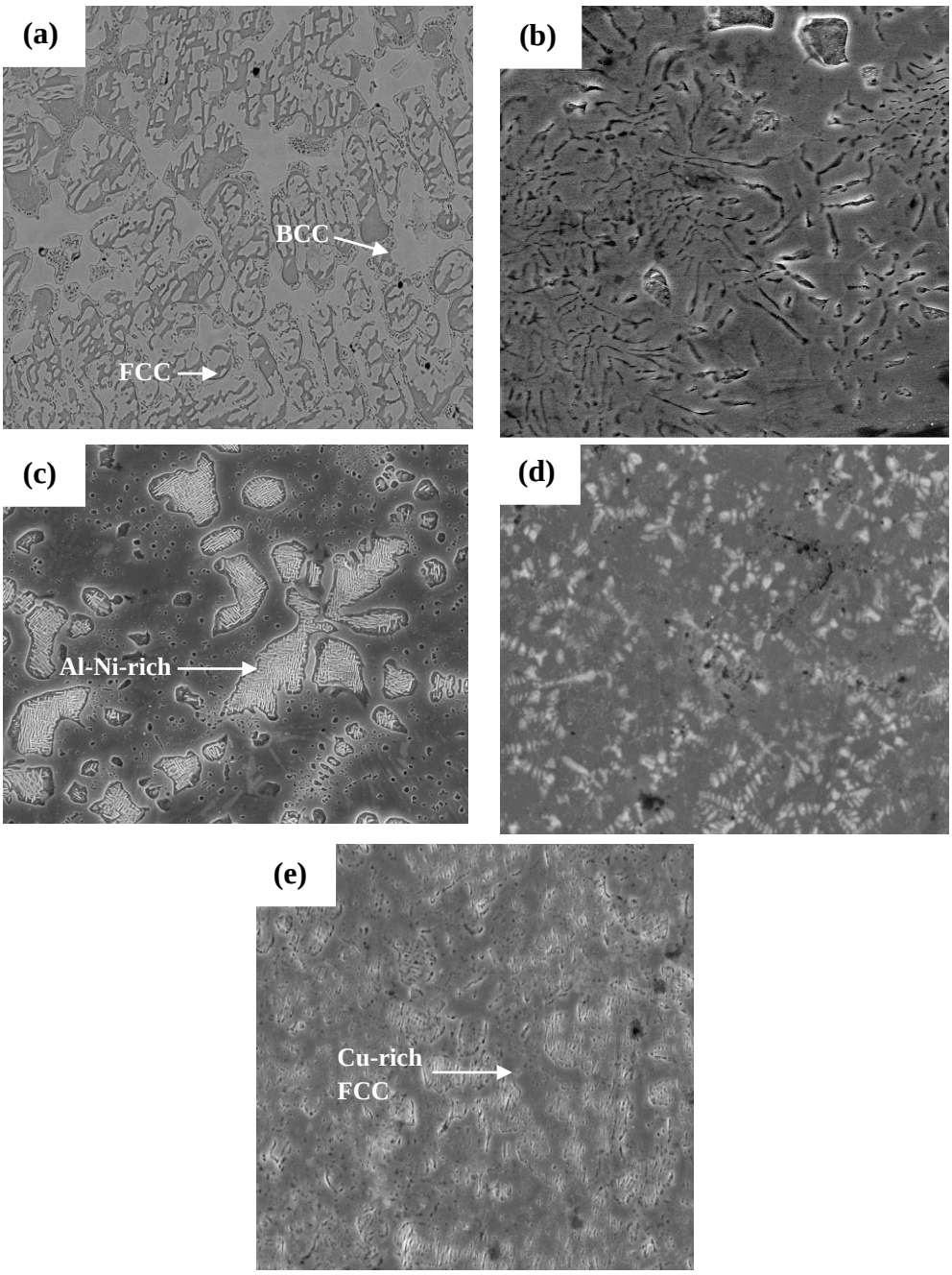

Figure 4.17.SEM images of $AlCr_{1.5}CuFeNi_2Ti_x$ alloys: (a) x=0, (b) x=0.25, (c) x=0.50, (d) x = 0.75 and (e) x=1

The TEM micrograph of the $AlCr_{1.5}CuFeNi_2Co$ alloy and its SAED pattern for region 1 and 2 is shown in Figure 4.18. There exist two distinct zones in the bright field image as shown in Figure 4.18 (a). The different zones are marked as 1 and 2 and the SAED pattern of

the same is shown in Figure 4.18 (b) and (c). The bright spots present in the SAED pattern signify the crystallinity of the elements present in the alloy.

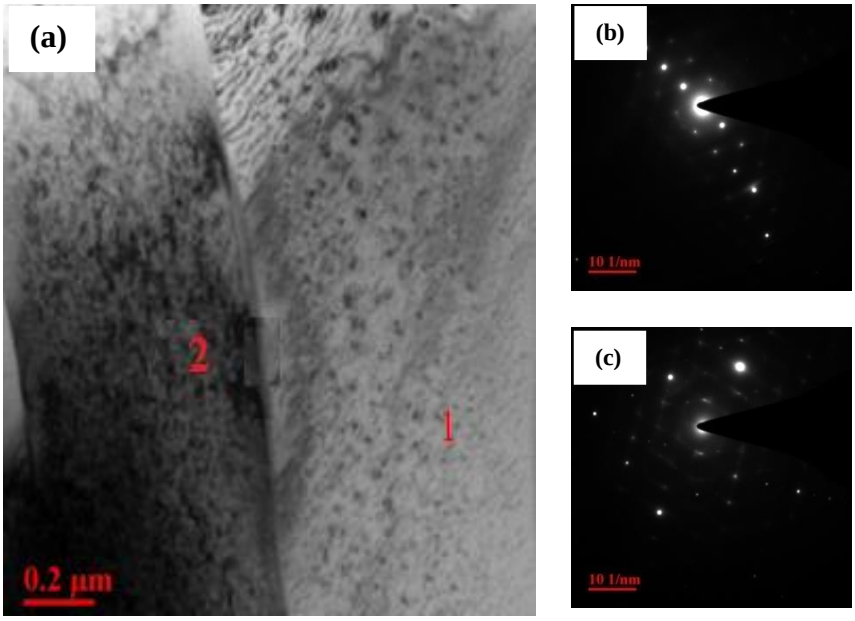

Figure 4.18.(a) TEM micrograph of $AlCr_{1.5}CuFeNi_2Ti$ alloy (b) SAED pattern for region1 (c) SAED pattern for region 2

Chapter in brief

The chapter includes following key points:

- The Thermodynamic analysis of $AlCr_{1.5}CuFeNi_2Mn_x$, $AlCr_{1.5}CuFeNi_2Co_x$ and $AlCr_{1.5}CuFeNi_2Ti_x$ alloys.
- The details of the phases evolved due to the addition of Mn, Co and Ti in the $AlCr_{1.5}CuFeNi_2$alloys.
- The microstructural examination of $AlCr_{1.5}CuFeNi_2Mn_x$, $AlCr_{1.5}CuFeNi_2Co_x$ and $AlCr_{1.5}CuFeNi_2Ti_x$ alloys through optical microscope, SEM and TEM.

The next chapter describes the physical, mechanical and thermal behaviour of high entropy alloys.

*****

Chapter 5

PHYSICAL, MECHANICAL AND THERMAL BEHAVIOUR OF HIGH ENTROPY ALLOYS

The addition of alloying elements strongly influences the physical, mechanical and thermal behaviour of high-entropy alloys (HEAs). In the present research work, the effect of Mn, Co and Ti on the various physical and mechanical properties of non-equimolar $AlCr_{1.5}CuFeNi_2$HEAs is investigated. As the properties of the individual alloying element drastically affects the behaviour of HEAs, it is very crucial to characterize the alloys for the purpose of understanding its applicability. The results are explained in relation with the microstructures of the alloys. This chapter includes the physical, mechanical and thermal properties of the $AlCr_{1.5}CuFeNi_2Mn_x$, $AlCr_{1.5}CuFeNi_2Co_x$ and $AlCr_{1.5}CuFeNi_2Ti_x$ HEAs in three separate sections.

5.1 Physical, mechanical and thermal behaviour of $AlCr_{1.5}CuFeNi_2Mn_x$ high- entropy alloys

The $AlCr_{1.5}CuFeNi_2Mn_x$(x = 0, 0.25, 0.5, 0.75 and 1.0) samples were used to determine the various physical, mechanical and thermal properties of the alloys. The specimens were prepared as per the ASTM standards described in section 3.7.3 for conducting the various tests. The interpretation of the results and their relation with the microstructure are explained in the subsequent section.

5.1.1 Density of $AlCr_{1.5}CuFeNi_2Mn_x$high-entropyalloys

The density of the alloy plays a major role in deciding its application in a particular field. It is mostly desirable to reduce the density of the alloy to the lowest possible value by adding the alloying element. The density of the HEAs is more on the higher side due to the presence of the transition elements and comparable to that of the steel. On the other hand, the formation of the solid solution in the HEAs helps in reducing the density of the alloys. The density of the alloys depends mainly on the alloying element and its compatibility with the other element.

The experimental density of $AlCr_{1.5}CuFeNi_2Mn_x$ alloy varies from 7.11±0.03 g/cm^3 to 7.23±0.08 g/cm^3 for x=0 to x=1. Each test is performed three times and its standard deviation is calculated. The increase in the value of the density of the alloy is due to the increase in the content of the high density Mn. These values are found to be higher than the calculated density of the alloys (Table 5.1). The minimum and the maximum difference in the

experimental and calculated density is 0.5% to 1.5%. The small difference in the density value may be attributed due to error while performing the experiment. The similar observation is also reported in the available literature [69, 123]. Thus it can be concluded that the density of alloys follows the rule of mixture. Further, the increase in the density of the alloy with the increase in the Mn content may be attributed due to the formation of the BCC phase.

Table 5.1 Density of $AlCr_{1.5}CuNi_2FeMn_x$ high-entropy alloys

Alloy designation	**Composition**	**$\rho_{expt,}$ (g/cm^3)**	**$\rho_{cal,}$(g/cm^3)**
Mn_0	$AlCr_{1.5}CuFeNi_2Mn_0$	7.11±0.03	7.07
$Mn_{0.25}$	$AlCr_{1.5}CuFeNi_2Mn_{0.25}$	7.16±0.05	7.09
$Mn_{0.5}$	$AlCr_{1.5}CuFeNi_2Mn_{0.5}$	7.20±0.07	7.10
$Mn_{0.75}$	$AlCr_{1.5}CuFeNi_2Mn_{0.75}$	7.22±0.04	7.11
Mn_1	$AlCr_{1.5}CuFeNi_2Mn$	7.23±0.08	7.13

5.1.2 Microhardness and tensile strength of $AlCr_{1.5}CuFeNi_2Mn_x$ high-entropy alloys

The microhardness and tensile strength of the $AlCr_{1.5}CuFeNi_2Mn_x$ high-entropy alloys are shown in Figure 5.1.The hardness of the HEAs is found to increase with the increase in the Mn content. The hardness of Mn_0, $Mn_{0.25}$, $Mn_{0.50}$, $Mn_{0.75}$ and Mn_1 alloys are found to be 471, 511, 537, 574 and 580 HV respectively. This can be easily justified due to the high hardness of BCC phase as compared to the FCC phase. The X-ray diffraction pattern establishes the formation of the BCC structure with addition of the Mn content in the $AlCr_{1.5}CuFeNi_2Mn_x$ alloys. It is observed from the Figure 5.1 that the hardness value increases almost linearly from x=0 to x=1. The predominant FCC phase in the base alloy due to the occurrence of Cu resulted in its lowest value of hardness among all alloys. With the increase in the Mn content, the crystal structures show more of the BCC phase in comparison to the FCC phase and eventually increase in the hardness of the alloy. The Mn addition also results in the strengthening of the solid solution and is another reason for the increase in the hardness of the alloys.

The tensile strength of the $AlCr_{1.5}CuFeNi_2Mn_x$ alloys varies from 611.47 MPa to 795.37 MPa for x=0 to x=1, respectively**.** In conventional alloys, there exists a dependency of the tensile strength on the hardness of the alloys. Similarly, the tensile strength of the HEAs

is also found to increase with the increase in the hardness value on addition of Mn content to $AlCr_{1.5}CuFeNi_2$ alloy. The increase in the tensile strength is due to the evolution of the BCC face from x=0 to x=1. The alloys exhibit an increase in the brittleness with addition of the Mn content and hence affecting the yield strength of the alloy. The plasticity of the alloys decreases whereas the ultimate tensile strength of the alloys increases with the addition of Mn.

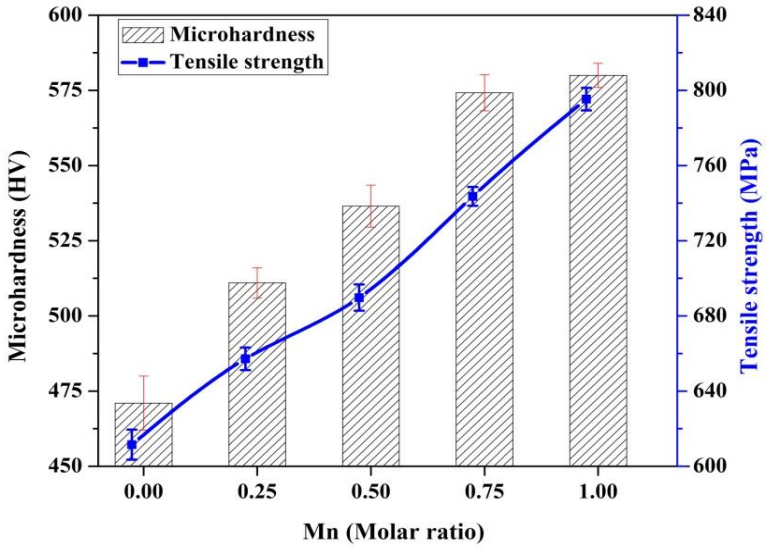

Figure 5.1. Microhardness and tensile strength of$AlCr_{1.5}CuFeNi_2Mn_x$ high-entropy alloys

5.1.3 Specific strength and Young's modulus of $AlCr_{1.5}CuFeNi_2Mn_x$high-entropyalloys

The mechanical properties of the conventional alloys are governed by the prominent elements present in the alloys instead of the alloying element. The role of the alloying elements is to improve the specific properties of the alloys. The alloy shows the dominant properties of the element having the highest content in spite of addition of other elements. However, the mechanical properties of HEAs are not dictated by any one of the elements and exhibits altogether different properties. The microstructures present in the developed alloy govern the mechanical properties of the alloy.

The specific strength and tensile strength of the $AlCr_{1.5}CuFeNi_2Mn_x$ high-entropy alloys are shown in Figure 5.2. The alloys depicting high strength to weight ratio are widely used in most of the structural component where the weight reduction is an important factor in addition to the increase in the strength. It is observed from the Figure 5.2 that the specific strength of the alloys increases on addition of the Mn content. The high specific strength of the alloys is very much desirable in most of the applications. However there is an increase in the density of the alloy but the ultimate tensile strength of the alloys also increase at a rate so

as to increase the specific strength of the alloys. The specific strength of the alloys increase from 0.08 to 0.11 from x=0 to x=1. The specific strength of the alloys increase up to $Mn_{0.75}$and then move towards the constant value as observed for Mn_1.

The Young's modulus of the Mn_0, $Mn_{0.25}$, $Mn_{0.50}$, $Mn_{0.75}$ and $Mn_1$is found to be 237.9. 241.6, 248.84, 257.16 and 259.87 GPa respectively. There is a continuous increase in the Young's modulus of the alloys with the addition of Mn. The XRD pattern for $AlCr_{1.5}CuFeNi_2Mn_x$ alloys (Fig. 4.3) clearly indicates the formation of the BCC structure on addition of the Mn content in the base alloy. It is also evident that peak shift from FCC to BCC structure takes place from x=0 to x=1 in addition to the diminishing of FCC peaks.The formation of BCC structure shows high strength and low plasticity at room temperature. The increase in the Young's modulus value is in accordance with the increase in the tensile strength of the alloys. There is an increase of 9.2 % in Young's modulus from Mn_0 to Mn_1.

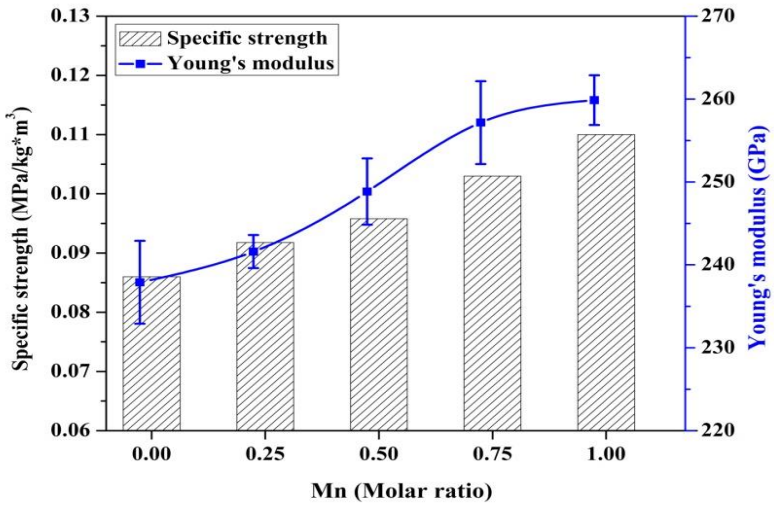

Figure 5.2. Specific strength and Young's modulus of$AlCr_{1.5}CuFeNi_2Mn_x$ high-entropy alloys

5.1.4 Compressive strength and flexural modulus of $AlCr_{1.5}CuFeNi_2Mn_x$ high-entropy alloys

Figure 5.3 shows the compressive strength and flexural modulus of $AlCr_{1.5}CuFeNi_2Mn_x$ high-entropy alloys at room temperature. The results show the gradual increase in the compressive strength of the alloy with the addition of Mn content. The compressive strength of $AlCr_{1.5}CuNi_2FeMn_x$ alloys varies from 1552 MPa to 1685 MPa on addition of Mn for x =0 to x=1. The additions of Mn in the base alloy leads to the formation BCC phase and hence increase in the compressive strength of the alloy. There is an increase of 8.56 % in the compressive strength of the alloy from x=0 to x=1. Further increase in the amount of Mn may

result in the lattice distortion and brings instability in the structure. Similarly, the flexural modulus of the $AlCr_{1.5}CuNi_2FeMn_x$ alloys increases from 274 GPa to 338 GPa on addition Mn for x=0 to x=1. The flexural modulus of the alloys does not increase to the large extent due to the increase in the brittleness of the alloy with the addition of Mn content. Therefore the $AlCr_{1.5}CuFeNi_2Mn_1$ alloys exhibits the maximum flexural modulus of 338 GPa.

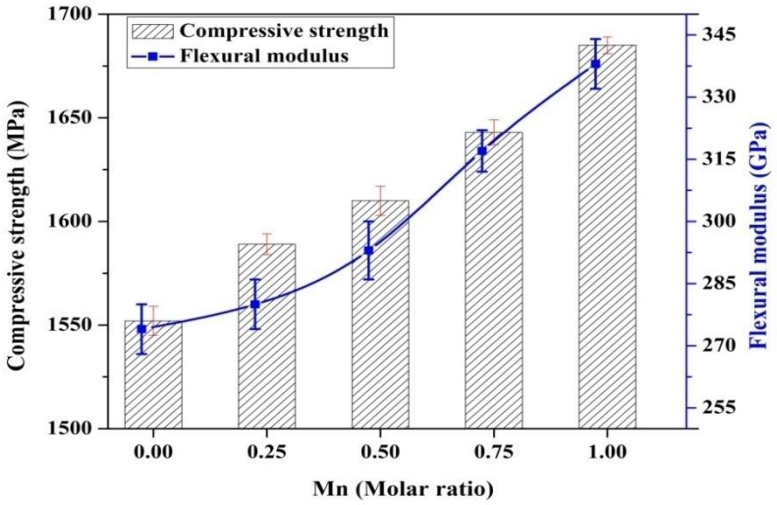

Figure 5.3. Compressive strength and flexural modulus of $AlCr_{1.5}CuNi_2FeMn_x$ high-entropy alloys

5.1.5 Thermal conductivity of $AlCr_{1.5}CuNi_2FeMn_x$ high-entropy alloys

This part of the study investigates the thermal behaviour of $AlCr_{1.5}CuFeNi_2Mn_x$HEAs. Thermal conductivity k (T) is a measure of thermal diffusion coefficient α (T), density ρ (T) and specific heat s (T) of the material at temperature T [175]. Figure 5.4(a) shows the graph between thermal conductivity and molar ratio x in $AlCr_{1.5}CuFeNi_2Mn_x$ HEAs. It is found that the thermal conductivity of the HEAs decreases with increase in the value of x. This is due to the dual phase FCC+BCC present in the HEAs. The phenomenon can be explained with respect to the larger scattering effect due to the addition of the Mn content and hence decrease in the thermal conductivity. The duplex phase is characterised by the more interface boundary as compared to the single phase resulting in the lowering of the heat transfer in the HEAs. Chou et al. found the similar observation while studying the thermal conductivity of $Al_xCoCrFeNi$ [175].

Figure 5.4(b) shows the variation of thermal conductivity of alloys as a function of temperature. Due to small carrier concentration in the lower range of temperatures along with the low sensitivity of the photon concentration, the thermal conductivity of the HEAs increases at higher temperatures. In addition to that, the mean free path of electrons increases

with temperature due to the large linear thermal expansion in the HEAs resulting in the higher thermal conductivity with respect to the increase in the temperature.

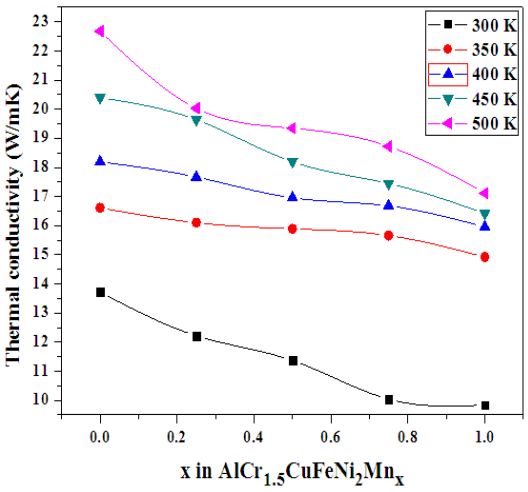

Figure 5.4 (a): Variation of thermal conductivity as a function of x in $AlCr_{1.5}CuFeNi_2Mn_x$.

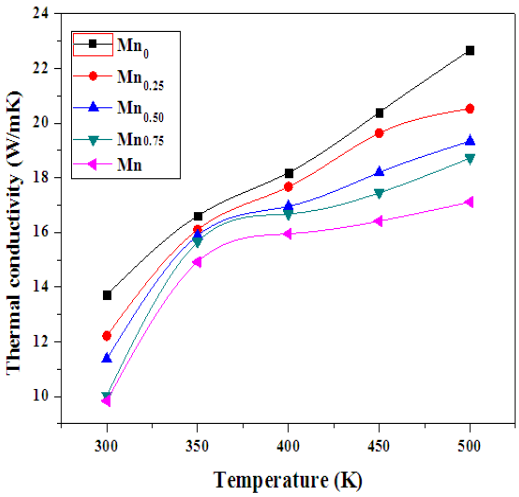

Figure 5.4 (b): Variation of thermal conductivity as a function of temperature.

5.2 Physical, mechanical and thermal behaviour of $AlCr_{1.5}CuFeNi_2Co_x$ high- entropy alloys

The $AlCr_{1.5}CuFeNi_2Co_x$ (x = 0, 0.25, 0.5, 0.75 and 1.0) samples were used to determine the various physical, mechanical and thermal properties of the alloys. The specimens were prepared as per the ASTM standards described in section 3.7.3 for conducting the various tests. The interpretation of the results and their relation with the microstructure are explained in the subsequent section.

5.2.1 Density of $AlCr_{1.5}CuFeNi_2Co_x$ high-entropy alloys

The density of alloys is one of the most important criteria considered while designing an alloy. Slight increase in the density of the developed alloy, if any can be ignored as compared to the benefits of the alloys in terms of the improved mechanical properties. The experimental density of $AlCr_{1.5}CuFeNi_2Co_x$ alloy varies from 6.94±0.02 g/cm^3 to 7.23±0.07 g/cm^3 for x=0 to x=1. These values are found to be in accordance with the calculated density of the alloys (Table 5.2). The minimum and the maximum difference in the experimental and calculated density is 0.008 % and 0.01 %. The minor difference in the density [20, 123] may be attributed due to the evaporation of the elements having low melting temperature such as Al. The other reason is the error in the weight measurement of the individual element during the

development of the alloy. Thus it can be concluded that the density of alloys follows the rule of mixture.

Table 5.2 Density of fabricated $AlCr_{1.5}CuNi_2FeCo_x$ high-entropy alloy.

Alloy designation	**Composition**	**$\rho_{expt.}$ (g/cm^3)**	**$P_{cal,}$(g/cm^3)**
Co_0	$AlCr_{1.5}CuFeNi_2Co_0$	6.94±0.02	7.07
$Co_{0.25}$	$AlCr_{1.5}CuFeNi_2Co_{0.25}$	7.01±0.03	7.13
$Co_{0.5}$	$AlCr_{1.5}CuFeNi_2Co_{0.5}$	7.10±0.04	7.19
$Co_{0.75}$	$AlCr_{1.5}CuFeNi_2Co_{0.75}$	7.15±0.05	7.24
Co_1	$AlCr_{1.5}CuFeNi_2Co$	7.23±0.07	7.29

5.2.2 Microhardness and tensile strength of $AlCr_{1.5}CuFeNi_2Co_x$high-entropyalloys

Figure 5.5 shows the variation of microhardness and the tensile strength of the $AlCr_{1.5}CuFeNi_2Co_x$HEAs. It is observed that there is a sudden drop in the microhradness value on addition of Co content upto 0.25 molar ratio. The decrease in the hardness value of the alloy from x=0.5 to x=1 shows a gradual decrease in the hardness value. This is due to the fact that the addition of Co in the $AlCr_{1.5}CuFeNi_2$alloy enhances the presences of FCC phase as compared to the presence of BCC phase in the base alloy. On addition of the Co content, there is an increase in the FCC phase in the alloy and hence increase in the hardness value. The hardness value is found to decrease from 471 HV for x=0 to 364 HV for x=1 on the addition of the Co in the base alloy. The decrease in the hardness value is attributed to the conversion of the BCC phase to FCC phase on the addition of the Co content.

The tensile strength of the Co_0, $Co_{0.25}$, $Co_{0.50}$, $Co_{0.75}$ and Co_1 alloy is found to be 611.47, 594.46, 557.26, 527.68 and 506.12 MPa respectively. It is observed that there is a continuous decrease in the tensile strength of $AlCr_{1.5}CuFeNi_2Co_x$ with the addition of Co content. The decrease in the tensile strength of the alloy is due to the evolution of FCC structure on addition of the Co in $AlCr_{1.5}CuFeNi_2$ alloy. Though there is an increase in the ductility of the material with the increase in the Co content, still the tensile strength of the alloy decreases. As the tensile strength is dependent on the hardness of the material, hence with the decrease in the hardness value tensile strength also decreases.

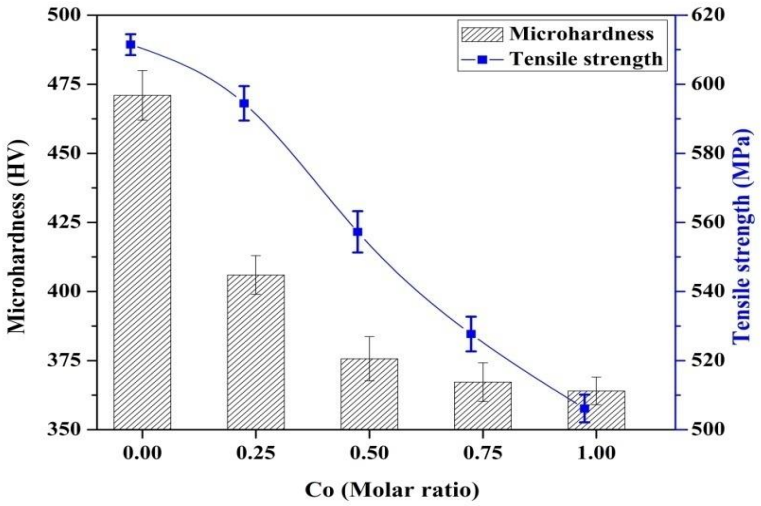

Figure 5.5. Microhardness and tensile strength of$AlCr_{1.5}CuFeNi_2Co_x$ high-entropy alloys

5.2.3 Specific strength and Young's modulus of $AlCr_{1.5}CuFeNi_2Co_x$high-entropyalloys

The specific strength of the alloy should be as high as possible for its use in heavy industries. The specific strength and tensile strength of the $AlCr_{1.5}CuFeNi_2Co_x$ high-entropy alloys are shown in Figure 5.6. The specific strength of the Co_0, $Co_{0.25}$, $Co_{0.50}$, $Co_{0.75}$, and Co_1 is found to be 0.086, 0.080, 0.075, 0.071 and 0.068 MPa/kg.m^3 respectively. The value of the specific strength continuously decreases with the addition of Co in $AlCr_{1.5}CuFeNi_2$ alloy. This is due to the high density of Co i.e. 8.9 g/cm^3 which results in the decreases the specific strength.

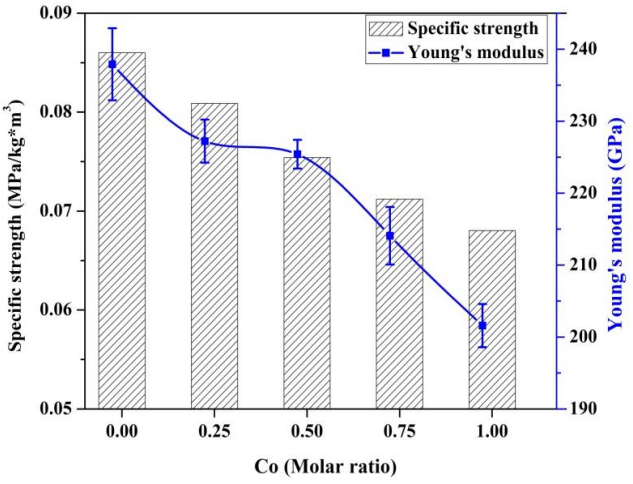

Figure 5.6. Specific strength and Young's modulus of$AlCr_{1.5}CuFeNi_2Co_x$ high-entropy alloys

The Young's modulus of the Co_0, $Co_{0.25}$, $Co_{0.50}$, $Co_{0.75}$, and Co_1 is found to be 237.9, 227.22, 225.4, 214.07 and 201.58 GPa respectively. The decreasing trend is in accordance with the

tensile strength of the alloy. As the Co content is increased in the $AlCr_{1.5}CuFeNi_2$ alloy, there is a gradual decrement in the Young's modulus value due to the transformation of FCC phase to BCC phase. However, the Young's modulus value for the HEAs is higher than most of the superalloys used in the higher temperature applications.

5.2.4 Compressive strength and flexural modulus of $AlCr_{1.5}CuFeNi_2Co_x$ high-entropy alloys

Figure 5.7 shows the compressive strength and flexural modulus of $AlCr_{1.5}CuFeNi_2Co_x$ high-entropy alloys at room temperature. The compressive strength values of Co_0, $Co_{0.25}$, $Co_{0.50}$, $Co_{0.75}$, and Co_1 alloys are 1552, 1753, 1734, 1719 and 1701 MPa. The results indicate a sudden increase in the compressive strength for $Co_{0.25}$ alloy. The increase in compressive strength is attributed to the presence of BCC phase in the alloys. As the Co content increases in $AlCr_{1.5}CuFeNi_2$ alloy, the BCC phase get transformed to the FCC phase. The conversion of the phases increases the ductility the alloys and hence decreases the compressive strength of the alloy. Overall the compressive strength of Co_1 is much more as compared to Co_0.

The flexural modulus of the AlCr1.5CuFeNi2Coxalloys varies from 274 GPa to 365 GPa for Co_0 to Co_1. The flexural modulus increase almost linearly upto $Co_{0.50}$ and then tends to straighten till Co_1. The increase in the flexural modulus is due to the transformation of BCC structure to FCC structure. The ductility of the alloy increases with the addition of Co content in $AlCr_{1.5}CuFeNi_2$alloy. Therefore, the flexural strength also increases with the addition of Co in $AlCr_{1.5}CuFeNi_2$alloy. The Co addition reached to the saturation stage, which can be easily concluded by the stagnant value of the flexural modulus for Co_1 alloy.

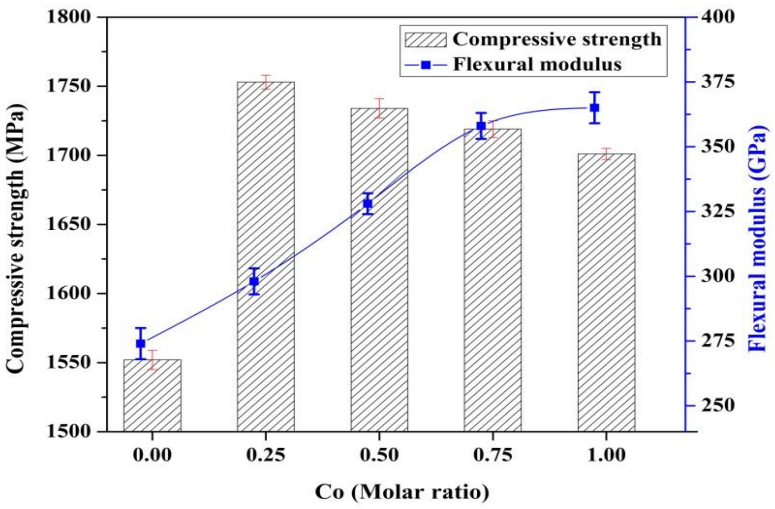

Figure 5.7. Compressive strength and flexural modulus of $AlCr_{1.5}CuNi_2FeCo_x$ high-entropy alloys

5.2.5 Thermal conductivity of $AlCr_{1.5}CuNi_2FeCo_x$ high-entropy alloys

Figure 5.8 (a) shows the Variation of thermal conductivity as a function of x in $AlCr_{1.5}CuFeNi_2Co_{x.}$ It is observed that the thermal conductivity of $AlCr_{1.5}CuFeNi_2Co_x$ alloys decreases with increase in the Co content. This is due to the dual phase FCC+BCC present in the HEAs. The phenomenon can be explained with respect to the larger scattering effect due to the addition of the Co content and hence decrease in the thermal conductivity. The duplex phase is characterised by the more interface boundary as compared to the single phase resulting in the lowering of the heat transfer in the HEAs. Chou et al. found the similar observation while studying the thermal conductivity of $Al_xCoCrFeNi$.

Figure 5.8 (a) shows the variation of thermal conductivity of $AlCr_{1.5}CuFeNi_2Co_x$ alloys as a function of temperature. The decrease in the thermal conductivity of the $AlCr_{1.5}CuFeNi_2Co_x$ alloys may be due to the very low thermal conductivity of the Co. As the Co is added to the $AlCr_{1.5}CuFeNi_2$ alloy, there is decrease in the mean free path of electrons resulting in the decrease in the thermal conductivity of the alloys.

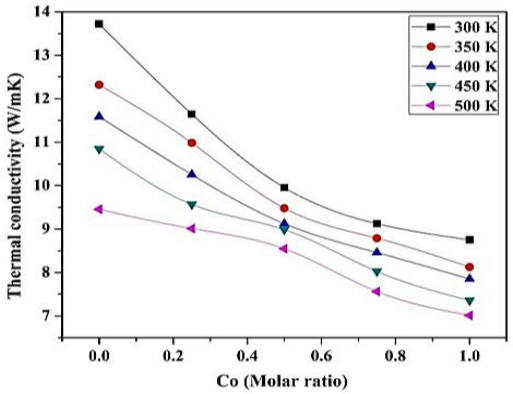

Figure 5.8 (a): Variation of thermal conductivity as a function of x in $AlCr_{1.5}CuFeNi_2Co_{x.}$

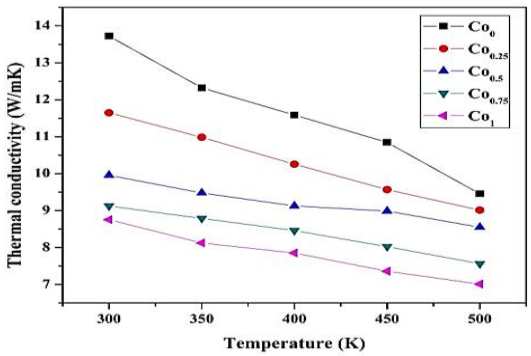

Figure 5.8 (b): Variation of thermal conductivity of $AlCr_{1.5}CuFeNi_2Co_x$ alloy as a function of temperature.

5.3 Physical, mechanical and thermal behaviour of $AlCr_{1.5}CuFeNi_2Ti_x$ high- entropy alloys

The $AlCr_{1.5}CuFeNi_2Ti_x$(x=0, 0.25, 0.5, 0.75 and 1.0) samples were used to determine the various physical, mechanical and thermal properties of the alloys. The specimens were prepared as per the ASTM standards described in section 3.7.3 for conducting the various tests. The interpretation of the results and their relation with the microstructure are explained in the subsequent section.

5.3.1 Density of $AlCr_{1.5}CuFeNi_2Ti_x$ high-entropy alloys

The lower value of density is the one of the most important preference for the selection of the material as it provides a lot of advantage in wide variety of application. The various physical and mechanical properties of the Ti are presented in Table 3.7. The density of Ti is 4.5 g/cm^3, which is an advantage over the Mn and Co.

Table 5.3 Density of $AlCr_{1.5}CuNi_2FeTi_x$ high-entropy alloys

Alloy designation	**Composition**	**$\rho_{expt.}$ (g/cm^3)**	**$P_{cal.}$ (g/cm^3)**
Ti_0	$AlCr_{1.5}CuFeNi_2Ti_0$	7.01±0.03	7.07
$Ti_{0.25}$	$AlCr_{1.5}CuFeNi_2Ti_{0.25}$	6.81± 0.04	6.94
$Ti_{0.5}$	$AlCr_{1.5}CuFeNi_2Ti_{0.5}$	6.70 ±0.07	6.82
$Ti_{0.75}$	$AlCr_{1.5}CuFeNi_2Ti_{0.75}$	6.65 ±0.02	6.71
Ti	$AlCr_{1.5}CuFeNi_2Ti$	6.57 ±0.03	6.61

The experimental density of Ti_0, $Ti_{0.25}$, $Ti_{0.50}$, $Ti_{0.75}$, and Ti_1 alloys is determined as 7.01, 6.81, 6.70, 6.65 and 6.57 g/cm^3 respectively. The experimental density and the calculated density of the $AlCr_{1.5}CuFeNi_2Ti_x$ alloys are presented in Table 5.3.In order to determine the experimental density, the test is performed thrice and the standard deviation is calculated. The experimental as well as the theoretical density of the alloys is decreasing due to the addition of the Ti content. The minimum and the maximum difference in the experimental and calculated density is 0.5% to 1.5%. The calculated values of the density for the alloys are found to be slightly higher than the experimental value. This may be attributed to theerror while performing the experiment. Thus it can be concluded that the density of alloys follows the rule of mixture. Further, the decrease in the density of the alloy with the increase in the Co content may be attributed due to the formation of the FCC phase.

5.3.2 Microhardness and tensile strength of $AlCr_{1.5}CuFeNi_2Ti_x$ high-entropy alloys

The microhardness and tensile strength of the $AlCr_{1.5}CuFeNi_2Ti_x$ high-entropy alloys are shown in Figure 5.9.The hardness of Ti_0, $Ti_{0.25}$, $Ti_{0.50}$, $Ti_{0.75}$ and Ti_1 alloys are found to be 471, 559, 600, 636 and 643 HV respectively. The hardness of the HEAs is found to increase with the increase in the Ti content. The increase in the microhardness is due to the transformation of the FCC+BCC phase to the intermetallic compounds. It is well established that intermetallic compounds are much harder than the FCC or BCC phase. The justification

for the increase in microhardness value is validated by the XRD results of the $AlCr_{1.5}CuFeNi_2Ti_x$ alloys. It is observed that the increase in hardness value of Ti_1 alloy is 36.5 % as compared to the Ti_0 alloy.

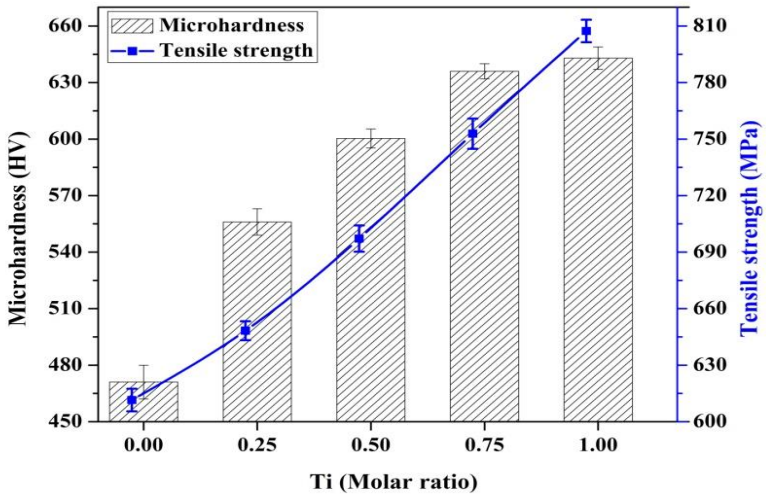

Figure 5.9. Microhardness and tensile strength of$AlCr_{1.5}CuFeNi_2Ti_x$ high-entropy alloys

The tensile strength of Ti_0, $Ti_{0.25}$, $Ti_{0.50}$, $Ti_{0.75}$ and Ti_1 alloys are found to be 611.47, 648.27, 697.14, 752.85 and 807.35 MPa respectively. The tensile strength of the alloys is found to increase with the increase in the molar ratio of Ti in $AlCr_{1.5}CuFeNi_2$ alloy. The tensile strength of the material depends on its hardness and similar trend can be easily observed in this case also. It is observed from the XRD graph that the addition of Ti content in $AlCr_{1.5}CuFeNi_2$ alloy results in the formation of FCC, BCC, Laves and some unknown phases. The intermetallic phases are present in the alloys in the large extent thereby increasing the hardness value and consequently the ultimate strength of the material. There is also reduction in the ductility of the material and hence though the yield strength increases but the tensile strength decreases.

5.3.3 Specific strength and Young's modulus of $AlCr_{1.5}CuFeNi_2Ti_x$ high-entropy alloys

The specific strength of an alloy is one of the most important criteria determining its suitability for a specific application. The advantage of the Ti as compared to other alloys is its low density. It is also found that the tensile strength of the $AlCr_{1.5}CuFeNi_2Ti_x$ alloys increases with the increase in the Ti content. Both the property i.e. low density and high tensile strength makes Ti one of the most favourable elements for the development of the alloys.

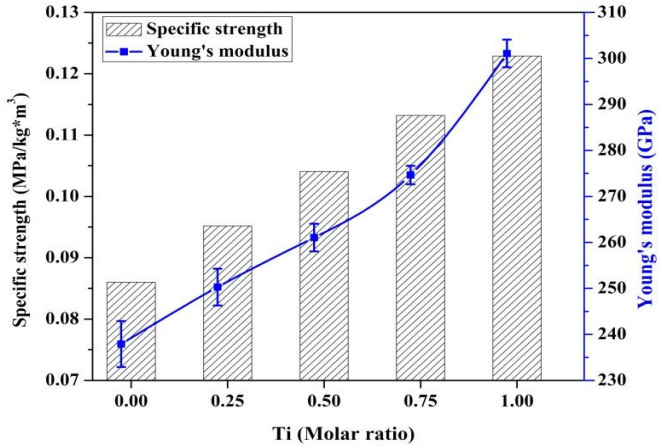

Figure 5.10. Specific strength and Young's modulus of$AlCr_{1.5}CuFeNi_2Ti_x$ high-entropy alloys

The specific strength of Ti_0, $Ti_{0.25}$, $Ti_{0.50}$, $Ti_{0.75}$ and Ti_1 alloys are found to be 0.086, 0.095, 0.104, 0.113 and 0.122 MPa/kgm^3 respectively. It is observed from the Figure 5.10 that the specific strength of the $AlCr_{1.5}CuFeNi_2Ti_x$ alloys linearly increase upto $Ti_{0.5}$ and then there is a sharp increase in the specific strength of the alloy. This is attributed to the addition of low density Ti in the alloy. Initially, as less amount of Ti is added to the alloy, there is linear increase in the specific strength of the alloy. With the increase in the Ti content above certain weight % the specific strength increases drastically. This property of $AlCr_{1.5}CuFeNi_2Ti_x$ alloy is very much useful for its applicability in the structural field.

The Young's modulus of Ti_0, $Ti_{0.25}$, $Ti_{0.50}$, $Ti_{0.75}$ and Ti_1alloys is found to be 237.9. 250.28, 261.05, 274.64 and 301.07 GPa. There is a continuous increase in the Young's modulus value for the alloys with the addition of Ti content. Since the tensile strength of the alloys increases, the Young's modulus value also increases. The trend for the increase in the Young's modulus value is similar to the trend obtained in the case of tensile strength.

5.3.4 Compressive strength and flexural modulus of $AlCr_{1.5}CuFeNi_2Ti_x$ high-entropy alloys

Figure 5.11 shows the compressive strength and flexural modulus of $AlCr_{1.5}CuFeNi_2Ti_x$ high-entropy alloys at room temperature. The results show the continuous increase in the compressive strength of the alloy with the addition of Ti. The compressive strength of Ti_0, $Ti_{0.25}$, $Ti_{0.50}$, $Ti_{0.75}$ and Ti_1 alloys is found to be 1552, 1589, 1624, 1662 and 1693 GPa. The presence of the hard laves phase along with the BCC structures helps in increase in the compressive strength of the alloys with the increase in the Ti percentage in the alloy. There

is almost constant increase in the value of the compressive strength in the alloys on addition of Ti.

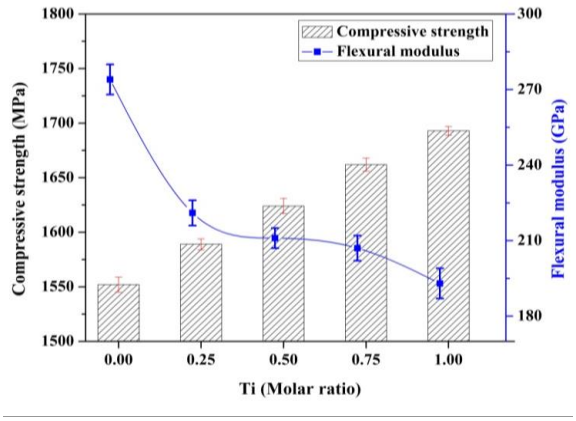

Figure 5.11. Compressive strength and flexural modulus of $AlCr_{1.5}CuNi_2FeTi_x$ high-entropy alloys

In contradiction to the compressive strength the flexural modulus of the alloys decreases sharply with the increase in the Ti percent. The flexural modulus of Ti_0, $Ti_{0.25}$, $Ti_{0.50}$, $Ti_{0.75}$ and Ti_1 alloys is found to be 274, 221, 211, 207 and 193 GPa. The decrease in the flexural modulus value of the $AlCr_{1.5}CuFeNi_2Ti_x$ alloy is due to the lack in ductility of the alloy. The $AlCr_{1.5}CuFeNi_2Ti_x$ alloys exhibits the brittle characteristic and hence there is a decrease in the flexural modulus.

5.3.5 Thermal conductivity of $AlCr_{1.5}CuNi_2FeTi_x$ high-entropy alloys

The thermal conductivity of the material is a deciding factor in case of the alloy to be used for the high temperature applications. The thermal conductivity of the alloy determines its ability to conduct heat. The thermal conductivity of the Ti is 21.9 W/mK, which is higher than that of Mn and Co. Figure 5.12 (a) and (b) shows the variation of thermal conductivity of $AlCr_{1.5}CuFeNi_2Ti_x$ alloys as a function of molar ratio and temperature.

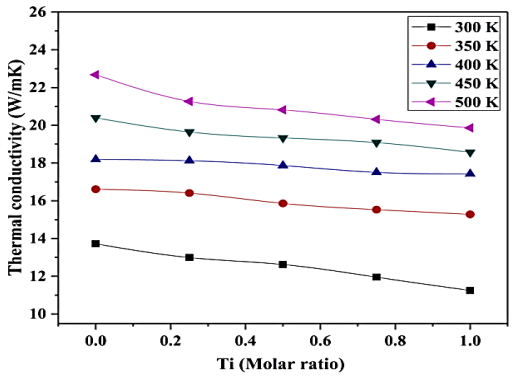

Figure 5.12 (a). Variation of thermal conductivity as a function of molar in $AlCr_{1.5}CuFeNi_2Ti_x$.

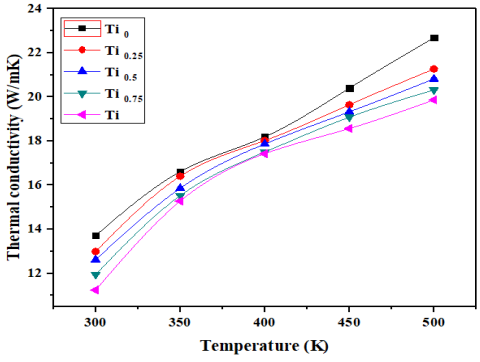

Figure 5.12 (b). Variation of thermal conductivity of $AlCr_{1.5}CuFeNi_2Ti_x$ alloy as a function of temperature.

It is found that the thermal conductivity of the alloys decreases with increase in the molar ratio of the Ti along with the increase in the temperature. However, at the same temperature, the thermal conductivity of the alloys increases with the increase in the temperature. This is due to the dual phase FCC+BCC present in the HEAs. The phenomenon can be explained with respect to the larger scattering effect due to the addition of the Ti content and hence decrease in the thermal conductivity. As the temperature is increased, the mean free path of the electron increases and consequently the thermal conductivity of the alloy increases. The duplex phase is characterized by the more interface boundary as compared to the single phase resulting in the lowering of the heat transfer in the HEAs. Chou et al. found the similar observation while studying the thermal conductivity of $Al_xCoCrFeNi$ [54].

Chapter in brief

This chapter provides the following information:

- The physical and mechanical properties of $AlCr_{1.5}CuFeNi_2Mn_x$, $AlCr_{1.5}CuFeNi_2Co_x$ and $AlCr_{1.5}CuFeNi_2Ti_x$high-entropy alloys.
- The effect of Mn, Co and Ti addition on the thermal conductivity of $AlCr_{1.5}CuFeNi_2$ alloy with the increase in the temperature.

The subsequent chapter describes the sliding wear and corrosion behaviour of $AlCr_{1.5}CuFeNi_2Mn_x$, $AlCr_{1.5}CuFeNi_2Co_x$ and $AlCr_{1.5}CuFeNi_2Ti_x$ high-entropy alloys using one factor at a time and Taguchi design of experiment. Further, multi criteria decision making is used to rank all the alloys based on the various properties.

****

Chapter 6

WEAR AND CORROSION ANALYSIS OF HIGH-ENTROPY ALLOYS

High-entropy alloys (HEAs) can be used in various application at high temperatures involving the tribological aspects such as nuclear reactors, automotive, aerospace, electricity generation etc. In order to investigate the application of the developed $AlCuCr_{1.5}FeNi_2Mn_x$, $AlCuCr_{1.5}FeNi_2Co_x$ and $AlCuCr_{1.5}FeNi_2Ti_x$ alloys in the field of tribology, the sliding wear behaviour of the alloys is studied. The sliding wear behaviour of HEAs deals with the direct contact between two bodies with relative motion. As the HEAs come in contact with the harder counter body, there is a mass loss from the surface and subsurface. The lesser the amount of mass loss more is the preference of the alloy for the sliding wear applications. The sliding wear behaviour of the alloys is studied based on the one factor at a time as well as the Taguchi design of experiment. Further, the corrosion wear behaviour of the alloys is studied in 3.5 wt.% NaCl solution, considered to be the most severe condition for performing the corrosion test. In the last section, multi-criteria decision making is used to rank the composition of the alloy based on the various properties.

6.1 Sliding wear behaviour of $AlCr_{1.5}CuFeNi_2Mn_x$ high- entropy alloys

The dry sliding wear behaviour of $AlCr_{1.5}CuFeNi_2Mn_x$ alloys is determined using the pin-on disc (POD) tribometer. The detail working of POD tribometer is described in the section 3.10. The sliding wear test is carried considering one factor at a time. The various factors considered in this study are: sliding speed, applied load and temperature. The influence of these factors on the specific wear rate of $AlCr_{1.5}CuFeNi_2Mn_x$ alloys is described in the subsequent sections.

6.1.1 Influence of load on specific wear rate of $AlCr_{1.5}CuFeNi_2Mn_x$ alloys

Figure 6.1 shows the effect of applied load on the specific wear rate of $AlCr_{1.5}CuFeNi_2Mn_x$ alloys while maintaining the other factors such as sliding velocity (0.5 m/s) and temperature (30 °C) constant. It is found that the addition of Mn improves the wear resistance of $AlCr_{1.5}CuFeNi_2$ alloys with the increase in the applied load. The specific wear rate of $AlCr_{1.5}CuFeNi_2Mn_x$ alloys continuously decreases with the increase in the Mn content. Similarly, an increase in the value of load from 10 N to 50 N also depicts a continuous decrease in the specific wear rate of the alloys. The Mn_0 alloy shows maximum specific rate of 15.9×10^{-4} mm^3/N-m at 10 N and Mn_1 alloy

shows the minimum specific wear rate of 0.84 × 10^{-4} mm^3/N-m at 50 N. The decrease in the specific wear rate of alloys is due to the increase in the hardness value with the addition of Mn content. As the Mn content increases, the hardness of the alloys increases. The specific wear rate of any material is inversely proportional to the hardness of the alloy. The reason for the increase in the hardness value of the alloys is the conversion of FCC phase to BCC phase with the addition of Mn. It is therefore concluded that the addition of Mn improves the wear resistance of the alloys with the increase in the applied load.

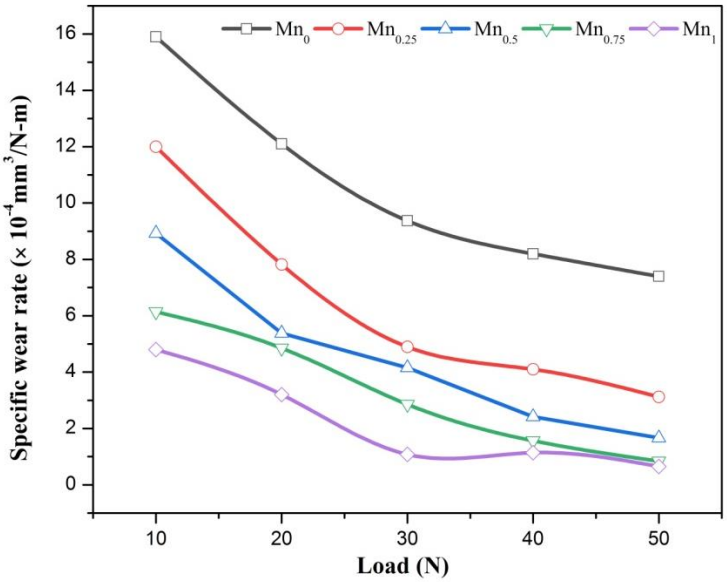

Figure 6.1. Effect of applied load on specific wear rate of $AlCr_{1.5}CuFeNi_2Mn_x$ alloys

6.1.2 Influence of sliding velocity on specific wear rate of $AlCr_{1.5}CuFeNi_2Mn_x$ alloys

Figure 6.2 shows the effect of sliding velocity on specific wear rate of $AlCr_{1.5}CuFeNi_2Mn_x$ alloys while maintaining the other factors such as applied load (10 N) and temperature (30 °C) constant. It is found that the addition of Mn improves the wear resistance of $AlCr_{1.5}CuFeNi_2$ alloys with the increase in sliding velocity. The specific wear rate of $AlCr_{1.5}CuFeNi_2Mn_x$ alloys continuously decreases with the increase in the Mn content. Similarly, increase in the value of sliding velocity from 0.5 m/s to 2.5 m/s also depicts continuous decrease in the specific wear rate of the alloys. The lowest specific wear rate of Mn_0, $Mn_{0.25}$, $Mn_{0.50}$, $Mn_{0.75}$ and Mn_1 alloys are determined as 5.12, 3.68, 2.75, 1.64 and 0.99 mm^3/N-m respectively, at 2.5 m/s sliding velocity. The decrease in the specific wear rate of alloys is due to the increase in the hardness value with the addition of Mn content. The reason for the increase in the hardness value of the alloys is the conversion of

FCC phase to BCC phase with addition of Mn. It is therefore concluded that the addition of Mn improves the wear resistance of the alloys with the increase in the sliding velocity.

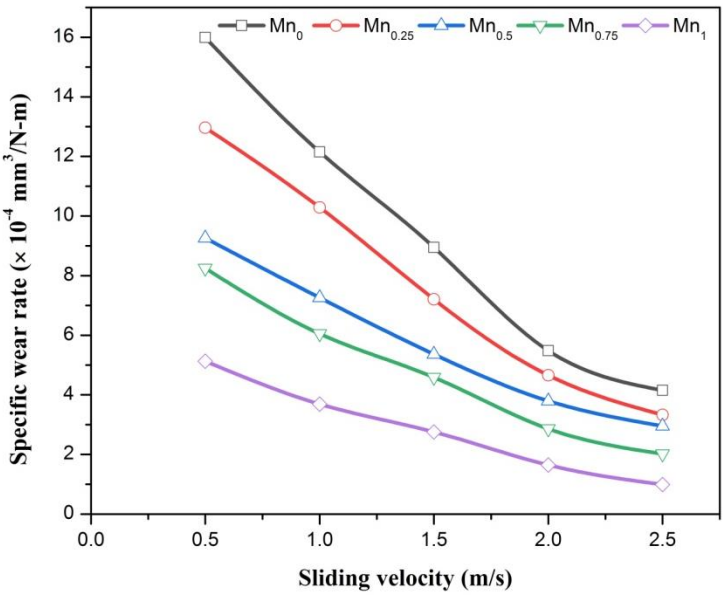

Figure 6.2. Effect of sliding velocity on specific wear rate of $AlCr_{1.5}CuFeNi_2Mn_x$ alloys

6.1.3 Influence of temperature on specific wear rate of $AlCr_{1.5}CuFeNi_2Mn_x$ alloys

Figure 6.3 shows the effect of temperature on specific wear rate of $AlCr_{1.5}CuFeNi_2Mn_x$ alloys while maintaining the other factors such as applied load (10 N) and sliding velocity (0.5 m/s) constant. It is found that the addition of Mn improves the wear resistance of $AlCr_{1.5}CuFeNi_2$ alloys with the increase in temperature up to 90 ºC. On further increasing the temperature, the wear resistance is found to decrease. The specific wear rate of $AlCr_{1.5}CuFeNi_2Mn_x$ alloys decreases with the increase in the Mn content up to 90 ºC and then further increases. Similarly, the specific wear rate also depicts the similar behaviour with the increase in temperature from 30 ºC to 110 ºC. The value of specific wear rate is lowest at 90 ºC for all the alloys and their corresponding values for Mn_0, $Mn_{0.25}$, $Mn_{0.50}$, $Mn_{0.75}$ and Mn_1 are found to be 5.12, 4.77, 3.85, 3.34 and 2.58 mm^3/N-m, respectively. The specific wear rate for Mn_0, $Mn_{0.25}$, $Mn_{0.50}$, $Mn_{0.75}$ and Mn_1 at 110 ºC is found to be 5.66, 5.1, 4.35, 3.9 and 3.45 mm^3/N-m, respectively. There is a slight increase in the value of specific wear rate by increasing the temperature by 20 ºC i.e. from 90 ºC to 110 ºC. The decrease in the value of specific wear rate of the alloys up to 90 ºC is due to the increase in the hardness with no effect of the temperature. However, with further increase in the temperature, the loose particles at the surface due to the sliding action becomes soft and gets

detached from the surface thereby increasing the specific wear rate. It is therefore concluded that the addition of Mn improves the wear resistance of the alloys with the increase in the temperature from room temperature to 90 ºC and then further decreases.

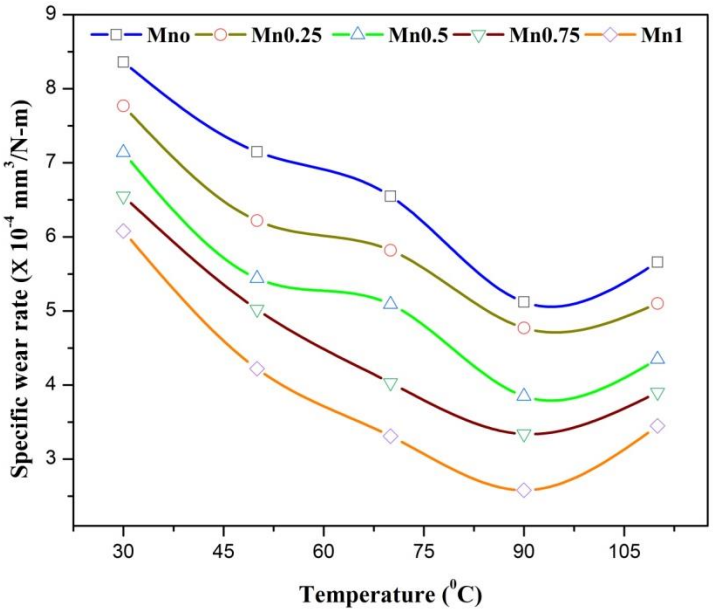

Figure 6.3. Effect of temperature on specific wear rate of $AlCr_{1.5}CuFeNi_2Mn_x$ alloys

6.1.4 Taguchi design of experiment and Analysis of variance (ANOVA) for $AlCr_{1.5}CuFeNi_2Mn_x$ alloys

A proper planning and execution of experiments is an important task to achieve an accurate conclusion. In 1920s, Fisher proposed a technique known as factorial design of experiments. In full factorial design of experiments, a combination of experiments is to be conducted for each factor and level. Taguchi has reduced the large number combination of experiments to a small set of experiments using the concept of orthogonal arrays (OA's). In the present study five factors each at five levels were considered for conducting the experiments as listed in Table 3.11. The L_{25}(5^6) orthogonal array was used to determine the optimal control parameter and the best level for each factor. Each experiment is repeated thrice and the average value of specific wear rate is calculated and tabulated in Table 6.1. A logarithmic function indicates the desired response in any of the orthogonal array via the S/N ratio. Table 6.2 presents the results of ANOVA for $AlCr_{1.5}CuFeNi_2Mn_x$ alloys. The objective function in the optimization technique is "smaller is better".

Table 6.1. Design of experiment using L_{25} orthogonal array for $AlCr_{1.5}CuFeNi_2Mn_x$ alloys

S.No.	Load (N)	Molar ratio, Mn	Temperature (°C)	Sliding speed (m/s)	Sliding distance (m)	Specific wear rate (10^{-3} mm^3/N-m)	S/N ratio
1	10	0.00	30	0.5	500	0.031	30.1728
2	10	0.25	50	1.0	1000	0.078	22.1581
3	10	0.50	70	1.5	1500	0.093	20.6303
4	10	0.75	90	2.0	2000	0.113	18.9384
5	10	1.00	110	2.5	2500	0.165	15.6503
6	20	0.00	50	1.5	2000	0.203	13.8501
7	20	0.25	70	2.0	2500	0.224	12.9950
8	20	0.50	90	2.5	500	0.042	27.5350
9	20	0.75	110	0.5	1000	0.058	24.7314
10	20	1.00	30	1.0	1500	0.081	21.8303
11	30	0.00	70	2.5	1000	0.123	18.2019
12	30	0.25	90	0.5	1500	0.098	20.1755
13	30	0.50	110	1.0	2000	0.145	16.7726
14	30	0.75	30	1.5	2500	0.177	15.0405
15	30	1.00	50	2.0	500	0.045	26.9357
16	40	0.00	90	1.0	2500	0.256	11.8352
17	40	0.25	110	1.5	500	0.049	26.1961
18	40	0.50	30	2.0	1000	0.084	21.5144
19	40	0.75	50	2.5	1500	0.101	19.9136
20	40	1.00	70	0.5	2000	0.112	19.0156
21	50	0.00	110	2.0	1500	0.169	15.4423
22	50	0.25	30	2.5	2000	0.212	13.4733
23	50	0.50	50	0.5	2500	0.174	15.1890
24	50	0.75	70	1.0	500	0.04	27.9588
25	50	1.00	90	1.5	1000	0.079	22.0475

Table 6.2. Results of ANOVA for $AlCr_{1.5}CuFeNi_2Mn_x$ alloys

Source	Degree of Freedom (f)	Sum of squares (SS)	Variance (Mean square), V	Variance Ratio (F)	P	Percentage contribution (%)
A: Normal load(N)	4	20.502	5.126	10.04	0.023	3.17
B: Co (molar ratio)	4	42.126	10.532	20.64	0.006	6.51
C: Temperature (^oC)	4	2.095	0.524	1.03	0.490	0.32
D: Sliding speed(m/s)	4	27.119	6.780	13.29	0.014	4.19
E: Sliding Distance (m)	4	552.736	138.184	270.80	0.000	85.48
Residual Error	4	2.041	0.510			0.33
Total	24	646.619				

The R-Sq and the R-Sq (adj) value for the set of experiments are 99.7% and 98.1%, which validates the design of experiment. The R-square and adjusted R-square values are near to unity which indicates the predicted model is significant. The P value of the input parameter temperature (°C) is greater than 0.05 and hence is not significant. It is also observed that the percentage contribution of the sliding distance is highest as compared to the other input parameters.

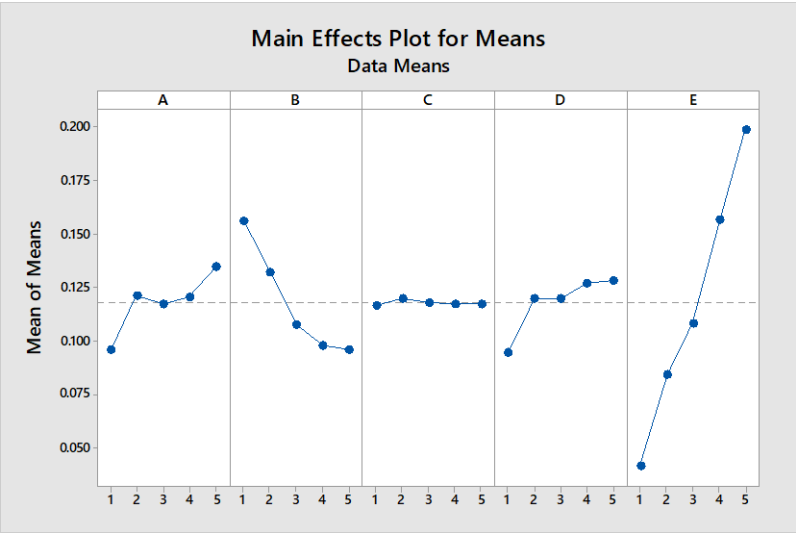

Figure 6.4. Influence of control parameters on means for $AlCr_{1.5}CuFeNi_2Mn_x$ alloys

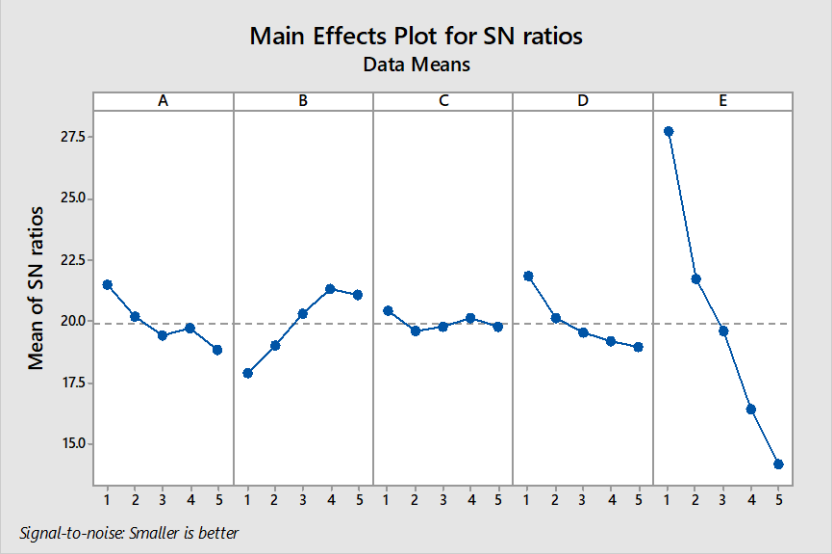

Figure 6.5. Influence of control parameters on average S/N ratio for $AlCr_{1.5}CuFeNi_2Mn_x$ alloys

It is observed from Table 6.3 that the most important input parameter affecting the specific wear rate is sliding distance followed by molar ratio, sliding velocity, load and temperature. The temperature being the least influencing input parameter.

Table 6.3. Mean response table for S/N ratio ($AlCr_{1.5}CuFeNi_2Mn_x$ alloys)

Level	Input parameter				
	Load (N)	**Molar ratio, Mn**	**Temperature (^oC)**	**Sliding velocity (m/s)**	**Sliding distance (m)**
1	21.51	17.90	20.41	21.86	27.76
2	20.19	19.00	19.61	20.11	21.73
3	19.43	20.33	19.76	19.55	19.60
4	19.69	21.32	20.11	19.17	16.41
5	18.82	21.10	19.76	18.95	14.14
Delta	2.69	3.42	0.80	2.90	13.62
Rank	4	2	5	3	1

The main effect response plot for means and S/N ratio are shown in Figure 6.4 and 6.5. As per the Taguchi design of experiment, the S/N ratio should have higher value and the corresponding mean value for the same factor and level should be low. As observed from Figure 6.4 and 6.5, the optimal value of the S/N ratio for each factor at specific level that will provide the optimal response is presented in Table 6.4. For the optimal value condition, it is always

essential to reduce the noise factors which are uncontrollable. Hence, the optimal level of parameter is selected at a higher value of S/N ratio.

Table 6.4. The optimal setting significant input parameters

Significant Input parameter	Optimal level	Optimal parameter value
A: Normal load(N)	A1	21.51
B: Mn (molar ratio)	B4	21.32
D: Sliding speed(m/s)	D1	21.86
E: Sliding Distance (m)	E1	27.76

To verify the results the confirmation test was conducted at the optimum levels of parameters such as A_1, B_4, D_1, E_1. The predicted mean response specific wear rate in terms of S/N ratio can be expressed as,

$\mu = T + (A_1 - T) + (B_4 - T) + (D_1 - T) + (E_1 - T)$

where T = grand average of S/N ratio = 19.928

$\mu = 32.666$

Confidence Interval (CI) = $\sqrt{F_\alpha(n_1, n_2) V_e \left[\frac{1}{N_e} + \frac{1}{R}\right]}$

Where $F_\alpha(1, n_2)$ = computed from F-table at $n_1 = 1$ and n_2 = error DOF at 95 % confidence level ($n_2 = 4$)

$F(1, 4) = 7.71$

V_e = variance of error = 0.510 (from ANOVA Table 6.2)

N_e = effective number of replications

$$= \frac{\text{Number of trials}}{1 + \text{DoF of all factors used in the estimate}} = \frac{25}{(1 + 20)} = 1.190$$

R = number of confirmation test runs

Therefore, the confidence interval CI = ± 4.615

At 95% confidence level, the predicted S/N ratio of the specific wear rate will be in the range of

$= [\mu - CI] < \mu < [\mu + CI]$

$= [32.666 – 4.615] < \mu < [32.666+4.615]$

$= 28.051 < \mu < 37.281$

Table 6.5. Comparison of predicted and confirmation experiment

	Predicted	**Experimental**
Level	$A_1B_4D_1E_1$	$A_1B_4D_1E_1$
Specific wear	0.0232	0.035
S/N Ratio	32.666	29.118

Three confirmation tests were conducted at the optimum levels and the average was shown in the Table 6.5. The corresponding S/N ratio was calculated and it is found to be within the range at the 95% confidence interval.

6.1.5 Microstructural examination of worn surface of $AlCr_{1.5}CuFeNi_2Mn_x$ alloys

The worn surfaces of the $AlCr_{1.5}CuFeNi_2Mn_x$ alloys are observed under SEM after the experiment. The worn surface of any material provides very important information at different test conditions. The wear mechanisms for the $AlCr_{1.5}CuFeNi_2Mn_x$ alloys are identified based on the careful study of surface morphology. The surface morphology of the $AlCr_{1.5}CuFeNi_2Mn_x$ alloys at one factor at a time by varying the load from 10 N to 50 N while maintaining the other factor such as sliding velocity and temperature constant is shown in Figure 6.6.

It is observed from the Figure 6.6 (a) that the maximum wear is takes place for Mn_0 alloy at 10 N load because of the ductile nature of the surface. Due to the combined FCC and BCC phase present in the alloy, the presences of the cracks are observed. The cracks present in the surface depict the brittle nature of the material. In addition to the number of particles as shown by debris can be observed. Figure 6.6 (b) represents the $Mn_{0.25}$ alloy, which is hard as compared to the Mn_0. Small crates and delamination is observed in the micrograph. As the load increases to 20 N, the hardness of the alloy also increases and hence removal of material is less. The increase in the load is very less as compared to the increase in the hardness of the alloys. The Figure 6.6

(c) depicts the ploughing action with the increase in the load to 30 N for $Mn_{0.5}$ alloy. As the hardness value of $Mn_{0.5}$ alloy increases along with the increase in the load, the materials declines in its plastic behaviour and transform to the hard material. Lip formation and the ploughing action can be seen in the image.

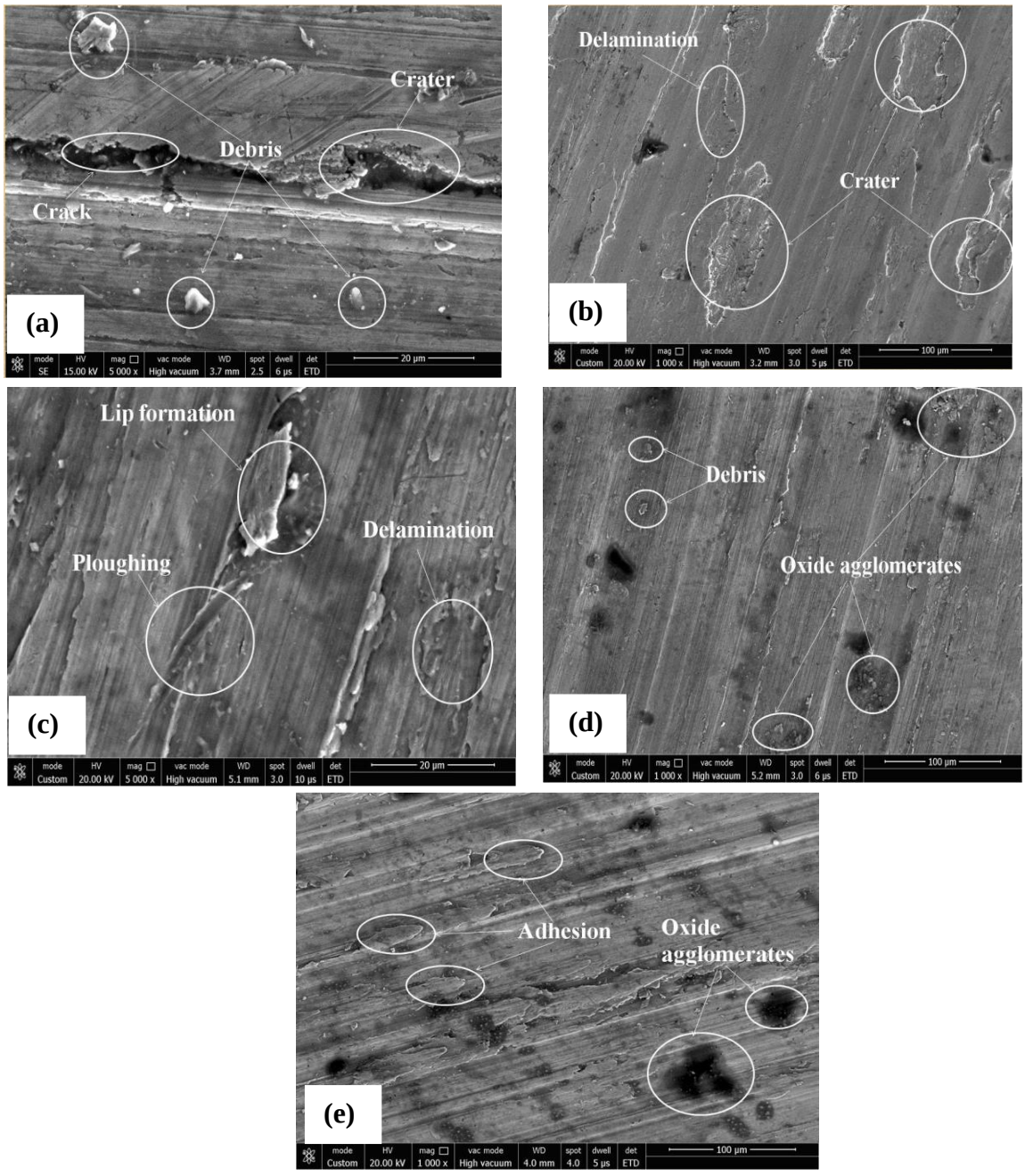

Figure 6.6. SEM images of $AlCr_{1.5}CuFeNi_2Mn_x$ alloys (a) $AlCr_{1.5}CuFeNi_2Mn_0$ (b) $AlCr_{1.5}CuFeNi_2Mn_{0.25}$ (c) $AlCr_{1.5}CuFeNi_2Mn_{0.5}$ (d) $AlCr_{1.5}CuFeNi_2Mn_{0.75}$ (e) $AlCr_{1.5}CuFeNi_2Mn$

Figure 6.6 (d) represents the SEM image for $Mn0._{75}$ at 40 N load. Very fine particles of the debris are observed due to the increase in the load and also increase in the hardness of the alloy. As the hardness and the applied load are high, there is a rise in the temperature at the junction of two materials. Therefore it results in the formation of oxide agglomeration. Figure 6.6 (e) represents the image of Mn_1 at 50 N load. It is observed that due to the sliding contact between the alloy and the hardened steel and rise in temperature at the contact of the two surfaces, the two surface particle of the parent material get adhere to its own surface, As the temperature generation between the alloys and the counter surface is very high, the oxide layer of the parent elements get exposed to the SEM images. The similar wear mechanism was identified by Wu et al. [149].

6.2 Corrosion behaviour of $AlCr_{1.5}CuFeNi_2Mn_x$ high- entropy alloys

Polarization curves of the $AlCr_{1.5}CuFeNi_2Mn_x$ high-entropy alloys are shown in Figure 6.7 and their electrochemical parameters are listed in Table 6.6. The results indicate that the corrosion resistance of the HEAs is improving with the addition of Mn content. The polarization curves of $Mn_{0.25}$ to Mn_1 HEAs almost overlap each other signifying that the alloys are almost alike in corrosion resistance behaviour. The corrosion resistance increases with the addition of Mn upto 0.75 molar ration but with further addition of manganese results in the decrease in the corrosion resistance.

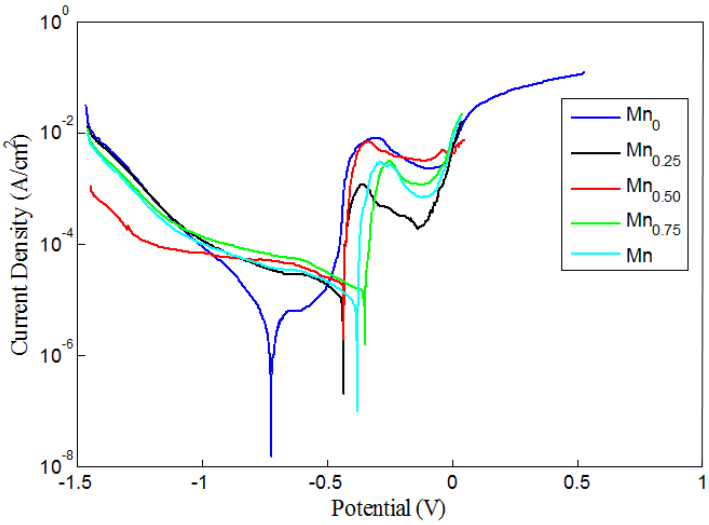

Figure 6.7. Potentiodynamic-polarization curves of $AlCr_{1.5}CuFeNi_2Mn_x$ HEAs in 3.5 wt. % NaCl at ambient temperature.

Table 6.6. Electrochemical parameters of Mn_0, $Mn_{0.25}$, $Mn_{0.5}$, $Mn_{0.75}$ and Mn_1 alloys from potentiodynamic- polarization curve.

High-entropy alloy	Designation	E_{corr}(V)	I_{corr}(mA/cm^2)	E_p(V)
$AlCr_{1.5}CuFeNi_2Mn_0$	Mn_0	-0.728	6.47	-0.7252
$AlCr_{1.5}CuFeNi_2Mn_{0.25}$	$Mn_{0.25}$	-0.44	29	-0.4346
$AlCr_{1.5}CuFeNi_2Mn_{0.5}$	$Mn_{0.5}$	-0.435	24.2	-0.4346
$AlCr_{1.5}CuFeNi_2Mn_{0.75}$	$Mn_{0.75}$	-0.354	18.5	-0.3475
$AlCr_{1.5}CuFeNi_2Mn$	Mn	-0.386	13.1	-0.3814

The HEAs with larger corrosion potential (E_{corr}) and smaller corrosion current density (i_{corr}) have better corrosion resistance. E_{pit} is the potential value where the current is suddenly increased, which means the HEAs start to pit. The improvement in the corrosion resistance of the HEAs is due to the proper distribution of the Ni and Cr in the solid solution due the addition of the Mn content. On the contrary, addition of Mn in $Al_{0.3}CoCrFeNiMn_x$ slightly decreases the corrosion resistance of the alloy [177].

6.3 Sliding wear behaviour of $AlCr_{1.5}CuFeNi_2Co_x$ high- entropy alloys

The dry sliding wear behaviour of $AlCr_{1.5}CuFeNi_2Co_x$ alloys is determined using the pin-on disc (POD) tribometer. The sliding wear test is carried considering one factor at a time. The various factors considered in this study are: sliding speed, applied load and temperature. The influence of these factors on the specific wear rate of $AlCr_{1.5}CuFeNi_2Co_x$ alloys is described in the subsequent sections.

6.3.1 Influence of applied load on specific wear rate of $AlCr_{1.5}CuFeNi_2Co_x$ alloys

Figure 6.8 shows the effect of applied load on specific wear rate of $AlCr_{1.5}CuFeNi_2Co_x$ alloys while maintaining the other factors such as sliding velocity (0.5 m/s) and temperature (30 °C) constant. It is found that the addition of Co decreases the wear resistance of $AlCr_{1.5}CuFeNi_2$ alloys with the increase in the applied load. The specific wear rate of $AlCr_{1.5}CuFeNi_2Co_x$ alloys continuously increases with the increase in the Co content. Similarly, increase in the value of load from 10 N to 50 N also depicts continuous increase in the specific wear rate of the alloys. The maximum value of specific wear rate for Co_0, $Co_{0.25}$, $Co_{0.5}$, $Co_{0.75}$ and Co_1 alloys is 27.04, 27.99, 29.12, 30.55 and 32.41 × 10^{-4} mm^3/N-m at 50 N load. The increase in the specific wear

rate of alloys is due to the decrease in the hardness of the alloy with the addition of Co content. As the Co content increases in the $AlCr_{1.5}CuFeNi_2$ alloy, the hardness of the alloys decreases. The specific wear rate of any material is inversely proportional to the hardness of the alloy. The reason for the decrease in the hardness value of the alloys is the conversion of BCC phase to FCC phase with addition of Co. It is therefore concluded that the addition of Co reduce the wear resistance of the alloys with the increase in the applied load.

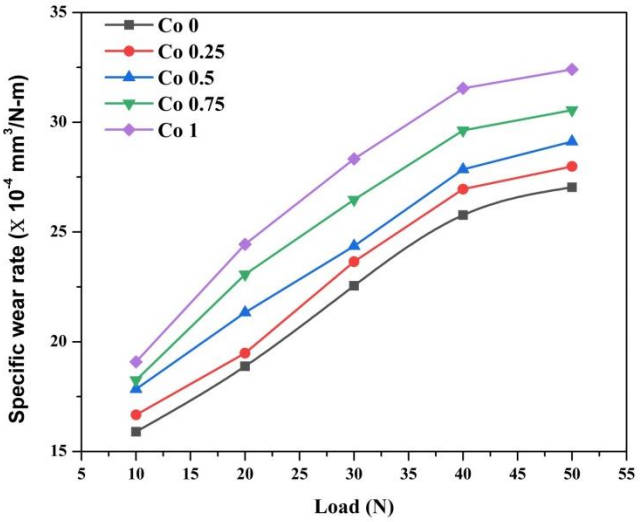

Figure 6.8. Effect of applied load on specific wear rate of $AlCr_{1.5}CuFeNi_2Co_x$ alloys

6.3.2 Influence of sliding velocity on specific wear rate of $AlCr_{1.5}CuFeNi_2Co_x$ alloys

Figure 6.9 shows the effect of sliding velocity on the specific wear rate of $AlCr_{1.5}CuFeNi_2Co_x$ alloys while maintaining the other factors such as applied load (10 N) and temperature (30 °C) constant. It is found that the addition of Co reduces the wear resistance of $AlCr_{1.5}CuFeNi_2$ alloys with the increase in sliding velocity. The specific wear rate of $AlCr_{1.5}CuFeNi_2Co_x$ alloys continuously increases with the increase in the Co content. Similarly, increase in the value of sliding velocity from 0.5 m/s to 2.5 m/s also depicts continuous increase in the specific wear rate of the alloys. The highest specific wear rate of Co_0, $Co_{0.25}$, $Co_{0.5}$, $Co_{0.75}$ and Co_1 alloys are determined as 19.88, 26.12, 30.5, 32.98 and 35.45 mm^3/N-m respectively, at 2.5 m/s sliding velocity. The increase in the specific wear rate of alloys is due to the decrease in the hardness value with the addition of Co content. The reason for the decrease in the hardness value of the alloys is the conversion of BCC phase to FCC phase with addition of Co. It is therefore

concluded that the addition of Co reduces the wear resistance of the alloys with the increase in the sliding velocity.

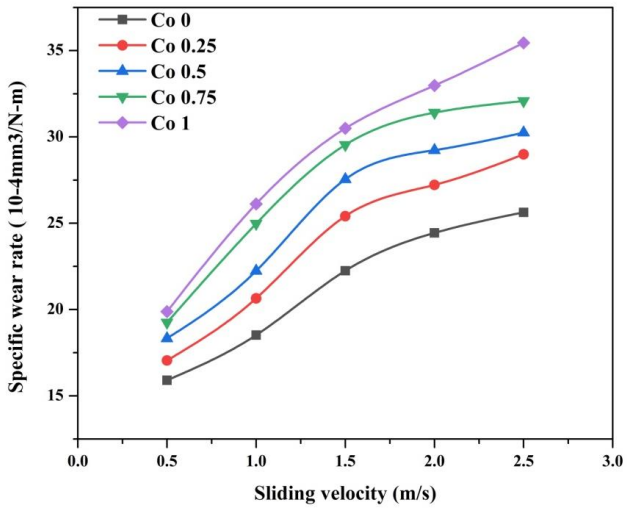

Figure 6.9. Effect of sliding velocity on specific wear rate of $AlCr_{1.5}CuFeNi_2Co_x$ alloys

6.3.3 Influence of temperature on specific wear rate of $AlCr_{1.5}CuFeNi_2Co_x$ alloys

Figure 6.10 shows the effect of temperature on specific wear rate of $AlCr_{1.5}CuFeNi_2Co_x$ alloys while maintaining the other factors such as applied load (10 N) and sliding velocity (0.5 m/s) constant. It is found that the addition of Co reduces the wear resistance of $AlCr_{1.5}CuFeNi_2$ alloys with the increase in temperature. There is a sharp increase in the specific wear rate up to 90 ºC and then a gradual increase at 110 ºC.

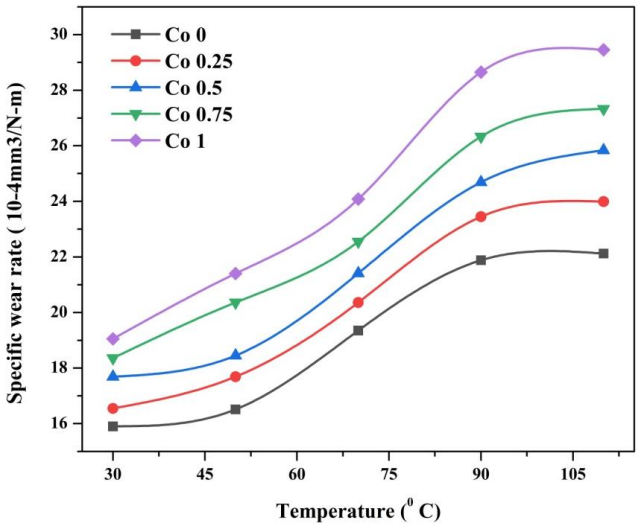

Figure 6.10. Effect of temperature on specific wear rate of $AlCr_{1.5}CuFeNi_2Co_x$ alloys

The specific wear rate of $AlCr_{1.5}CuFeNi_2Co_x$ alloys increases with the increase in the Co content. Similarly, the specific wear rate also depicts the similar behaviour with the increase in temperature from 30 ºC to 110 ºC. The value of specific wear rate is highest at 110 ºC for all the alloys and their corresponding values for Co_0, $Co_{0.25}$, $Co_{0.5}$, $Co_{0.75}$ and Co_1 are found to be 5.12, 4.77, 3.85, 3.34 and 2.58 mm^3/N-m, respectively. The specific wear rate for Mn_0, $Mn_{0.25}$, $Mn_{0.50}$, $Mn_{0.75}$ and Mn_1 at 110 ºC is found to be 22.12, 23.99, 25.84, 27.33 and 39.45 mm^3/N-m, respectively. The increase in the value of specific wear rate of the alloys is due to the decrease in the hardness with. The soft particles on the surface of the alloys are get easily removed with the increase in the temperature. It is therefore concluded that the addition of Co reduces the wear resistance of the alloys with the increase in the temperature from room temperature to 110 ºC.

6.3.4 Taguchi design of experiment and Analysis of variance (ANOVA) for $AlCr_{1.5}CuFeNi_2Co_x$ alloys

In the present study five factors each at five levels were considered for conducting the experiments as listed in Table 3.11. The L_{25}(5^6) orthogonal array was used to determine the optimal control parameter and the best level for each factor. Each experiment is repeated thrice and the average value of specific wear rate is calculated and tabulated in the Table 6.7. The desired response in any of the orthogonal array is indicated by a logarithmic function via the S/N ratio. Table 6.8 presents the results of ANOVA for $AlCr_{1.5}CuFeNi_2Co_x$ alloys. The objective function in the optimization technique is smaller is better response.

Table 6.7. Design of experiment using L_{25} orthogonal array for $AlCr_{1.5}CuFeNi_2Co_x$ alloys

S.No.	Load (N)	Molar ratio, Co	Temperature (ºC)	Sliding speed (m/s)	Sliding distance (m)	Specific wear rate 10^{-3} mm^3/N-m	S/N ratio
1	10	0.00	30	0.5	500	0.031	30.1728
2	10	0.25	50	1.0	1000	0.096	20.3546
3	10	0.50	70	1.5	1500	0.125	18.0618
4	10	0.75	90	2.0	2000	0.160	15.9176
5	10	1.00	110	2.5	2500	0.182	14.7986
6	20	0.00	50	1.5	2000	0.203	13.8501
7	20	0.25	70	2.0	2500	0.261	11.6672
8	20	0.50	90	2.5	500	0.088	21.1103

9	20	0.75	110	0.5	1000	0.071	22.9748
10	20	1.00	30	1.0	1500	0.159	15.9721
11	30	0.00	70	2.5	1000	0.123	18.2019
12	30	0.25	90	0.5	1500	0.118	18.5624
13	30	0.50	110	1.0	2000	0.166	15.5978
14	30	0.75	30	1.5	2500	0.221	13.1122
15	30	1.00	50	2.0	500	0.091	20.8192
16	40	0.00	90	1.0	2500	0.256	11.8352
17	40	0.25	110	1.5	500	0.097	20.2646
18	40	0.50	30	2.0	1000	0.128	17.8558
19	40	0.75	50	2.5	1500	0.200	13.9794
20	40	1.00	70	0.5	2000	0.161	15.8635
21	50	0.00	110	2.0	1500	0.169	15.4423
22	50	0.25	30	2.5	2000	0.267	11.4698
23	50	0.50	50	0.5	2500	0.210	13.5556
24	50	0.75	70	1.0	500	0.144	16.8328
25	50	1.00	90	1.5	1000	0.172	15.2894

Table 6.8. Results of ANOVA for $AlCr_{1.5}CuFeNi_2Co_x$ alloys

Source	**Degree of Freedom (f)**	**Sum of squares (SS)**	**Variance (Mean square), V**	**Variance Ratio (F)**	**P**	**Percentage contribution (%)**
A: Normal load (N)	4	77.460	19.6350	27.47	0.004	18.64
B: Co (molar ratio)	4	7.661	1.9152	2.72	0.178	1.83
C: Temperature (^oC)	4	11.871	2.9677	4.21	0.096	2.86
D: Sliding speed (m/s)	4	67.837	16.9592	24.05	0.005	16.40
E: Sliding Distance (m)	4	248.061	62.0154	87.96	0.000	59.70
Residual Error	4	2.820	0.7050			0.57
Total	24	415.710				100

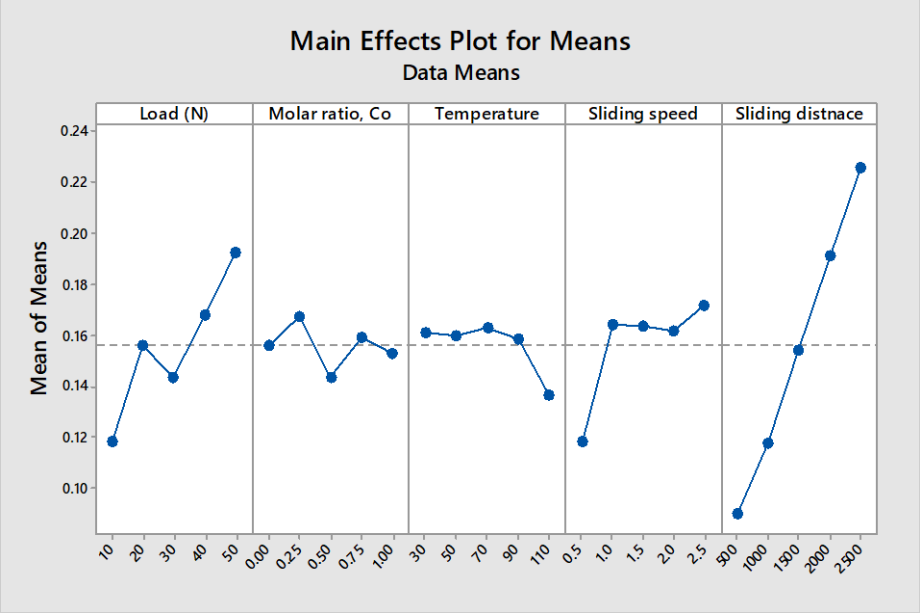

Figure 6.11. Influence of control parameters on means for $AlCr_{1.5}CuFeNi_2Co_x$ alloys

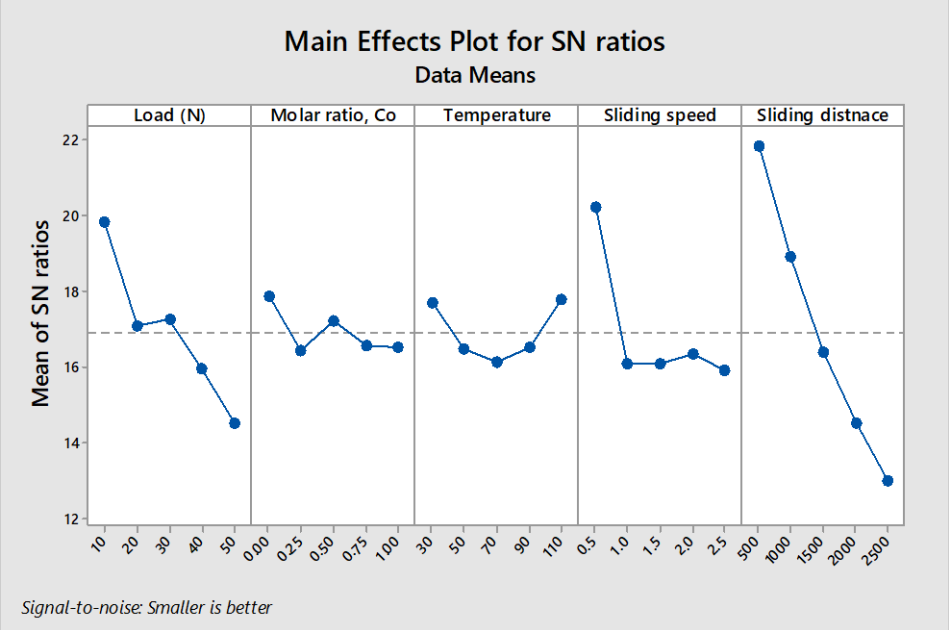

Figure 6.12. Influence of control parameters on average S/N ratio for $AlCr_{1.5}CuFeNi_2Co_x$ alloys

The R-Sq and the R-Sq (adj) value for the set of experiments are 99.3% and 95.9%, which are within the prescribed range proposed for the design of experiment. The R-square and adjusted R-square values are near to unity which indicates the predicted model is significant. The P value of the input parameters molar ratio and temperature is greater than 0.05 and hence are

not significant. It is found that the percentage contribution of the sliding distance is highest as compared to the other input parameters.

The main effect response plot for means and S/N ratio are shown in Figure 6.11 and 6.12. As per the Taguchi design of experiment, the S/N ratio should have higher value and the corresponding mean value for the same factor and level should be low. It is observed from Table 6.9 that the most important input parameter affecting the specific wear rate is sliding distance followed by normal load, sliding speed, temperature and molar ratio. The molar ratio of Co being the least influencing input parameter. The highest value of the S/N ratio for the selected input parameter provides the optimal value as presented in Table 6.10. For the optimal value condition, it is always essential to reduce the noise factors which are uncontrollable. Hence, the optimal level of parameter is selected at higher value of S/N ratio.

Table 6.9. Mean response table for S/N ratio ($AlCr_{1.5}CuFeNi_2Co_x$ alloys)

Level	Input parameter				
	Load (N)	Molar ratio, Co	Temperature (^oC)	Sliding speed (m/s)	Sliding distance (m)
1	19.86	17.90	17.72	20.23	21.84
2	17.11	16.46	16.51	16.12	18.94
3	17.26	17.24	16.13	16.12	16.40
4	15.96	16.56	16.54	16.34	14.54
5	14.52	16.55	17.82	15.91	12.99
Delta	5.34	1.44	1.69	4.31	8.85
Rank	2	5	4	3	1

Table 6.10. The optimal setting significant input parameters

Input parameter	Optimal level	Optimal parameter value
A: Normal load(N)	A1	19.86
D: Sliding speed(m/s)	D1	20.23
E: Sliding Distance (m)	E1	21.84

To verify the results the confirmation test was conducted at the optimum levels of parameters such as A_1, D_1, E_1. The predicted mean response specific wear rate in terms of S/N ratio can be expressed as,

$\mu = T + (A_1 - T) + (D_1 - T) + (E_1 - T)$

where T = grand average of S/N ratio = 16.9424

$\mu = 28.0452$

Confidence Interval (CI) = $\sqrt{F_\alpha(n_1, n_2) V_e \left[\frac{1}{N_e} + \frac{1}{R}\right]}$

Where $F_\alpha(1, n_2)$ = computed from F-table at $n_1 = 1$ and n_2 = error DOF at 95 % confidence level ($n_2 = 4$)

$F(1, 4) = 7.71$

V_e = variance of error =0.7050 (from ANOVA Table 6.8)

N_e = effective number of replications

$$= \frac{\text{Number of trials}}{1 + \text{DoF of all factors used in the estimate}} = \frac{25}{(1 + 20)} = 1.190$$

Therefore, the confidence interval CI = ± 2.525

At 95% confidence level, the predicted S/N ratio of the specific wear rate will be in the range of

= [μ - CI]< μ <[μ + CI]

= [28.0452 – 2.525] <μ< [28.0452 + 2.525]

= 25.5202<μ<30.5702

Table 6.11. Comparison of predicted and confirmation experiment

	Predicted	**Experimental**
Level	$A_1D_1E_1$	$A_1D_1E_1$
Specific wear	0.039	0.032
S/N Ratio	28.0452	29.897

Three confirmation tests were conducted at the optimum levels and average is shown in the table 6.11. The corresponding S/N ratio is calculated and it is found to be within the range at the 95% confidence interval.

6.3.5 Microstructural examination of worn surface of $AlCr_{1.5}CuFeNi_2Co_x$ alloys

The worn surfaces of the $AlCr_{1.5}CuFeNi_2Co_x$ alloys are observed under SEM after the experiment. The wear mechanisms for the $AlCr_{1.5}CuFeNi_2Co_x$ alloys are identified based on the

careful study of surface morphology. The surface morphology of the $AlCr_{1.5}CuFeNi_2Co_x$ alloys considering one factor at a time by varying the load from 10 N to 50 N while maintaining the other factor such as sliding velocity and temperature constant is shown in Figure 6.13.

It is observed from the Figure 6.13(a) that the wear in the form of craters and cracks are evident on the surface due to the brittle nature of Co_0 alloy. The hardness of the alloy is also one of the reasons for the wear mechanism exhibited by the alloy. It is already established from the XRD graph that the phase change take place from BCC to FCC with the addition of Co, hence the alloys shows brittle to semi ductile nature with the addition Co.

Figure 6.13 (b) represents the morphology of the worn surface for $Co_{0.25}$ alloy at 50 N load. Delamination of the upper layer of the surface is observed along with the small debris from the surface. The phenomenon of delamination becomes from prominent at $Co_{0.5}$ alloy as shown in thee Figure 6.13 (c). This is attributed to the reduction of hardness value with the increase in Co content. As the material becomes more ductile with addition of Co, the small cracks are observed in Figure 6.13 (d). It is also accompanied with the oxide agglomeration due to the heat generation between the contacting surfaces.

Figure 6.6 (e) represents the SEM image of Co_1 alloy at 50 N load. The Co_1 alloy has less hardness as compared to the remaining alloys. Due to this, the large displaced material can be easily observed in the image. The counter body is much hardened as compared to the Co_1 alloy and hence the large extruded lips are also found evident on the surface.

The surface morphology of the $AlCr_{1.5}CuFeNi_2Co_x$ alloys depicts large amount of mass loss with the increase in the Co content, which is also evident from the specific wear rate of the alloys. Thus it can be concluded that the wear mechanism transform from brittle material to semi ductile material from Co_0 to Co_1.

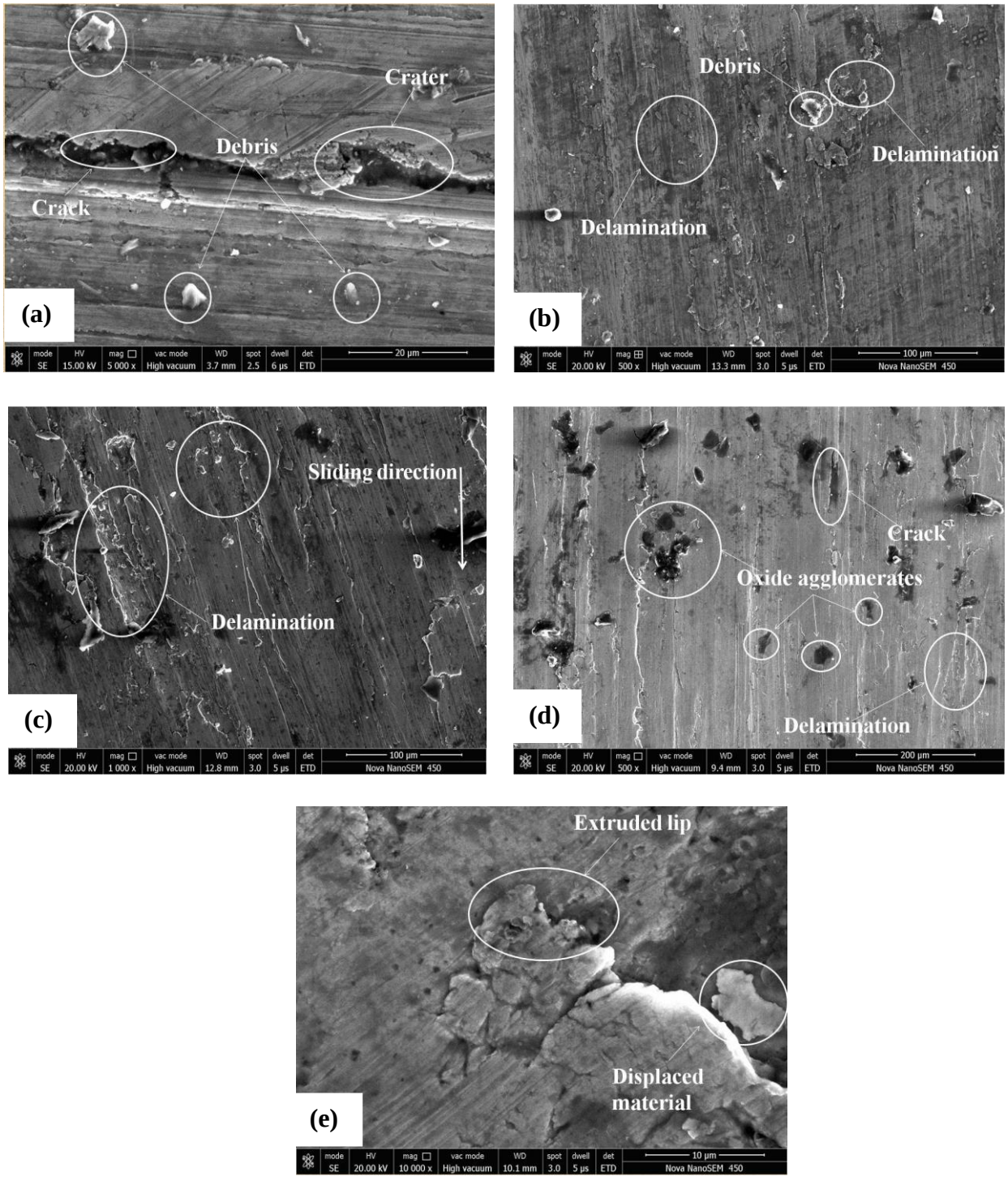

Figure 6.13. SEM images of $AlCr_{1.5}CuFeNi_2Co_x$ alloys (a) $AlCr_{1.5}CuFeNi_2Co_0$ (b) $AlCr_{1.5}CuFeNi_2Co_{0.25}$ (c) $AlCr_{1.5}CuFeNi_2Co_{0.5}$ (d) $AlCr_{1.5}CuFeNi_2Co_{0.75}$ (e) $AlCr_{1.5}CuFeNi_2Co_1$

6.4 Corrosion behaviour of $AlCr_{1.5}CuFeNi_2Co_x$ high- entropy alloys

Polarization curves of the $AlCr_{1.5}CuFeNi_2Cox$ high-entropy alloys are shown in Figure 6.14 and their electrochemical parameters are listed in Table 6.12.

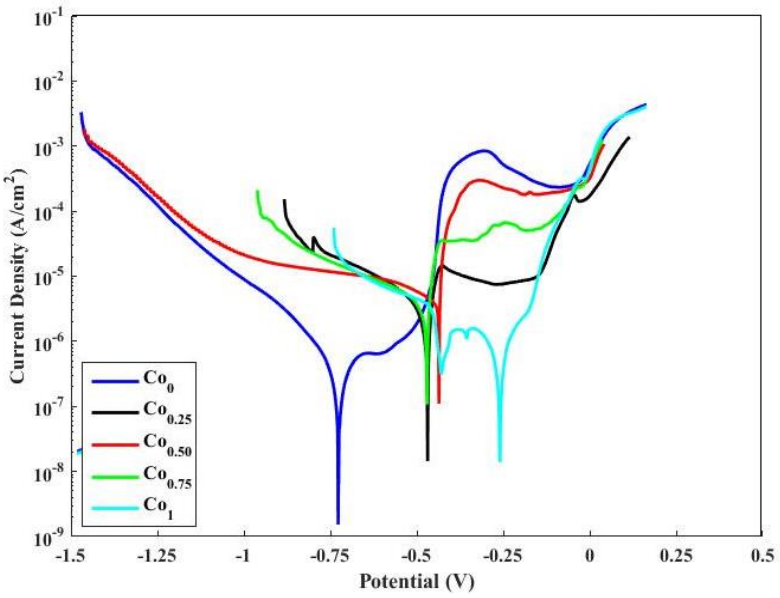

Figure 6.14. Potentiodynamic-polarization curves of $AlCr_{1.5}CuFeNi_2Co_x$ HEAs in 3.5 wt. % NaCl at ambient temperature.

Table 6.12. Electrochemical parameters of Co_0, $Co_{0.25}$, $Co_{0.5}$, $Co_{0.75}$ and Co_1 alloys from potentiodynamic- polarization curve.

Alloy	**E_{corr}(V)**	**I_{corr}(mA/cm^2)**	**Corrosion rate (mpy)**
Co_0	-0.728	0.089	6.676
$Co_{0.25}$	-0.44	0.071	6.520
$Co_{0.5}$	-0.436	0.056	6.131
$Co_{0.75}$	-0.354	0.045	5.987
Co_1	-0.259	0.033	5.745

The results indicate that the corrosion resistance of the HEAs is improving with the addition of Co content. The polarization curves shows that the Co_1 and Co_0 alloy shows the minimum and maximum corrosion rate as compared to the other alloys. The corrosion rate of

Co_0, $Co_{0.25}$, $Co_{0.5}$, $Co_{0.75}$ and Co_1 alloys are found to be 6.67, 6.52, 6.13, 5.98 and 5.74 mpy respectively. The HEAs with larger corrosion potential (E_{corr}) and smaller corrosion current density (i_{corr}) have better corrosion resistance. The improvement in the corrosion resistance of the HEAs is due to the proper distribution of the Ni and Cr in the solid solution due the addition of the Co content.

6.5 Sliding wear behaviour of $AlCr_{1.5}CuFeNi_2Ti_x$ high- entropy alloys

The dry sliding wear behaviour of $AlCr_{1.5}CuFeNi_2Ti_x$ alloys is determined using the pin-on disc (POD) tribometer. The detail working of POD tribometer is described in the section 3.10. The sliding wear tests are performed considering one factor at a time. The various factors considered in this study are: sliding speed, applied load and temperature. The influence of these factors on the specific wear rate of $AlCr_{1.5}CuFeNi_2Ti_x$ alloys is described in the subsequent sections.

6.5.1 Influence of applied load on specific wear rate of $AlCr_{1.5}CuFeNi_2Ti_x$ alloys

Figure 6.15 shows the effect of applied load on specific wear rate of $AlCr_{1.5}CuFeNi_2Co_x$ alloys keeping the other factors such as sliding velocity (0.5 m/s) and temperature (30 °C) constant. It is found that the addition of Ti improves the wear resistance of $AlCr_{1.5}CuFeNi_2$ alloys with the increase in the applied load. The specific wear rate of $AlCr_{1.5}CuFeNi_2Ti_x$ alloys continuously decreases with the increase in the Ti content. Similarly, increase in the value of load from 10 N to 50 N also depicts continuous decrease in the specific wear rate of the alloys.

The specific wear rate of Ti_0, $Ti_{0.25}$, $Ti_{0.5}$, $Ti_{0.75}$ and Ti_1 alloys is found to be 6.64, 5.26, 4.35, 3.56 and 3.07 x 10^{-4} mm^3/N-m respectively at maximum load of 50 N. The lowest value of specific wear rate is found to be for Ti_1 at 50 N and highest value is found to be for Ti_0 at 10 N. There is a huge difference in the specific wear rate in terms of the percentage (80.7%). The tremendous decrease in the specific wear rate of the Ti_x alloys is due to the formation of hard BCC phase and the intermetallic compound. As the Ti content increases in $AlCr_{1.5}CuFeNi_2$ alloy, the hardness value also increases to the large extent and it is also well known fact that the specific wear rate of any material is inversely proportional to the hardness of the alloy. Initially the Ti_0 alloy consists of the FCC+BCC phase which gradually changes to laves phase in addition to FCC+BCC phase. Few unknown phases are also present in the Ti_x alloys, which further increases the hardness of alloys. The formation of intermetallic compounds in the alloy with the increase in Ti content is one of the reasons for the decrease in the specific wear rate. It is

therefore concluded that the addition of Ti improves the wear resistance of the alloys with the increase in the applied load from 10 N to 50 N.

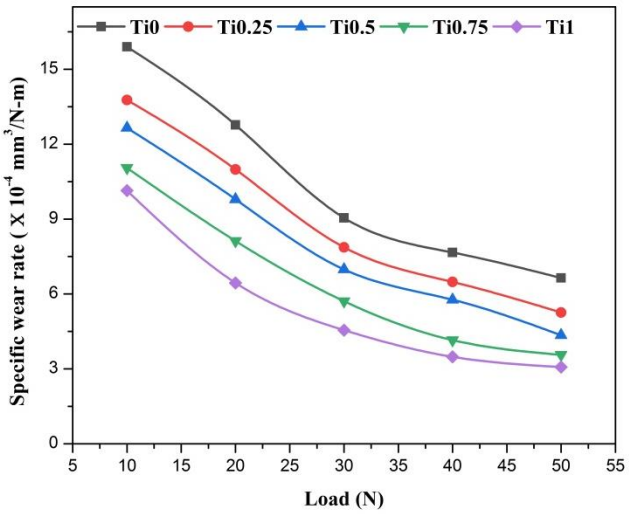

Figure 6.15. Effect of applied load on specific wear rate of $AlCr_{1.5}CuFeNi_2Ti_x$ alloys

6.5.2 Influence of sliding velocity on specific wear rate of $AlCr_{1.5}CuFeNi_2Ti_x$ alloys

Figure 6.16 shows the effect of sliding velocity on specific wear rate of $AlCr_{1.5}CuFeNi_2Mn_x$ alloys while maintaining the other factors such as applied load (10 N) and temperature (30 °C) constant. It is found that the addition of Ti improves the wear resistance of $AlCr_{1.5}CuFeNi_2$ alloys with the increase in sliding velocity.

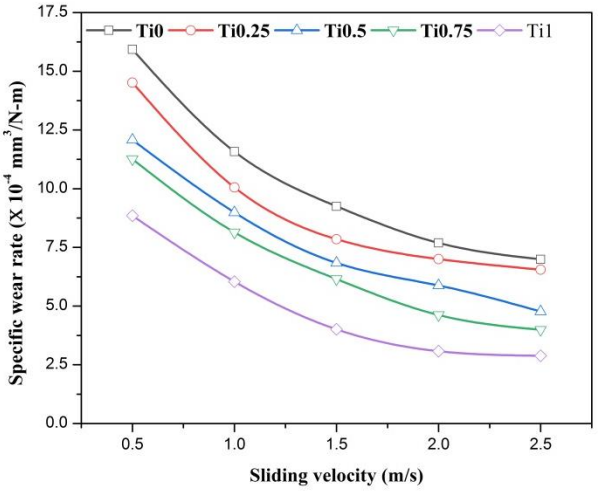

Figure 6.16. Effect of sliding velocity on specific wear rate of $AlCr_{1.5}CuFeNi_2Ti_x$ alloys

The specific wear rate of $AlCr_{1.5}CuFeNi_2TI_x$ alloys continuously decreases with the increase in the Ti content. Similarly, increase in the value of sliding velocity from 0.5 m/s to 2.5 m/s also

depicts continuous decrease in the specific wear rate of the alloys. The lowest specific wear rate of Ti_0, $Ti_{0.25}$, $Ti_{0.5}$, $Ti_{0.75}$ and Ti_1 alloys are determined as 6.99, 6.55, 4.77, 3.99 and 2.88 x 10^{-4} mm^3/N-m respectively, at 2.5 m/s sliding velocity. The decrease in the specific wear rate of alloys is due to the increase in the hardness value with the addition of Ti content. The reason for the increase in the hardness value of the alloys is the formation of BCC phase along with the intermetallic compounds with addition of Ti. It is therefore concluded that the addition of Ti improves the wear resistance of the alloys with the increase in the sliding velocity.

6.5.3 Influence of temperature on specific wear rate of $AlCr_{1.5}CuFeNi_2Ti_x$ alloys

Figure 6.17 shows the effect of temperature on specific wear rate of $AlCr_{1.5}CuFeNi_2Ti_x$ alloys while maintaining the other factors such as applied load (10 N) and sliding velocity (0.5 m/s) constant. It is found that the addition of Ti improves the wear resistance of $AlCr_{1.5}CuFeNi_2$ alloys with the increase in temperature up to 110 ºC. The specific wear rate of $AlCr_{1.5}CuFeNi_2Ti_x$ alloys decreases with the increase in the Ti content up to 110 ºC.

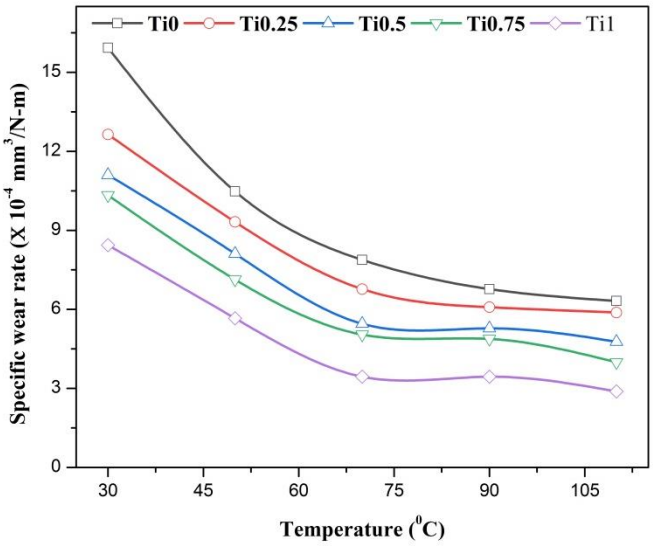

Figure 6.17. Effect of temperature on specific wear rate of $AlCr_{1.5}CuFeNi_2Ti_x$ alloys

The value of specific wear rate is lowest at 110 ºC for all the alloys and their corresponding values for Ti_0, $Ti_{0.25}$, $Ti_{0.5}$, $Ti_{0.75}$ and Ti_1 are found to be 6.32, 5.88, 4.77, 3.99 and 2.88 x 10^{-4} mm^3/N-m, respectively. The reason for the decrease in the specific wear rate of the alloys is the increase in the hardness of the alloys with addition of Ti in the alloy. The increase in temperature of the alloys has least effect on the specific wear rate of the alloys. It is therefore

concluded that the addition of Ti improves the wear resistance of the alloys with the increase in the temperature up to 110 ºC.

6.5.4 Taguchi design of experiment and Analysis of variance (ANOVA) for $AlCr_{1.5}CuFeNi_2Ti_x$ alloys

It is very tedious work to determine the mass loss of material for large number of factors and the levels. Taguchi proposed a design of experiment for various combinations of factor and levels and reduced the large number combination of experiments to a small set of experiments using the concept of orthogonal arrays (OA's). In the present study five factors each at five levels were considered for conducting the experiments as listed in Table 3.11.

Table 6.13. Design of experiment using L_{25} orthogonal array for $AlCr_{1.5}CuFeNi_2Ti_x$ alloys

S.No.	Load (N)	Molar ratio, Ti	Temperature (^oC)	Sliding speed (m/s)	Sliding distance (m)	Specific wear rate 10^{-3} mm^3/N-m	S/N ratio
1	10	0.00	30	0.5	500	0.031	30.1728
2	10	0.25	50	1.0	1000	0.071	22.9748
3	10	0.50	70	1.5	1500	0.101	19.9136
4	10	0.75	90	2.0	2000	0.135	17.3933
5	10	1.00	110	2.5	2500	0.175	15.1392
6	20	0.00	50	1.5	2000	0.203	13.8501
7	20	0.25	70	2.0	2500	0.249	12.0760
8	20	0.50	90	2.5	500	0.071	22.9748
9	20	0.75	110	0.5	1000	0.065	23.7417
10	20	1.00	30	1.0	1500	0.151	16.4205
11	30	0.00	70	2.5	1000	0.123	18.2019
12	30	0.25	90	0.5	1500	0.108	19.3315
13	30	0.50	110	1.0	2000	0.155	16.1934
14	30	0.75	30	1.5	2500	0.208	13.6387
15	30	1.00	50	2.0	500	0.07	23.0980

16	40	0.00	90	1.0	2500	0.256	11.8352
17	40	0.25	110	1.5	500	0.086	21.3100
18	40	0.50	30	2.0	1000	0.116	18.7108
19	40	0.75	50	2.5	1500	0.189	14.4708
20	40	1.00	70	0.5	2000	0.152	16.3631
21	50	0.00	110	2.0	1500	0.169	15.4423
22	50	0.25	30	2.5	2000	0.258	11.7676
23	50	0.50	50	0.5	2500	0.199	14.0229
24	50	0.75	70	1.0	500	0.133	17.5230
25	50	1.00	90	1.5	1000	0.164	15.7031

Table 6.14. Results of ANOVA for $AlCr_{1.5}CuFeNi_2Ti_x$ alloys

Source	Degree of Freedom (f)	Sum of squares (SS)	Variance (Mean square), V	Variance Ratio (F)	P	Percentage contribution (%)
A: Normal load(N)	4	105.453	26.3633	18.36	0.008	22.12
B: Ti (molar ratio)	4	3.845	0.9612	0.67	0.647	0.80
C: Temperature (^oC)	4	7.420	1.8550	1.29	0.405	1.55
D: Sliding speed(m/s)	4	59.359	14.8397	10.34	0.022	12.45
E: Sliding Distance (m)	4	294.850	73.7125	51.34	0.001	61.85
Residual Error	4	5.743	1.4357			1.23
Total	24	476.670				

The L_{25} (5^6) orthogonal array was used to determine the optimal control parameter and the best level for each factor. Each experiment is repeated thrice and the average value of specific wear rate is calculated and tabulated in the Table 6.13. The desired response in any of the orthogonal array is indicated by a logarithmic function via the S/N ratio. Table 6.14 presents the results of ANOVA for $AlCr_{1.5}CuFeNi_2TI_x$ alloys. The objective function in the optimization technique is “smaller is better”.

The R-square and adjusted R-square values are near to unity which indicates the predicted model is significant. The R-Sq and the R-Sq(adj) value for the set of experiments are 98.8% and 92.8%, which validates the design of experiment. The P value of the input parameter molar ratio and temperature (°C) is greater than 0.05 and hence implies that the input parameters are not significant. It is also observed that the percentage contribution of the sliding distance is highest as compared to the other input parameters. It is observed from Table 6.15 that the most important input parameter affecting the specific wear rate is sliding distance followed by load, sliding velocity, temperature and molar ratio. The effect of the increase in the molar ratio has least influence on the specific wear rate.

Table 6.15. Mean response table for S/N ratio ($AlCr_{1.5}CuFeNi_2Ti_x$ alloys)

Level	**Input parameter**				
	Load (N)	**Molar ratio, Ti**	**Temperature (^oC)**	**Sliding velocity (m/s)**	**Sliding distance (m)**
1	21.12	17.90	18.14	20.73	23.02
2	17.81	17.49	17.68	16.99	19.87
3	18.09	18.36	16.82	16.88	17.12
4	16.54	17.35	17.45	17.34	15.11
5	14.89	17.34	18.37	16.51	13.34
Delta	6.23	1.02	1.55	4.22	9.67
Rank	2	5	4	3	1

The main effect response plot for means and S/N ratio are shown in Figure 6.18 and 6.19. As per the Taguchi design of experiment, the S/N ratio should have higher value and the corresponding mean value for the same factor and level should be low. As observed from the Figure 6.18 and 6.19, the optimal value of the S/N ratio for each factor at specific level that will provide the optimal response which is presented in Table 6.16. For the optimal value condition, it is always essential to reduce the noise factors which are uncontrollable. Hence, the optimal level of parameter is selected at higher value of S/N ratio.

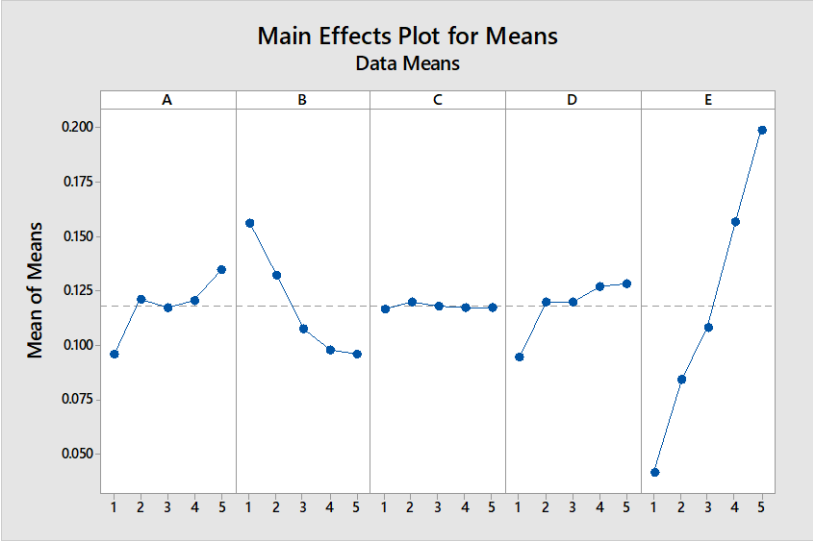

Figure 6.18. Influence of control parameters on means for $AlCr_{1.5}CuFeNi_2Ti_x$ alloys

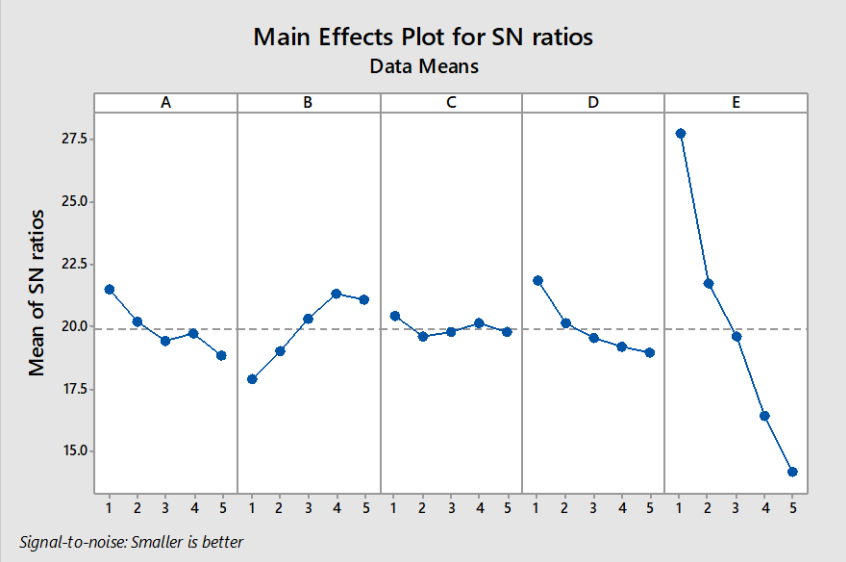

Figure 6.19. Influence of control parameters on average S/N ratio for $AlCr_{1.5}CuFeNi_2Ti_x$ alloys

Table 6.16. The optimal setting significant input parameters

Input parameter	Optimal level	Optimal parameter value
A: Normal load(N)	A1	21.12
D: Sliding speed(m/s)	D1	20.73
E: Sliding Distance (m)	E1	23.02

To verify the results the confirmation test was conducted at the optimum levels of parameters such as A_1, D_1, E_1. The predicted mean response specific wear rate in terms of S/N ratio can be expressed as,

$\mu = T + (A_1 - T) + (D_1 - T) + (E_1 - T)$

where T = grand average of S/N ratio = 17.6907

$\mu = 29.4886$

Confidence Interval (CI) = $\sqrt{F_\alpha(n_1, n_2) V_e \left[\frac{1}{N_e} + \frac{1}{R}\right]}$

Where $F_\alpha(1, n_2)$ = computed from F-table at $n_1 = 1$ and n_2 = error DOF at 95 % confidence level ($n_2 = 4$) , F(1, 4) = 7.71

V_e = variance of error = 1.4357 (from ANOVA Table 6.14)

N_e = effective number of replications

$$= \frac{\text{Number of trials}}{1 + \text{DoF of all factors used in the estimate}} = \frac{25}{(1 + 20)} = 1.190$$

Therefore, the confidence interval CI = ± 3.604

At 95% confidence level, the predicted S/N ratio of the specific wear rate will be in the range of

$= [\mu - CI] < \mu < [\mu + CI]$

$= [29.4886 - 3.604] < \mu < [29.4886 + 3.604]$

$= 25.5202 < \mu < 30.5702$

Table 6.17: Comparison of predicted and confirmation experiment

	Predicted	**Experimental**
Level	$A_1D_1E_1$	$A_1D_1E_1$
Specific wear	0.033	0.035
S/N Ratio	29.4886	29.1186

Three confirmation tests were conducted at the optimum levels and average was shown in the above Table 6.17. The corresponding S/N ratio was calculated and it is within the range at the 95% confidence interval.

6.5.5 Microstructural examination of worn surface of $AlCr_{1.5}CuFeNi_2Ti_x$ alloys

The worn surfaces of the $AlCr_{1.5}CuFeNi_2Ti_x$ alloys are observed under SEM after the experiment. The hardness of the Ti_x alloys increases with the addition of Ti in the $AlCr_{1.5}CuFeNi_2$ alloy. When the two hard body slides against each other, there exists different types of the wear mechanism. The surface morphology of the $AlCr_{1.5}CuFeNi_2Ti_x$ alloys considering one factor at a time at a load of 50 N while maintaining the other factor such as sliding velocity and temperature constant is shown in Figure 6.20.

It is observed from the Figure 6.20 (a) that the maximum wear is takes place for Ti_0 alloy because of the ductile nature of the alloy surface. The Ti_0 alloy consists of the combined FCC and BCC phase, which governs the wear mechanism taking place in the alloy. It is observed from the figure that there exist large craters and few small debris particles. The craters are formed on the surface due to the hard counter surface sliding against the semi ductile alloy materials. During the sliding action, small amount of material get detached from the surface in the form of debris. Figure 6.20 (b) shows the worn surface of $Ti_{0.25}$ alloy. Delamination and oxide agglomerate are found at the surface of the alloy. As the Ti content increases in the $AlCr_{1.5}CuFeNi_2$ alloy, the hardness of the alloy increases to the large extent. This is the main reason for the change in the wear mechanism of the different types of the alloys. The Figure 6.20 (c) depicts the adhesion of the particle of the parent material due to the generation of heat during the sliding of two hard surfaces. The increase in the heat at the junction of two surface is evident from the oxide aggomerates.

Figure 6.20 (d) shows the worn surface of $Ti_{0.75}$ alloy, which clearly indicates wedge formation along with the creation of the grooves. The small sharp edge debris generated during the rubbing action of the two surfaces causes the formation of the groove due to the three body abrasion. The Figure 6.20 (e) represents the image of Ti_1 at 50 N load. It is observed that due to the sliding action between the alloy and the hardened steel, distinct groves are formed on the surface. This is due to the sharp edge debris particle sliding against the alloy surface.

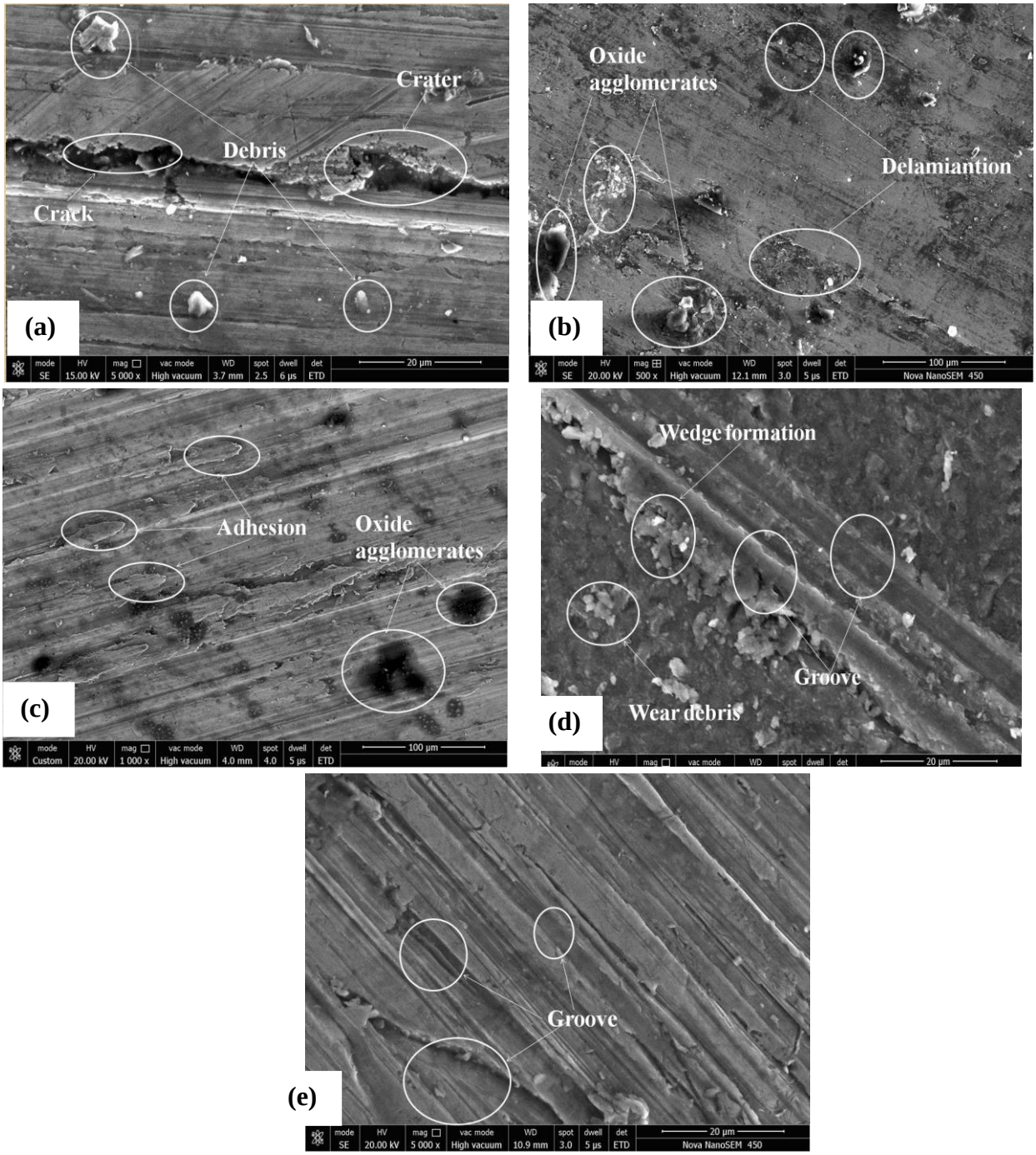

Figure 6.20. SEM images of $AlCr_{1.5}CuFeNi_2Ti_x$ alloys (a) $AlCr_{1.5}CuFeNi_2Ti_0$ (b) $AlCr_{1.5}CuFeNi_2Ti_{0.25}$ (c) $AlCr_{1.5}CuFeNi_2Ti_{0.5}$ (d) $AlCr_{1.5}CuFeNi_2Ti_{0.75}$ (e) $AlCr_{1.5}CuFeNi_2Ti_1$

6.6 Corrosion behaviour of $AlCr_{1.5}CuFeNi_2Ti_x$ high- entropy alloys

Polarization curves of the $AlCr_{1.5}CuFeNi_2Ti_x$ high-entropy alloys are shown in Figure 6.21 and their electrochemical parameters are listed in Table 6.18. The polarization curves of Ti_0, $Ti_{0.25}$, $Ti_{0.5}$, $Ti_{0.75}$ and Ti almost overlap each other signifying similar behaviour with respect to the

corrosion resistance. The elements present in the base alloy such as Cr already provide the corrosion resistant and hence addition of Ti further improves the corrosion properties of the HEAs.

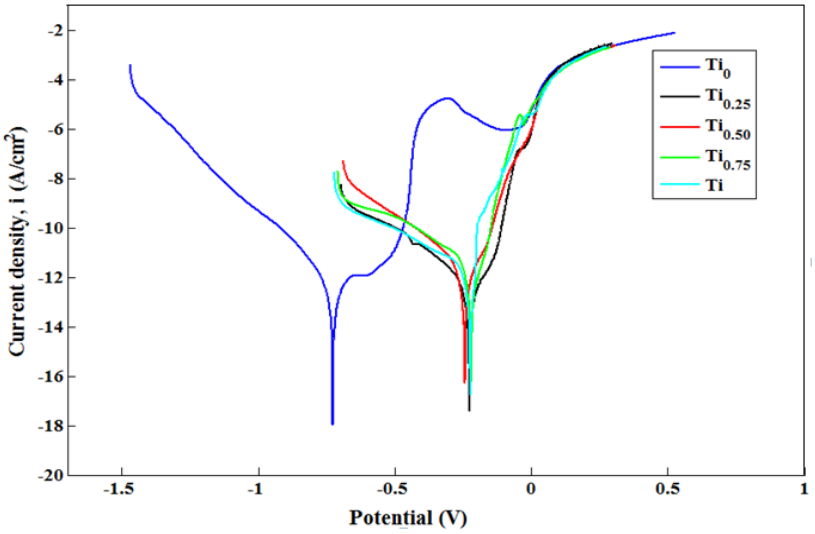

Figure 6.21. Potentiodynamic-polarization curves of $AlCr_{1.5}CuFeNi_2Ti_x$ HEAs in 3.5 wt. % NaCl at ambient temperature.

Conversely, Al present in the alloy depreciates the corrosion resistance by forming the unstable layer at the surface leaving it exposed to the surrounding environment. The elements (Cr and Ti) form a protective layer at the external surface of the alloys thus enhancing the corrosion resistance. Since the developed HEAs consists of duplex phase i.e. BCC+FCC, there is an improvement in the corrosion property of the alloys on addition of Ti. It can be found from the Table 6.18 that the corrosion resistance continuously increases on addition of Ti content till 0.75 molar ratio and there is a slight decrease in the value of corrosion resistance on further increasing the Ti content. This may be due to the formation of susceptible BCC phase in the alloy as compared to the FCC phase. The minimum and maximum value of corrosion rate is found to be 0.068 and 0.300 mmpy for Ti_0 and $Ti_{0.75}$ respectively. As compared to the previous studies the $AlCr_{1.5}CuFeNi_2Ti_x$ shows a remarkable enhancement in the corrosion resistance properties.

Table 6.18. Electrochemical parameters of $AlCr_{1.5}CuFeNi_2Ti_x$ derived from the potentiodynamic polarization curves by linear fitting

Alloy	E_{corr}(mV)	I_{corr}(μA/cm^2)	Corrosion rate (mmpy)
Ti_0	-231.9	7.974	0.068
$Ti_{0.25}$	-227	14.7	0.111
$Ti_{0.5}$	-243.6	28.14	0.214
$Ti_{0.75}$	-220.6	39.13	0.300
Ti_1	-372	33.64	0.259

6.7 Multi Criteria Decision Making for ranking of alternatives

Multi Criteria Decision Making (MCDM), a statistical analytical tool helps in ease the decision making by solving the conflicting criteria (cost or price, quality and etc.) of the day to day life. The technique for order of preference by similarity to ideal solution (TOPSIS) is a member of MCDM technique, and an ideal alternative to find the best possible solution with minimum of deviation (i.e. positive ideal solution) and to deviate strongly from worst alternative (i.e. negative ideal solution). TOPSIS is, one such a fast technique; with numerical output on the basis of rank for every variable with the asymptotic combination of similarity between the variables.

A decision matrix; by performing the tabulation of the alternatives considered, whose output decides the contribution of alternatives such as performance defining attribute (PDA). Primarily, a decision matrix is framed with set of values, and the units of the values are eliminated to normalize the matrix in order to assign weight criteria for every alternative. Upon the outcome of the weight criteria, i.e. benefit; helps in finding the positive and negative ideal solutions (maximum and minimum values may be assigned as positive and negative ideal solutions respectively, where strength is the criteria of the benefit. Whereas, a case like wear rate; cost is the criteria of benefit and therefore, minimum value is considered to be positive ideal solution and maximum value to be negative ideal solution).

The values from positive and negative ideal solution are measured for every alternative to ensure the best possible alternative. In the present work, twelve PDAs were considered as shown in Table 6.19 with its subsequent experimental data. The descriptions of the PDAs are given in Table 3.13. The details of the normalized values without the influence of units are tabulated in

Table 6.20 and 6.21, respectively. The weight criteria of the alternatives and the normalized weighted matrix are presented in Tables 6.22 and 6.23 respectively and in Table 6.24 the closeness index and the rank assigned for the alternatives are presented. Arranging the alternatives with respect to its rank and the closeness index in descending order is the final step and thus, the optimum alternative is selected on the basis of the rank.

Table 6.19. Performance Defining Attribute (PDA)

Performance defining Attribute (PDA)	**Description of the individual PDA**	**Performance implications of different PDA**
P-1	Density	Lower is better
P-2	Hardness	Higher is better
P-3	Compressive strength	Higher is better
P-4	Flexural strength	Higher is better
P-5	Young's modulus	Higher is better
P-6	Thermal conductivity	Higher is better
P-7	Corrosion rate	Lower is better
P-8	Specific wear rate	Lower is better
P-9	Specific wear rate	Lower is better
P-10	Specific wear rate	Lower is better
P-11	Specific wear rate	Lower is better
P-12	Specific wear rate	Lower is better

Table 6.20. Experimental data of PDAs

PDA → / Alloy ↓	P-1	P-2	P-3	P-4	P-5	P-6	P-7	P-8	P-9	P-10	P-11	P-12
Mn_0	7.11	471	1552	274	237.9	13.72	6.676	15.9	12.1	9.37	8.2	7.4
$Mn_{0.25}$	7.16	511	1589	280	241.6	12.22	6.41	12	7.824	4.9	4.1	3.12
$Mn_{0.5}$	7.2	537	1610	293	248.84	11.37	6.129	8.925	5.38	4.157	2.42	1.663
$Mn_{0.75}$	7.22	574	1643	317	257.16	10.04	5.983	6.142	4.85	2.856	1.56	0.84
Mn_1	7.23	580	1685	338	259.87	9.84	5.461	4.8	3.2	1.0757	1.14	0.65
$Co_{0.25}$	7.35	406	1753	298	227.22	11.6464	6.52	16.67	19.48	23.65	26.95	27.99
$Co_{0.50}$	7.39	376	1734	328	225.4	9.9545	6.131	17.84	21.33	24.36	27.85	29.12
$Co_{0.75}$	7.41	367	1719	358	214.07	9.125	5.987	18.25	23.07	26.47	29.63	30.55
Co_1	7.44	364	1701	365	201.58	8.754	5.745	19.08	24.44	28.33	31.55	32.41
$Ti_{0.25}$	6.81	556	1589	221	250.28	12.99254	6.625	12.77	9.048	7.66	6.64	12.77
$Ti_{0.50}$	6.7	600	1624	211	261.05	12.623	6.05	10.99	7.87	6.48	5.26	10.99
$Ti_{0.75}$	6.65	636	1662	207	274.64	11.952	5.546	9.79	6.98	5.77	4.35	9.79
Ti_1	6.57	643	1693	193	301.07	11.25	5.099	8.12	5.71	4.15	3.56	8.12

Table 6.21. Normalized decision matrix

PDA → / Alloy ↓	P-1	P-2	P-3	P-4	P-5	P-6	P-7	P-8	P-9	P-10	P-11	P-12
Mn_0	0.0771	0.0711	0.0720	0.0744	0.0743	0.0943	0.0852	0.0986	0.0800	0.0628	0.0535	0.0422
$Mn_{0.25}$	0.0776	0.0772	0.0737	0.0760	0.0755	0.0840	0.0818	0.0744	0.0517	0.0328	0.0268	0.0178
$Mn_{0.5}$	0.0781	0.0811	0.0747	0.0796	0.0777	0.0782	0.0782	0.0553	0.0356	0.0279	0.0158	0.0095
$Mn_{0.75}$	0.0783	0.0867	0.0762	0.0861	0.0803	0.0690	0.0764	0.0381	0.0321	0.0191	0.0102	0.0048
Mn_1	0.0784	0.0876	0.0782	0.0918	0.0812	0.0676	0.0697	0.0298	0.0212	0.0072	0.0074	0.0037
$Co_{0.25}$	0.0797	0.0613	0.0813	0.0809	0.0710	0.0801	0.0832	0.1034	0.1288	0.1585	0.1759	0.1596
$Co_{0.50}$	0.0801	0.0568	0.0804	0.0891	0.0704	0.0684	0.0782	0.1106	0.1410	0.1632	0.1818	0.1660
$Co_{0.75}$	0.0803	0.0554	0.0798	0.0972	0.0669	0.0627	0.0764	0.1132	0.1525	0.1774	0.1934	0.1742
Co_1	0.0807	0.0550	0.0789	0.0991	0.0630	0.0602	0.0733	0.1183	0.1616	0.1898	0.2059	0.1848
$Ti_{0.25}$	0.0738	0.0840	0.0737	0.0600	0.0782	0.0893	0.0845	0.0792	0.0598	0.0513	0.0433	0.0728
$Ti_{0.50}$	0.0726	0.0906	0.0753	0.0573	0.0816	0.0868	0.0772	0.0681	0.0520	0.0434	0.0343	0.0627
$Ti_{0.75}$	0.0721	0.0961	0.0771	0.0562	0.0858	0.0822	0.0708	0.0607	0.0461	0.0387	0.0284	0.0558
Ti_1	0.0712	0.0971	0.0785	0.0524	0.0941	0.0773	0.0651	0.0503	0.0377	0.0278	0.0232	0.0463

Table 6.22. Evaluation of criteria weights by entropy method

PDA	**Entropy E_j**	**Degree of Diversity Ψj**	**Weight, ω_j**
P-1	0.9997	0.0003	0.0006
P-2	0.9925	0.0075	0.0126
P-3	0.9997	0.0003	0.0004
P-4	0.9920	0.0080	0.0135
P-5	0.9980	0.0020	0.0034
P-6	0.9966	0.0034	0.0058
P-7	0.9989	0.0011	0.0019
P-8	0.9718	0.0282	0.0475
P-9	0.9260	0.0740	0.1248
P-10	0.8659	0.1341	0.2259
P-11	0.8193	0.1807	0.3045
P-12	0.8463	0.1537	0.2590

Table 6.23. Weighted normalized decision matrix

PDA → / Alloy ↓	P-1	P-2	P-3	P-4	P-5	P-6	P-7	P-8	P-9	P-10	P-11	P-12
Mn_0	0.0002	0.0032	0.0001	0.0036	0.0009	0.0020	0.0006	0.0158	0.0304	0.0390	0.0418	0.0298
$Mn_{0.25}$	0.0002	0.0034	0.0001	0.0036	0.0009	0.0017	0.0006	0.0120	0.0197	0.0204	0.0209	0.0126
$Mn_{0.5}$	0.0002	0.0036	0.0001	0.0038	0.0010	0.0016	0.0005	0.0089	0.0135	0.0173	0.0123	0.0067
$Mn_{0.75}$	0.0002	0.0039	0.0001	0.0041	0.0010	0.0014	0.0005	0.0061	0.0122	0.0119	0.0079	0.0034
Mn_1	0.0002	0.0039	0.0001	0.0044	0.0010	0.0014	0.0005	0.0048	0.0081	0.0045	0.0058	0.0026
$Co_{0.25}$	0.0002	0.0027	0.0001	0.0039	0.0009	0.0017	0.0006	0.0166	0.0490	0.0984	0.1373	0.1128
$Co_{0.50}$	0.0002	0.0025	0.0001	0.0043	0.0009	0.0014	0.0005	0.0178	0.0537	0.1014	0.1419	0.1174
$Co_{0.75}$	0.0002	0.0025	0.0001	0.0047	0.0008	0.0013	0.0005	0.0182	0.0580	0.1102	0.1510	0.1231
Co_1	0.0002	0.0025	0.0001	0.0047	0.0008	0.0012	0.0005	0.0190	0.0615	0.1179	0.1607	0.1306
$Ti_{0.25}$	0.0002	0.0037	0.0001	0.0029	0.0010	0.0018	0.0006	0.0127	0.0228	0.0319	0.0338	0.0515
$Ti_{0.50}$	0.0001	0.0040	0.0001	0.0027	0.0010	0.0018	0.0005	0.0110	0.0198	0.0270	0.0268	0.0443
$Ti_{0.75}$	0.0001	0.0043	0.0001	0.0027	0.0011	0.0017	0.0005	0.0098	0.0176	0.0240	0.0222	0.0395
Ti_1	0.0001	0.0043	0.0001	0.0025	0.0012	0.0016	0.0004	0.0081	0.0144	0.0173	0.0181	0.0327

Table 6.24. Closeness coefficient and ranking of alloys

Alloys	D_i^+	D_i^-	CI	Ranking
Mn_0	0.062069	0.177539	0.740955	8
$Mn_{0.25}$	0.027729	0.211683	0.884179	4
$Mn_{0.5}$	0.016499	0.223419	0.931229	3
$Mn_{0.75}$	0.008945	0.231048	0.962728	2
Mn_1	0.000796	0.237334	0.996656	1
$Co_{0.25}$	0.200218	0.037547	0.157918	10
$Co_{0.50}$	0.208171	0.029499	0.124117	11
$Co_{0.75}$	0.222375	0.015133	0.063718	12
Co_1	0.237331	0.002237	0.009339	13
$Ti_{0.25}$	0.064857	0.17697	0.731803	9
$Ti_{0.50}$	0.053516	0.188345	0.778732	7
$Ti_{0.75}$	0.046109	0.195845	0.809431	6
Ti_1	0.035754	0.205904	0.852048	5

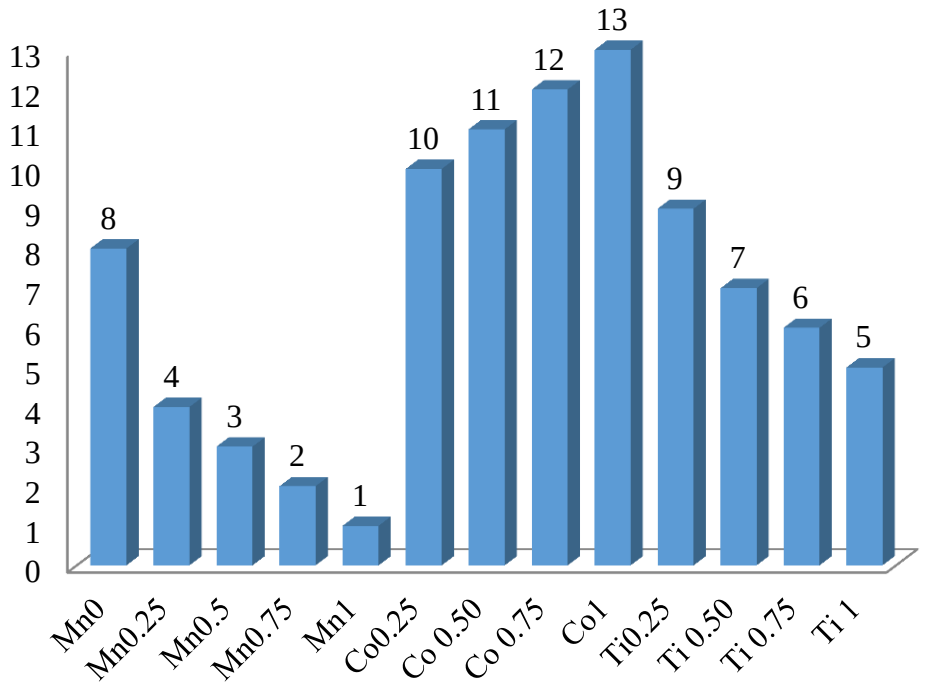

Figure 6.22. Graph Ranking of Alternatives

The ranking obtained from implementation of hybrid TOPSIS Entropy method is as shown in Figure 6.22: Mn_1> (Rank 1) >$Mn_{0.75}$ (Rank 2) >$Mn_{0.50}$ (Rank 3) >$Mn_{0.25}$ (Rank 4)>Ti_1 (Rank 5)>$Ti_{0.75}$ (Rank 6)>$Ti_{0.50}$ (Rank 7)>Mn_0 (Rank 8)>$Ti_{0.25}$ (Rank 9)> $Co_{0.25}$ (Rank 10)>$Co_{0.50}$ (Rank 11)> $Co_{0.50}$ (Rank 12)> Co_1(Rank 13).

This chapter describes:

1. The current chapter describes the sliding wear analysis of $AlCr_{1.5}CuFeNi_2Mn_x$, $AlCr_{1.5}CuFeNi_2Co_x$ and $AlCr_{1.5}CuFeNi_2Ti_x$ alloys for considering one factor at a time and Taguchi design of experiment.

2. The corrosion behaviour of $AlCr_{1.5}CuFeNi_2Mn_x$, $AlCr_{1.5}CuFeNi_2Co_x$ and $AlCr_{1.5}CuFeNi_2Ti_x$ in 3.5 % NaCl solution is investigated.

The last chapter describes the conclusion of the present research work along with the scope for future work.

****

Chapter 7

CONCLUSIONS AND FUTURE SCOPE

The present research work deals with development and characterization of the high-entropy alloy. The purpose of this study is to investigate the influence of Manganese (Mn) Cobalt (Co) and Titanium (Ti) on the physical, mechanical, thermodynamic, microstructural, thermal, corrosion and wear behaviour of $AlCr_{1.5}CuFeNi_2$ high entropy alloy. An attempt is made to develop bulk samples of HEAs through high temperature vacuum induction furnace. The wear analysis of all the developed samples was comprehensively studied based on one factor at a time approach and Taguchi design of experiment. The most significant and the least significant factor were determined using the design of experiment. Finally, all the developed alloys were compared on the basis of various properties using the TOPSIS, a MCDM technique.

7.1 Summary of research findings

Over the past several years, researchers are continuously working for the development of new materials that can sustain extreme conditions for longer period. Existing metals and alloys in some manner are vulnerable to environmental degradation at high temperatures, which causes rapid oxidation and hence loss of strength. Such materials undergo undesirable phase transformations, rapid microstructure alterations, enhanced creep, and thus much-reduced life. Nickel, Cobalt, Chromium, Titanium and stainless steels are some of the common alloys that find wide applications as structural materials for high temperature applications in different industries. In spite of their superior capabilities, these alloys too suffer from the limitations of temperature, pressure and environment over a period. Therefore, it has become very crucial to develop novel materials such as high-entropy alloys with significantly improved physical, mechanical, thermal, corrosion and wear properties to be operated at higher temperature.

It is imperative to develop novel material and investigate their microstructure so as to find its suitability for a particular application. The first criterion for designing a new alloy is the selection of appropriate elements. The property of all the elements needs to be understood before its usability. Keeping this in view, samples of novel non-equimolar high-entropy alloy was developed by high temperature vacuum induction furnace. The microstructure of the developed alloys governs the behaviour of the material under various test condition. Therefore the alloy is homogenised under suitable test parameters for the modification of the grains present in the

alloy. Further, the influence of Mn, Co and Ti on thermodynamic, microstructure, physical, mechanical, thermal, wear and corrosion behaviour of $AlCr_{1.5}CuFeNi_2$ alloy was investigated.

The alloying elements were carefully selected based on the comprehensive literature review. All the alloying elements belong the transition metal of the periodic table and hence their properties are comparable. The Mn was selected as an alloying element as it enhances the solid solution strengthening and results in the single phase structure. It was observed that the addition of Mn not only enhances the solid solution strengthening but also facilitates in overall increase in the required properties of the alloys. The Co was selected as an alloying element as its addition to $AlCr_{1.5}CuFeNi_2$ enhances the softness to a large extent and increases the ductility of the alloy. The low density of titanium is an advantage over the other alloys. As the melting temperature of the developed alloys is greater than 1600 °C, the alloys can be used in the various high temperature applications such as nuclear reactor, automotive and aerospace industries replacing the steel and superalloys.

The samples of $AlCr_{1.5}CuFeNi_2Mn_x$, $AlCr_{1.5}CuFeNi_2Co_x$ and $AlCr_{1.5}CuFeNi_2Ti_x$ (where x =0, 0.25, 0.5, 0.75 and 1) alloys were prepared as per ASTM standards for conducting various physical and mechanical test. The $AlCr_{1.5}CuFeNi_2Mn_x$ and $AlCr_{1.5}CuFeNi_2Co_x$ alloys tend to form the solid solution exhibiting mainly BCC+FCC phase. The thermodynamic parameters were also in agreement with the results obtained from XRD and EDS. The $AlCr_{1.5}CuFeNi_2Ti_x$ alloys showed typical behaviour depicting the intermetallic phase along with the FCC and BCC phase. As expected, the hardness of $AlCr_{1.5}CuFeNi_2Mn_x$ and $AlCr_{1.5}CuFeNi_2Ti_x$ alloys increased with the addition of alloying elements whereas the hardness of $AlCr_{1.5}CuFeNi_2Co_x$ alloys decreased with addition of Co. The mechanical properties of the alloy were in accordance with the microstructure and the hardness values.

The alloys were also subjected to thermal, corrosion and wear tests. The alloys were found suitable for the high temperature applications as per the results obtained from the measurement of thermal conductivity. The alloys also exhibited the improved corrosion resistance with the addition of the alloying elements. However, the wear resistance of the $AlCr_{1.5}CuFeNi_2Mn_x$ and $AlCr_{1.5}CuFeNi_2Ti_x$ alloys increased with the addition of alloying element whereas the wear resistance of the $AlCr_{1.5}CuFeNi_2Co_x$ alloy is found to decrease. Therefore, the present investigation aims to develop alloys for the high temperature application with improved corrosion and wear properties.

7.2. Conclusions

The conclusions drawn from the various results reported in the present research work are summarized below:

1. The $AlCr_{1.5}CuNi_2FeMn_x$, $AlCr_{1.5}CuNi_2FeCo_x$ and $AlCr_{1.5}CuNi_2FeTi_x$ (where x =0, 0.25, 0.5, 0.75 and 1) high-entropy alloys were successfully cast by high-temperature vacuum induction furnace in a controlled environment. The cast samples were homogenized by heat treatment in the furnace at a temperature of 1150 °C for 48 h and then furnace cooled.
2. The entropy of mixing (ΔS) value for Mn_0, $Mn_{0.25}$, $Mn_{0.5}$, $Mn_{0.75}$ and Mn_1 are found to be 13.01, 13.85, 14.22, 14.43 and 14.54 $Jk^{-1}mol^{-1}$, respectively. The ΔS value for Co_0, $Co_{0.25}$, $Co_{0.5}$, $Co_{0.75}$ and Co_1 are found to be 13.01, 13.85, 14.22, 14.42 and 14.54 $Jk^{-1}mol^{-1}$ respectively. The ΔS of Ti_0, $Ti_{0.25}$, $Ti_{0.50}$, $Ti_{0.75}$ and Ti_1 alloys are calculated as 13.01, 13.85, 14.22, 14.43 and 14.54 $Jk^{-1}mol^{-1}$ respectively. There is a continuous increase in the ΔS value with addition alloying element in the multi-component alloys. The increase in the ΔS value increases the possibility of solid solution formation.
3. The values of thermodynamic parameters of all the cast alloys are compared with the proposed values for the formation of the solid solution. All the calculated value of the thermodynamic parameter and the experimental analysis exhibits the typical characteristics of HEAs.
4. It is found that the alloys of Mn and Co consist of the duplex phase i.e. both FCC and BCC whereas the Ti alloys result in the formation of the intermetallic compounds. There is a phase change from FCC structure to BCC structure with the increase in the Mn and Ti content whereas the reverse results on the addition of the Co.
5. The microstructures of $AlCr_{1.5}CuFeNi_2Mn_x$ alloys depict mainly two regions i.e. one dark and another light. The examination of SEM images of the alloys in the homogenised condition indicates dark dendrite core (DC) regions as compared to bright interdendritic (ID) regions. The dark region (DC) represents the presence of BCC phase as compared to the bright region (ID) which is due to the formation of FCC phase. Almost similar microstructures are found in case of $AlCr_{1.5}CuFeNi_2Ti_x$ and $AlCr_{1.5}CuFeNi_2Co_x$.
6. The experimental density of $AlCr_{1.5}CuFeNi_2Mn_x$ alloy varies from 7.11 ±0.03 g/cm^3 to 7.23±0.08 g/cm^3 for x=0 to x= 1, $AlCr_{1.5}CuFeNi_2Co_x$ alloy varies from 6.94±0.02 g/cm^3 to

7.23±0.07 g/cm^3 for x=0 to x=1 and the $AlCr_{1.5}CuFeNi_2Ti_x$ alloy varies from 7.01 to 6.57 g/cm^3 for x=0 to x=1 respectively.

7. The hardness of Mn_0, $Mn_{0.25}$, $Mn_{0.50}$, $Mn_{0.75}$ and Mn_1 alloys are found to be 471, 511, 537, 574 and 580 HV respectively. The tensile strength of the $AlCr_{1.5}CuFeNi_2Mn_x$ alloys varies from 611.47 MPa to 795.37 MPa for x = 0 to x= 1, respectively**.** The Young's modulus of the Mn_0, $Mn_{0.25}$, $Mn_{0.50}$, $Mn_{0.75}$ and Mn_1 is found to be 237.9. 241.6, 248.84, 257.16 and 259.87 GPa respectively. It is also found that the thermal conductivity of the HEAs decreases with increase in the value of x. HEAs resulting in the higher thermal conductivity with respect to the increase in the temperature. The properties of the alloys are comparable with the properties of the superalloys and hence can be used in the high temperature application.
8. The tensile strength of the Co_0, $Co_{0.25}$, $Co_{0.50}$, $Co_{0.75}$ and Co_1 alloy is found to be 611.47, 594.46, 557.26, 527.68 and 506.12 MPa respectively. The Young's modulus of the Co_0, $Co_{0.25}$, $Co_{0.50}$, $Co_{0.75}$, and Co_1 is found to be 237.9, 227.22, 225.4, 214.07 and 201.58 GPa respectively. The compressive strength values of Co_0, $Co_{0.25}$, $Co_{0.50}$, $Co_{0.75}$, and Co_1 alloys are 1552, 1753, 1734, 1719 and 1701 MPa. The mechanical properties of the $AlCr_{1.5}CuNi_2FeCo_x$ alloy suggests that the alloy is capable of carrying both tensile and compressive loading under severe conditions.
9. The microhardness and tensile strength of the $AlCr_{1.5}CuFeNi_2Ti_x$ high-entropy alloys increases with the increase in the addition of Ti. Similarly the specific strength of the alloys and the Young's modulus also increases with the addition of Ti. However, the flexural modulus of alloys decrease as compared to the other properties.
10. The addition of Mn, Co and Ti improve the corrosion resistance of HEAs at room temperature in 3.5 wt.% NaCl solution. The formation of the protective layer and the BCC structure of the system results in the improvement in the corrosion resistance. The best corrosion results are obtained for the $AlCr_{1.5}CuFeNi_2Ti_x$ alloys. The thermal conductivity of the alloys decreases with the increase in the molar ratio and increases with the increase in the temperature.
11. The addition of Mn and Ti improves the wear resistance of the alloys as compared to the Co. For $AlCr_{1.5}CuFeNi_2Mn_x$ alloy, a substantial decrease in wear rate can be found with the increase in load from 10 N to 50 N. The decrease in wear rate can be attributed to constitute the smooth contact between the rotating disc and the sample surface as the time taken to

remove the asperities is reduced. The lowest specific wear rate of (0.65×10^{-4} mm^3/N-m) was observed for Mn_1 at 50N load, which was 4.08% lower than the specific wear rate of (15.9×10^{-4} mm^3/N-m) occurred at 10 N load for the same sliding distance and sliding speed.

12. As per the Taguchi design of experiment, the sliding distance is the most significant factor for $AlCr_{1.5}CuNi_2FeMn_x$, $AlCr_{1.5}CuNi_2FeCo_x$ and $AlCr_{1.5}CuNi_2FeTi_x$ alloys. Therefore the sliding distance plays a significant role in determining the sliding wear behavior of the developed alloy.
13. The surface morphology of the worn surface depicts some common phenomenon such as wear debris, delamination, crater formation, ploughing, extruded lip and oxide agglomerates. The most of the phenomenon results due to the sliding of one hard surface over another hard surface.
14. The ranking obtained from implementation of hybrid TOPSIS Entropy method is: Mn_1> (Rank 1) >$Mn_{0.75}$ (Rank 2) >$Mn_{0.50}$ (Rank 3) >$Mn_{0.25}$ (Rank 4)>Ti_1 (Rank 5)>$Ti_{0.75}$ (Rank 6)>$Ti_{0.50}$ (Rank 7)>Mn_0 (Rank 8)>$Ti_{0.25}$ (Rank 9)> $Co_{0.25}$ (Rank 10)>$Co_{0.50}$ (Rank 11)> $Co_{0.50}$ (Rank 12)> Co_1(Rank 13).

7.3. Scope for future work

There are numerous combinations of elements that can be developed with different molar ratio and their properties can be investigated. One such novel attempt was made in this research work. Still the research work can be extended to determine the same properties at different test parameters. Some of the scopes for future work are as follows:

1. The same set alloys can be developed by other fabrication technique and the properties can be compared with the results presented in this paper.
2. The mechanical properties of the alloy can be investigated at elevated temperature so as to confirm its applicability to a particular application.
3. The use of the developed alloy in actual area will provide confirmation of proposed area of application.
4. The corrosion and wear behaviour of the alloy can be studied in the other environment such as in acidic medium.

****

REFERENCES

1. Bernard AB, Jones CI. Productivity across industries and countries: time series theory and evidence. The review of economics and statistics. 1996.
2. Stroosnijder MF, Van de Voorde MH. High Temperature Materials–Their development and prospects. Mater Sci Eng. 1990.
3. Van de Voorde MH. High-temperature materials and industrial applications. Bulletins of the Catalan Societies of Physics, Chemistry, Mathematics and Technology. 1991.
4. Donachie MJ, Donachie SJ. Superalloys: A Technical Guide. ASM international. 2002.
5. Morris DG, Naka S, Caron P. Intermetallics and superalloys. German Society for Materials Science. 2000.
6. Reed RC. The superalloys: fundamentals and applications. Cambridge university press. 2008.
7. Yeh JW, Chen SK, Lin SJ, Gan JY, Chin TS, Shun TT, et al. Nanostructured high-entropy alloys with multiple principal elements: Novel alloy design concepts and outcomes. Adv Eng Mater. 2004; 6:299-303.
8. Cantor B, Chang ITH, Knight P, Vincent AJ. Microstructural development in equiatomic multicomponent alloys. Mater Sci Eng A. 2004; 375:2013-8.
9. Yeh JW. Recent Progress in High Entropy Alloys, Annals of Chemistry Materials Science. 2006; 31:633-648.
10. Huang YS, Chen L, Lui HW, Cai MH, Yeh JW. Microstructure, hardness, resistivity and thermal stability of sputtered oxide films of $AlCoCrCu_{0.5}NiFe$ high-entropy alloy. Mater Sci Eng: A. 2007; 457:77-83.
11. Hsieh KC, Yu CF, Hsieh WT, Chiang WR, Ku JS, Lai JH, Tu CP and CC Yang. The microstructure and phase equilibrium of new high performance high-entropy alloys. J Alloy Compd. 2009; 483: 209-212.
12. Ma SG, Qiao JW, Wang ZH, Yang HJ, Zhang Y. Microstructural features and tensile behaviors of the $Al_{0.5}CrCuFeNi_2$ high-entropy alloys by cold rolling and subsequent annealing. Mater Design. 2015; 88:1057-1062.
13. Shun TT, Chang LY, Shiu MH. Microstructure and mechanical properties of multiprincipal component $CoCrFeNiMo_x$ alloys. Mater Charact. 2012; 70: 63-67.
14. Zhang KB, Fu ZY, Zhang JY, Wang WM, Wang H, Wang YC, Zhang QJ, Shi J.

Microstructure and mechanical properties of $CoCrFeNiTiAl_x$ high-entropy alloys. Mater Sci Eng: A. 2009; 508: 214-219.

15. Jinhong P, Ye P, Hui Z, Lu Z. Microstructure and properties of $AlCrFeCuNi_x$ ($0.6 \leq x \leq 1.4$) high-entropy alloys. Mater Sci Eng: A. 2012; 534: 228-33.
16. Wang YP, Li DY, Parent L, Tian H. Improving the wear resistance of white cast iron using a new concept–High-entropy microstructure. Wear. 2011; 271: 1623-1628.
17. Hsu CY, Sheu TS, Yeh JW, Chen SK. Effect of iron content on wear behavior of $AlCoCrFe_xMo_{0.5}Ni$ high-entropy alloys. Wear. 2010; 268: 653-659.
18. Dąbrowa J, Cieslak G, Stygar M, Mroczka K, Berent K, Kulik T, Danielewski M. Influence of Cu content on high temperature oxidation behavior of $AlCoCrCu_xFeNi$ high entropy alloys (x= 0; 0.5; 1). Intermetallics. 2017; 84: 52-61.
19. Ye Q, Feng K, Li Z, Lu F, Li R, Huang J, Wu Y. Microstructure and corrosion properties of CrMnFeCoNi high entropy alloy coating. Applied Surface Science. 2017; 396: 1420-1426.
20. Zhang Y, Zhou YJ, Lin JP, Chen GL, Liaw PK. Solid-solution phase formation rules for multi-component alloys. Advanced Engineering Materials. 2008; 10:534–538.
21. Ranganathan S. Alloyed pleasures: Multimetallic cocktails, Current Science. 2003; 85:1404-1406.
22. Yeh JW, Chen SK, Gan JW, Lin SJ, Chin TS, Shun TT, Tsau CH, Chang SY. Formation of simple crystal structures in Cu-Co-Ni-Cr-Al-Fe-Ti-V alloys with multiprincipal metallic elements. Metall. Mater. Trans. A. 2004; 35A: 2533-2536.
23. Murty BS, Yeh JW, Ranganathan S. High-entropy Alloys. 2014.
24. Zhou YJ, Zhang Y, Wang YL, Chen GL. Solid solution alloys of $AlCoCrFeNiTi_x$ with excellent room-temperature mechanical properties. Appl Phys Lett 2007; 90(18):181904.
25. Wang XF, Zhang Y, Qiao Y, Chen GL. Novel microstructure and properties of multicomponent $CoCrCuFeNiTi_x$ alloys. Intermetallics. 2007; 15(3):357–62.
26. Singh S, Wanderka N, Murty BS, Glatzel U, Banhart J. Decomposition in multi-component AlCoCrCuFeNi high-entropy alloy. Acta Mater. 2011; 59:182–90.
27. Li C, Li JC, Zhao M, Jiang Q. Effect of alloying elements on microstructure and properties of multiprincipal elements high entropy alloys. J Alloy Compd. 2009; 475(1–

2):752–757.

28. Senkov ON, Wilks GB, Miracle DB, Chuang CP, Liaw PK. Refractory high-entropy alloys. Intermetallics. 2010; 18:1758–1765.
29. Senkov ON, Wilks GB, Scott JM, Miracle DB. Mechanical properties of $Nb_{25}Mo_25Ta_{25}W_{25}$ and $V_{20}Nb_{20}Mo_{20}Ta_{20}W_{20}$ refractory high entropy alloys. Intermetallics. 2011; 19(5):698-706.
30. Senkov ON, Senkova SV, Woodward C. Effect of aluminum on the microstructure and properties of two refractory high-entropy alloys. Acta Mater. 2014; 68:214-28.
31. Juan CC, Yeh JW, Chin TS, A novel light high-entropy alloy $Al_{20}Be_{20}Fe_{10}Si_{15}Ti_{35}$. In Proceedings of the E-MRS Fall Meeting, Warsaw, Poland, 14–18 September 2009.
32. Stepanov ND, Shaysultanov DG, Salishchev GA, Tikhonovsky MA. Structure and mechanical properties of a light-weight AlNbTiV high entropy alloy. Mater. Lett. 2015; 142:153–155.
33. Youssef KM, Zaddach AJ, Niu C, Irving DL, Koch CC, A novel low-density, high-hardness, high-entropy alloy with close-packed single-phase nanocrystalline structures. Mater. Res. Lett. 2015; 3: 95–99.
34. Guo S. Liu CT. Phase stability in high entropy alloys: Formation of solid-solution phase or amorphous phase. Prog. Nat. Sci. Mater. Int. 2011; 21: 433–446.
35. Xia MX, Zhang SG, Ma CL, Li JG. Evaluation of glass-forming ability for metallic glasses based on order-disorder competition. Appl. Phys. Lett. 2006; 89:091917.
36. Inoue A. Stabilization of metallic supercooled liquid and bulk amorphous alloys. Acta Mater. 2000; 48:279–306.
37. Guo S, Hu Q, Ng C, Liu CT. More than entropy in high-entropy alloys: forming solid solutions or amorphous phase. Intermetallics. 2013; 41: 96–103.
38. Yeh AC, Tsao TK, Chang YJ, Chang KC, Yeh JW, Chiou MS, Jian SR, Kuo CM, Wang WR. Murakami H. Developing New Type of High Temperature Alloys - High Entropy Superalloys. Int. J. Metall. Mater. Eng. 2015; 1:107.
39. Chang YJ, Yeh AC. The evolution of microstructures and high temperature properties of $Al_xCo_{1.5}CrFeNi_{1.5}Ti_y$ high entropy alloys. J. Alloys Compd. 2015; 653:379-85.
40. Senkov O, Isheim D, Seidman D, Pilchak A. Development of a refractory high entropy superalloy. Entropy. 2016; 18(3): 102.

41. Shankar V, Rao KB, Mannan SL. Microstructure and mechanical properties of Inconel 625 superalloy. J. Nucl. Mater. 2001; 288(2-3):222-32.
42. Rao MN. Application of superalloys in petrochemical and marine sectors in India. Transactions of the Indian Institute of Metals. 2008; 61(2-3):87-91.
43. Sheng GU, Liu CT. Phase stability in high entropy alloys: formation of solid-solution phase or amorphous phase. Progress in Natural Science: Materials International. 2011; 21(6):433-46.
44. Guo S, Ng C, Lu J, Liu CT. Effect of valence electron concentration on stability of fcc or bcc phase in high entropy alloys. J. Appl. Phys. 2011; 109(10):103505.
45. Pi J, Pan Y. Thermodynamic analysis for microstructure of high-entropy alloys. Rare Rare Metal Mat Eng. 2013; 42(2):232-7.
46. Dong Y, Lu Y, Jiang L, Wang T, Li T. Effects of electro-negativity on the stability of topologically close-packed phase in high entropy alloys. Intermetallics. 2014; 52:105-9.
47. Tian F, Varga LK, Chen N, Shen J, Vitos L. Empirical design of single phase high-entropy alloys with high hardness. Intermetallics. 2015; 58:1-6.
48. Melnick AB, Soolshenko VK. Thermodynamic design of high-entropy refractory alloys. J Alloy Compd. 2017; 694:223-7.
49. Sonkusare R, JananiPD, Gurao NP, Sarkar S, Sen S, Pradeep KG, Biswas K. Phase equilibria in equiatomic CoCuFeMnNi high entropy alloy. Mater. Chem. Phys. 2017; 210:269-278.
50. Hume-Rothery W, Smallman RE, Haworth CW. The structure of metals and alloys. The Institute of Metals, 1 Carlton House Terrace, London SW1Y5DB, UK, 1988.
51. Wang YP, Li BS, Ren MX, Yang C, Fu HZ. Microstructure and compressive properties of AlCrFeCoNi high entropy alloy. Mater Sci Eng A. 2008; 491:154-8.
52. Li BS, Wang YP, Ren MX, Yang C, Fu HZ. Effects of Mn, Ti and V on the microstructure and properties of AlCrFeCoNiCu high entropy alloy. Mater Sci Eng A. 2008; 498(1-2):482-6.
53. Zhang KB, Fu ZY, Zhang JY, Wang WM, Wang H, Wang YC, Zhang QJ, Shi J. Microstructure and mechanical properties of $CoCrFeNiTiAl_x$ high-entropy alloys. Mater Sci Eng A. 2009; 508(1-2):214-9.
54. Chou HP, Chang YS, Chen SK, Yeh JW. Microstructure, thermophysical and electrical

properties in $Al_xCoCrFeNi$ ($0 \leq x \leq 2$) high-entropy alloys. Mater Sci. Eng. B. 2009; 163(3):184-9.

55. Li C, Li JC, Zhao M, Jiang Q. Effect of aluminum contents on microstructure and properties of $Al_xCoCrFeNi$ alloys. J Alloy Compd. 2010; 504:S515-8.
56. Wang WR, Wang WL, Wang SC, Tsai YC, Lai CH, Yeh JW. Effects of Al addition on the microstructure and mechanical property of AlxCoCrFeNi high-entropy alloys. Intermetallics. 2012; 26:44-51.
57. Liu Z, Guo S, Liu X, Ye J, Yang Y, Wang XL, Yang L, An K, Liu CT. Micromechanical characterization of casting-induced inhomogeneity in an $Al_{0.8}CoCrCuFeNi$ high-entropy alloy. Scripta Mater. 2011; 64(9):868-71.
58. Lin CM, Tsai HL. Evolution of microstructure, hardness, and corrosion properties of high-entropy $Al_{0.5}CoCrFeNi$ alloy. Intermetallics. 2011; 19(3):288-94.
59. Zhang K, Fu Z. Effects of annealing treatment on phase composition and microstructure of $CoCrFeNiTiAl_x$ high-entropy alloys. Intermetallics. 2012; 22:24-32.
60 Zhuang YX, Liu WJ, Chen ZY, Xue HD, He JC. Effect of elemental interaction on microstructure and mechanical properties of FeCoNiCuAl alloys. Mater Sci Eng: A 2012; 556:395-9.
61. Guo S, Ng C, Liu CT. Anomalous solidification microstructures in Co-free $Al_xCrCuFeNi_2$ high-entropy alloys. J Alloy Compd. 2013; 557:77-81.
62. Zhuang YX, Xue HD, Chen ZY, Hu ZY, He JC. Effect of annealing treatment on microstructures and mechanical properties of FeCoNiCuAl high entropy alloys. Materials Science and Engineering: A. 2013; 572:30-35.
63. Chen W, Fu Z, Fang S, Xiao H, Zhu D. Alloying behavior, microstructure and mechanical properties in a FeNiCrCo0. 3Al0. 7 high entropy alloy. Mater. Design. 2013; 51:854-60.
64. Fan QC, Li BS, Zhang Y. The microstructure and properties of (FeCrNiCo) Al_xCu_y high-entropy alloys and their TiC-reinforced composites. Mater Sci Eng: A. 2014; 598:244-50.
65. Wang WR, Wang WL, Yeh JW. Phases, microstructure and mechanical properties of $Al_xCoCrFeNi$ high-entropy alloys at elevated temperatures. J Alloy Compd. 2014; 589:143-52.

66. He JY, Liu WH, Wang H, Wu Y, Liu XJ, Nieh TG, Lu ZP. Effects of Al addition on structural evolution and tensile properties of the FeCoNiCrMn high-entropy alloy system. Acta Mater. 2014 Jan 1; 62:105-13.
67. Vida A, Varga LK, Chinh NQ, Molnar D, Huang S, Vitos L. Effects of the sp element additions on the microstructure and mechanical properties of NiCoFeCr based high entropy alloys. Mater Sci Eng: A. 2016; 669:14-9.
68. Sun X, Zhang H, Lu S, Ding X, Wang Y, Vitos L. Phase selection rule for Al-doped CrMnFeCoNi high-entropy alloys from first-principles. Acta Mater. 2017; 140:366-74.
69. Poletti MG, Branz S, Fiore G, Szost BA, Crichton WA, Battezzati L. Equilibrium high entropy phases in X-NbTaTiZr (X= Al, V, Cr and Sn) multiprincipal component alloys. J Alloy Compd. 2016; 655:138-46.
70. Hsu CY, Juan CC, Wang WR, Sheu TS, Yeh JW, Chen SK. On the superior hot hardness and softening resistance of $AlCoCr_xFeMo_{0.5}Ni$ high-entropy alloys. Mater Sci Eng: A. 2011; 528(10-11):3581-8.
71. Fu Z, Chen W, Fang S, Li X. Effect of Cr addition on the alloying behavior, microstructure and mechanical properties of twinned $CoFeNiAl_{0.5}Ti_{0.5}$ alloy. Mater Sci Eng: A. 2014; 597:204-11.
72. Wu PH, Liu N, Yang W, Zhu ZX, Lu YP, Wang XJ. Microstructure and solidification behavior of multicomponent $CoCrCu_xFeMoNi$ high-entropy alloys. Mater Sci Eng: A 2015; 642:142-9.
73. Lin CM, Tsai HL, Bor HY. Effect of aging treatment on microstructure and properties of high-entropy $Cu_{0.5}CoCrFeNi$ alloy. Intermetallics. 2010; 18(6):1244-50.
74. Lin CM, Tsai HL. Effect of annealing treatment on microstructure and properties of high-entropy $FeCoNiCrCu_{0.5}$ alloy. Mater. Chem. Phys. 2011; 128(1-2):50-6.
75. Hsu YJ, Chiang WC, Wu JK. Corrosion behavior of $FeCoNiCrCu_x$ high-entropy alloys in 3.5% sodium chloride solution. Mater Chem Phys. 2005; 92 (1):112-7.
76. Dong Y, Lu Y, Kong J, Zhang J, Li T. Microstructure and mechanical properties of multi-component $AlCrFeNiMo_x$ high-entropy alloys. J Alloy Compd. 2013; 573:96-101.
77. Shun TT, Hung CH, Lee CF. The effects of secondary elemental Mo or Ti addition in $Al_{0.3}CoCrFeNi$ high-entropy alloy on age hardening at 700˚C. J Alloy Compd. 2010; 495(1):55-8.

78. Wang Z, Wu M, Cai Z, Chen S, Baker I. Effect of Ti content on the microstructure and mechanical behavior of $(Fe_{36}Ni_{18}Mn_{33}Al_{13})_{100-x}Ti_x$ high entropy alloys. Intermetallics 2016; 75:79-87.
79. Fu Z, Chen W, Chen Z, Wen H, Lavernia EJ. Influence of Ti addition and sintering method on microstructure and mechanical behavior of a medium-entropy $Al_{0.6}CoNiFe$ alloy. Mater. Sci. Eng: A. 2014; 619:137-45.
80. Hsueh HT, Shen WJ, Tsai MH, Yeh JW. Effect of nitrogen content and substrate bias on mechanical and corrosion properties of high-entropy films $(AlCrSiTiZr)_{100-x}N_x$. Surf. Coat. Technol. 2012; 206(19-20):4106-12.
81. Wang LM, Chen CC, Yeh JW, Ke ST. The microstructure and strengthening mechanism of thermal spray coating $NixCo_{0.6}Fe_{0.2}CrySi_zAlTi_{0.2}$ high-entropy alloys. Mater. Chem. Phys. 2011; 126(3):880-5.
82. Fras E, Kawalec M, Lopez HF. Solidification microstructures and mechanical properties of high-vanadium Fe–C–V and Fe–C–V–Si alloys. Mater Sci Eng: A 2009; 524(1-2):193-203.
83. Pi JH, Pan Y, Zhang L, Zhang H. Microstructure and property of AlTiCrFeNiCu high-entropy alloy. J Alloy Compd. 2011; 509(18):5641-5.
84. Senkov ON, Scott JM, Senkova SV, Miracle DB, Woodward CF. Microstructure and room temperature properties of a high-entropy TaNbHfZrTi alloy. J Alloy Compd. 2011; 509(20):6043-8.
85. Praveen S, Murty BS, Kottada RS. Alloying behavior in multi-component AlCoCrCuFe and NiCoCrCuFe high entropy alloys. Mater Sci Eng: A. 2012; 534:83-9.
86. Liu L, Zhu JB, Zhang C, Li JC, Jiang Q. Microstructure and the properties of FeCoCuNiSnx high entropy alloys. Mater Sci Eng: A. 2012; 548:64-8.
87. Shun TT, Chang LY, Shiu MH. Microstructure and mechanical properties of multiprincipal component $CoCrFeNiMo_x$ alloys. Mater Charact. 2012; 70:63-7.
88. Fu Z, Chen W, Xiao H, Zhou L, Zhu D, Yang S. Fabrication and properties of nanocrystalline $Co_{0.5}FeNiCrTi_{0.5}$ high entropy alloy by MA–SPS technique. Mater. Design. 2013; 44:535-9.
89. Chen W, Fu Z, Fang S, Wang Y, Xiao H, Zhu D. Processing, microstructure and properties of Al0. 6CoNiFeTi0. 4 high entropy alloy with nanoscale twins. Mater Sci

Eng: A. 2013; 565:439-44.

90. Pradeep KG, Wanderka N, Choi P, Banhart J, Murty BS, Raabe D. Atomic-scale compositional characterization of a nanocrystalline AlCrCuFeNiZn high-entropy alloy using atom probe tomography. Acta Mater. 2013; 61(12):4696-706.
91. Salishchev GA, Tikhonovsky MA, Shaysultanov DG, Stepanov ND, Kuznetsov AV, Kolodiy IV, Tortika AS, Senkov ON. Effect of Mn and V on structure and mechanical properties of high-entropy alloys based on CoCrFeNi system. J Alloy Compd. 2014; 591:11-21.
92. Otto F, Hanold NL, George EP. Microstructural evolution after thermomechanical processing in an equiatomic, single-phase CoCrFeMnNi high-entropy alloy with special focus on twin boundaries. Intermetallics. 2014; 54:39-48.
93. Fang S, Chen W, Fu Z. Microstructure and mechanical properties of twinned $Al_{0.5}CrFeNiCo_{0.3}C_{0.2}$ high entropy alloy processed by mechanical alloying and spark plasma sintering. Mater. Design (1980-2015). 2014; 54:973-9.
94. Jiang L, Cao ZQ, Jie JC, Zhang JJ, Lu YP, Wang TM, Li TJ. Effect of Mo and Ni elements on microstructure evolution and mechanical properties of the $CoFeNi_xVMo_y$ high entropy alloys. J Alloy Compd. 2015; 649:585-90.
95. Sistla HR, Newkirk JW, Liou FF. Effect of Al/Ni ratio, heat treatment on phase transformations and microstructure of $Al_xFeCoCrNi_{2-x}$ (x= 0.3, 1) high entropy alloys. Mater Design. 2015; 81:113-21.
96. Wang Z, Wang X, Yue H, Shi G, Wang S. Microstructure, thermodynamics and compressive properties of AlCoCrCuMn-x (x= Fe, Ti) high-entropy alloys. Mater Sci Eng: A. 2015; 627:391-8.
97. Stepanov ND, Yurchenko NY, Tikhonovsky MA, Salishchev GA. Effect of carbon content and annealing on structure and hardness of the CoCrFeNiMn-based high entropy alloys. J Alloy Compd. 2016; 687:59-71.
98. Maulik O, Kumar D, Kumar S, Fabijanic DM, Kumar V. Structural evolution of spark plasma sintered $AlFeCuCrMg_x$ (x = 0, 0.5, 1, 1.7) high entropy alloys. Intermetallics. 2016; 77:46-56.
99. Zhang Z, Axinte E, Ge W, Shang C, Wang Y. Microstructure, mechanical properties and corrosion resistance of CuZrY/Al, Ti, Hf series high-entropy alloys. Mater. Design.

2016; 108:106-13.

100. Hsu US, Hung UD, Yeh JW, Chen SK, Huang YS, Yang CC. Alloying behavior of iron, gold and silver in AlCoCrCuNi-based equimolar high-entropy alloys. Mater Sci Eng: A. 2007; 460:403-8.
101. Wang FJ, Zhang Y. Effect of Co addition on crystal structure and mechanical properties of $Ti_{0.5}$CrFeNiAlCo high entropy alloy. Mater Sci Eng: A 2008; 496(1-2):214-6.
102. Varalakshmi S, Kamaraj M, Murty BS. Synthesis and characterization of nanocrystalline AlFeTiCrZnCu high entropy solid solution by mechanical alloying. J Alloy Compd. 2008; 460(1-2):253-7.
103. Paradkar A, Kamat SV, Gogia AK, Kashyap BP. Effect of Al and Nb on the trigger stress for stress-induced martensitic transformation during tensile loading in Ti–Al–Nb alloys. Mater Sci Eng: A. 2008; 487(1-2):14-9.
104. Varalakshmi S, Kamaraj M, Murty BS. Processing and properties of nanocrystalline CuNiCoZnAlTi high entropy alloys by mechanical alloying. Mater Sci Eng: A. 2010; 527(4-5):1027-30.
105. Ye X, Ma M, Cao Y, Liu W, Ye X, Gu Y. The property research on high-entropy alloy AlxFeCoNiCuCr coating by laser cladding. Physics Procedia. 2011; 12:303-12.
106. Zhang H, Pan Y, He YZ. Synthesis and characterization of FeCoNiCrCu high-entropy alloy coating by laser cladding. Mater. Design. 2011; 32(4):1910-5.
107. Tsao LC, Chen CS, Chu CP. Age hardening reaction of the $Al_{0.3}CrFe_{1.5}MnNi_{0.5}$ high entropy alloy. Mater. Design (1980-2015). 2012; 36:854-8.
108. Kuznetsov AV, Shaysultanov DG, Stepanov ND, Salishchev GA, Senkov ON. Tensile properties of an AlCrCuNiFeCo high-entropy alloy in as-cast and wrought conditions. Mater Sci Eng: A 2012; 533:107-18.
109. Gang Zhu, Ying Liu, Jinwen Ye. Fabrication and properties of Ti(C,N)-based cermets with multi-component AlCoCrFeNi high-entropy alloys binder. Materials Letters. 2013; 113:80–82
110. Yuhu F, Yunpeng Z, Hongyan G, Huimin S, Li H. $AlNiCrFe_xMo_{0.2}CoCu$ high entropy alloys prepared by powder metallurgy. Rare Metal Mat Eng. 2013; 42(6):1127-9.
111. Fu Z, Chen W, Fang S, Zhang D, Xiao H, Zhu D. Alloying behavior and deformation twinning in a $CoNiFeCrAl_{0.6}Ti_{0.4}$ high entropy alloy processed by spark plasma

sintering. J Alloy Compd. 2013; 553:316-23.

112. Lilensten L, Couzinié JP, Perrière L, Bourgon J, Emery N, Guillot I. New structure in refractory high-entropy alloys. Mater. Lett. 2014; 132:123-5.

113. Ng C, Guo S, Luan J, Wang Q, Lu J, Shi S, Liu CT. Phase stability and tensile properties of Co-free $Al_{0.5}CrCuFeNi_2$ high-entropy alloys. J Alloy Compd. 2014; 584:530-7.

114. Ma SG, Liaw PK, Gao MC, Qiao JW, Wang ZH, Zhang Y. Damping behavior of Al_xCoCrFeNi high-entropy alloys by a dynamic mechanical analyzer. J Alloy Compd. 2014; 604:331-9.

115. Wu YD, Cai YH, Wang T, Si JJ, Zhu J, Wang YD, Hui XD. A refractory $Hf_{25}Nb_{25}Ti_{25}Zr_{25}$ high-entropy alloy with excellent structural stability and tensile properties. Mater. Lett. 2014; 130:277-80.

116. Babu CS, Koundinya NT, Sivaprasad K, Szpunar JA. Thermal analysis and nanoindentaion studies on nanocrystalline AlCrNiFeZn high entropy alloy. Procedia Mater. Sci. 2014; 6:641-7.

117. Sriharitha R, Murty BS, Kottada RS. Alloying, thermal stability and strengthening in spark plasma sintered Al_xCoCrCuFeNi high entropy alloys. J Alloy Compd. 2014; 583:419-26.

118. Juan CC, Tsai MH, Tsai CW, Lin CM, Wang WR, Yang CC, Chen SK, Lin SJ, Yeh JW. Enhanced mechanical properties of HfMoTaTiZr and HfMoNbTaTiZr refractory high-entropy alloys. Intermetallics. 2015; 62:76-83.

119. Zaddach AJ, Scattergood RO, Koch CC. Tensile properties of low-stacking fault energy high-entropy alloys. Mater Sci Eng: A. 2015; 636:373-8.

120. E. Fazakasa, V. Zadorozhnyyd, D.V. Louzguine-Luzgin. Effect of iron content on the structure and mechanical properties of $Al_{25}Ti_{25}Ni_{25}Cu_{25}$ and $(AlTi)_{60-x}Ni_{20}Cu_{20}Fe_x$(x=15, 20) high-entropy alloys. Appl Surf Sci. 2015; 358:549–555.

121. Juan CC, Tseng KK, Hsu WL, Tsai MH, Tsai CW, Lin CM, Chen SK, Lin SJ, Yeh JW. Solution strengthening of ductile refractory HfMoxNbTaTiZr high-entropy alloys. Mater. Lett. 2016; 175:284-7.

122. He JY, Wang H, Wu Y, Liu XJ, Mao HH, Nieh TG, Lu ZP. Precipitation behavior and its effects on tensile properties of FeCoNiCr high-entropy alloys. Intermetallics. 2016;

79:41-52.

123. Yurchenko NY, Stepanov ND, Shaysultanov DG, Tikhonovsky MA, Salishchev GA. Effect of Al content on structure and mechanical properties of the $Al_xCrNbTiVZr$ (x= 0; 0.25; 0.5; 1) high-entropy alloys. Mater Charact. 2016; 121:125-34.
124. Varvenne C, Luque A, Curtin WA. Theory of strengthening in fcc high entropy alloys. Acta Mater. 2016; 118:164-76.
125. Rao ZY, Wang X, Zhu J, Chen XH, Wang L, Si JJ, Wu YD, Hui XD. Affordable FeCrNiMnCu high entropy alloys with excellent comprehensive tensile properties. Intermetallics. 2016; 77:23-33.
126. Kim KB, Warren PJ, Cantor B, Eckert J. Enhanced thermal stability of the devitrified nanoscale icosahedral phase in novel multicomponent amorphous alloys. J. Mater. Res. 2006; 21(4):823-31.
127. Dolique V, Thomann AL, Brault P, Tessier Y, Gillon P. Thermal stability of AlCoCrCuFeNi high entropy alloy thin films studied by in-situ XRD analysis. Surf.Coat. Technol. 2010; 204(12-13):1989-92.
128. Tariq NH, Naeem M, Hasan BA, Akhter JI, Siddique M. Effect of W and Zr on structural, thermal and magnetic properties of AlCoCrCuFeNi high entropy alloy. J Alloy Compd. 2013; 556:79-85.
129. Lu CL, Lu SY, Yeh JW, Hsu WK. Thermal expansion and enhanced heat transfer in high-entropy alloys. J. Appl. Crystallogr. 013; 46(3):736-9.
130. Laplanche G, Gadaud P, Horst O, Otto F, Eggeler G, George EP. Temperature dependencies of the elastic moduli and thermal expansion coefficient of an equiatomic, single-phase CoCrFeMnNi high-entropy alloy. J Alloy Compd. 2015; 623:348-53.
131. Caro M, Béland LK, Samolyuk GD, Stoller RE, Caro A. Lattice thermal conductivity of multi-component alloys. J Alloy Compd. 2015; 648:408-13.
132. Giri A, Braun JL, Rost CM, Hopkins PE. On the minimum limit to thermal conductivity of multi-atom component crystalline solid solutions based on impurity mass scattering. Scripta Mater. 2017; 138:134-8.
133. Chen YY, Hong UT, Shih HC, YehJW, Duval T. Electrochemical kinetics of the high entropy alloys in aqueous environments – a comparison with type 304 stainless steel. Corros. Sci. 2005; 47(11):2679-99.

134. Chen YY, Hong UT, YehJW, Shih HC. Selected corrosion behaviors of a $Cu_{0.5}$NiAlCoCrFeSi bulk glassy alloy in 288˚C high-purity water. Scripta Mater.2006; 54(12):1997-2001.
135. Lee CP, Chang CC, Chen YY, Yeh JW, Shih HC. Effect of the aluminium content of $AlxCrFe_{1.5}MnNi_{0.5}$ high-entropy alloys on the corrosion behaviour in aqueous environments. Corros. Sci. 2008; 50(7):2053-60.
136. Lee CP, Chen YY, Hsu CY, YehJW, Shih HC. Enhancing pitting corrosion resistance of $AlxCrFe_{1.5}MnNi_{0.5}$ high-entropy alloys by anodic treatment in sulfuric acid. Thin Solid Films. 2008; 517(3):1301-5.
137. Chou YL, Yeh JW, Shih HC. The effect of molybdenum on the corrosion behaviour of the high-entropy alloys $Co_{1.5}CrFeNi_{1.5}Ti_{0.5}Mo_x$ in aqueous environments. Corros. Sci. 2010; 52(8):2571-81.
138. Chou YL, Wang YC, Yeh JW, Shih HC. Pitting corrosion of the high-entropy alloy $Co_{1.5}CrFeNi_{1.5}Ti_{0.5}Mo_{0.1}$ in chloride-containing sulphate solutions. Corros. Sci. 2010; 52(10):3481-91.
139. Qiu XW, Zhang YP, He L, Liu CG. Microstructure and corrosion resistance of AlCrFeCuCo high entropy alloy. J Alloy Compd. 2013; 549:195-9.
140. Middleburgh SC, King DM, Lumpkin GR, Cortie M, Edwards L. Segregation and migration of species in the CrCoFeNi high entropy alloy. J Alloy Compd. 2014; 599:179-82.
141. Zhang S, Wu CL, Zhang CH, Guan M, Tan JZ. Laser surface alloying of FeCoCrAlNi high-entropy alloy on 304 stainless steel to enhance corrosion and cavitation erosion resistance. Opt Laser Technol. 2016; 84:23-31.
142. Shang C, Axinte E, Sun J, Li X, Li P, Du J, Qiao P, Wang Y. CoCrFeNi ($W_{1-x}Mo_x$) high-entropy alloy coatings with excellent mechanical properties and corrosion resistance prepared by mechanical alloying and hot pressing sintering. Mater. Design. 2017; 117:193-202.
143. Xiao DH, Zhou PF, Wu WQ, Diao HY, Gao MC, Song M, Liaw PK. Microstructure, mechanical and corrosion behaviors of AlCoCuFeNi-(Cr, Ti) high entropy alloys. Mater.Design. 2017; 116:438-47.
144. Wang R, Zhang K, Davies C, Wu X. Evolution of microstructure, mechanical and

corrosion properties of AlCoCrFeNi high-entropy alloy prepared by direct laser fabrication. J Alloy Compd. 2017; 694:971-81.

145. Wu CL, Zhang S, Zhang CH, Zhang H, Dong SY. Phase evolution and cavitation erosion-corrosion behavior of $FeCoCrAlNiTi_x$ high entropy alloy coatings on 304 stainless steel by laser surface alloying. J Alloy Compd. 2017; 698:761-70.
146. Shi Y, Collins L, Feng R, Zhang C, Balke N, Liaw PK, Yang B. Homogenization of AlxCoCrFeNi high-entropy alloys with improved corrosion resistance. Corros. Sci. 2018; 133:120-31.
147. Luo H, Li Z, Mingers AM, Raabe D. Corrosion behavior of an equiatomic CoCrFeMnNi high-entropy alloy compared with 304 stainless steel in sulfuric acid solution. Corros. Sci. 2018; 134:131-9.
148. Shi Y, Collins L, Balke N, Liaw PK, Yang B. In-situ electrochemical-AFM study of localized corrosion of AlxCoCrFeNi high-entropy alloys in chloride solution. App. Surf. Sci. 2018; 439:533-44.
149. Wu JM, Lin SJ, Yeh JW, Chen SK, Huang YS, Chen HC. Adhesive wear behavior of Al_xCoCrCuFeNi high-entropy alloys as a function of aluminum content. Wear. 2006; 261(5-6):513-9.
150. Huang C, Zhang Y, Vilar R, Shen J. Dry sliding wear behavior of laser clad TiVCrAlSi high entropy alloy coatings on Ti–6Al–4V substrate. Mater. Design. 2012; 41:338-43.
151. Liu Y, Ma S, Gao MC, Zhang C, Zhang T, Yang H, Wang Z, Qiao J. Tribological properties of $AlCrCuFeNi_2$ high-entropy alloy in different conditions. Metall. Mater. Trans. A. 2016; 47(7):3312-21.
152. Yu Y, Wang J, Li J, Kou H, Duan H, Li J, Liu W. Tribological behavior of AlCoCrCuFeNi and $AlCoCrFeNiTi_{0.5}$ high entropy alloys under hydrogen peroxide solution against different counterparts. Tribology International. 2015; 92:203-10.
153. Yadav S, Kumar A, Biswas K. Wear behavior of high entropy alloys containing soft dispersoids (Pb, Bi). Mater. Chem.Phys. 2017; 210:222-32.
154. Yu Y, Wang J, Li J, Yang J, Kou H, Liu W. Tribological behavior of AlCoCrFeNi ($Ti_{0.5}$) high entropy alloys under oil and MACs lubrication. J. Mater. Sci.Technol. 2016; 32(5):470-6.
155. Xiaotao L, Wenbin L, Lijuan M, Jinling L, Jing L, Jianzhong C. Effect of Boron on the

Microstructure, Phase Assemblage and Wear Properties of $Al_{0.5}$CoCrCuFeNi High-Entropy Alloy. Rare Metal Mat Eng. 2016; 45(9):2201-7.

156. Ye YX, Liu CZ, Wang H, Nieh TG. Friction and wear behavior of a single-phase equiatomic TiZrHfNb high-entropy alloy studied using a nanoscratch technique. Acta Mater. 2018; 147:78-89.
157. Callister WD. Fundamentals of materials science and engineering. London: Wiley; 2000.
158. Totten GE, MacKenzie DS. Handbook of Aluminum: Vol. 1: Physical Metallurgy and Processes. CRC Press; 2003.
159. Nriagu JO, Nieboer E. Chromium in the natural and human environments. John Wiley & Sons; 1988.
160. Davis JR. Copper and copper alloys. ASM international; 2001.
161. Fairbairn W. Iron: its history, properties, & processes of manufacture. A. and C. Black; 1869.
162. Davis JR. Nickel, cobalt, and their alloys. ASM international; 2000.
163. Sully AH. Metallurgy of the Rarer Metals: 3, Manganese. Butterworths; 1955.
164. Peters M, Hemptenmacher J, Kumpfert J, Leyens C. Structure and properties of titanium and titanium alloys. Titanium and titanium alloys: fundamentals and applications. 2003:1-36.
165. Yang X, Zhang Y, Liaw PK. Microstructure and compressive properties of NbTiVTaAlx high entropy alloys. Procedia Engineering. 2012;36:292-8.
166. Takeuchi A, Inoue A. Classification of bulk metallic glasses by atomic size difference, heat of mixing and period of constituent elements and its application to characterization of the main alloying element. Materials Transactions. 2005; 46(12):2817-29.
167. Taguchi G, Chowdhury S, Wu Y. Taguchi's quality engineering handbook. Hoboken, NJ: John Wiley & Sons; 2005.
168. Zhang Y, Yang X, Liaw PK. Alloy design and properties optimization of high-entropy alloys. Jom. 2012; 64(7):830-8.
169. Cullity BD, Cullity SR, Stock SR. Elements of X-ray Diffraction. Prentice-Hall Inc.; 2001.
170. Ma D, Yao M, Pradeep KG, Tasan CC, Springer H, Raabe D. Phase stability of non-

equiatomic CoCrFeMnNi high entropy alloys. Acta Materialia. 2015; 98:288-96.

171. Yang X, Zhang Y. Prediction of high-entropy stabilized solid-solution in multi-component alloys. Mater. Chem. Phys. 2012; 132:233–8.
172. Miedema A R, Chatel P FD, Boer F RD. Cohesion in alloys—fundamentals of a semi-empirical model. Physica B+c. 1980; 100:1–28.
173. Juan CC, Hsu CY, Tsai CW, Wang WR, Sheu TS, Yeh JW, Chen SK. On microstructure and mechanical performance of $AlCoCrFeMo_{0.5}Ni_x$ high-entropy alloys Intermetallics. 2013; 32:401–7.
174. Wang C, Ji W, Fu Z. Mechanical alloying and spark plasma sintering of CoCrFeNiMnAl high-entropy alloy. Adv Powder Technol. 2014; 25:1334–8.
175. Shafeie S, Guo S, Hu Q, Fahlquist H, Erhart P, Palmqvist A. High-entropy alloys as high-temperature thermoelectric materials. Journal of Applied Physics. 2015; 118(18):184905.
176. Zhang Y, Zhou YJ, Lin JP, Chen GL, Liaw PK. Solid-solution phase formation rules for multi-component alloys. Advanced Engineering Materials. 2008; 10(6):534-8.
177. Wong SK, Shun TT, Chang CH, Lee CF. Microstructures and properties of $Al_{0.3}CoCrFeNiMn_x$ high-entropy alloys. Materials Chemistry and Physics. 2017; 210:146-51.

Appendix-I

LIST OF PUBLICATIONS

Papers published in International Journals

[1] **Vikas Kukshal**, Amar Patnaik and I. K. Bhat, 2018. Effect of cobalt on microstructure and properties of $AlCr_{1.5}CuFeNi_2Co_x$ high-entropy alloys. Materials Research Express, doi.org/10.1088/2053-1591/aaba5f.

[2] **Vikas Kukshal**, Amar Patnaik and I. K. Bhat, 2018. Corrosion and thermal behaviour of $AlCr_{1.5}CuFeNi_2Ti_x$ high-entropy alloys. Materials Today: Proceedings, 5(9), 17073-17079.

[3] **Vikas Kukshal**, Amar Patnaik, I. K. Bhat, 2018. Effect of Mn on corrosion and thermal behaviour of $AlCr_{1.5}CuFeNi_2Mn_x$ high-entropy alloys. IOP Conference Series: Materials Science and Engineering, doi:10.1088/1757-899X/377/1/012023.

Papers published in International Conferences

[1] **Vikas Kukshal**, Amar Patnaik, I. K. Bhat, "Effect of Mn on microstructure and hardness of $AlCr_{1.5}CuFeNi_2Mn_X$ (x = 0, 0.25, 0.5, 0.75,1 in molar ratio) high-entropy alloys", International Conference on High-Entropy Materials (ICHEM 2016), National Tsing Hua University, Hsinchu, Taiwan from November 6^{th} – 9^{th} 2016.

[2] **Vikas Kukshal**, Amar Patnaik, I. K. Bhat, "Microstructures and mechanical properties of $AlCr_{1.5}CuFeNi_2$ high- entropy alloys", International Conference on Emerging trends in Materials and Manufacturing Engineering (iMME17), NIT Trichy from 10^{th} -12^{th} March, 2017.

[3] **Vikas Kukshal**, Amar Patnaik, I. K. Bhat, "Corrosion and thermal behaviour of $AlCr_{1.5}CuFeNi_2Ti_x$ high-entropy alloys", Advances in Materials & Processing: Challenges & Opportunities (AMPCO -2017) at IIT Roorkee from 30^{th} November to 2^{nd} December, 2017.

[4] **Vikas Kukshal**, Amar Patnaik, I. K. Bhat, "Phase evolution and hardness of $AlCr_{1.5}CuFeNi_2Co_x$ high- entropy alloy", International Conference on Nanotechnology: Ideas, Innovations & Initiatives (ICN:3I-2017), IIT Roorkee, from 6^{th} – 8^{th} December, 2017.

Appendix- II

BRIEF BIO-DATA OF THE AUTHOR

Mr. Vikas Kukshal was born on 1st January 1985 in the small town of Srinagar Garhwal, Uttarakhand, India. He completed his bachelors' degree in Mechanical Engineering from Uttar Pradesh Technical University, Uttar Pradesh and post gradation from National Institute of Technology, Hamirpur, Himachal Pradesh with specialization in CAD-CAM. He has total professional experience of about 9 years, out of which two years are in automobile sector and remaining in academics.

He has published six research papers in International journals and presented five research papers in International conference. Since July 2013, he has been engaged in his Doctoral research in the area of development and characterization of high-entropy alloy for high temperature applications at Mechanical Engineering Department, Malaviya National Institute of Technology Jaipur, Rajasthan, India. Presently he is working as an Assistant Professor in the Department of Mechanical Engineering at NIT Uttarakhand, Uttarakhand, India.

****